LA-UR-13-27045
Approved for public release; distribution is unlimited.

Title: Constraining source terms, regional attenuation models, geometric spreading, and site terms for Eurasia

Author(s): Fisk, Mark D.
Phillips, William S.

Intended for: arXiv
Report
Web

Issued: 2013-09-10

AFRL-RV-PS-TR-2013-0081

AFRL-RV-PS-TR-2013-0081

CONSTRAINING SOURCE TERMS, REGIONAL ATTENUATION MODELS, GEOMETRIC SPREADING, AND SITE TERMS FOR EURASIA

Mark Dawson Fisk and William Scott Phillips

Alliant Techsystems
8560 Cinderbed Road, Suite 700
Newington, VA 22122

22 November 2012

Final Report

.

APPROVED FOR PUBLIC RELEASE; DISTRIBUTION IS UNLIMITED.

AIR FORCE RESEARCH LABORATORY
Space Vehicles Directorate
3550 Aberdeen Ave SE
AIR FORCE MATERIEL COMMAND
KIRTLAND AIR FORCE BASE, NM 87117-5776

NOTICE AND SIGNATURE PAGE

AFRL-RV-PS-TR-2013-0081 HAS BEEN REVIEWED AND IS APPROVED FOR PUBLICATION IN ACCORDANCE WITH ASSIGNED DISTRIBUTION STATEMENT.

Robert Raistrick	Edward J. Masterson, Colonel, USAF
Project Manager, AFRL/RVBYE	Chief, Battlespace Environment Division

REPORT DOCUMENTATION PAGE

Form Approved
OMB No. 0704-0188

1. REPORT DATE *(DD-MM-YYYY)*	2. REPORT TYPE	3. DATES COVERED *(From - To)*
22-11-2012	Final Report	22 May 2009 – 22 Nov 2012

4. TITLE AND SUBTITLE
Constraining Source Terms, Regional Attenuation Models, Geometric Spreading, and Site Terms for Eurasia

5a. CONTRACT NUMBER
FA8718-09-C-0005

5b. GRANT NUMBER

5c. PROGRAM ELEMENT NUMBER
62601F

6. AUTHOR(S)
Mark Dawson Fisk and William Scott Phillips*

5d. PROJECT NUMBER
1101

5e. TASK NUMBER
PPM00005939

5f. WORK UNIT NUMBER
EF004581

7. PERFORMING ORGANIZATION NAME(S) AND ADDRESS(ES)

Alliant Techsystems
8560 Cinderbed Road, Suite 700
Newington, VA 22122

*Los Alamos National Laboratory
PO Box 1663
Los Alamos, NM 87545

8. PERFORMING ORGANIZATION REPORT NUMBER

9. SPONSORING / MONITORING AGENCY NAME(S) AND ADDRESS(ES)
Air Force Research Laboratory
Space Vehicles Directorate
3550 Aberdeen Avenue SE
Kirtland AFB, NM 87117-5776

10. SPONSOR/MONITOR'S ACRONYM(S)
AFRL/RVBYE

11. SPONSOR/MONITOR'S REPORT NUMBER(S)
AFRL-RV-PS-TR-2013-0081

12. DISTRIBUTION / AVAILABILITY STATEMENT Approved for public release; distribution is unlimited.

13. SUPPLEMENTARY NOTES

14. ABSTRACT
We develop and evaluate methods to separate seismic source, attenuation (Q), spreading, and site effects, to improve corrections for regional amplitudes. We use relative spectra for nearby, similar event pairs, to cancel path and site effects, and estimate reliable corner frequencies and relative moments. We process a large dataset for Eurasia. We compare source terms estimated from direct phases and Lg coda to verify the results or flag discrepancies. We then fit source-corrected spectra to estimate Q, spreading, and site terms, and obtain a consistent set of absolute moments. At every stage, we compare our results to existing calibration terms, showing good agreement in many cases, but also serious errors that impact P/S discrimination, as shown for Iran. Our delivered results can be used as constraints in amplitude tomography analyses to improve calibration.

15. SUBJECT TERMS
Regional seismic phases, Lg coda, source terms, attenuation, geometric spreading, site effects, calibration, regional discrimination

16. SECURITY CLASSIFICATION OF:			17. LIMITATION OF ABSTRACT	18. NUMBER OF PAGES	19a. NAME OF RESPONSIBLE PERSON
a. REPORT	**b. ABSTRACT**	**c. THIS PAGE**			Robert Raistrick
Unclassified	Unclassified	Unclassified	SAR	124	**19b. TELEPHONE NUMBER** *(include area code)* 505-846-6057

Standard Form 298 (Rev. 8-98)
Prescribed by ANSI Std. 239.18

This page is intentionally left blank.

Table of Contents

List of Figures

1 INTRODUCTION

Many studies have shown that reliable P/S discrimination requires valid distance corrections (e.g., Sereno et al., 1988; Fisk et al., 1993, 1996, 2001, 2010; Phillips et al., 1998; Phillips, 1999; Bottone et al., 2002; and references therein). To use combinations of regional amplitudes in different frequency bands further requires valid corrections for source corner-frequency effects. Regional magnitudes also need accurate corrections. Procedures that simultaneously invert for source, geometric spreading, attenuation (Q), and site parameters are known to have many trade-offs (e.g., Taylor and Hartse, 1998), resulting in large errors for source and distance corrections, as shown by Fisk and Taylor (2006) and Fisk and Phillips (2009), and described in Section 2. This motivated our development and testing of methods to constrain the trade-offs, to improve the accuracy of these parameters.

To do so, we start by computing and fitting relative spectra for nearby, similar event pairs of different moments, to cancel path, site, and radiation pattern effects, and estimate reliable corner frequencies and relative moments. We used the Preliminary Determination of Epicenters (PDE) bulletin from 1989 to 2009 (almost 21 years) to find 46,494 candidate earthquake pairs with different moments, corresponding to 9,395 unique events throughout Eurasia. We acquired regional recordings from IRIS for these events, and processed waveform cross-correlations to assess similar event pairs. We then computed millions of spectra of Pn, Pg, Sn, and Lg, as well as coda envelopes, formed network-median relative spectra, and fit a relative Brune (1970) earthquake source model. We used comparisons of source terms estimated from direct phases and Lg coda to confirm reliable corner frequencies and relative moments. Section 3 describes the approach, dataset, and the estimated source parameters in more detail. To build confidence in the procedure and the resulting source terms, Section 4 presents detailed investigations of their reliability, inter-station variability, and various causes of discrepancies. The results indicate the benefits of incorporating independent measurements of coda and direct-phases, leading to a large set of corroborated source terms for earthquakes throughout Eurasia. Discrepancies of source estimates from coda versus direct phases indicate problems, often due to data quality issues.

Using a subset of corroborated source terms, we then corrected the spectra of various regional phases for source effects, and fit the corrected spectra to estimate frequency-dependent Q for fixed paths. This is a distinct (*orthogonal*) approach to amplitude tomography that estimates the path dependence of Q for fixed frequency bands. Comparing the results from independent measurements and inversion methods verifies paths with reliable Q estimates and identifies necessary improvements. The Q_0 estimates from the two approaches generally agree reasonably well, particularly for areas with good station coverage. Section 57 describe the assumptions, the approach, detailed comparisons with tomography, and the overall Q results for various phases. Section 8 investigates large discrepancies in the Q estimates, usually for higher frequencies, in low Q regions and/or at the edges of the tomography grid. Section 9 describes how the fits of source-corrected spectra are also used to estimate the geometric spreading rate for each phase. We also show that this analysis provides a way to estimate a very consistent set of absolute moments for the earthquakes. We find that constant power-law models (Street et al., 1975) fit the Lg, Sn, and Pg data quite well, and yield similar spreading exponents to previous studies. Pn clearly departs from constant power-law spreading behavior at far regional distances (beyond about 1500 km), due to sphericity, upper mantle triplication, and other propagation effects. As described in Section 10, we subsequently corrected the spectra for source, Q, and spreading terms, and computed the median spectral residual for each regional seismic phase and station, to estimate frequency-dependent site effects. We compare our results to independent site terms estimated from Lg coda tomography. We find that many of our estimates of site frequency dependence agree with Lg coda site terms, even for Pg at many stations, verifying these terms. We also highlight some discrepancies and discuss the causes. We have also applied the site corrections to the spectra, to quantify residual variances versus frequency, partitioned by physical contributions. Throughout, the structure of this report is to describe (1) the approach, (2) representative examples to indicate the utility, (3) the overall results and comparisons to independent analyses, and (4) discrepancies, including their physical causes, to both indicate the benefits of the current results and areas for future improvements.

We have demonstrated the benefit of using multiple observations and analysis methods to both confirm physical correction parameters and determine discrepancies that need to be redressed. From this work, we have identified three critical ways that Q and spreading models must be improved and evaluated. First, tomography results are unreliable near grid edges, particularly important for the Middle East, where data sampling issues (i.e., limited crossing ray paths, particularly for higher frequencies) lead to large errors for tomography, but not our method. Tomography can be adapted to use our results as constraints. Second, data quality has a direct impact on calibration. Existing signal-to-noise (S/N) tests do not exclude enough bad data, while retaining a majority of good data, particularly for secondary phases that are in the coda of preceding phases. We describe enhanced (physically-based) data quality criteria to determine useful frequency ranges. Third, Pn is the most complicated regional phase, with highly variable spectral measurements, the least reliable tomography results, and more complicated spreading effects than other phases. Although Pg is typically more stable than Pn, there is only a fraction of Pg observations compared to Pn, due to propagation distances. Thus, improving and validating Pn Q and spreading models are paramount for application of P/S discriminants to broad areas. We show that existing tomography results by LANL and LLNL have order-of-magnitude errors that directly impact P/S discrimination results, and recommend efforts to rectify these issues.

We show that our approach is very effective at separating various physical effects, but it does have some limitations and assumptions. It is applicable to larger pairs, a much smaller subset of events than used for tomography. In principle, the approach can be applied to any similar event pairs with about a 1 magnitude unit (m.u.) difference, needed to adequately resolve the corner frequencies. However, for practical applications, using the sparse IRIS seismic network, the smaller event of each pair must usually be larger than about magnitude 4 to 4.5, to have adequate S/N. Requiring agreement of source estimates between direct phases and coda further limits the number of events considered. Despite the limitations, we show good spatial distribution of many solutions. Our objective is fundamentally unique, i.e., not to just reduce variability by including as much data as possible, but to establish a set of carefully-reviewed, high-quality calibration solutions that can be used to constrain amplitude tomography runs. Such runs will promulgate our results, impacting nearby areas and crossing ray paths. Unlike tomography, our approach does not require crossing ray paths to resolve the various physical parameters, providing constraints for many paths and extending calibration to the grid edges (e.g., Russia, India, and the Middle East), where tomography results are known to have significant errors. Thus, our approach combines the strengths of both methods in a complementary fashion.

At the outset of our analysis, we fit relative spectra for event pairs to estimate corner frequencies and relative moments. We assume that the radiation pattern effects are canceled, based on our comparisons of relative spectra for direct phases to coda, and the well-documented result that coda measurements are insensitive to focal mechanism, event separation, and station coverage (Mayeda et al., 2007). The spectra, corrected for moment and corner frequency effects, used to estimate distance and site effects, do include radiation pattern effects. However, such effects are assumed to be independent of frequency (e.g., Brune, 1970), so they do not affect our estimates of corner frequencies, *Q(f),* or frequency-dependent site effects. They can affect spreading and constant site factors, but we assume these effects are minimal by averaging over many events and/or stations. Note also that we initially tied the absolute moments to PDE Mw values for the larger events, which we assumed to be better recorded and, hence, more accurate. Based on our subsequent analysis of source-corrected spectral fits to quantify geometric spreading, we found that some PDE Mw estimates have errors as large as 0.5-0.8 m.u., although most are in the range of 0.1-0.2 m.u. As for radiation pattern effects, absolute moment errors do not impact our corner frequency estimates, which, in turn, do not affect our *Q(f)* estimates. A high/low Mw estimate simply shifts all source-corrected spectra for the event low/high. Our ultimate goal is to improve tomography results, which can be affected by Mw errors. Using the constants of source-corrected spectra for a given event, as compared to the Eurasian average, we have now updated the results to give a consistent set of absolute moments, corner frequencies, *Q* parameters, and spreading rates. We delivered these correction parameters to LANL for future use as constraints.

2 BACKGROUND AND MOTIVATION

Following Sereno et al. (1988), Taylor and Hartse (1998), Taylor et al. (2002), and many others, the amplitude spectrum for a given seismic phase and station, for event *i*, is modeled by

$$A_i(f) = S_i(f; M_0, f_c) G(r_i; r_0, \eta) \exp\left(-\frac{\pi f^{1-\gamma}}{Q_0 \nu} r_i\right) P(f), \tag{1}$$

where $S_i(f)$ is the source spectrum with moment M_0 (and radiation pattern terms) and corner frequency f_c (related to stress drop), r_i is distance, $G(r_i;r_0,\eta)$ represents frequency-independent geometrical spreading, inversely proportional to distance to a power η, beyond a reference distance r_0, $Q_0 f^{\gamma}$ represents attenuation, ν is group velocity, and $P(f)$ is a frequency-dependent site term. Because this model has been used so prevalently in the U.S. nuclear explosion monitoring community, we refer to Eq. (1) as "the Standard Model". While advances have been made to compute the physical parameters, methods that invert for all parameters simultaneously (e.g., grid searches) are known to have many trade-offs and instabilities over the parameter space (e.g., Taylor and Hartse, 1998; Fisk and Taylor, 2006; Fisk and Phillips, 2009). Such calibration errors lead to serious discrimination errors, as shown in Section 8.3 for Iran.

Figure 1 illustrates the problem for a pair of earthquakes in January 1999 at the Lop Nor test site (LNTS). Shown are relative spectra of Pn, Pg, Sn, Lg, and Lg coda for the larger (mb 5.9) to smaller (mb 4.5) events, and our relative source model fits (see legend). For each phase, we formed the ratios for 25 regional stations, and computed the network median. High waveform cross-correlations indicate that the events have similar epicenters and focal mechanisms. Both events also have similar depths of about 20 km, based on well-constrained depth-phase solutions.

Thus, radiation pattern, path, and station effects cancel in the relative spectra. Also shown are Brune (1970) predictions using the Pn and Lg moment and corner-frequency scaling relations of Xie and Patton (1999) [XP99] (thick red and blue curves, respectively) from their grid-search inversion of Eq. (1) for the Lop Nor area. Their source predictions are clearly inconsistent with the relative spectrum, giving Pn and Lg corner frequencies of 1.32 Hz and 0.26 Hz for the larger event, factors of 1.9 too high for Pn and 2.7 too low for Lg, compared to f_c of about 0.7 Hz from the relative spectra. Their ratio of $f_c(Pn)/f_c(Lg) = 5.1$ is much higher than results of between 1.0 and 1.73 for earthquakes (e.g., Madariaga, 1976; Choy and Boatwright, 1995; Walter and Taylor, 2002, Fisk and Taylor, 2008). Correspondingly, their Q estimates are too low for Pn and too high for Lg, causing high-frequency Pn/Lg for earthquakes to appear explosion-like.

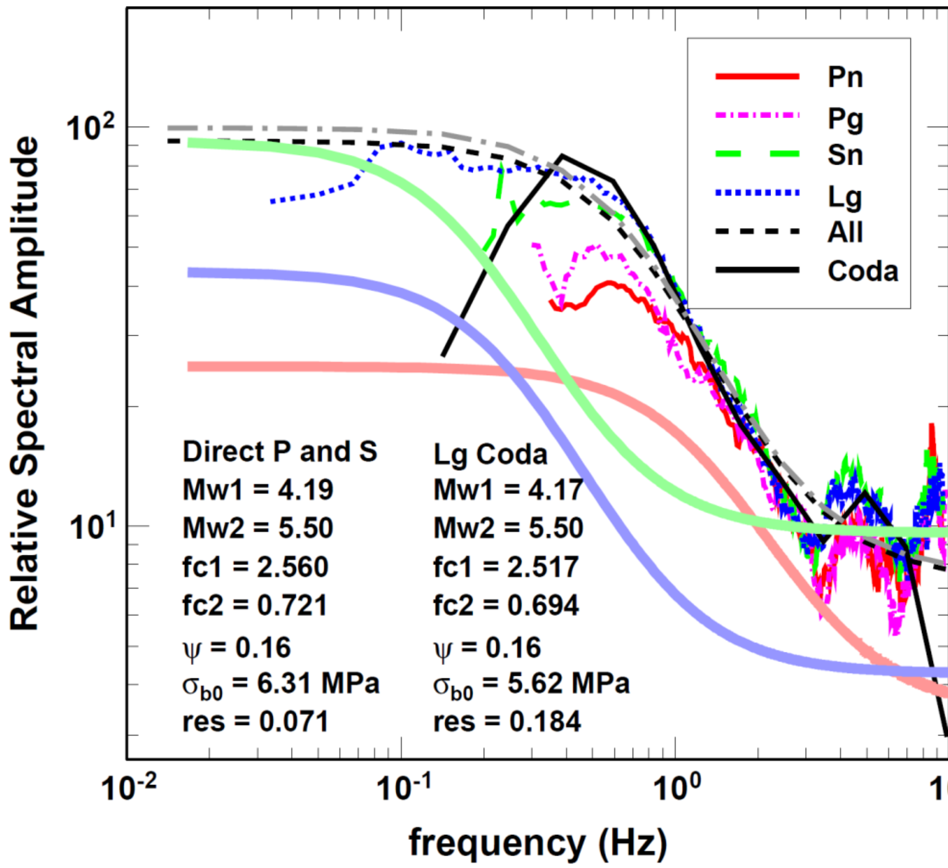

Figure 1. Network relative spectra and source model fits, for two similar earthquakes at LNTS. Also shown are Brune model predictions using the Pn (thick red) and Lg (thick blue) scaling relations of XP99, and from the MDAC grid-search estimate of stress drop (thick green).

Fisk and Phillips (2009) also showed that Magnitude and Distance Amplitude Corrections (MDAC) parameters, using a grid search inversion (cf. Taylor et al., 2002), have large f_c and Q errors for Lop Nor events, due to similar trade-offs. The thick red curve in Figure 1 shows the relative Brune model for these events, using the MDAC estimate of stress drop (0.1 MPa, Taylor, 2008, pers. comm.), about a factor of 60 lower than estimated by fitting the empirical relative spectra. As a consequence of the trade-off between stress drop and attenuation, the MDAC grid search over-estimates Q. To demonstrate this, as described in Section 5, we use the source-corrected spectra to estimate distance and site effects. Figure 2 shows the source-corrected Lg spectra at MAKZ for the same pair of earthquakes, our Q model fit (dashed curve), and the MDAC Q prediction (dotted curve). The two model curves are fairly similar for frequencies up to about 1 Hz, which is expected because the Q_0 estimates are similar, but diverge significantly at higher frequencies. This discrepancy is caused by an unconstrained MDAC estimate of stress drop that is more than an order of magnitude too low, compared to the estimate from the relative spectra (Figure 1). Note that if the stress drop is under-estimated, so is the corner frequency, which leads to under-correcting the spectra for the source term at higher, relative to lower, frequencies. This leads to the appearance of more efficient propagation at higher frequencies than actually exists and, hence, yields a higher estimate of Q. This is why the dotted black curve in Figure 2, using the MDAC parameters, is more than an order of magnitude too high at higher frequencies. Without constraints, the estimated MDAC corrections are very inaccurate for both source and distance effects at LNTS. This highlights the importance and benefit of our approach, which first constrains the source terms, leading also to more accurate estimates of Q.

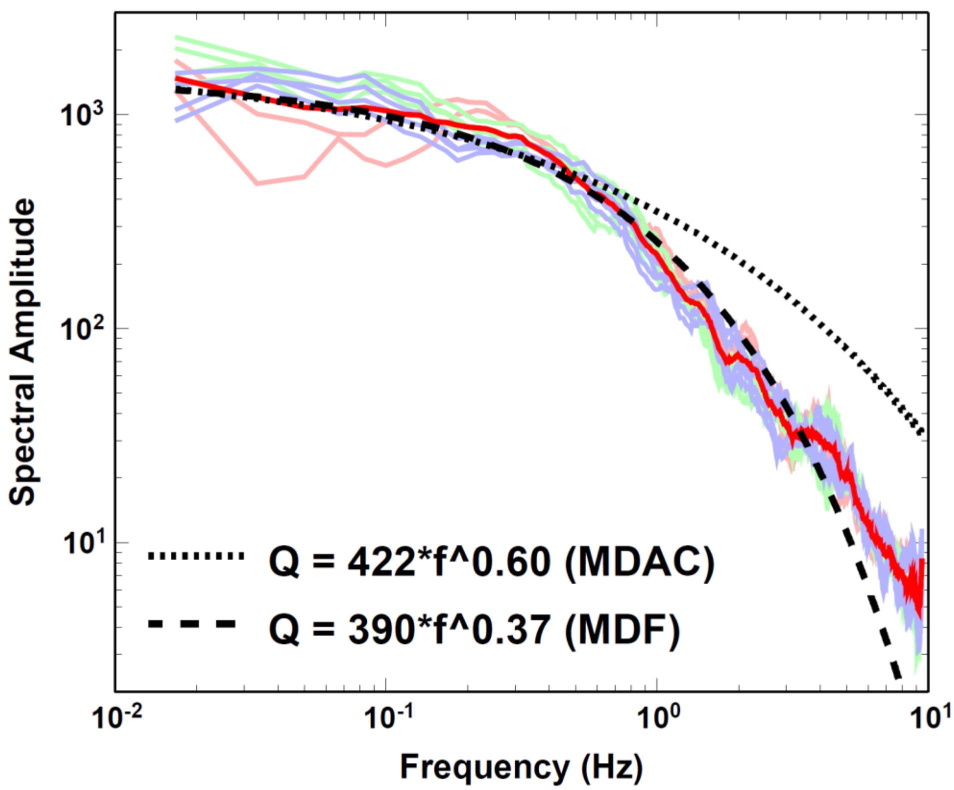

Figure 2. Source-corrected Lg spectra for LNTS earthquakes recorded by station MAKZ, our Q model fit (dashed), and using unconstrained MDAC Q parameters (dotted).

These results motivated us to develop a procedure to constrain more accurate parameter estimates. In the remainder of this report, we describe (1) the dataset used for our analysis; (2) our approach for estimating source terms and the results for earthquakes throughout Eurasia; (3) how we estimate Q, spreading and site effects from source-corrected spectra. We then discuss the implications of the results and comparisons to independent data and methods, and provide recommendations for further improvements of calibration terms for Eurasia.

3 ESTIMATING SOURCE TERMS

3.1 Technical Approach

Rather than inverting for all parameters of Eq. (1) simultaneously, we start by computing and fitting relative spectra for similar event pairs (assessed by waveform cross-correlations) of different moments, to cancel path and site effects, and estimate reliable corner frequencies and relative moments. That is, for a pair of nearby earthquakes with similar locations and radiation patterns (canceling all of the densities, velocities, and radiation pattern terms), the relative spectra for a given seismic phase type is modeled (Brune, 1970) by

$$\frac{A_1(f)}{A_2(f)} = \frac{S_1(f)}{S_2(f)} = \frac{M_0^{(1)}\left[1+\left(f/f_c^{(2)}\right)^2\right]}{M_0^{(2)}\left[1+\left(f/f_c^{(1)}\right)^2\right]}. \tag{2}$$

The corner frequencies are related to stress drop by

$$f_c = cv\left(\frac{\sigma_b}{M_0}\right)^{1/3} \quad \text{and} \quad \sigma_b = \sigma_b^{(0)}\left(\frac{M_0}{M_0^{(0)}}\right)^{\psi} \tag{3}$$

where v is the source medium velocity for P or S waves, c is a constant that can depend on phase type, M_0 is the moment, and σ_b is stress drop, which can be defined in terms of apparent stress or a reference stress drop, $\sigma_b^{(0)}$, at a reference moment, $M_0^{(0)}$, and an exponent ψ to allow for non-constant scaling (Walter and Taylor, 2002). In the results shown below, we provide the estimates of moment magnitudes, corner frequencies, and their relations to the stress drop, $\sigma_b^{(0)}$ and ψ. Broad applicability of this empirical Green's function (EGF) approach requires many similar pairs. Using waveform cross-correlations, Schaff and Richards (2004) showed that there are indeed many repeating events (i.e., with similar locations and focal mechanisms) throughout China. Fisk et al. (2008) confirmed this result for events throughout Eurasia.

In addition, Mayeda et al. (2007) showed that coda measurements are less sensitive to focal mechanism, event separation, and station coverage, allowing the requirement of similar events to be relaxed, augmenting the number of pairs for which we can estimate source terms. Thus, in addition to fitting relative spectra of direct regional phases, we compute coda envelopes, using the method of Mayeda et al. (2003) and Phillips et al. (2008), compute a pseudo relative spectrum as the median ratio of coda envelopes in 16 frequency bands, and fit it. For example, Figure 3 shows an example of coda envelopes based on MK31/BHZ (broadband, vertical-component) data. The magenta curves were computed by Dr. Scott Phillips for a subset of the frequency bands (i.e., except for the highest and two lowest bands) to validate the program. There are differences at the ends of the waveform segments, due to processing artifacts for the different lengths of the waveform segments used, but they are well outside the measurement windows. Frequency bands, smoothing widths, parameters for coda onset, and measurements windows are from Phillips et al. (2008). (Some of the measurement windows for the lowest frequency bands have been truncated due to length of the waveform segment. We have since acquired longer segments from IRIS so that this is not an issue for the large-scale processing we performed.) We also established frequency-dependent noise windows, prior to Pn or Pg onset.

Following Phillips et al. (2008), the coda amplitude at frequency *f* may be expressed as

$$A_{ij}^{coda}(f) = S_i(f)T(\phi_i,\theta_i,f)P'(\phi_i,\theta_i,\phi_j,\theta_j,f)R'(f)D'_j\left[r,f,t_c(r,f)+t_m(f)\right], \qquad (4)$$

where *i* and *j* are the source and site indices, respectively; ϕ and θ are the latitude and longitude of the event or station (depending on the indices); *S* represents the source spectrum; *T* is a 2D, frequency-dependent, source-to-coda transfer term; *P′* is a 2-D path term; *R′* is a site amplification term; and *D′* is a coda decay function that depends on the propagation distance, frequency, coda start time (t_c), and the measurement time (t_m). The primes indicate relative or dimensionless terms. Typically, considerable effort has been required to calibrate all of the transfer, path, site, and coda decay terms. Similar to Eq. (2), note all but the source term, *S*, cancel when taking the ratio of amplitudes in the same band for closely located events. To compute a pseudo relative spectrum from the coda envelope measurements (viz. Figure 3), we compute the median relative amplitude over the measurement time window for each of the 16 bands. This approach avoids the need to perform the usual coda calibration, a vast simplification.

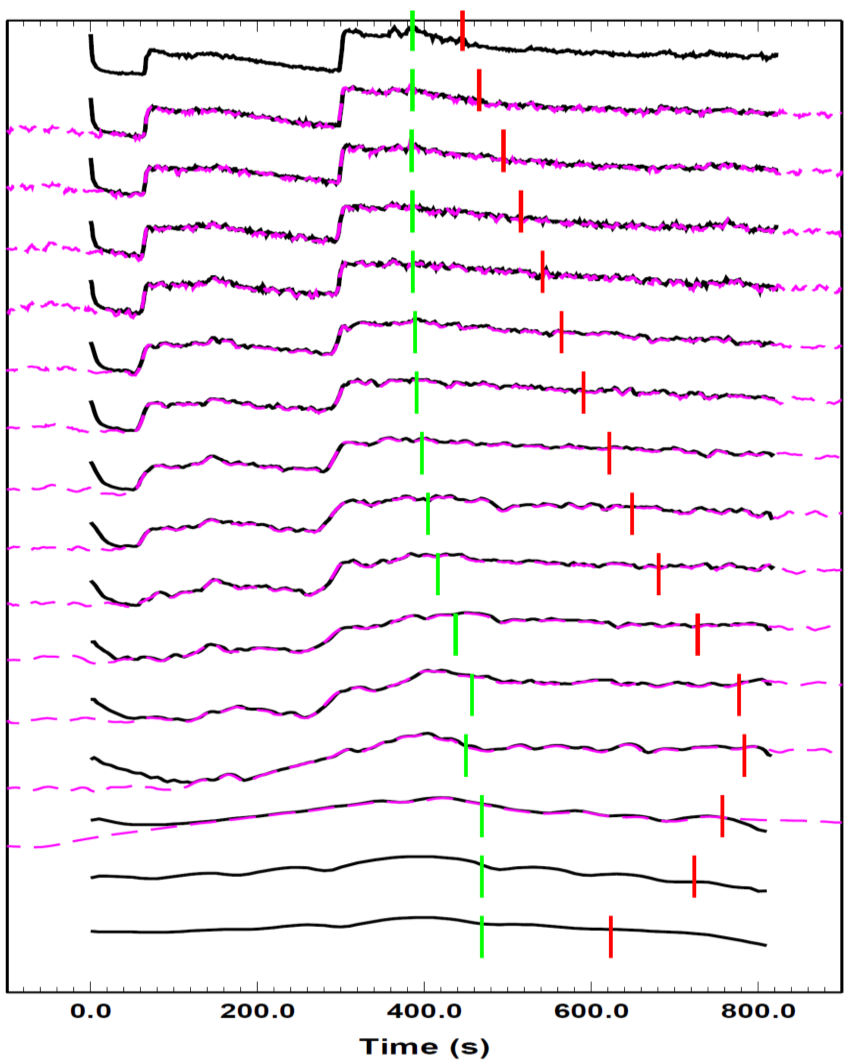

Figure 3. Example of Lg coda envelopes in 16 frequency bands ranging from 0.01-0.02 Hz (bottom) to 8-12 Hz (top). The vertical green and red lines indicate measurement windows.

Figure 4 shows relative spectra of Pn, Sn, Lg, and Lg coda, along with source model fits for an earthquake pair in southwestern Siberia. The estimated source parameters from direct phases and coda agree very well. Note that the relative coda spectrum, just using MK31 three-component (3C) data (magenta curve), is nearly the same as the network results for coda or direct phases using 19 stations. Using independent measurement windows and processing methods for direct-phase spectra and coda envelopes corroborates the estimated relative moments and corner frequencies. Note also that, modulo differences in S/N and variability for the various seismic phases, the relative spectra for all of the phases have very similar corner frequencies. This is a very common observation for earthquakes, in contrast to underground explosions, which have considerably lower corner frequencies for S waves than P waves, scaling approximately as the ratio of S and P velocities in the near source emplacement medium (Fisk, 2006, 2007).

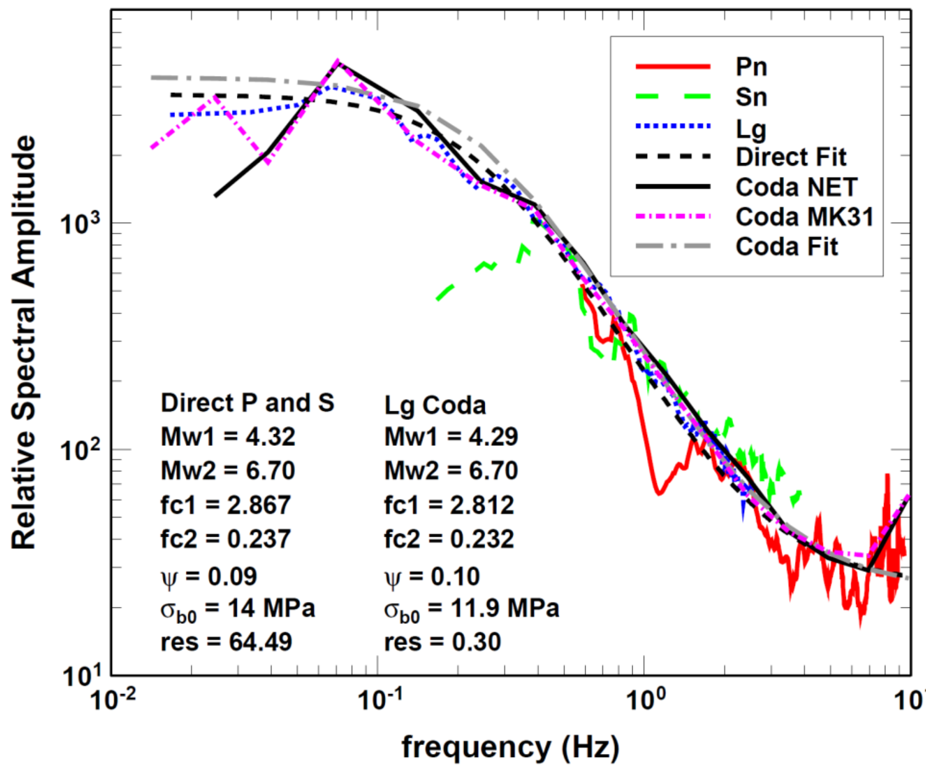

Figure 4. Network-median relative spectra of Pn, Sn, Lg, and Lg coda (using 19 stations and just MK31) for an event pair in southwestern Siberia.

Figure 5 and Figure 6 show two more examples of relative spectra and source model fits for smaller pairs of earthquakes in northwestern China and Russia. The fits and estimated source parameters from direct phases and coda agree very well, although some Pg and Sn spectra are more variable than the previous example. In fitting the relative spectra of direct phases, we weight Lg four times higher than Pn, Pg, and Sn, because Lg spectra are generally the most stable. These cases are indicative of the agreement between coda and direct phases for many pairs at this magnitude level. Note that the coda relative spectra at frequencies less than 0.1 Hz dip lower than for direct Lg because coda is biased more by noise for the smaller events (Mw 4.2 and 4.5) of each pair. Also shown are corresponding source model predictions based on corner frequencies and moments estimated from an amplitude tomography run at LANL (see upper right legends) that used multiple bands and multiple seismic phases. Some of those estimates moments and corner frequencies are very inconsistent with the estimates from relative spectra (listed in the legends), similar to the comparisons shown in Figure 1. For example, the corner frequency estimates from tomography in Figure 5 are about a factor of three too high for this pair. As shown above, this has a direct impact on Q estimates. There are many such cases. We have also found many cases for which the estimates of source and Q parameters from tomography are very consistent with ours. Below, we illustrate additional representative cases, but it is important to note the level of errors in source parameters estimated from unconstrained inversion methods (grid searches or tomography). In Eq. (2), we assume a Brune (1970) source model with f^2 roll-off. Abercrombie et al. (2009) have suggested that alternate earthquake source models may fit some data better. We do not dispute this, but somewhat different earthquake source models are second order, compared to the errors of existing inversion methods.

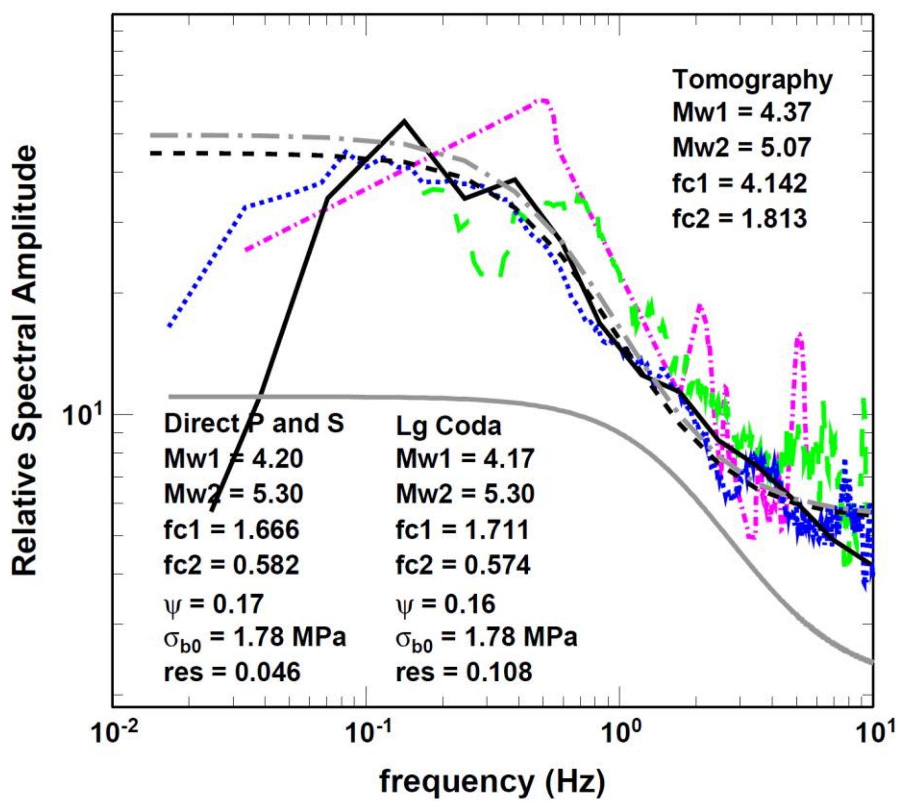

Figure 5. Network-median relative spectra of Pg, Sn, Lg, and Lg coda for a smaller earthquake pair in northwestern China. The solid gray curve represents source predictions for the events from a multi-band, multi-phase tomography run at LANL.

3.2 Large-Scale Application

Given our approach, a substantial task was to find candidate pairs and acquire regional seismic recordings for analysis. Figure 7 shows events listed in the United States Geological Survey (USGS) Preliminary Determination of Epicenters (PDE) bulletin from 1989 to 2009 (almost 21 years of data) for the rectangular region shown. From the bulletin information, we found a subset of candidate event pairs, from which might be able to estimate source parameters, based on proximity and magnitude difference. That is, we selected events that have epicenters within 50 km of another event, with a magnitude difference of at least 0.7 magnitude units and the larger (*master*) event of each pair at least mb 5. Their criteria were based on previous analysis by Fisk et al. (2008) and Schaff and Richards (2004), and are somewhat lax to account for location and magnitude errors in the PDE. We have found that about 1 (one) magnitude unit (m.u.) difference in the events is generally needed to adequately resolve the corner frequencies. The set includes 46,495 such candidate pairs, corresponding to 9,395 unique events, shown in Figure 8, giving upper bounds of 46,000 estimates of source terms and up to 225,000 ray paths (blue curves in Figure 8) to estimate path and site correcti ons.

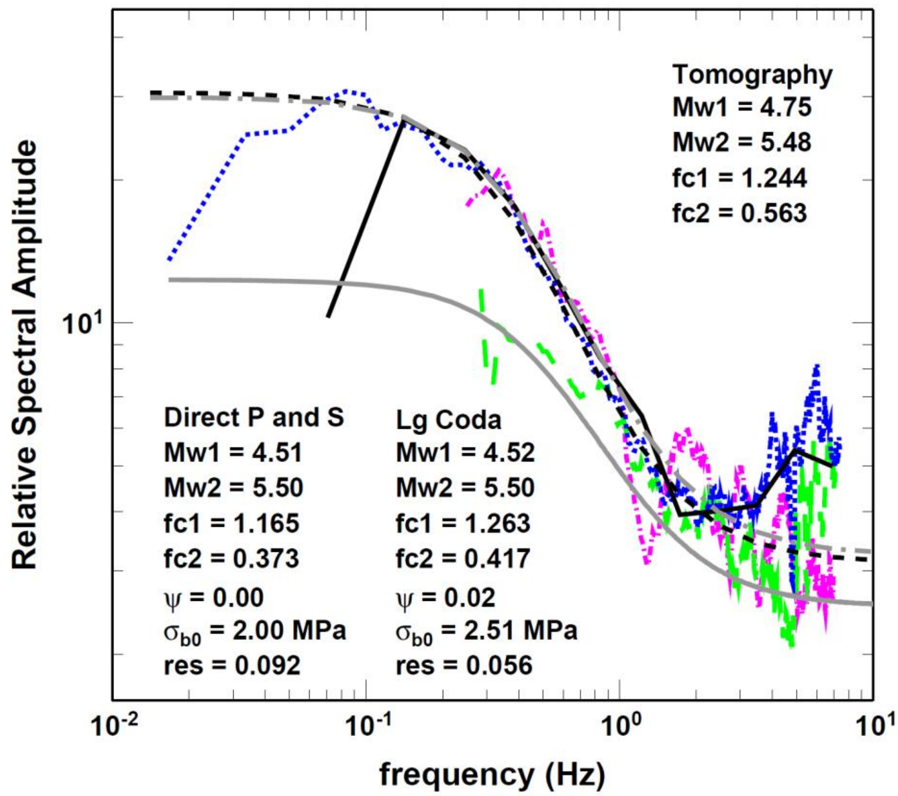

Figure 6. Similar to Figure 5, but for an earthquake pair in Russia.

As described above, a key aspect of this project has been to incorporate Lg coda measurements, which are less sensitive than direct seismic phases to focal mechanism effects, spatial separation of the events, and the number and coverage of recording stations. However, measuring coda envelopes, particularly in low frequency bands, requires long time windows. Thus, we formatted Breqfast email requests, corresponding to the events and ray paths shown in Figure 8, allowing for adequate coda measurement windows, submitted them to the IRIS Data Management Center (DMC), and downloaded a very large volume of regional seismic data (approximately 600,000 waveforms, some as much as 2000 seconds long, depending on epicentral distance).

We then parsed the PDE information (origin time, location, depth, and magnitudes) into origin files, assigning an orid to each event, and parsed the wfdisc files and waveforms from the SEED volumes, based on distance-dependent time intervals for each event, into event solutions in CSS

3.0 format. We used a program to automatically make theoretical phase picks, based on IASP91 travel-time tables for Pn, Pg (as appropriate), Sn, and Lg at all stations for which waveforms are available, and to format this information as arrival and assoc files for each event. As a final step in parsing the data, we wrote and used a program to check for redundancies and whether the waveform segments actually include the predicted regional phase arrivals. Without going into the details, parsing the PDE catalog and IRIS data into event solutions, and checking/rectifying problems for nearly 10,000 events and hundreds of thousands of waveforms is nontrivial.

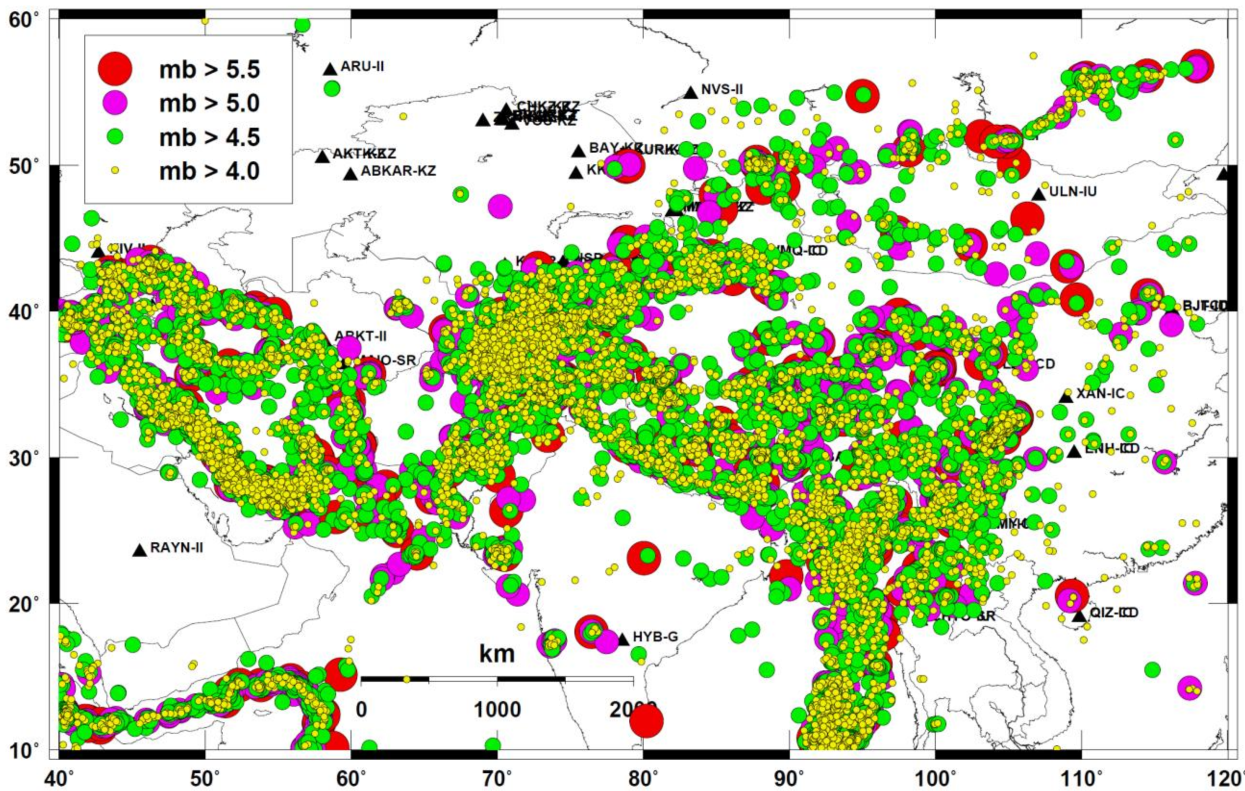

Figure 7. Map of events listed in the PDE from 1989 to 2009 for the rectangular region shown.

We then processed waveform cross-correlations for each station and all candidate pairs, i.e., for the events and paths shown in Figure 8. We processed about 2,000,000 spectra of regional phases and about 10,000,000 coda envelopes. In previous analyses of spectra for direct phases, we computed and fit relative spectra only for pairs with significant cross-correlations, indicating events with similar hypocenters and focal mechanisms. However, because we now also process coda, which is insensitive to differences in radiation pattern and location, we computed network-median relative spectra and fit Eq. (2) for all candidate pairs. We primarily use comparisons of results from direct phases and coda to determine consistent (i.e., corroborated) source parameter estimates. Rather than as a specific criterion for processing relative spectra of candidate pairs, here we use the waveform cross-correlations in an ancillary role, to understand discrepancies between direct and coda results that are due to non-similar event pairs. This will be highlighted below. All of the processing to this point (from requesting the data, forming event solutions, to fitting relative spectra) is performed in a largely automated mode.

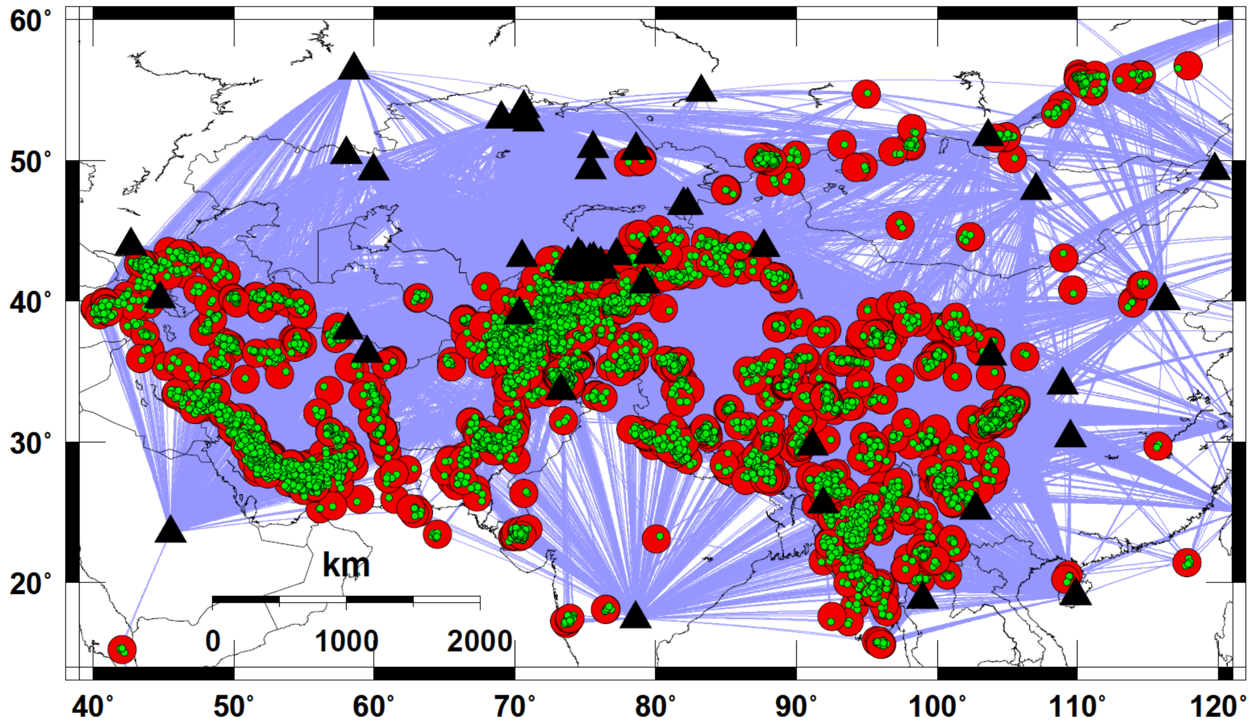

Figure 8. Map of candidate event pairs (red and green circles), ray paths (blue curves), and IRIS stations (triangles) for which regional seismic data were requested from the IRIS DMC, indicating very good coverage throughout much of Eurasia.

We subsequently reviewed the results for $Mw \geq 5.4$ master events, as well as smaller events in areas of interest. Figure 9 is similar to Figure 8, but depicts the results after this review. The bright markers in Figure 9 indicate events with consistent source estimates from coda and direct phases (cf. Figure 10). The faint markers correspond to smaller processed pairs, and ones with inconsistent source parameters from coda and direct phases, that need further review. Figure 9 also shows ray paths to regional IRIS stations only for events with corroborated source terms, fewer than in Figure 8, but still indicating good coverage for much of Eurasia. Unlike amplitude tomography, our approach does not require crossing ray paths to estimate the parameters of Eq. (1), providing constraints for many paths and extending calibration to the edges (e.g., Russia, India, and the Middle East). Below, we discuss the importance of this issue.

Figure 10 compares estimates of moment magnitudes (left) and corner frequencies (right) for event pairs with good agreement from coda and direct phases. Recall that we fixed the moments of the master events, using PDE values; thus, the Mw values are identical (for coda and direct phases) for these larger events. These values were not included in the regression of Mw estimates, which have excellent correlation (slope of 1.0), negligible bias (0.02) and small standard deviation (0.07). Likewise, the log corner frequency estimates have high correlation, negligible bias, and small standard deviation. We consider this set of events to have good, corroborated source parameters. We show in Section 9, in conjunction with the geometric spreading analysis, that some PDE Mw estimates, even for the large master events have errors, typically in the 0.1-0.2 m.u. range, but some as high as 0.8 m.u. We show how we obtain a very consistent set of absolute moments from this information.

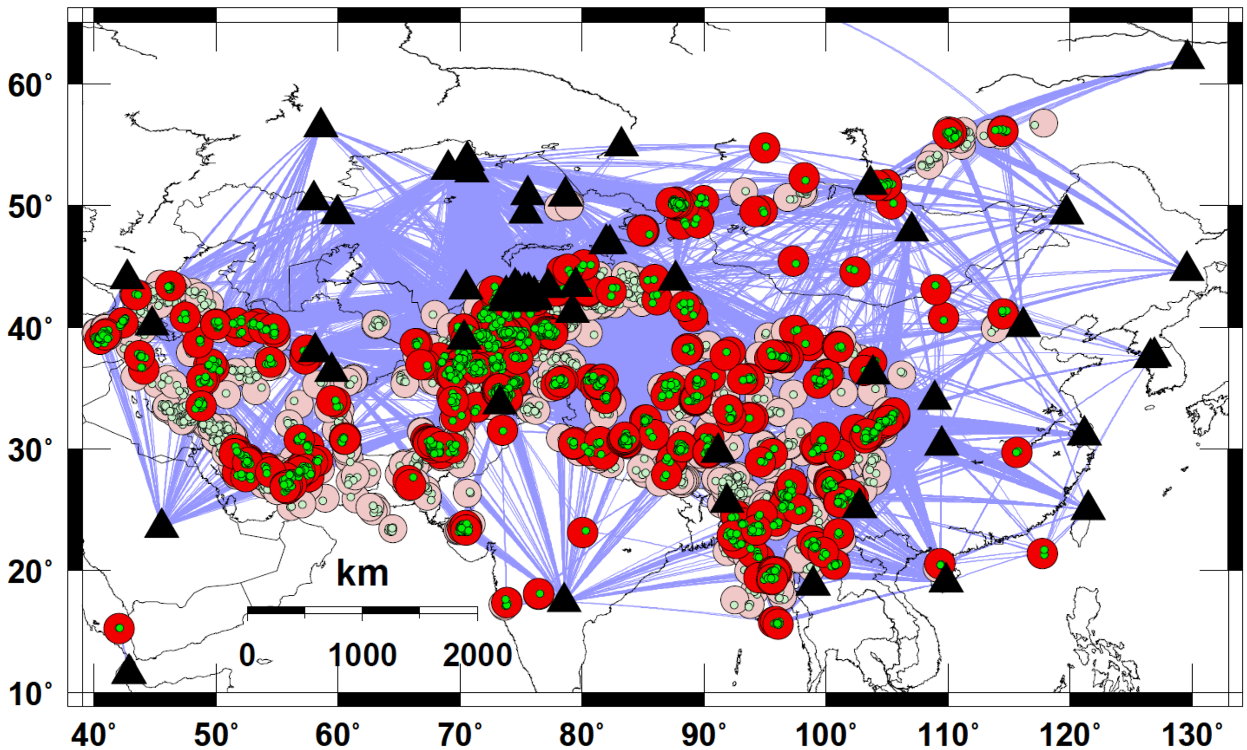

Figure 9. Earthquakes listed in the PDE (1989-2009) for which we processed and fit relative spectra. Red circles indicate larger events within 50 km of smaller events (green circles). Bright circles and paths are shown for events with consistent source terms from coda and direct phases.

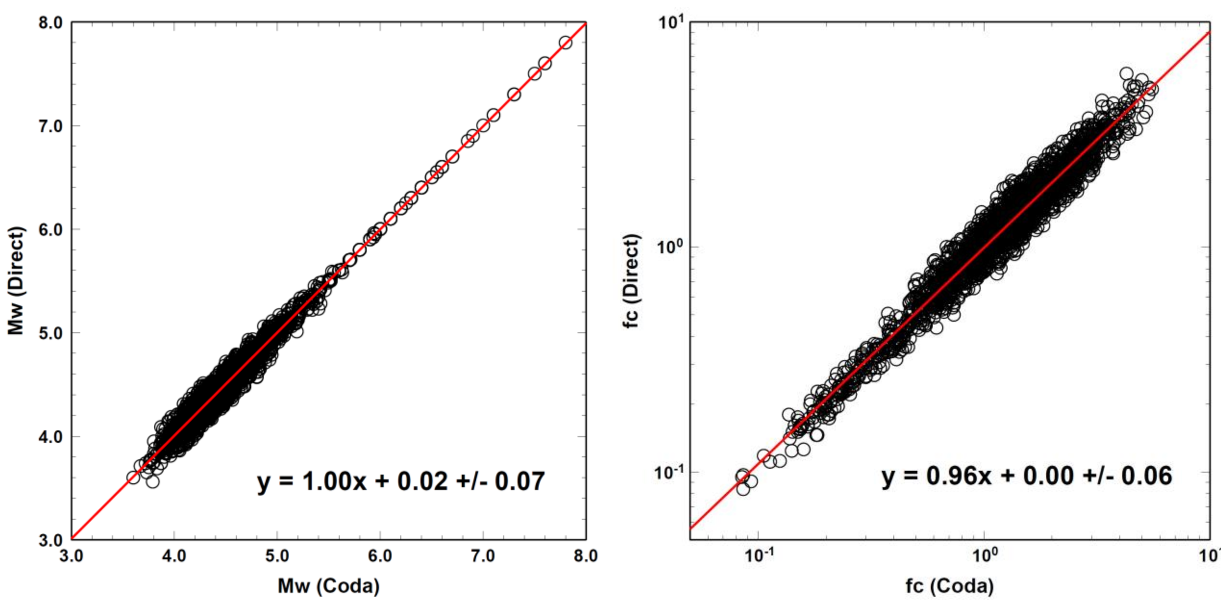

Figure 10. Comparisons of Mw (left) and corner-frequency (right) estimates from direct phases versus coda that are consistent. Moments of the large master events were fixed using values in the PDE; they were not used in the linear regression (left plot).

4 DETAILED INVESTIGATIONS OF SOURCE TERMS

Because the source terms are the foundation for estimating reliable attenuation, spreading, and site terms from source-corrected spectra, and automatic processing was needed for this very large data set, to build confidence in the procedure and the resulting source terms, we compared coda and direct-phase results in detail for many cases and to published results. It is important to understand the dependence of the source parameter estimates on station coverage, distance, and data quality, the uncertainties, and the physical causes of various discrepancies. We computed single-station results for over 100 representative event pairs. We start with a nearly ideal case, at least for the sparse IRIS network, and progressively examine cases for smaller events and worse coverage. We also compare our results to published source terms by other researchers, using local networks or teleseismic data. Last, we investigate discrepancies between coda and direct-phase results, highlighting the causes and the benefit of using independent observations to verify or reject source estimates. Fisk and Phillips (2010) presented many of these investigations, which (1) confirm the stability of coda, (2) give similar source terms estimated from coda and direct-phases for a large set of event pairs, (3) agree with available published studies based on local networks, and (4) indicate discrepancies due to various data quality issues and focal mechanism effects. Although Lg coda is very stable, it is also more prone to data quality problems because measurement windows are longer, increasing the probability of including spurious signals, and signal-to-noise is lower than for direct Lg. The results demonstrate the benefits of our approach, incorporating multiple, independent measurements of coda and direct phases, to provide a large set of corroborated source terms for earthquakes throughout Eurasia.

4.1 Dependence on Station Coverage: Southwestern Siberia

Here we show a few cases that highlight the dependence of the source parameter estimates on station coverage and distance. For example, coda results at even a single station are often comparable to network results, as illustrated in Figure 4. Since not all pairs are equally well recorded or have similar focal mechanisms, an important question is how sensitive the direct-phase results are. We examine this for progressive cases, starting with an ideal one. Figure 11 shows the locations of a large, similar pair in a cluster of over a hundred well-recorded events in southwestern Siberia. These Mw 6.7 and 5.1 events were recorded by 19 stations within 14 degrees. The waveform cross-correlations are as high as 0.8, using a frequency band of 0.1-5 Hz and time window lengths as long as 75 seconds. Figure 12 shows the network-median relative spectra and source model fits for this pair. The coda and direct Lg results are remarkably similar, even agreeing for subtle Sn, Lg, and coda fluctuations above 1 Hz. This level of agreement of the network results for direct phases and coda provides quasi ground-truth (GT) source parameters. It can be argued that these results are so good for direct Lg because these events were so well recorded (19 regional 3C station with good coverage and data quality). However, Figure 13 shows that the coda and direct results also agree just as well using only station CHKZ.

To examine the dependence on station coverage and distance, we treat this pair as though they were recorded by only a single station, one at a time, and compile the results. Figure 14 depicts the results for each station. It is not surprising that the coda results are largely the same as the network result. However, the single-station direct results are also comparable for most stations.

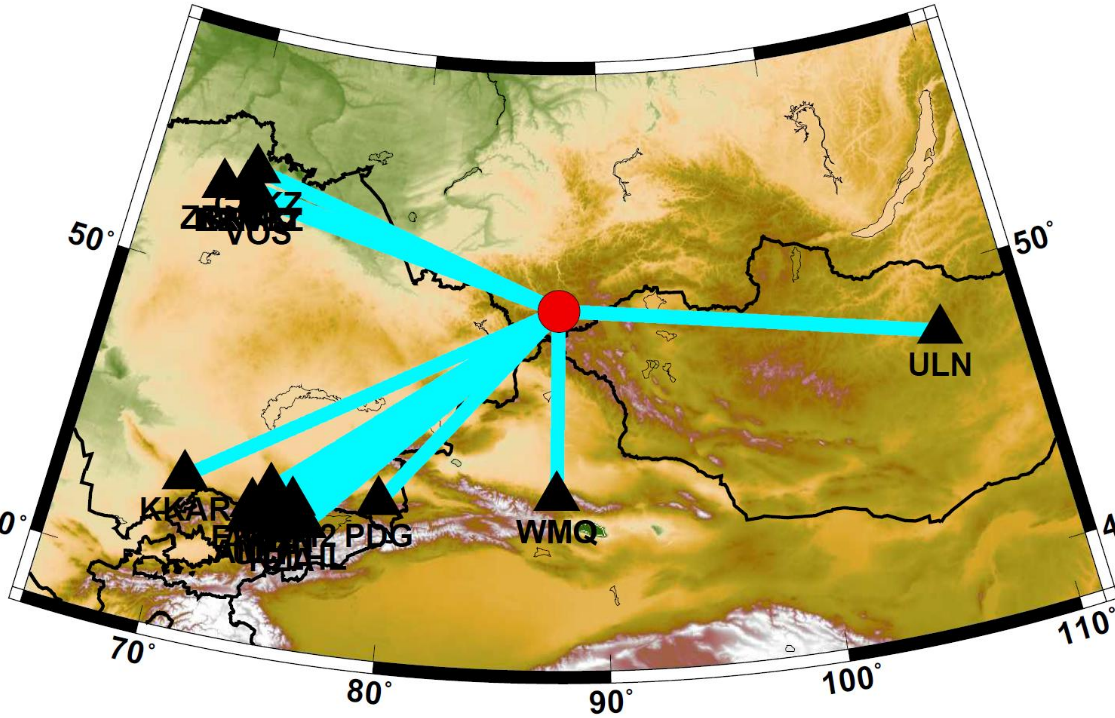

Figure 11. Locations of event pair (19957/20050) and regional stations with recording.

Figure 15 shows the estimated corner frequencies versus log moment for each station from coda and direct-phases, generated by automatic processing. The gray markers show outliers that were interactively refined or excluded from the regression fits. The most obvious discrepancy is for MK31, which had severe clipping for the larger event, as shown in Figure 16. Thus, the Lg spectrum for the larger event is too low at lower frequencies (leading to a relative moment for the smaller event that is too high) and too high at higher frequencies. Coda is less sensitive to clipping than the direct Lg. We refit the MK31 relative spectra (Figure 17). (Note that MKAR is the IRIS naming convention for the 3C broadband sensor, MK31, of the Makanchi array.) Using frequencies greater than 0.04 Hz leads to source parameter estimates from coda that agree with the rest of the network. The direct result cannot be fixed and is excluded.

ULHL and WMQ are outliers for the coda results. The ULHL recording of the larger event was truncated, which did not allow for coda measurements in the lowest bands. Thus, we excluded the ULHL coda result. We also refit the WMQ relative spectra for coda and direct phases, restricting to frequencies above 0.04 Hz. Figure 18 shows the new source model fits for WMQ, which are now consistent. Except for data quality issues at three stations, the single-station results agree very well. The reviewed coda results are tighter than direct results (standard deviations of 0.03 versus 0.06), as expected, but they are very comparable, even using single stations, for these large, similar events. Data quality issues at a small fraction of stations do not impact the network median, but could affect the results if recorded by fewer stations. Discrepancies of source terms from coda and direct phases indicate such problems, without having to examine many thousands of waveforms.

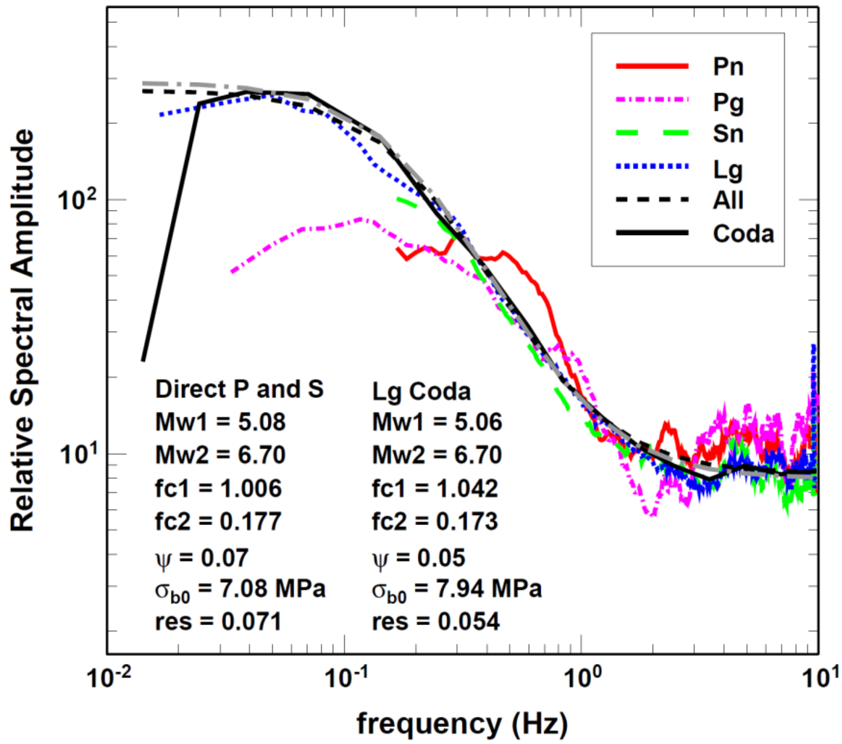

Figure 12. Comparison of network-median relative spectra from direct phases and Lg coda, along with source model fits and parameter estimates for an event pair in southwestern Siberia.

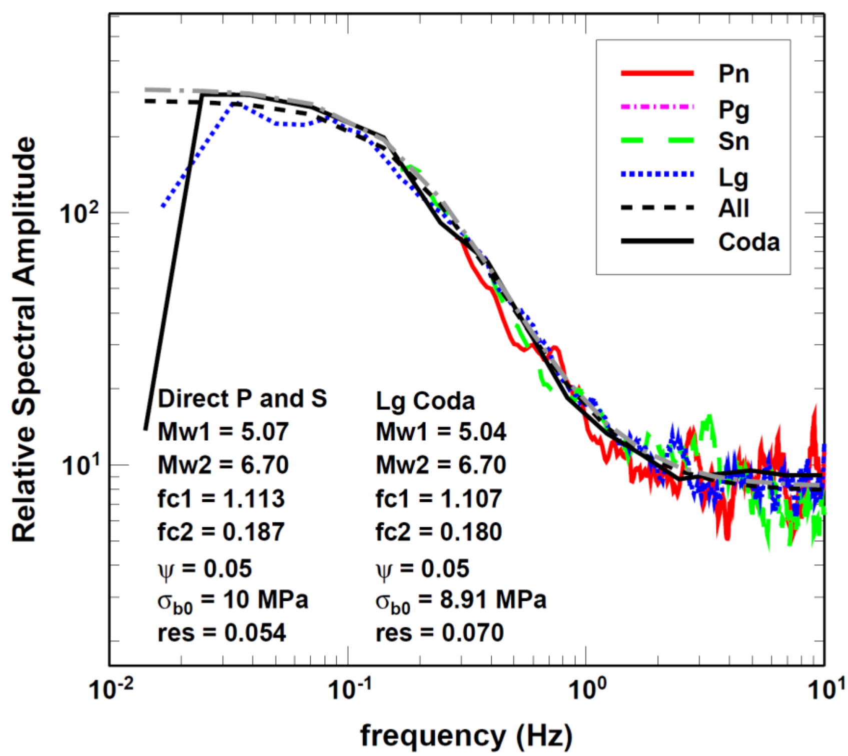

Figure 13. Similar to Figure 12, but using data from a single station (CHKZ in Kazakhstan).

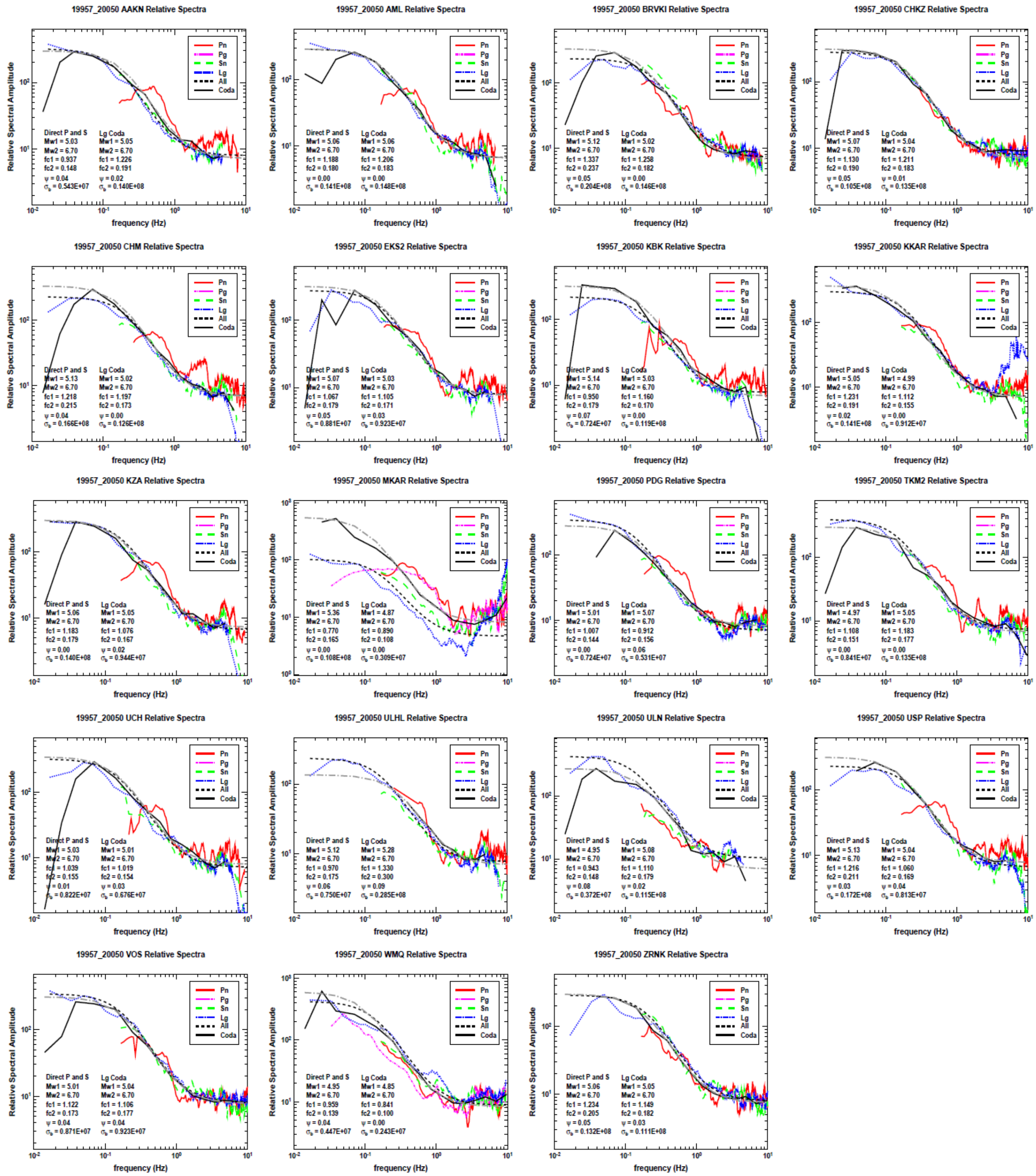

Figure 14. Comparisons of relative spectra and source model fits from direct phases and Lg coda for each of 19 regional stations, generated entirely by automatic processing.

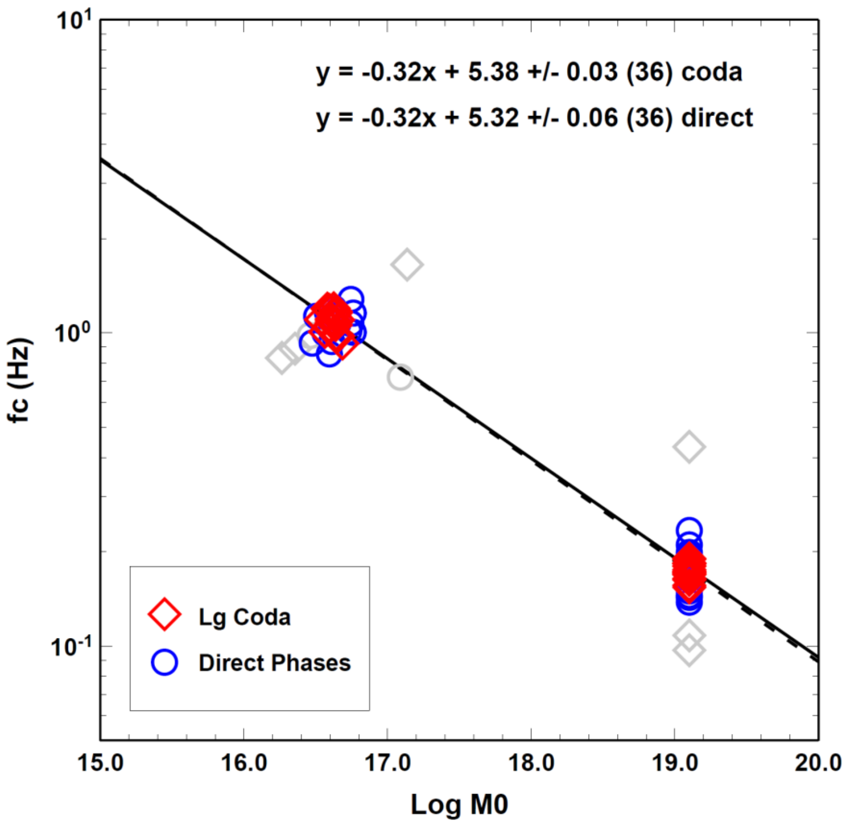

Figure 15. Single-station estimates of corner frequency versus log moment and regression from direct phases and Lg coda. Gray markers show automatic results that were refined or excluded.

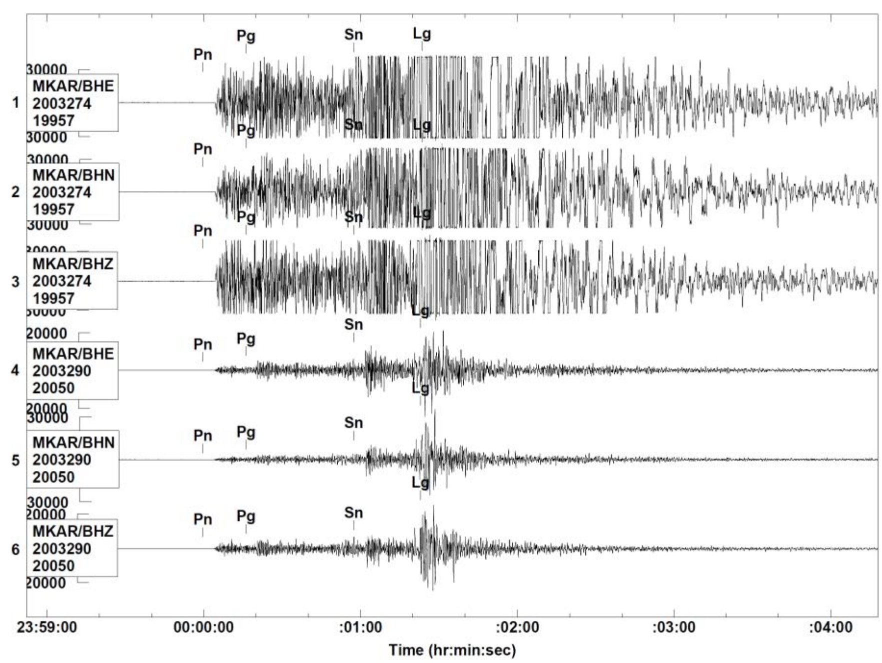

Figure 16. MK31 3C recordings of the two earthquakes in southwestern Siberia. The larger (Mw 6.7) event exhibits clear evidence of clipping (top three traces).

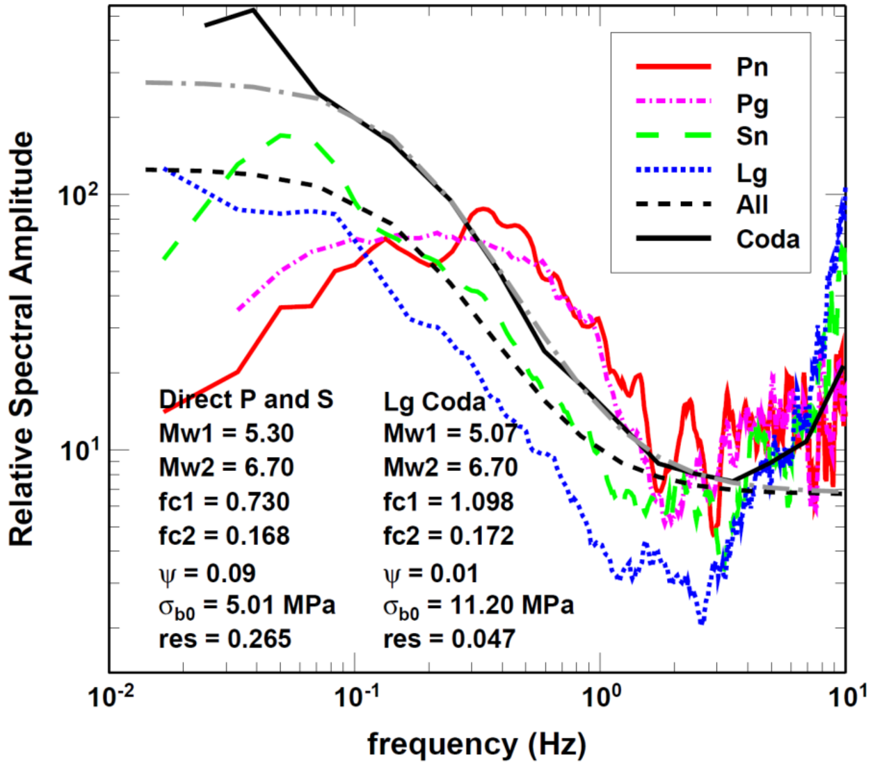

Figure 17. Similar to Figure 13, but for MKAR data which are clipped for the Mw 6.7 event.

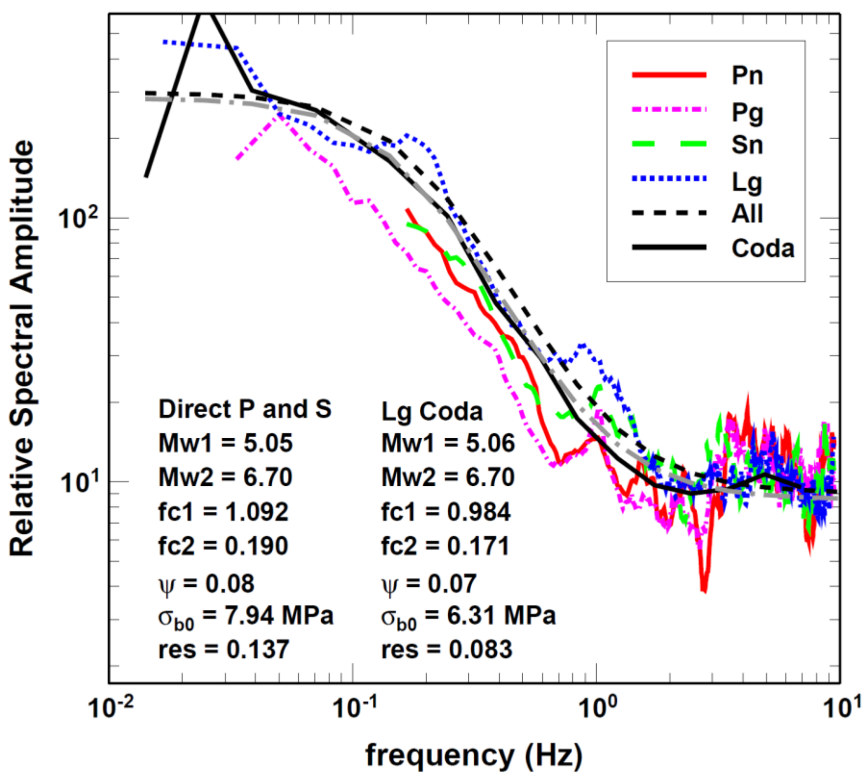

Figure 18. Similar to Figure 13, but refitting WMQ relative spectra above 0.04 Hz.

Figure 19 shows the dependence of the source parameter estimates on epicentral distance. The gray markers are automatic results that were excluded or refined by interactive review, as described above. The moment estimates (left plot) from relative spectra of both Lg coda and direct phases are very similar and stable versus distance. Recall that the moment of the larger event was fixed. For the smaller event, coda gives more stable moments, but the direct results are consistent, and neither have noticeable distance dependence over this range of 5-15 degrees, for these relatively large events. For the corner frequency estimates versus distance (right plot), again, the coda results are tighter, particularly for the smaller event, although the results from direct phases are comparable. There is no significant distance dependence. Note that S/N is typically worse at longer propagation distances, which can bias both the moments and corner frequencies higher with increasing distance. Such effects are minimal for this case, but are more apparent in subsequent cases we show.

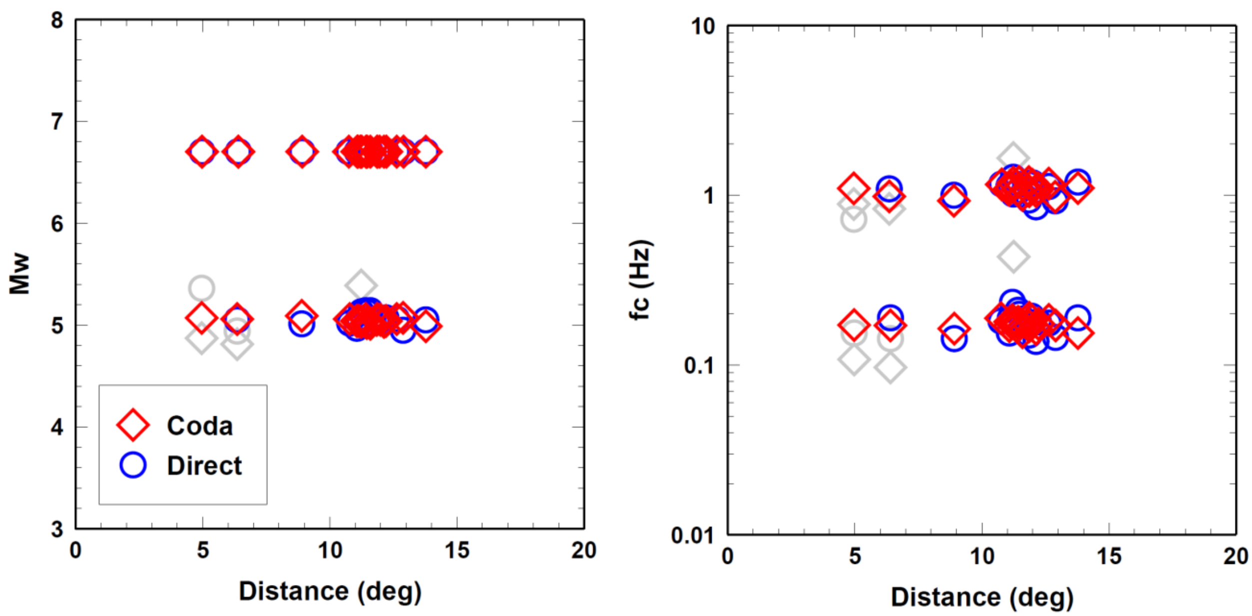

Figure 19. Comparisons of Mw (left) and corner frequency (right) estimates versus epicentral distance to each station. Blue and red markers correspond to the results after interactive review.

Because we are processing about 46,000 pairs, corresponding to about 10,000 unique events, recorded by up to 25 regional stations, our goal is to automate the processing as much as possible, limiting required efforts of interactive review. Note that our source model fitting procedure automatically determines the frequency range, based on departures at low and high frequency from expected physical behavior. The program we implemented generally performs quite well at excluding anomalous spectral behavior; however, in reviewing the fits, we find that interactively selecting the frequency range is the main change required.

4.2 Dependence on Station Coverage: Mongolia

As a less ideal case, we now examine a smaller (Mw 5.8 and 4.5) earthquake pair in Mongolia. The waveforms correlate, but not as well as the previous pair, and the stations cover a broader range of epicentral distances, up to 2000 km (Figure 20). We again compute single-station results to compare the robustness and distance dependence of the source estimates from coda and direct phases. The results shown are entirely from automatic processing, with some outliers excluded.

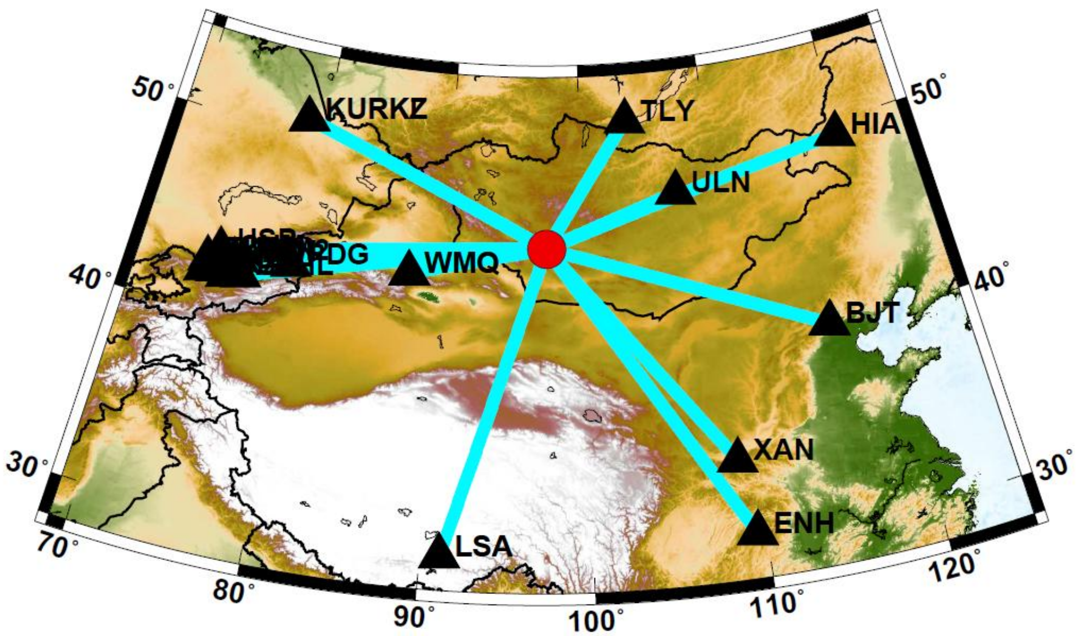

Figure 20. Locations of an event pair in Mongolia and regional stations with recording.

Figure 21 shows the network-median relative spectra and source model fits from coda and direct phases for this pair, exhibiting good agreement. Figure 22 shows single-station results for PDG and TLY, showing excellent agreement for the former and some variability in Mw estimates for the latter. Figure 23 shows the scaling of the corner frequencies versus log moment estimated from Lg coda and direct phases. If we ignore the outliers, coda provides more stable moments and corner frequencies for both events. Overall, the results have somewhat more scatter than the previous case, but still give comparable results. The lowest outliers for both coda and direct phases were for station LSA because of poor Lg propagation efficiency along this path.

The left plot of Figure 24 shows Mw estimates versus distance. Some from direct phases are biased slightly higher for longer paths, but the results are good for an Mw 4.5 event recorded out to 18 degrees (2000 km). The right plot of Figure 24 compares corner frequency estimates versus distance. The outliers occur for stations beyond 15 degrees. The results for this case indicate that (1) coda is, again, more stable, (2) direct-phase results are consistent for this similar pair; and (3) it can be beneficial to restrict the analysis of coda and direct phases to closer, high-quality stations or arrays, rather than include results from all stations at distances up to 2000 km.

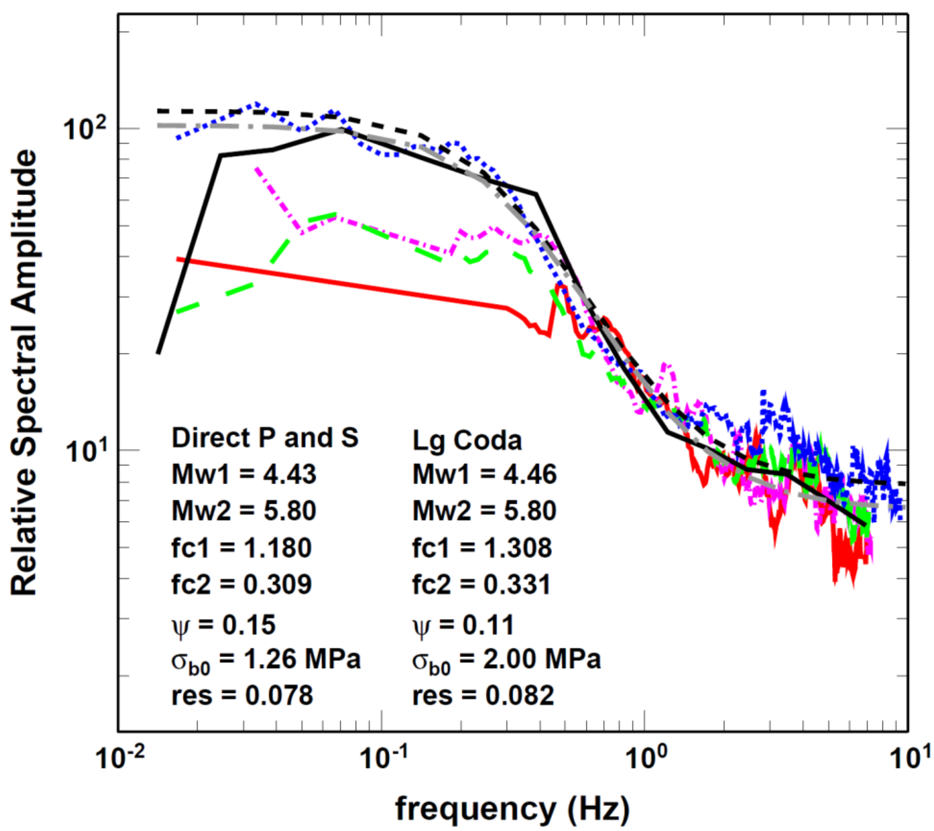

Figure 21. Network-median relative spectra and source model fits for an event pair in Mongolia.

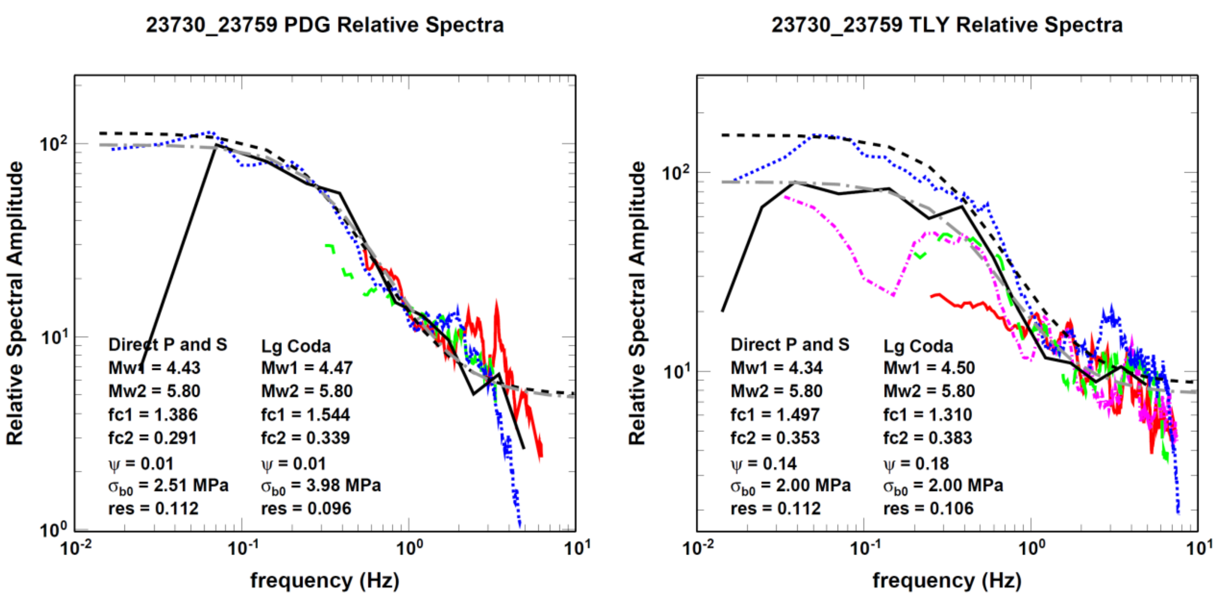

Figure 22. Examples of relative spectra and source model fits for PDG (left) and TLY (right).

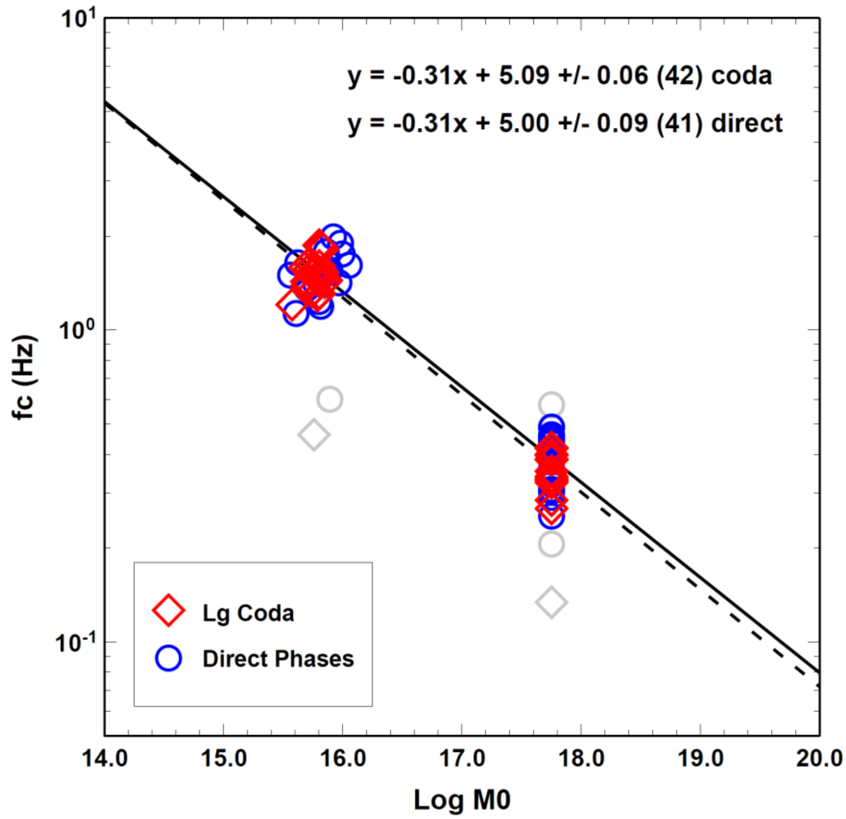

Figure 23. Single-station estimates of corner frequency versus log moment and regressions from direct phases and Lg coda. Gray markers show automatic results that were refined or excluded.

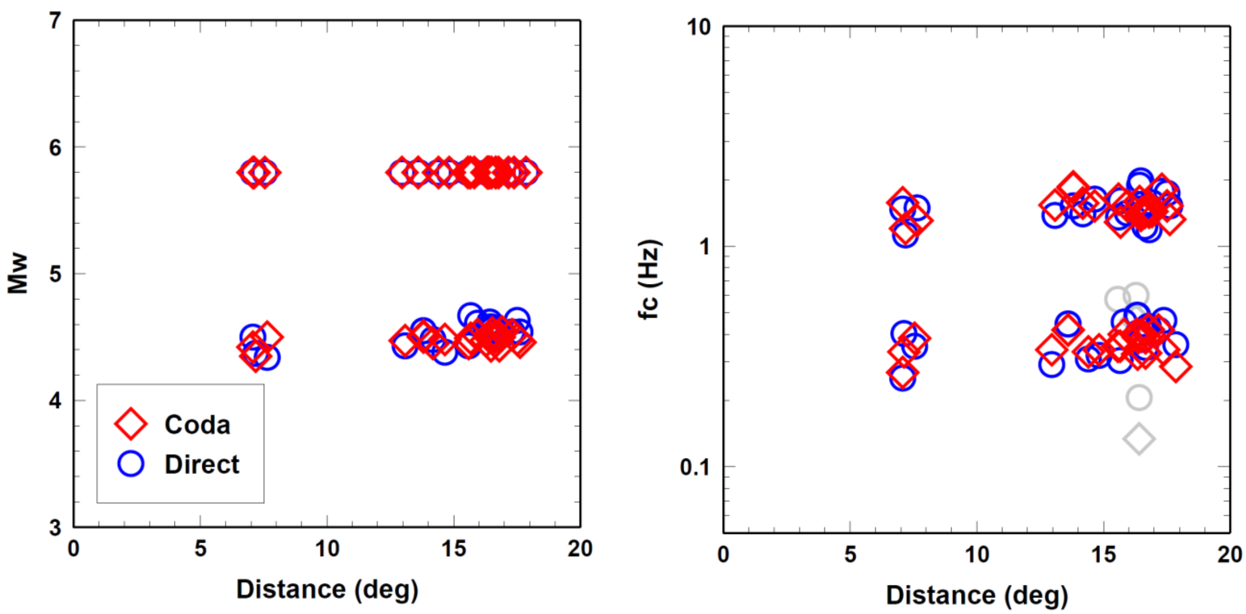

Figure 24. Comparisons of Mw (left) and corner frequency (right) estimates versus epicentral distance to each regional station for the Mongolian pair.

4.3 Dependence on Station Coverage: Lop Nor Test Site

A well-known pair of earthquakes (Mw 5.5 and 4.2) with similar hypocenters and mechanisms occurred in January 1999 at the Lop Nor test site (LNTS). This case is particularly interesting because it is at a nuclear test site and the earthquakes are smaller than the previous examples. Figure 25 depicts the locations of the events and the ray paths to regional stations. Figure 26 shows good agreement of the network-median relative spectra and source model fits from coda and direct phases, although Lg coda for the Mw 4.2 earthquake is significantly corrupted by noise for frequencies less than 0.4 Hz. Direct Lg has good S/N down to about 0.07 Hz. Figure 27 shows the estimates of corner frequency versus log moment from automatic processing of single-station data. The scatter is similar to the previous case. The low coda outlier is for station NIL because Lg coda is corrupted by noise for the smaller event. Both coda and direct results for XAN are high outliers due to weak Lg propagation on this long path, partially through the Tibetan Plateau. Data quality was too poor for the LSA recording of the smaller event to process and fit relative spectra for coda or direct phases. Thus, the Mw 4.2 event has unusable signals for long, low-Q propagation paths.

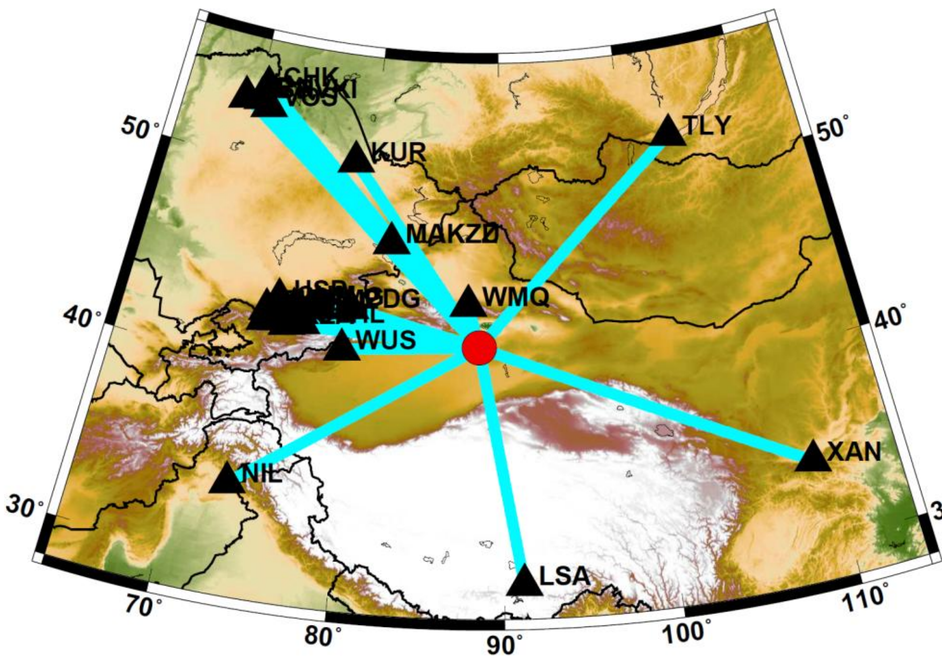

Figure 25. Locations of an earthquake pair at LNTS in January 1999 and recording stations.

Figure 28 compares Mw (left) and corner frequency (right) estimates from direct phases and Lg coda versus epicentral distance. The moments are stable and consistent, except for the farthest stations, quite good for an Mw 4.2 event. The estimates of corner frequencies versus distance have more scatter and bias with increasing distance, beyond 13 degrees. Even requiring S/N > 3, data quality degrades for longer paths and smaller events, causing biases and apparent distance dependence in the corner frequency estimates for both events. This case, like many others examined, provides further evidence that it is better to restrict the analysis of coda and direct phases to closer, high-quality stations or arrays, than to include data from all regional stations.

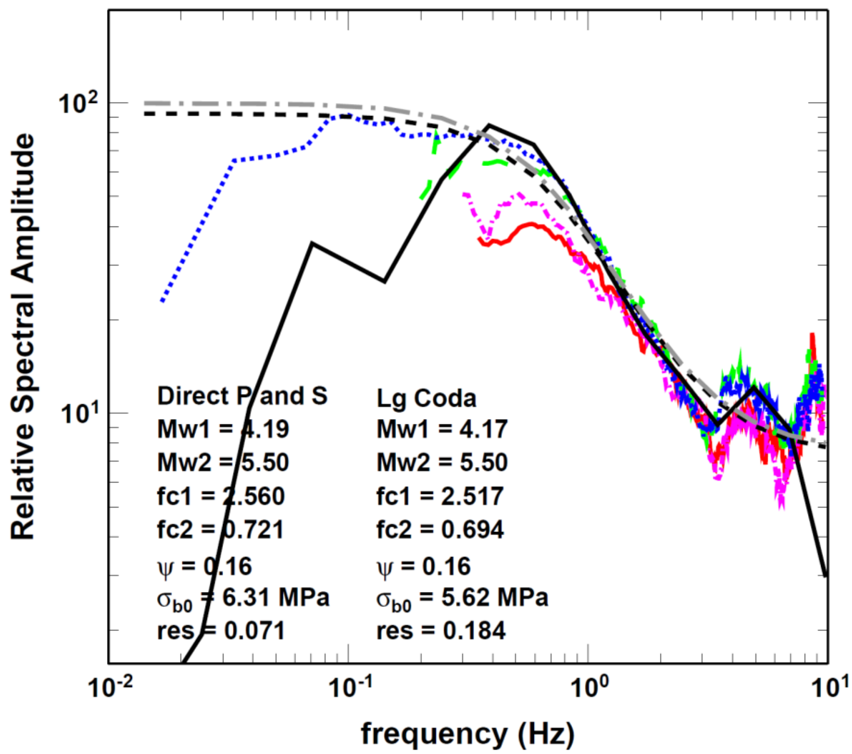

Figure 26. Network-median relative spectra and source fits for an earthquake pair at LNTS.

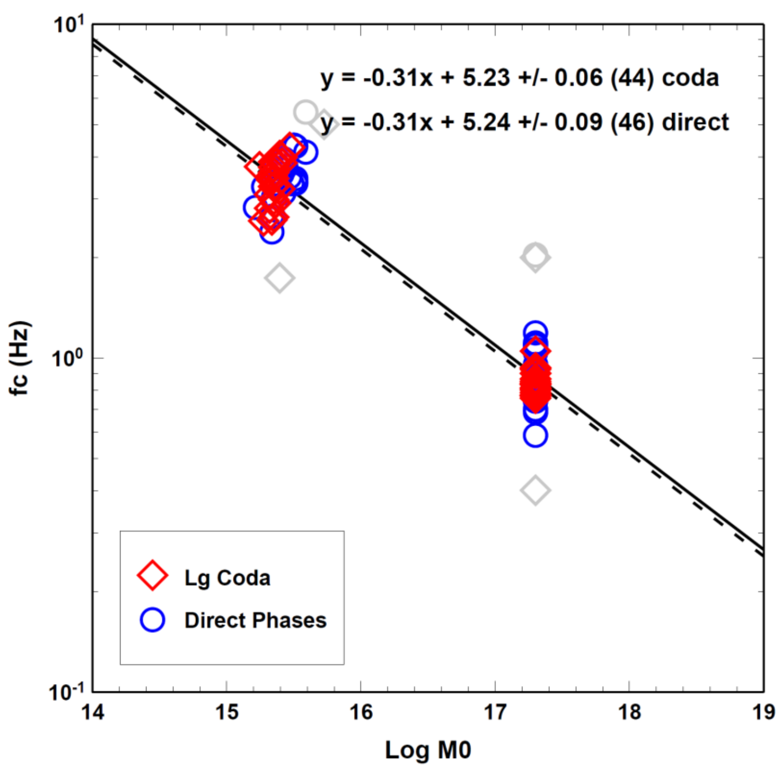

Figure 27. Single-station estimates of corner frequency versus log moment from direct phases and Lg coda for an earthquake pair at LNTS.

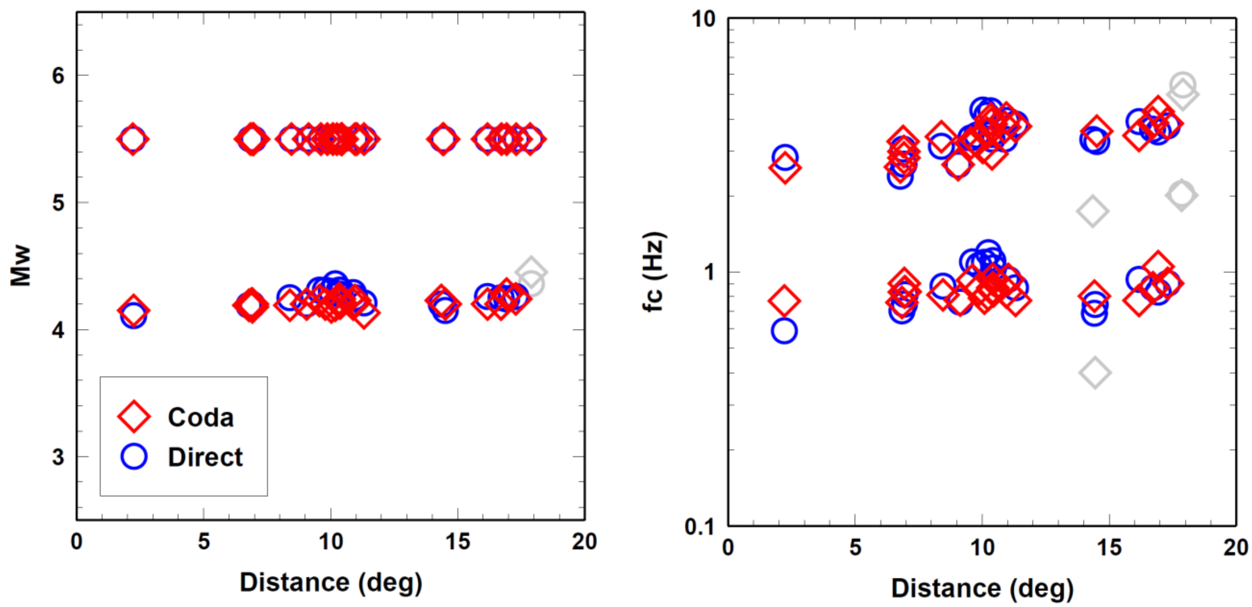

Figure 28. Single-station estimates of Mw (left) and corner frequencies (right) versus distance for the earthquake pair at LNTS.

In light of these results, we considered criteria based on magnitude and distance to restrict the data. As a basis, we used past work by Phillips et al. (2008) and Phillips (2010, pers. comm.), shown by the dotted red line segments and dashed red curve, respectively, in Figure 29. As seen in the previous examples, the criterion does not need to be overly restrictive to obtain reliable moments. However, to estimate reliable corner frequencies, it needs to be more stringent than considered by Phillips. We tested criteria represented by the black dashed curve (shifting the red dashed curve higher) and the green region. Both typically exclude poor data for smaller events recorded at longer distances, improving the results for cases examined. The lower bound (dashed green line) is given by $\Delta = 500(mb - 1.6)$, where Δ is distance in km. It only limits the data for events smaller than mb 5.6. This relation is consistent with the black dashed curve over the magnitude range relevant to our dataset (i.e., events larger than mb 4).

Clipping is also problematic for some larger master events, as shown in Figure 16. In an attempt to exclude clipped data, we tested the upper green dashed curve in Figure 29, restricting data to longer distances for very large events,. As described in our progress reports, we found some evidence of improvements. In general, however, we found that this criterion has limited efficacy because there are not that many recording for such large events in this distance range, and clipping depends on the dynamic range of the instrumentation. For some stations, it usefully excludes clipped signals. For others, it excludes good data or does not exclude bad. Because clipping can have variable effects for various events, phases, stations, and instrumentation, and there are relatively few very large events, it is more effective to simply review and treat them manually, using comparisons of the coda and direct relative spectra (e.g., Figure 17) to indicate cases that need review. It is also worth emphasizing the robustness of the results based on network-median relative spectra; i.e., clipping at one or two stations has no effect on the majority of network results. Thus, in addition to requiring S/N > 3, we used the green region (bounded by the lower dashed green line) in Figure 29 to restrict the data in all subsequent processing.

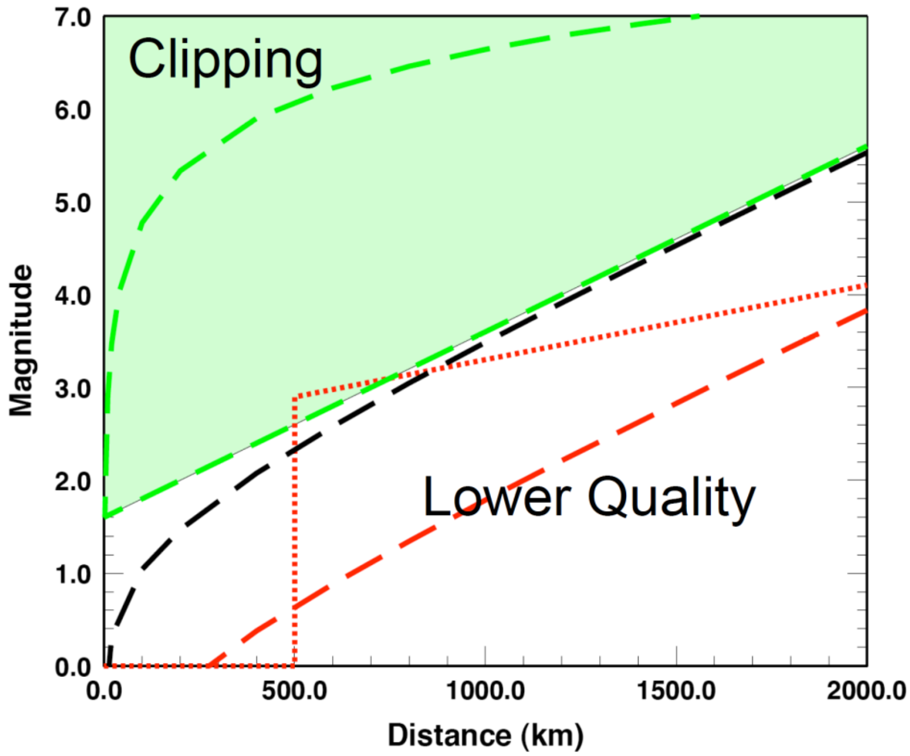

Figure 29. Various magnitude-distance criteria we tested to improve data quality.

To illustrate the benefit, we processed eight crustal earthquake pairs near LNTS, using all regional data and restricting the data by the magnitude-distance criterion. Figure 30 compares the results, showing the improvements for both direct phases and, especially, coda. These results show the expected high degree of stability for coda, when limited to stations with good data.

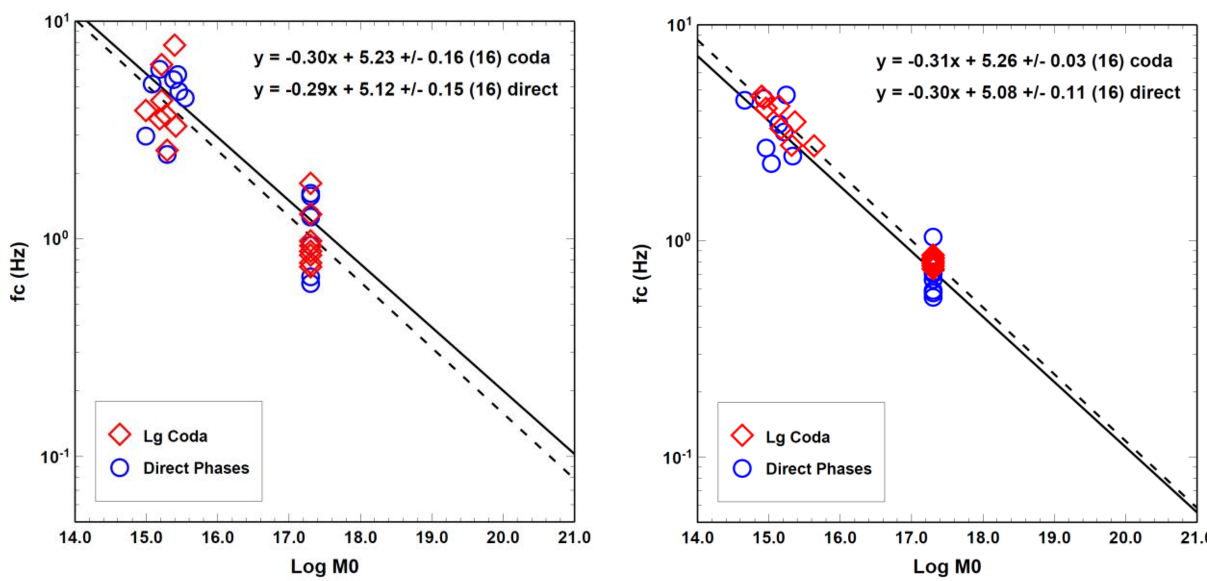

Figure 30. Source parameter estimates for eight crustal earthquake pairs near LNTS using all regional data (left) and restricting the data by magnitude and distance (right).

4.4 Data Quality Effects on Coda: Myanmar Cluster

Given the stability of coda, one could question whether direct phases are needed. We now show two cases that highlight the benefit of using both coda and direct phases. The first is for a cluster in Myanmar that were recorded by up to 5 stations. The largest event (Mw 5.9) occurred on 1994/04/06. Figure 31 shows its location and the regional stations with recordings. The cluster includes 11 other events (approximately Mw 3.9 to 5.0) that occurred from 1989 to 2008, nearly the full time span of our data set. The smaller events have Lg cross-correlations with the larger event of at least 0.5 at one or more stations, many at 0.6 or higher. Figure 32 compares the network-median relative spectra for two pair. The results from coda and direct phases are consistent for the pair shown on the left. The coda result for the pair on the right is an outlier.

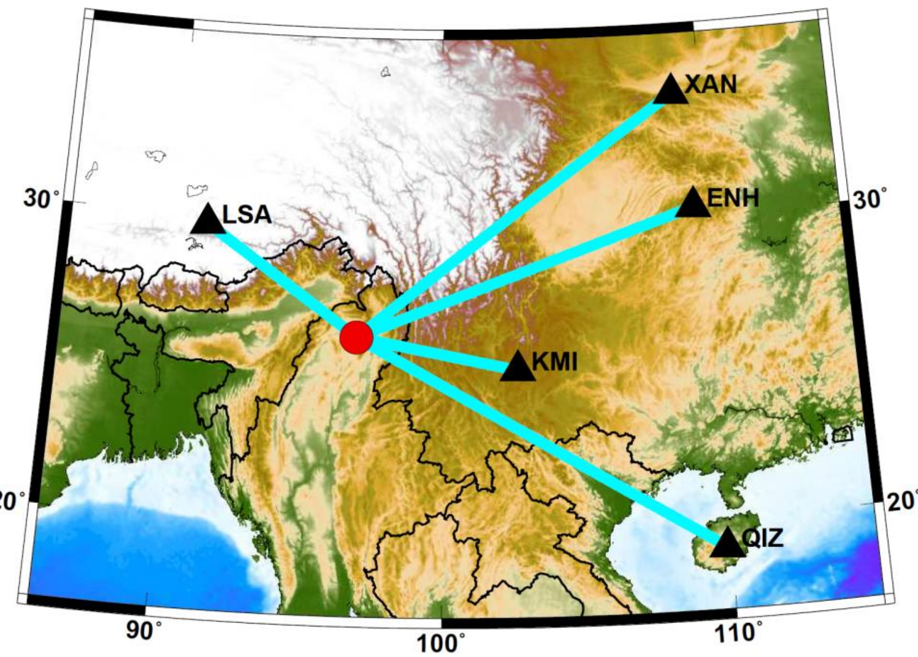

Figure 31. Location of an Mw 5.9 earthquake in Myanmar and regional recording stations.

Figure 33 shows estimates of corner frequencies versus log moments for the 11 pairs, illustrating some key points. First, including all of the results, the corner frequencies from direct phases scale more tightly than coda (standard deviations of 0.08 versus 0.13). If five high *outliers* of the coda results are treated (four omitted and one revised using only KMI data), then the coda results all lie along a straight line with smaller standard deviation (0.05). That is, the coda results are tighter than those for direct phases, but there are more problems. Second, the second largest event (Mw 5.0) in the cluster occurred about 13 minutes after the largest; its signals are in the coda of the largest shock. Figure 34 shows the KMI/BHZ recordings of these two events. As expected, such interference can lead to anomalous estimates of the source parameters. The corner frequency estimates from coda for this pair are the most inconsistent with all of the other results from coda and direct phases. The corner frequency from direct phases is also an outlier, but not nearly as bad. The direct result is less sensitive to the interference problem because the direct Lg of the second event, compared to its coda, is higher above the coda of the first event. Coda can also be more prone to data quality issues because the lengths of the measurement windows give a higher probability of including spurious signals. These results indicate that the coda results are still fundamentally better than those from direct phases, if outliers are treated, but can be less robust (more sensitive to data quality issues) for automated processing. The automated direct results are good, with the caveat that these are correlated pairs (i.e., similar events).

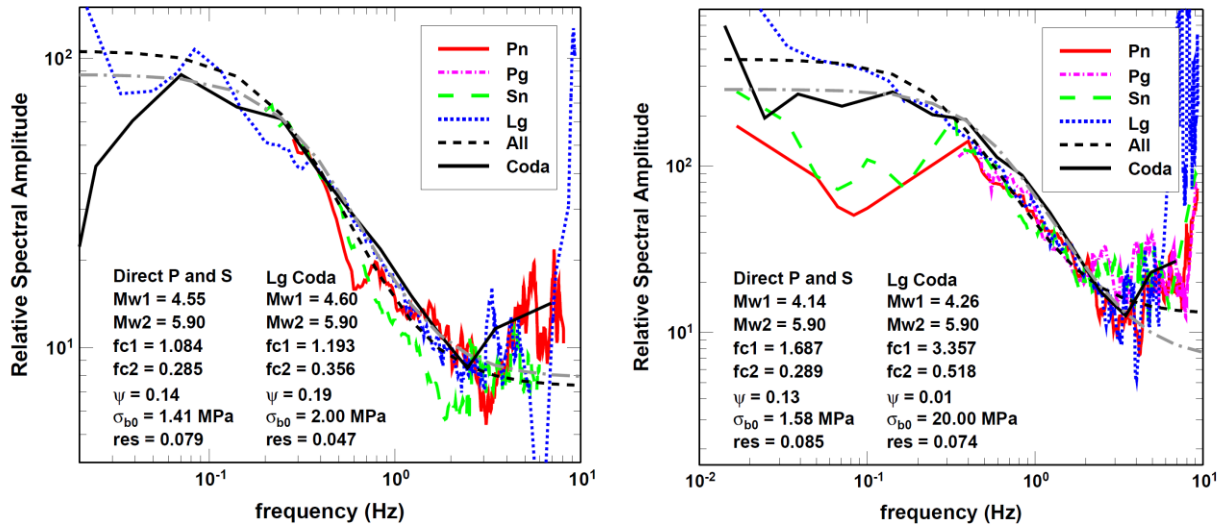

Figure 32. Relative spectra and source model fits for two earthquake pairs in Myanmar.

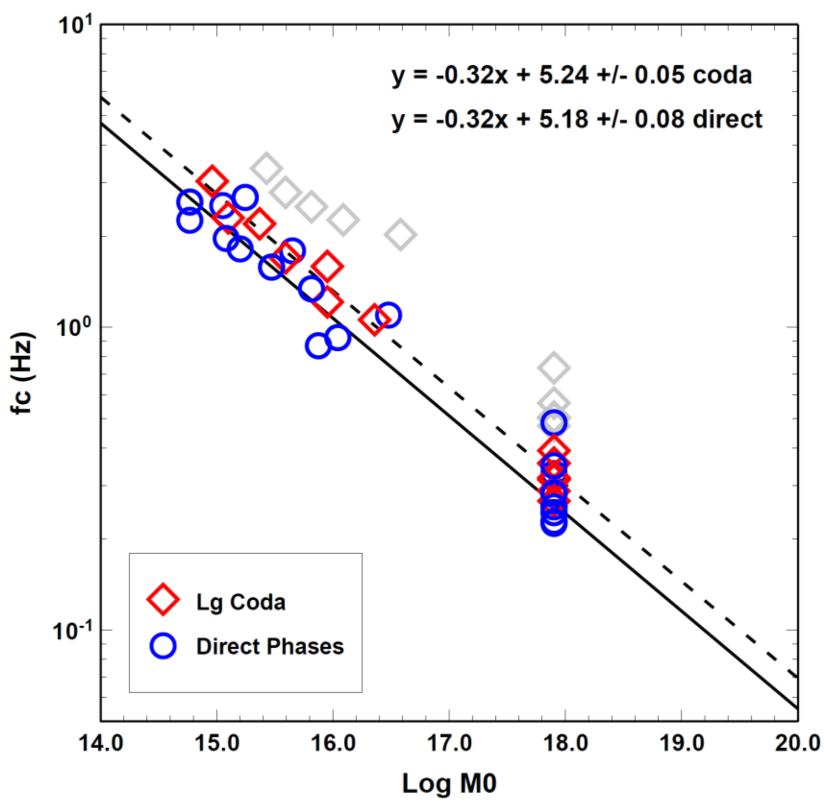

Figure 33. Estimates of corner frequency versus log moment and scaling relations from direct phases and Lg coda, using up to five common stations. Gray markers are outliers of coda results.

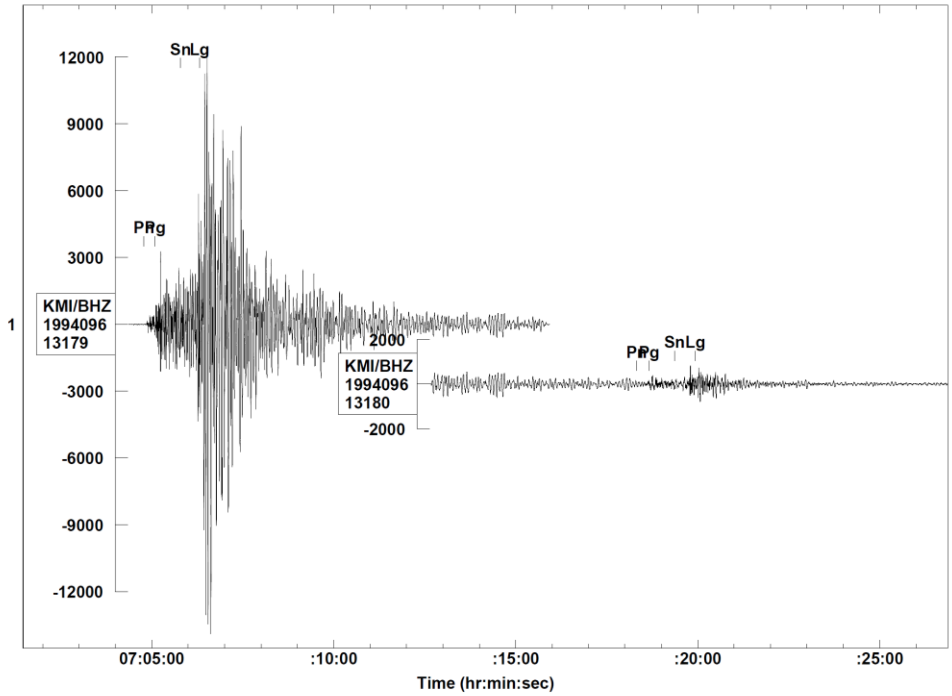

Figure 34. Unfiltered KMI/BHZ recordings of the two largest events in the cluster.

4.5 Data Quality Effects on Coda: Caspian Sea Cluster

Figure 35 shows another cluster near the western shore of the Caspian Sea, also highlighting how discrepancies of results from coda versus direct phases can indicate problems that need to be checked and addressed. Figure 36 shows corner frequency estimates versus log moment for these events. Separately, the coda and direct results both have relatively small scatter, appearing very reasonable. However, the comparison indicates a clear bias. Examining the waveforms shows that there were actually two large events (PDE Mw 6.2 and 6.5), the second has interfering signals in the coda of the first at many of the stations, causing the bias. In principle, examining the waveforms would uncover many of these problems for either direct phases or coda. However, doing this for almost 600,000 waveforms and 46,000 pairs is not practical. The redundancy of multiple observations can be used to flag discrepancies for further review. Incidentally, using the corner frequencies estimated from direct phases, leads to Q estimates from source-corrected Lg spectra for these paths that are very consistent with available estimates (i.e., all but GNI, KIV, and RAYN) from amplitude tomography. We find, however, that the PDE Mw estimate of 6.5 for the second event is biased high, due to interference from the previous event.

4.6 Effects of Non-Similar Focal Mechanisms: Turkmenistan Cluster

We have seen many cases for which the source terms estimated from coda and direct phases agree very well, typically for event pairs with similar focal mechanisms. It is also instructive to examine discrepancies of coda and direct results, including the impact of earthquake pairs with non-similar focal mechanisms. Figure 37 depicts the location of one such cluster in western Turkmenistan, near the Caspian Sea, consisting of 16 earthquakes with epicenter estimates within 50 km of the master event. (Six have spurious data for both coda and direct phases.)

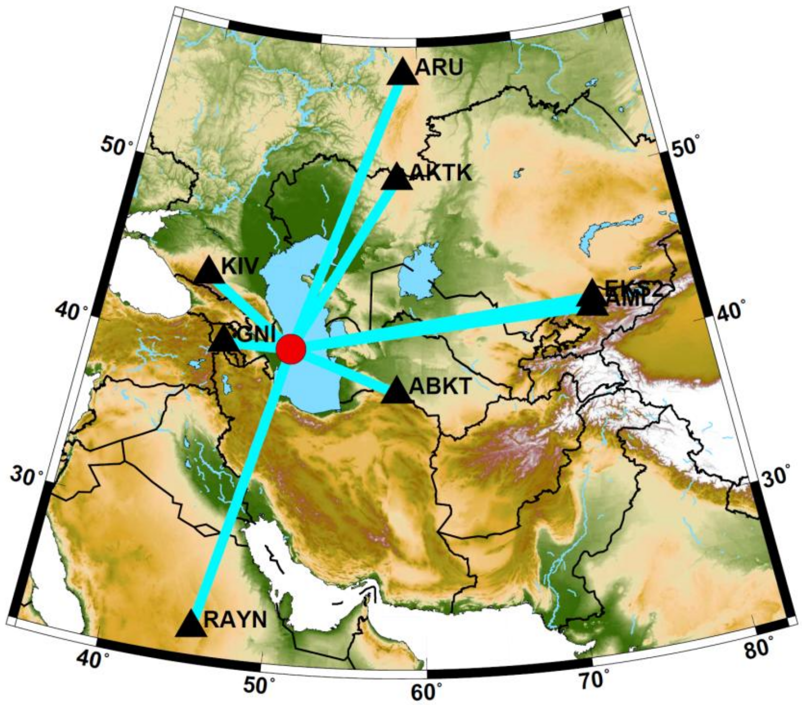

Figure 35. Locations of an event cluster near or beneath the Caspian Sea.

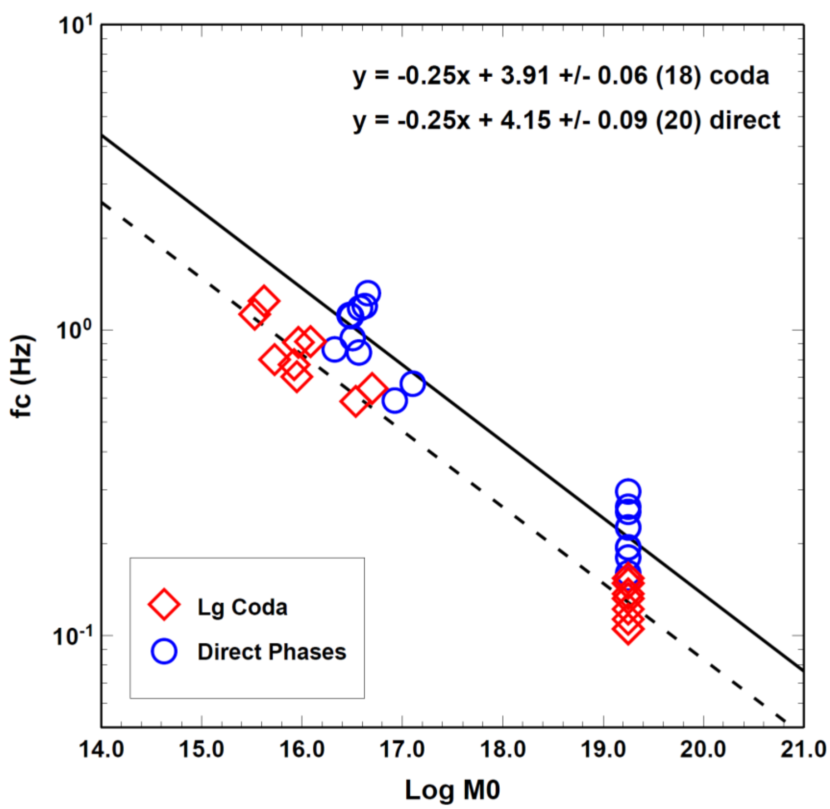

Figure 36. Estimated source parameters for a cluster near the western shore of the Caspian Sea. Both coda and direct results have relatively small scatter, but show a clear bias.

Figure 38 (left) shows the estimates of corner frequencies versus log moments for all 10 pairs. The results from direct phases have much more scatter and bias compared to those from coda. Figure 38 (right) shows the results, restricting the events to those that have maximum waveform cross-correlations greater than 0.6 (i.e., similar mechanisms). The coda results are very similar in both cases, illustrating the well-documented stability of coda to source effects. The direct results exhibit much less scatter and bias by restricting the events to those that are similar to the master.

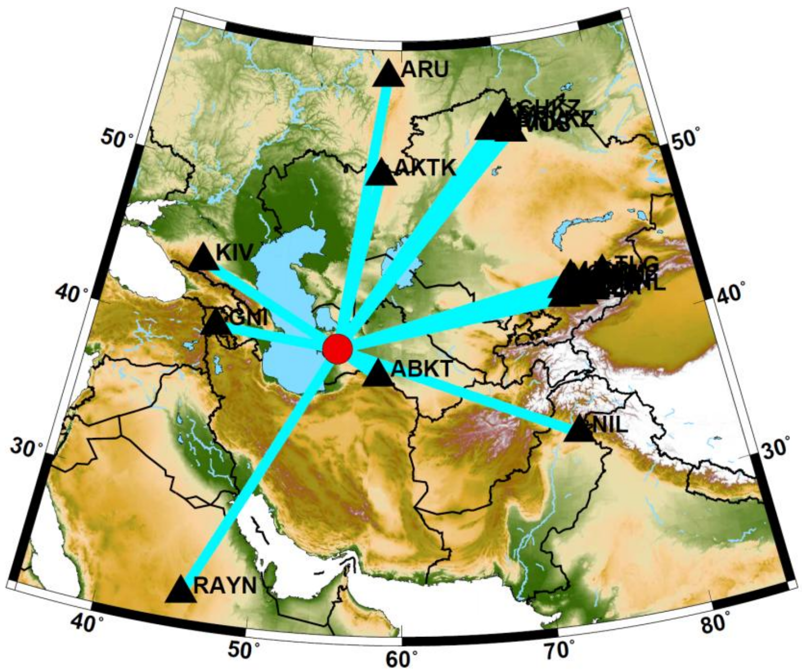

Figure 37. Locations of an event cluster in Turkmenistan and regional stations with recordings.

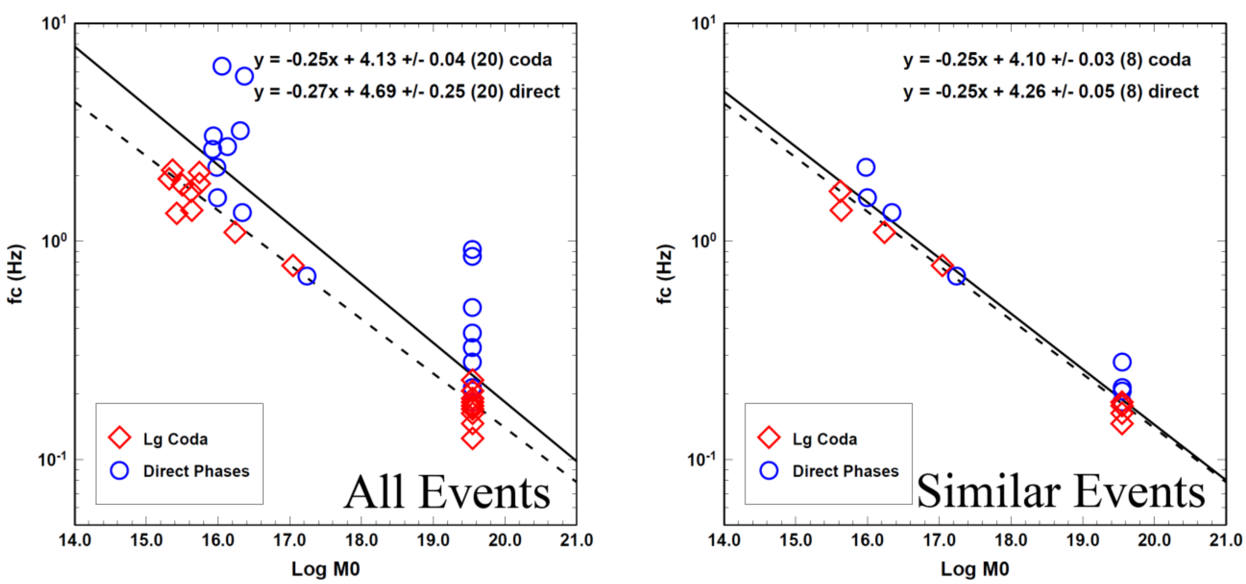

Figure 38. Source scaling relations for a cluster in Turkmenistan, (left) using 10 events within 50 km of the master and (right) restricting the events to those with significant cross-correlations.

4.7 Comparison to Published Results: Wells, Nevada Cluster

To further examine the sensitivity of the results to focal mechanism, we processed selected earthquakes near Wells, Nevada, which are known to exhibit strong source directivity effects. Thus, direct phases are expected to have considerable variability. (Although these events are outside of our primary study region, this case study is intended to improve our understanding and processing capabilities.) We selected the main Mw 5.8 event and a subsequent Mw 4.3 event. These events were recorded by several permanent broadband networks and by numerous portable broadband stations of the Earthscope TransportableArray (USArray), a dense network (70-km spacing) of 400 seismic stations. For the analysis, we limited the networks to give 39 stations at more typical regional distances (Figure 39). Source parameter estimates by Mendoza and Hartzell (2009), who used a much denser network, provide quasi-GT to assess our results.

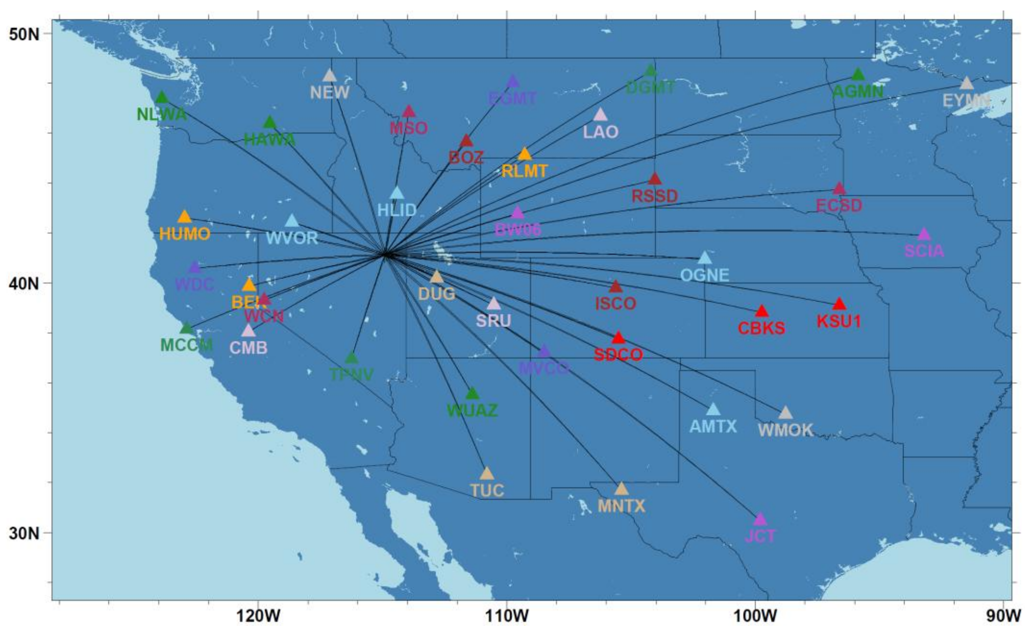

Figure 39. Locations of earthquakes near Wells, Nevada and 39 regional IRIS stations.

Figure 40 shows that the network-median relative spectra from coda and direct phases agree, even for Pn (often the most variable) over frequencies with adequate SNR. In addition, our Mw estimates of 4.27 and 4.29 for the smaller event, fixing Mw 5.8 for the larger, agree with the estimates of 4.3 and 5.8 by Mendoza and Hartzell (2009), who used a different empirical Green's function (EGF) approach. They estimate a static stress drop of 7.2 MPa for the larger event (noting that it is higher than expected for the Basin and Range), equivalent to a corner frequency of 0.39 Hz. We obtain corner frequency estimates of 0.29-0.31 Hz, corresponding to static stress drop estimates of 2.9-3.7 MPa. We discussed this comparison with Steve Hartzell.

Figure 41 shows the estimated source parameters at each of the 39 stations and the scaling relations, based on 22 stations with good data. As expected, the single-station coda results have less variability. However, on average, the direct and coda results are very consistent. Further improvements in these results would likely be obtained by interactive processing. However, our goal was to largely automate the analyses, to allow very large scale processing.

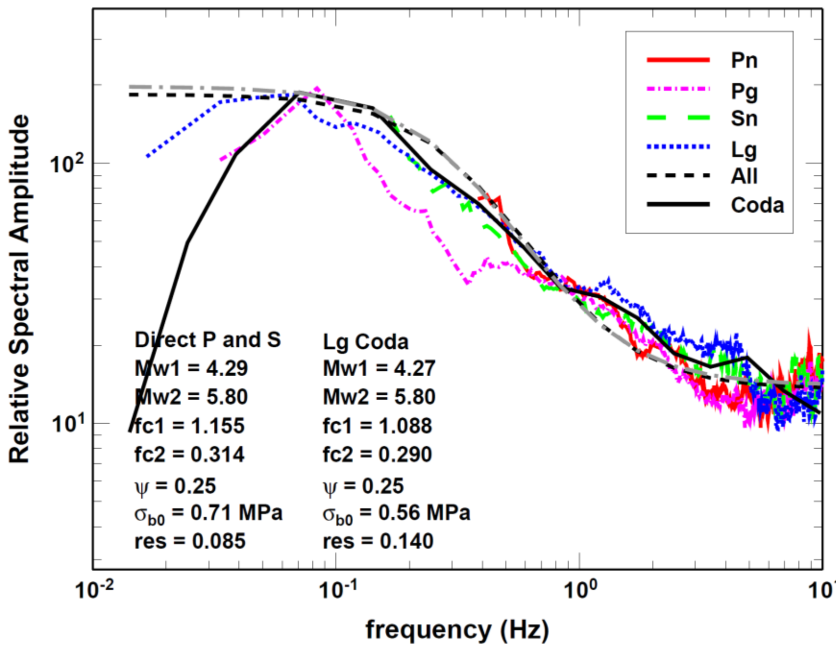

Figure 40. Network relative spectra and source model fits from coda and direct phases for a pair of Wells earthquakes.

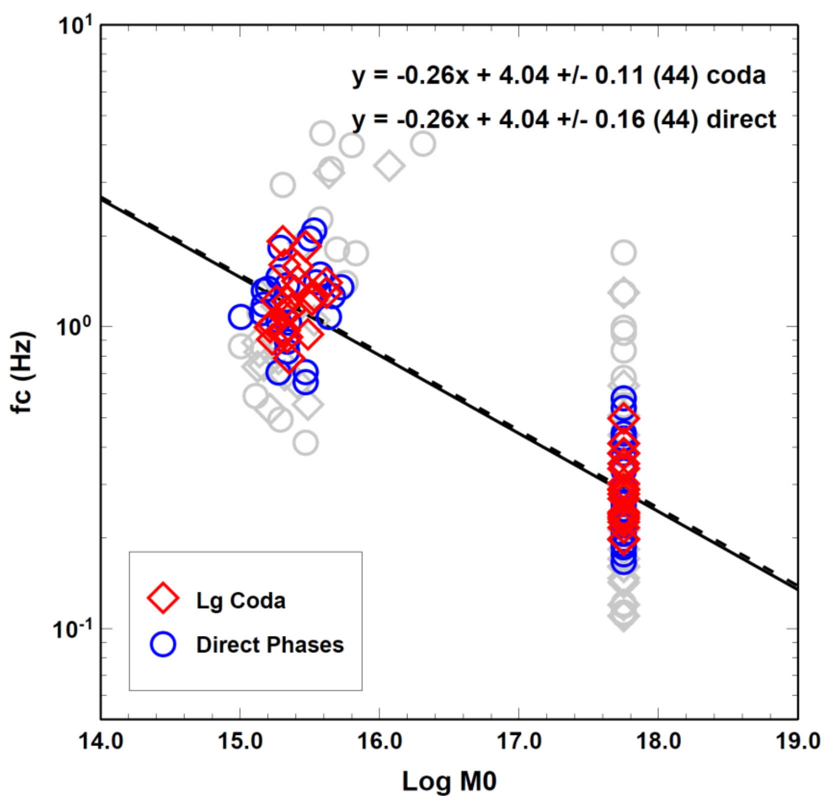

Figure 41. Estimates of corner frequencies versus log moment at each of the 39 stations, showing considerable variability. Stations with poor data are shown in gray. The linear regressions correspond to 22 stations with good data.

4.8 Comparison to Published Results: Bhuj, India Cluster

A sequence of earthquakes near Bhuj, India is interesting for several reasons. First, IRIS data are available from only three regional stations (Figure 42). Second, direct Lg is clipped for HYB recordings (at a distance of 1100 km) of the main shock (Mw 7.6). Third, one NIL channel is missing. Fourth, high-frequency Lg propagates poorly to ABKT, at a distance of about 2000 km. Only the largest events have adequate S/N. The magnitude-distance criterion excludes ABKT for all but the largest events. Fifth, many aftershocks occurred throughout the crust, with a range of locations, depths, and mechanisms (Bodin and Horton, 2004). Thus, this is a case of very limited regional data and considerable source variability. Of particular utility, several studies using local network data have been published (e.g., Bodin and Horton, 2004; Bodin et al., 2004; Malagnini et al., 2006), which provide quasi ground truth on source parameters.

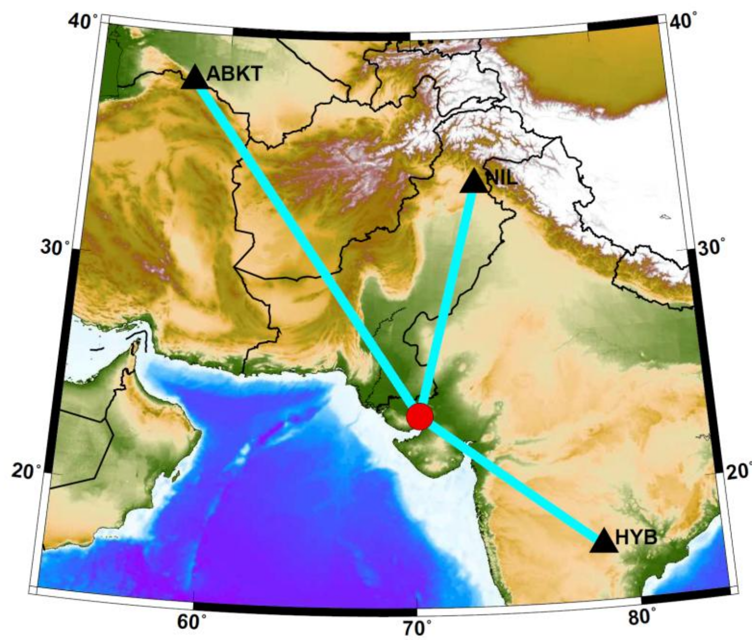

Figure 42. Locations of Bhuj earthquakes with regional recordings by ABKT, HYB, and NIL.

For most events, we could only use NIL data (two channels) to compute relative spectra of direct Lg, and only HYB and NIL data for Pn, Sn, and coda. Figure 43 shows such a case for a similar pair. Coda and direct phases agree very well. Figure 44 shows our estimates of source parameters using 45 events; 7 do not have adequate direct Lg without using HYB for the master event. Except for screening out spurious results, the analyses (from phase picks to source model fits) are automatic. From the fits, using 1-3 regional stations, we estimate f_c = 0.072 Hz and 0.084 Hz from coda and direct phases, respectively, for the main shock. Using 8 local stations, Bodin and Horton (2004) and Bodin et al. (2004) estimate static stress drop of 16-20 MPa, equivalent to f_c = 0.066-0.071 Hz. Our results are also consistent with published source estimates by Antolik and Dreger (2003) and Singh et al. (2003), using finite-fault analysis of teleseismic data. Thus, using very limited regional data, our results are consistent with GT source information. The scatter and bias of the estimates for the smaller events (Figure 44) are due to a combination of noise effects and events with varying hypocenters and mechanisms, which we have yet to unravel.

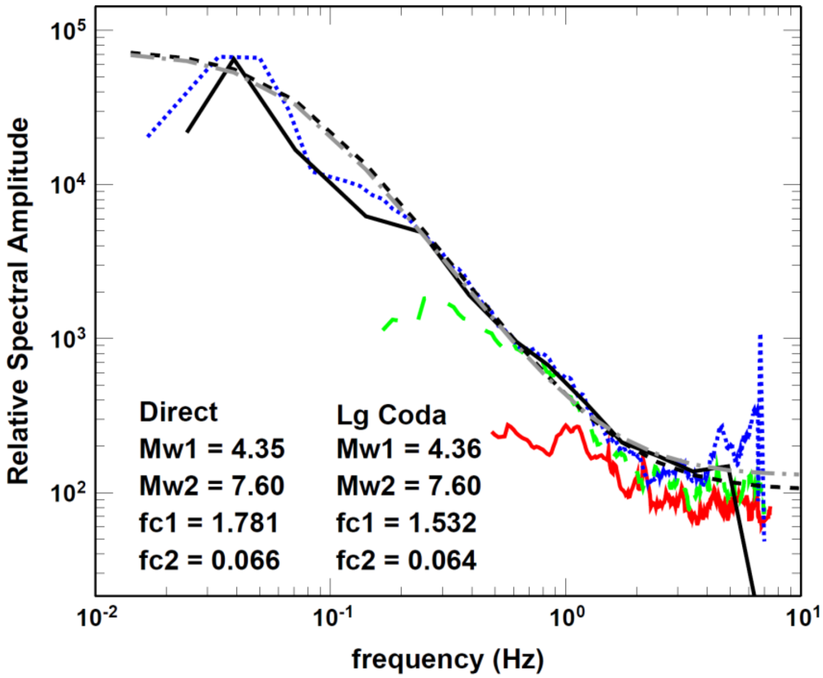

Figure 43. Relative spectra and source model fits for a Bhuj pair, using NIL data for direct Lg, and NIL and HYB data for all other phases.

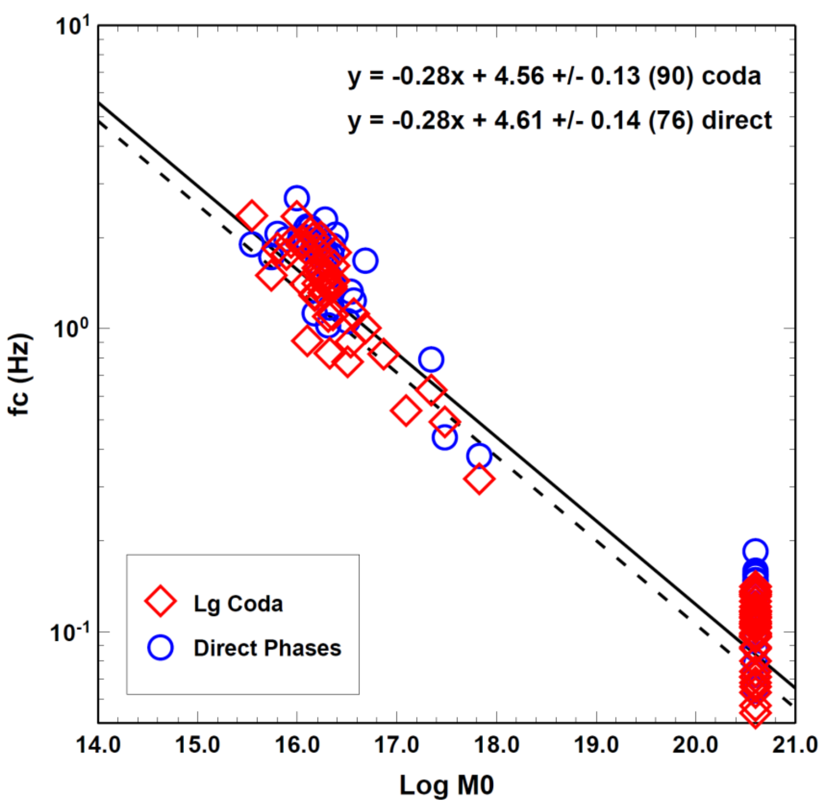

Figure 44. Corner frequencies versus moments for the Bhuj sequence. The linear regressions are weighted by moment to reduce the bias in the scaling relations from many small events.

5 ESTIMATING DISTANCE-RELATED EFFECTS

Given our large set of corroborated source terms, we fit source-corrected spectra to estimate distance and site terms, using the following equation for each station/path and phase:

$$\ln \widetilde{A}(f) \equiv \ln \frac{A(f)}{S(f)} = \ln G + b + \ln \varepsilon(f) - \frac{\pi f^{1-\gamma}}{Q_0 \nu} r, \tag{5}$$

where G is frequency-independent spreading, b is a constant site factor, $\varepsilon(f)$ is the residual site frequency dependence, and the last term is attenuation. Figure 45 illustrates source-corrected Lg (3C) spectra and the fit at VOS for an earthquake in eastern Kazakhstan. The constant of the fit, c_0, is related to spreading and the site factor, the first two terms on the right-hand side of Eq. (5). In Section 9, we describe how these effects are separated by regression analysis. The spectral shape depends on attenuation (Q) and site frequency dependence. Source-corrected spectral fits estimate effective Q as a function of frequency for fixed paths. This approach is *orthogonal* to the tomography analysis by LANL, which estimates the path dependence of Q for fixed (discrete) frequency bands. Comparing the results of independent measurements and methods corroborates paths with reliable Q estimates and identifies discrepancies, for which Q needs to be improved.

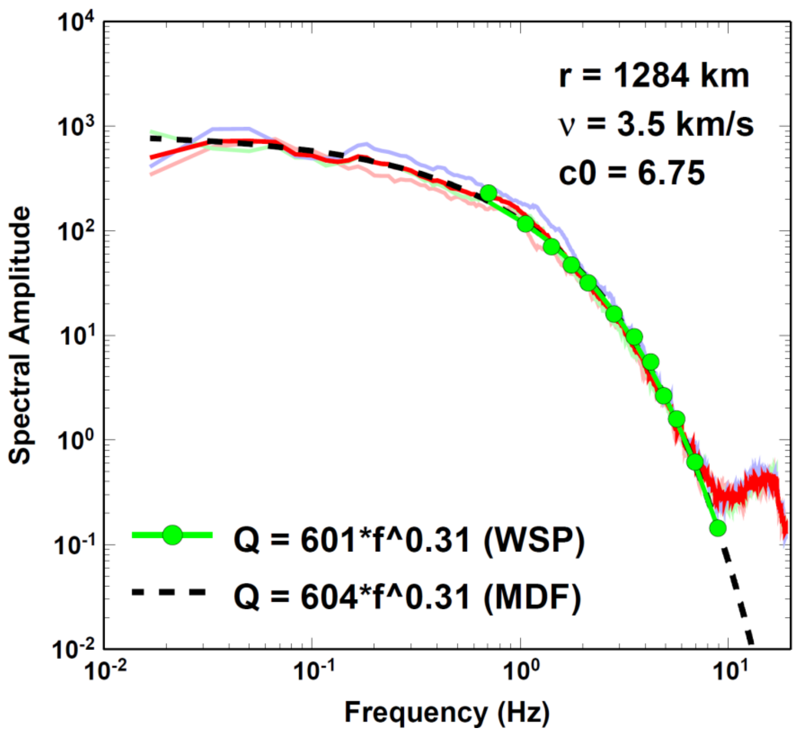

Figure 45. Source-corrected Lg spectra at VOS for an event in Kazakhstan, the fit (black curve), and Q estimates. Green circles are tomography Q results in discrete bands for this path.

To compare Q_0 and γ estimates of the two methods, we average Q^{-1} from tomography over grid cells along each path, for each of 12 frequency bands. We then linearly regress the tomography $Q(f)$ values, using $\log Q(f) = \log Q_0 + \gamma \log f$ to estimate Q_0 and γ for each path. Figure 45 shows that the independent Lg Q parameter estimates are nearly identical for that path. Figure 46 is an equivalent Q representation, showing the linear scaling of log *Q(f)* versus log frequency and how the actual tomography *Q(f)* values (green circles) are regressed to give Q_0 and γ estimates. To estimate Q from source-corrected spectra, we implemented two approaches. One is a simple grid search over the space of Q_0 and γ values, selecting the ones that minimize the RMS residual. The second is to convert the source-corrected spectrum to the *Q(f)* representation, as in Figure 46, and then use linear least-squares regression, as used for the tomography *Q(f)* values.

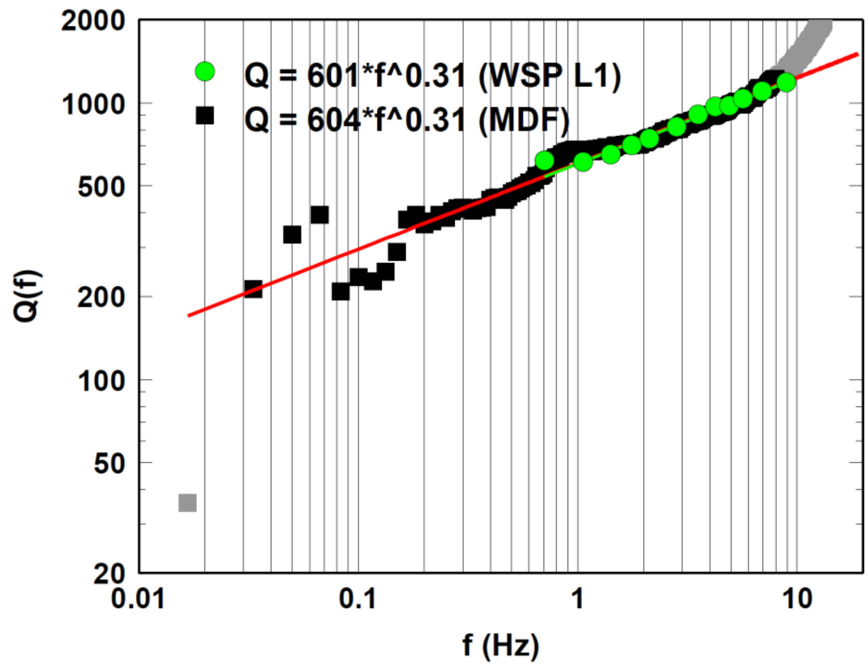

Figure 46. Representation of log *Q(f)* versus log frequency, equivalent to Figure 45.

An important caveat is that the Q-model fits for this case, and the remainder of this section, do not separate out frequency-dependent site effects, which can bias our Q estimates. In subsequent sections, we show the impact for stations with strong, systematic, frequency-dependent effects (e.g., KMI) and present approaches we investigated to treat them. Strong trends in site frequency dependence do affect Q estimates. Stations with resonances and/or random site fluctuations do not have appreciable impact on the Q estimates. For now, we assume that the residual site frequency dependence at most stations does not systematically bias the Q estimates. Based on comparisons to Q estimates from amplitude tomography and to independent site terms estimated from coda analysis, we find that this is a reasonable assumption for most, but not all, stations.

5.1 Examples of Q Comparisons: Tibet

Figure 47 compares Lg *Q* estimates for a case with excellent station coverage, corresponding to an earthquake in Tibet. The Q_0 and γ estimates of the two methods agree very well (Figure 48), both giving, e.g., low *Q* for paths to LSA, KMI, and ENH, expected for Lg propagation through the Tibetan Plateau. Figure 49 compares source-corrected Lg spectra and Q results for KNET stations. Many cases show excellent agreement, particularly where ray-path sampling is good, which is needed for tomography, but not for our fitting of source-corrected spectra. Below we also highlight some significant discrepancies and how the results can be improved.

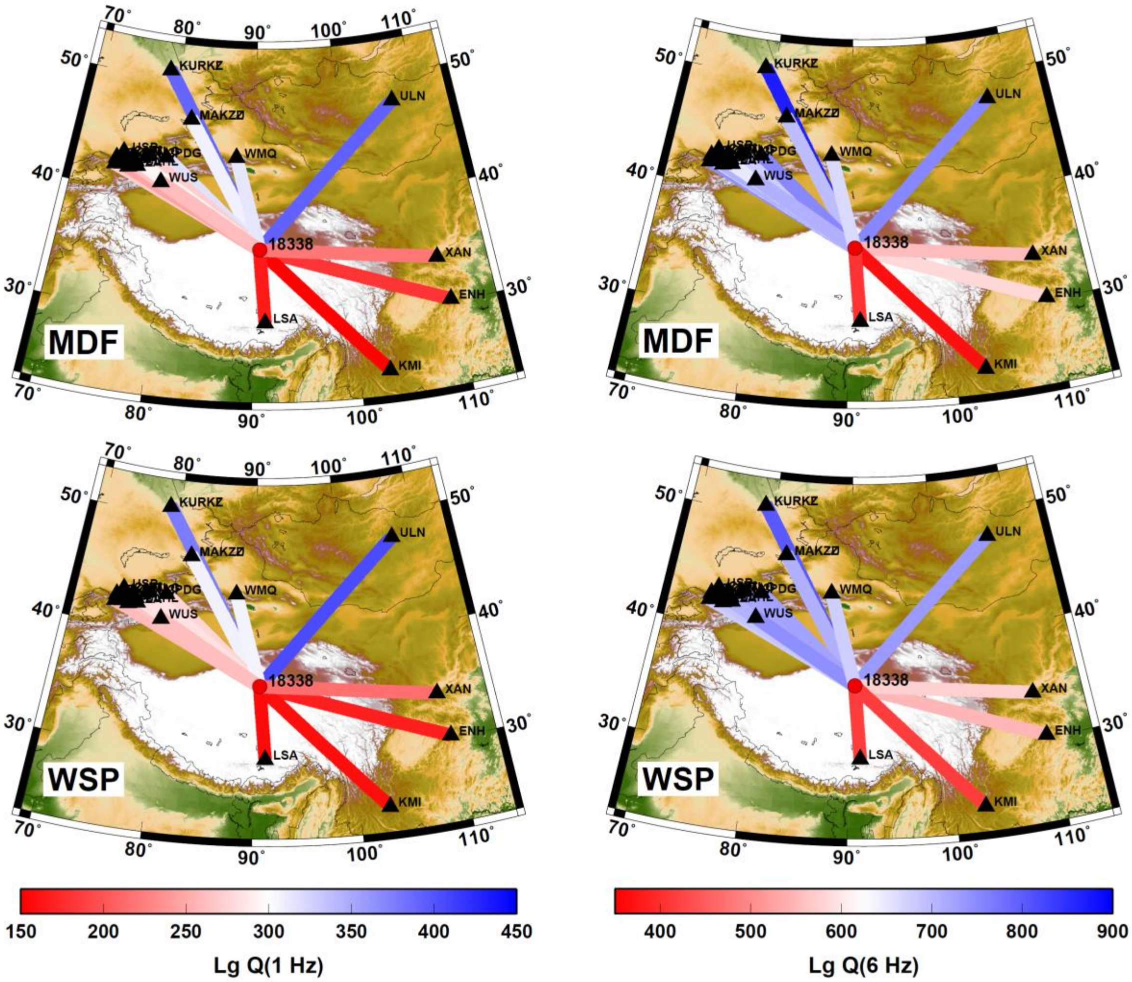

Figure 47. Comparisons of Lg *Q* estimates at 1 Hz (left) and 6 Hz (right) from fitting source-corrected spectra (top) and tomography (bottom) for paths from an earthquake pair in Tibet.

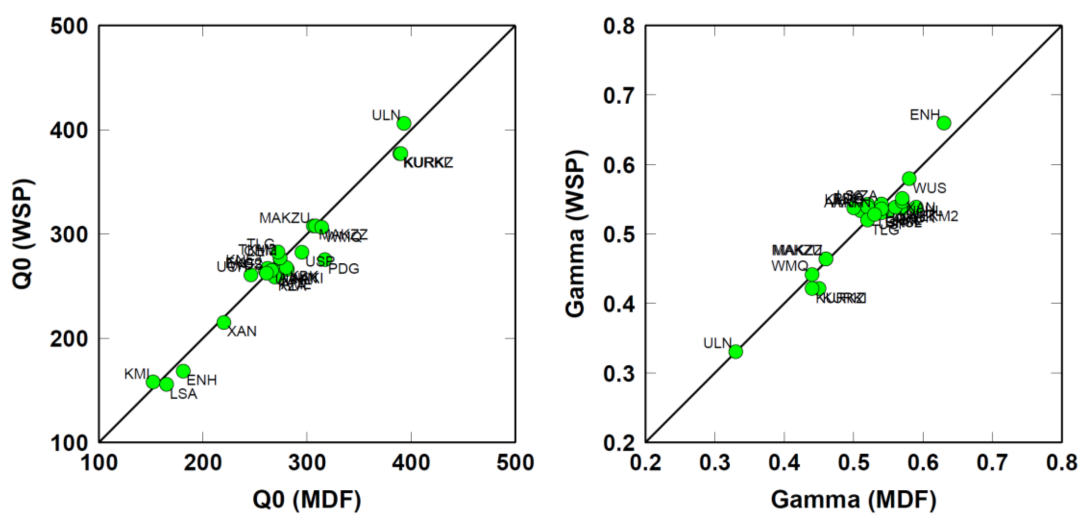

Figure 48. Direct comparison of Q_0 (left) and γ (right) estimates for the paths in Figure 47.

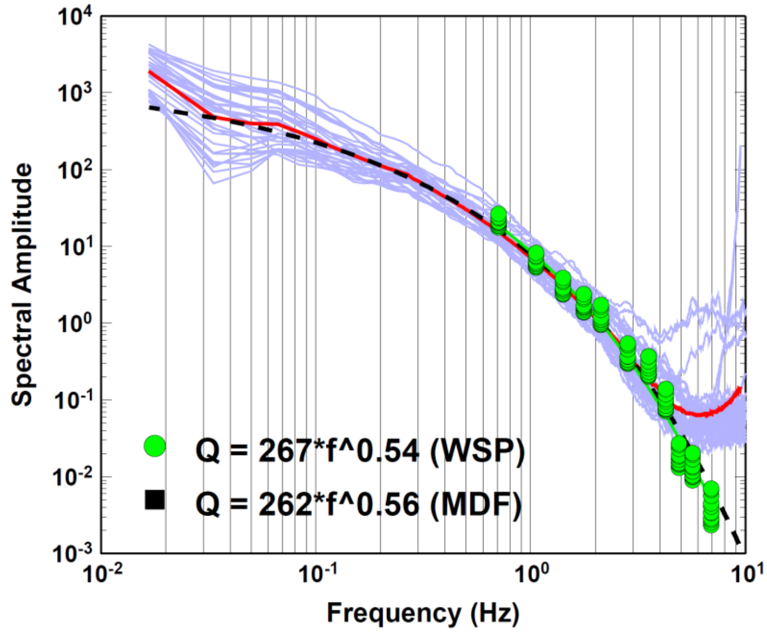

Figure 49. Source-corrected Lg spectra at KNET stations and comparison of Q estimates.

Note that a multi-band, multi-phase amplitude tomography run by LANL also provides source parameter estimates that are very consistent with our fits of relative spectra (Figure 50), except that the Mw estimate for the smaller event is slightly lower than ours. For cases with good station coverage and data quality, tomography often gives consistent source and Q estimates with ours.

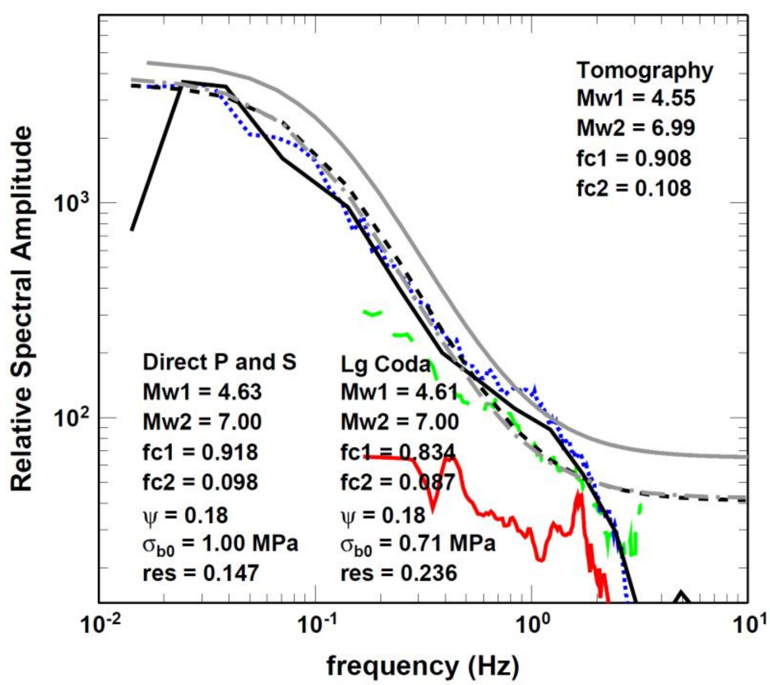

Figure 50. Comparisons of network-median relative spectra and source parameter estimates for an earthquake pair in Tibet. The solid gray curve and upper annotation are tomography results.

5.2 Examples of Q Comparisons: Northwest China

As a second case, Figure 51 compares Lg Q results for a cluster in northwestern China. The Q_0 and γ estimates from the two methods agree quite well, although there is somewhat more scatter for this Mw 5.3 earthquake, compared to Mw 7.0 for the previous case (cf. Figure 52 to Figure 48). The most noticeable difference is that our γ estimate for NIL is significantly lower than from tomography. Figure 53 shows source-corrected Lg spectra and source model fits for BRVK and NIL. The lower plots are equivalent Q representations of the upper plots, showing linear scaling of log *Q(f)* versus log *f*. The comparison for BRVK is excellent. For NIL, the Q_0 estimates are similar, but tomography Q estimates deviate higher for bands higher than 2 Hz, except for the Q estimate in the highest band that dips dramatically lower. This is a frequent observation, explored further in subsequent examples. Overall, our independent analysis corroborates tomography Q results for most of these paths, again for a case with excellent station coverage.

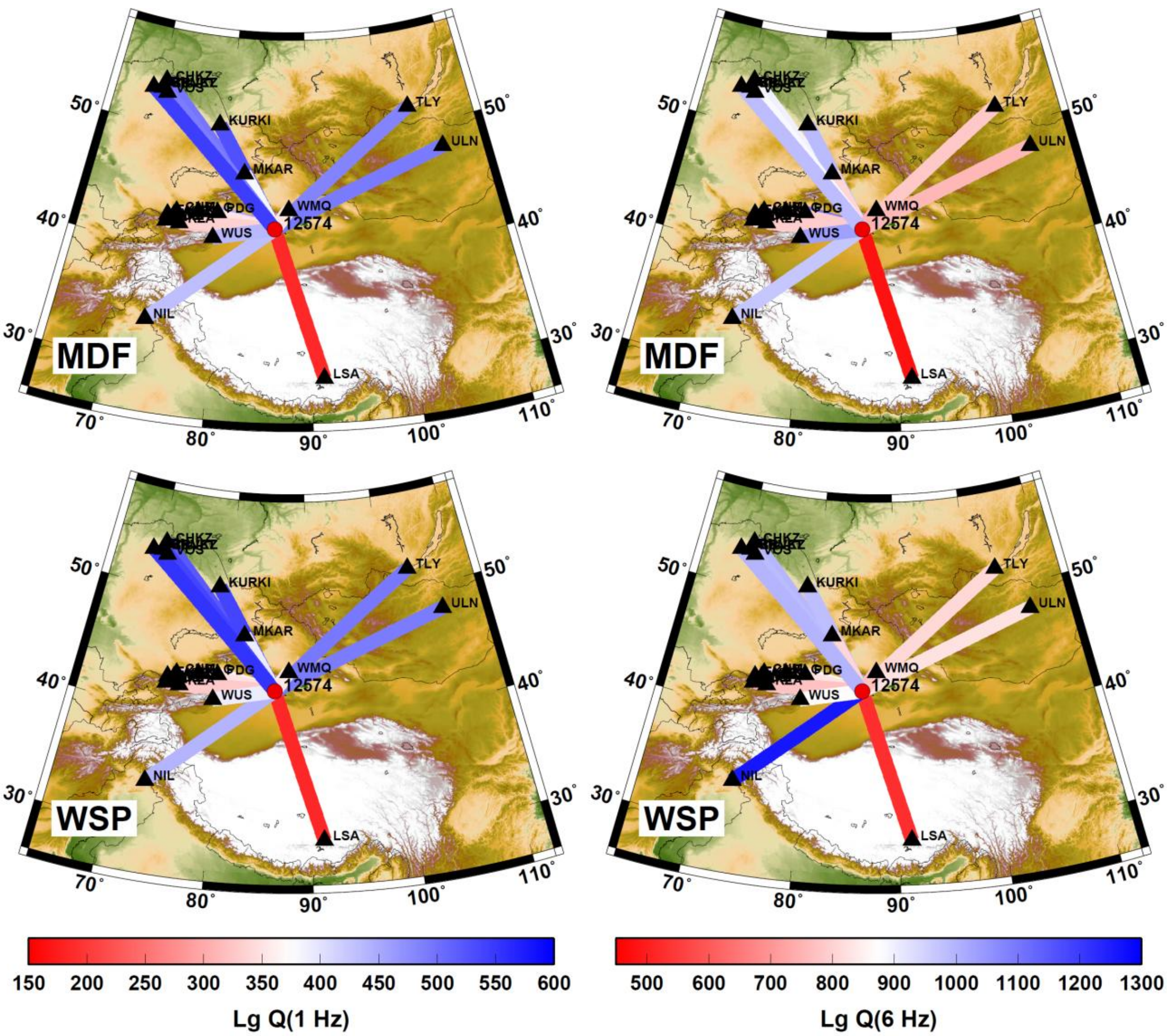

Figure 51. Comparison of effective Lg *Q* estimates at 1 Hz (left) and 6 Hz (right) for paths from a cluster in northwestern China to regional stations.

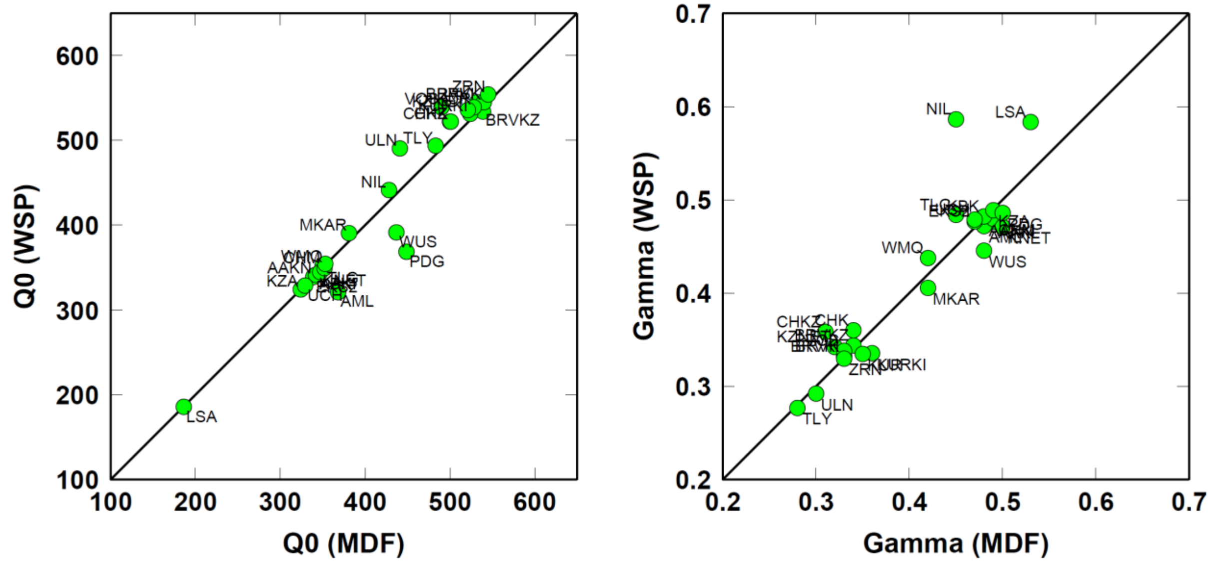

Figure 52. Comparisons of Lg *Q_0*(left) and γ (right) estimates for the paths in Figure 51.

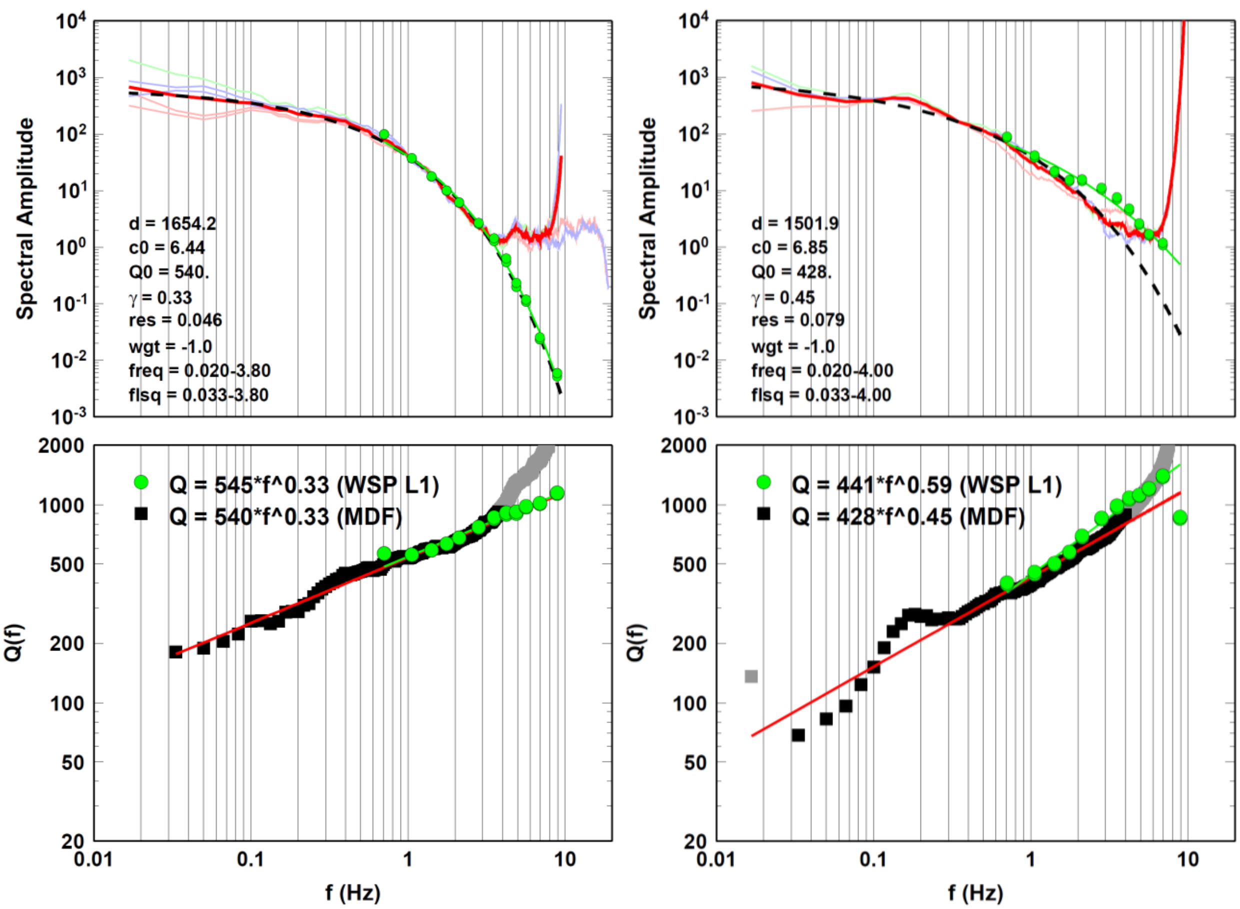

Figure 53. Examples of source-corrected spectra and Q estimates for BRVK (left) and NIL (right), which recorded the earthquake cluster in northwestern China. Green circles are tomography results, and black squares are results from source corrected paths.

5.3 Examples of Q Comparisons: Southwest Siberia

As a third case, Figure 54 depicts Lg Q estimates at 1 Hz (left) and 6 Hz (right) from the two approaches for a cluster in southwestern Siberia. Figure 55 is a direct comparison of the Lg Q_0 and γ estimates. The Q_0 (1-Hz Q) estimates agree quite well, while tomography Q estimates at 6 Hz are systematically higher than ours. We investigated possible explanations. One possibility is that the estimated corner frequencies from relative spectra are too high, causing our Q estimates to be biased low. We checked the relative spectra and source terms for this cluster and they appear valid (viz. Figure 12). Alternatively, the tomography Lg Q estimates in the higher bands may be biased high. To understand the underlying physical cause, it is instructive to also examine the Sn spectra and Q results for this case. Figure 56 shows the ZRNK 3C recordings, highpass filtered above 3 Hz. Sn is known to propagate very efficiently in the Kazakh Platform. The waveforms show that Sn coda significantly interferes with Lg at frequencies higher than 3 Hz. This effect appears to be biasing the tomography Lg Q estimates high for higher bands.

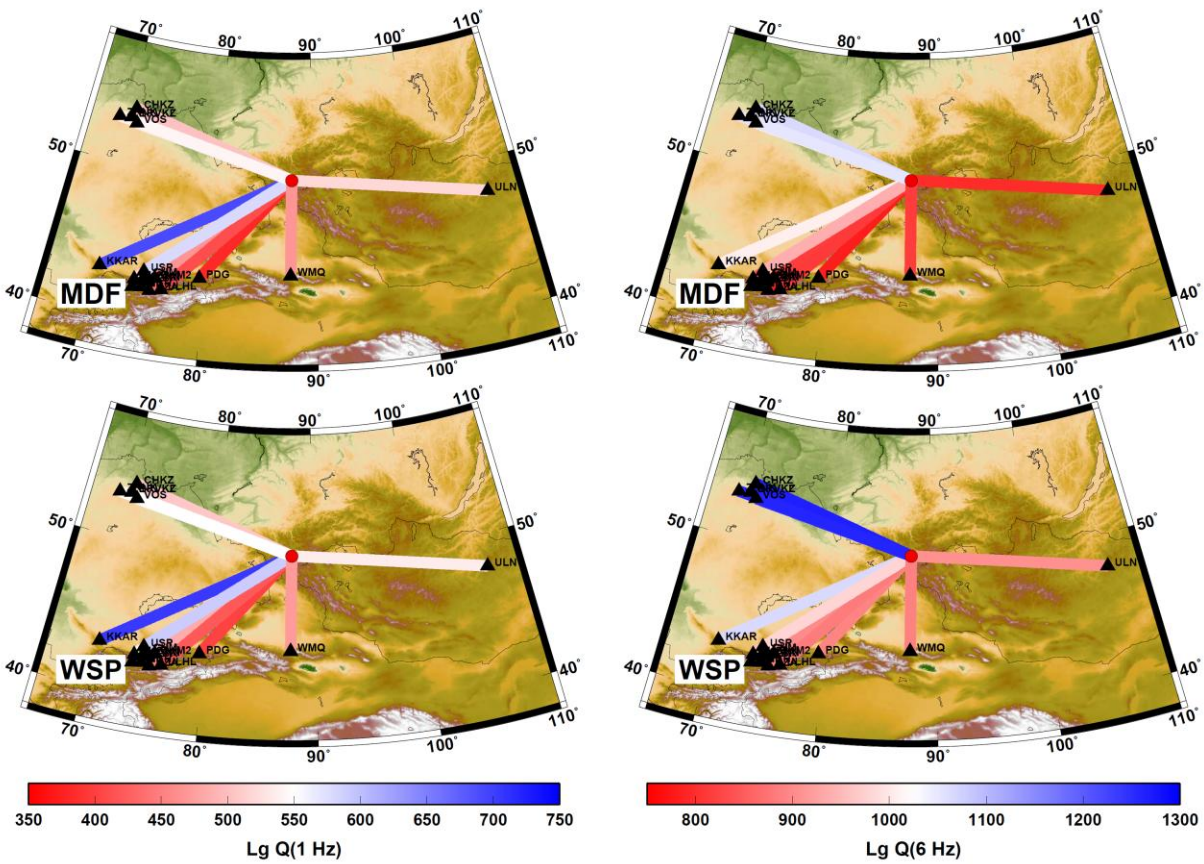

Figure 54. Comparison of effective Lg *Q* estimates at 1 Hz (left) and 6 Hz (right) for paths from a cluster in southwestern Siberia to regional stations.

To demonstrate this effect, Figure 57 shows source-corrected Lg and Sn spectra, averaged over Kazakhstan Network (KZNET) stations BRVK, CHKZ, VOS, and ZRNK, and comparison of Lg Q results. Tomography results agree with the source-corrected Lg spectrum up to 2-3 Hz, but then deviate for higher bands, following the source-corrected Sn spectrum, rather than Lg. This biases the tomography Lg Q estimates high. The tomography Q in the highest band is lower than the trend in the lower bands, because S/N is sufficiently poor to not satisfy the criteria, as seen in many cases. Note that noise effects are even more significant for smaller events than considered here, affecting tomography results that use such data. For our analysis, we use the larger events in each cluster to optimize data quality. This suggests that the pre-phase S/N criteria should be more stringent to eliminate Lg amplitude measurements that are corrupted by Sn coda.

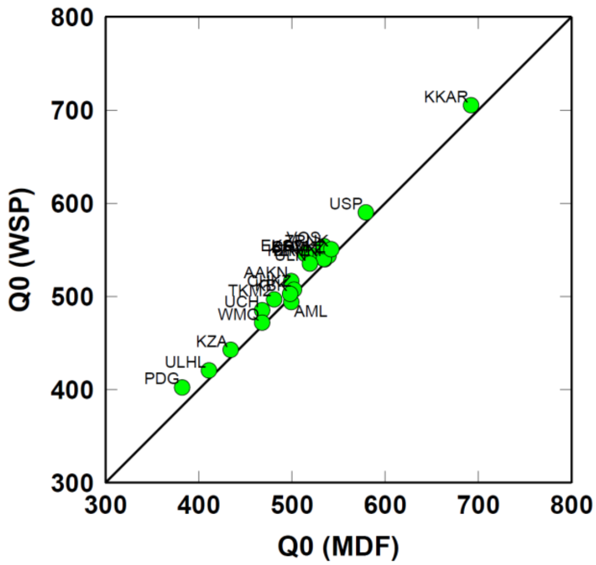

Figure 55. Comparisons of Lg Q_0 (left) and γ (right) estimates for the paths in Figure 54.

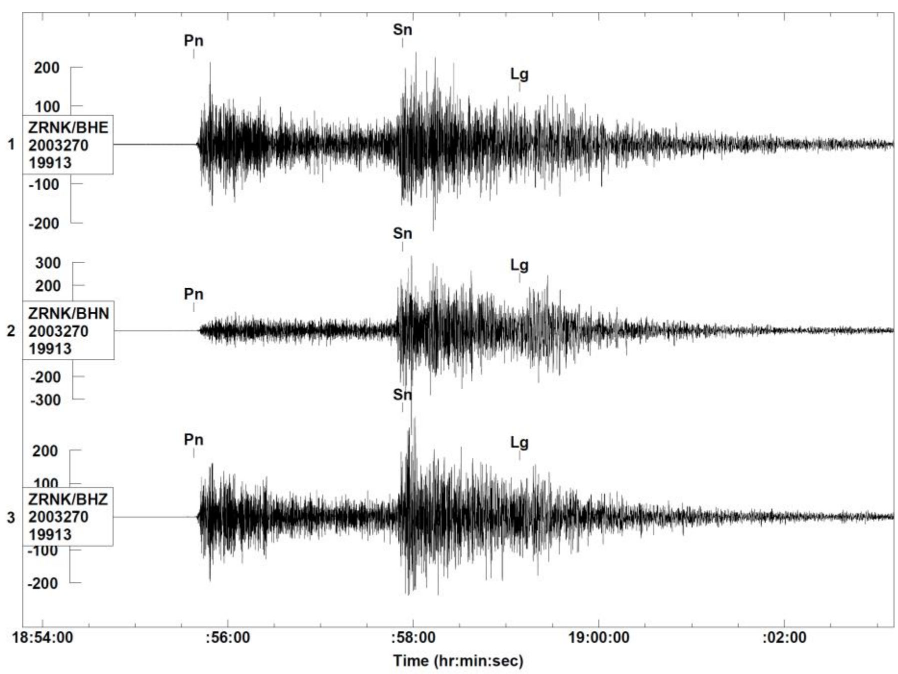

Figure 56. ZRNK recordings of orid 19913, high-pass filtered above 3 Hz. Sn and its coda are very strong for this and other paths at higher frequency, interfering with higher-frequency Lg.

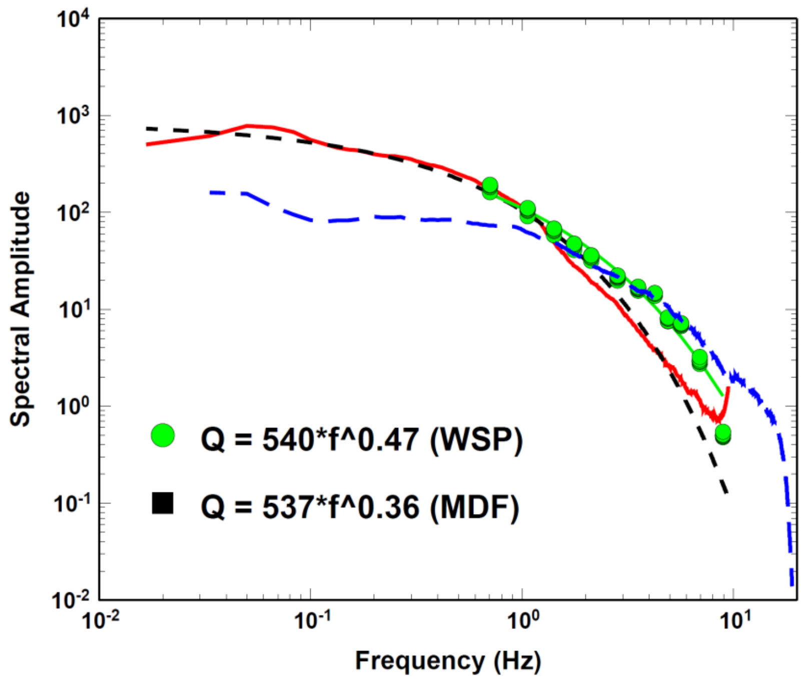

Figure 57. Source-corrected Lg (red) and Sn (blue) spectra, averaged over KZNET stations, and comparison of Lg Q results.

Note that if the Q discrepancy for Lg was due to a source effect (i.e., corner frequency error), Q estimates for other phases should differ similarly. Figure 58 compares our Sn Q estimates to those of tomography. There is more scatter than for the best Lg Q cases, which is not surprising because Lg is usually more stable. Nevertheless, the results of the two methods agree well, and there is no evidence of the bias seen in Figure 55. Figure 59 shows Sn spectral comparisons for EKS2 and WMQ. The higher spectral level, *c0*, for WMQ is related to geometric spreading.

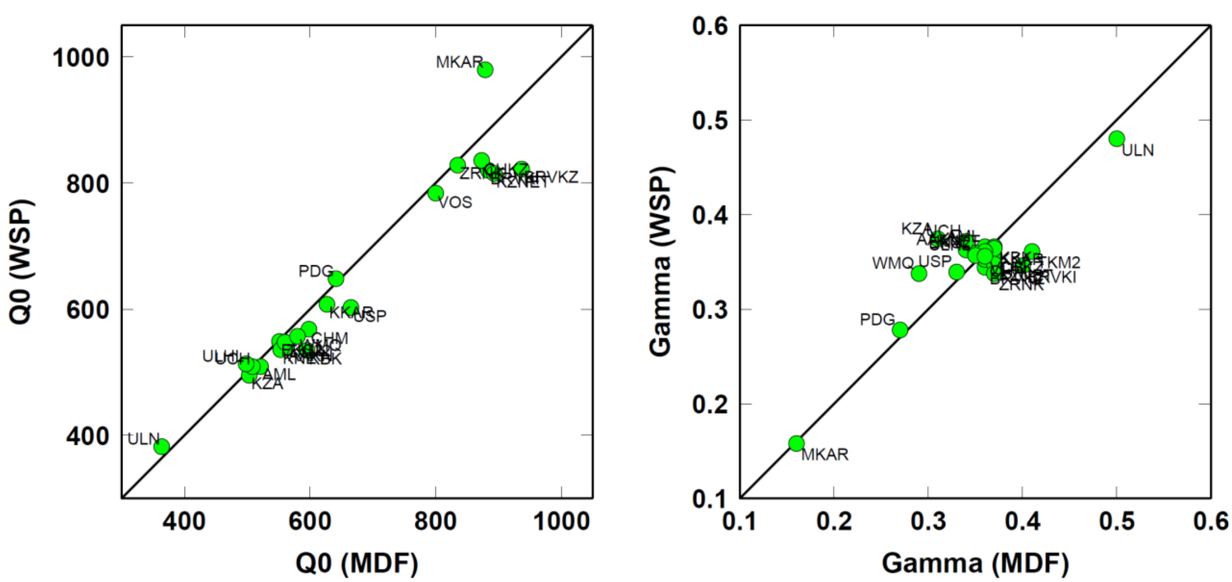

Figure 58. Similar to Figure 55, but comparing Sn Q estimates for the same set of paths.

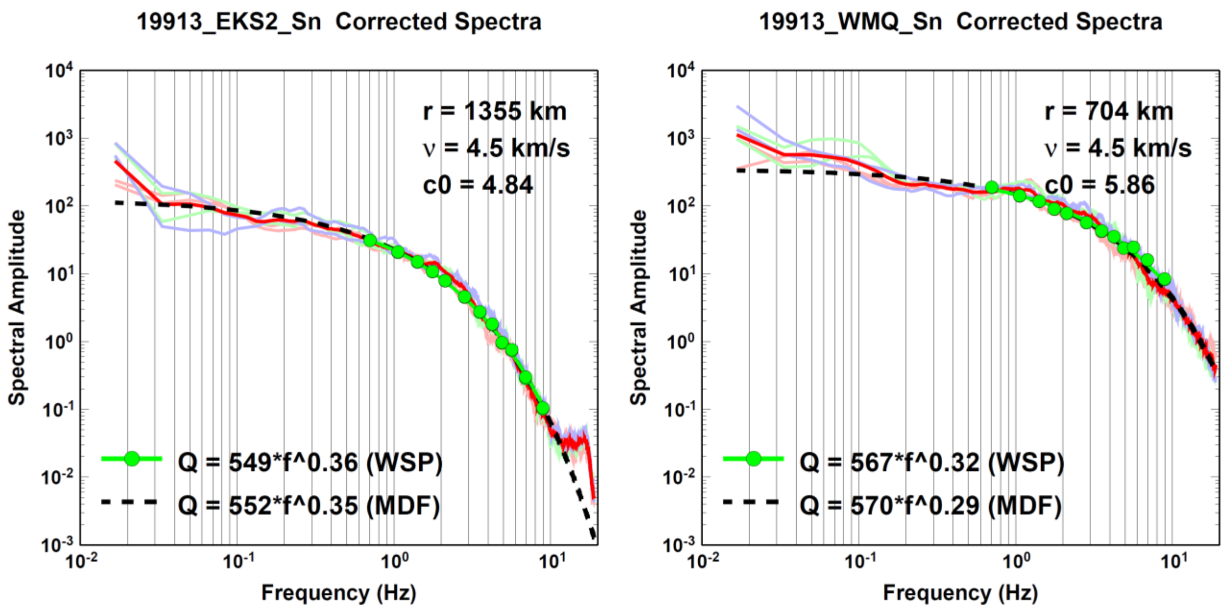

Figure 59. Comparison of the source-corrected Sn spectral fits to Q estimates from tomography.

We also processed source-corrected Pg and Pn spectra. As expected, these regional P phases are considerably more complicated and challenging than regional S phases, but equally important for valid application of regional discriminants to broad areas. Figure 60 compares Pg Q results for the same cluster, for the only two stations with Pg picks. Pg at WMQ has considerable spectral variability at low frequency. (Using the median of 3C spectra, rather than the average, often improves such results. However, the median of only three observations can also be unstable.) Otherwise, the Q estimates compare well with tomography. Figure 61 compares the Pn Q results. Many agree fairly well, but there are also some large differences (e.g., for ULN and WMQ). Figure 62 shows that the Pn Q_0 estimates agree for MKAR and UCH, but the γ estimates are considerably higher for tomography, especially for MKAR. Note in lower plots of Figure 62 that the tomography Pn Q estimates in the lowest frequency band (0.5-1.0 Hz) are much higher than the trend in the other bands. This is seen ubiquitously for Pn tomography results. We exclude this band in the regression fits of Q_0 and γ. Similarly, tomography Pn Q estimates for the higher frequency bands (e.g., greater than 3 Hz) also trend higher for this and many other cases, usually due to noise effects, causing the higher γ estimates. Our approach of using larger events with good S/N and reliable source terms allows many of the similarities and differences to be observed and understood, leading to improvements.

In general, Pn spectral measurements for distances less than about 200-300 km are complicated by short automatic time windows and/or ones that are actually measuring Pg or pre-event noise, depending on actual versus predicted (IASP91) arrival times. For many other cases we have examined, the Pn spectral bandwidths are limited and/or low-frequency Pn spectra are highly variable, due to these much shorter time windows than for Lg and Sn, complications from depth phases, and propagation effects, all inducing spectral variability and limiting the reliability of the Q estimates. In addition to treating automatic processing problems (e.g., phase picks and time windowing errors), more work is needed to improve Pn spectral stability (e.g., using pseudo-spectral measurements in the time domain, averaging over more events, etc.).

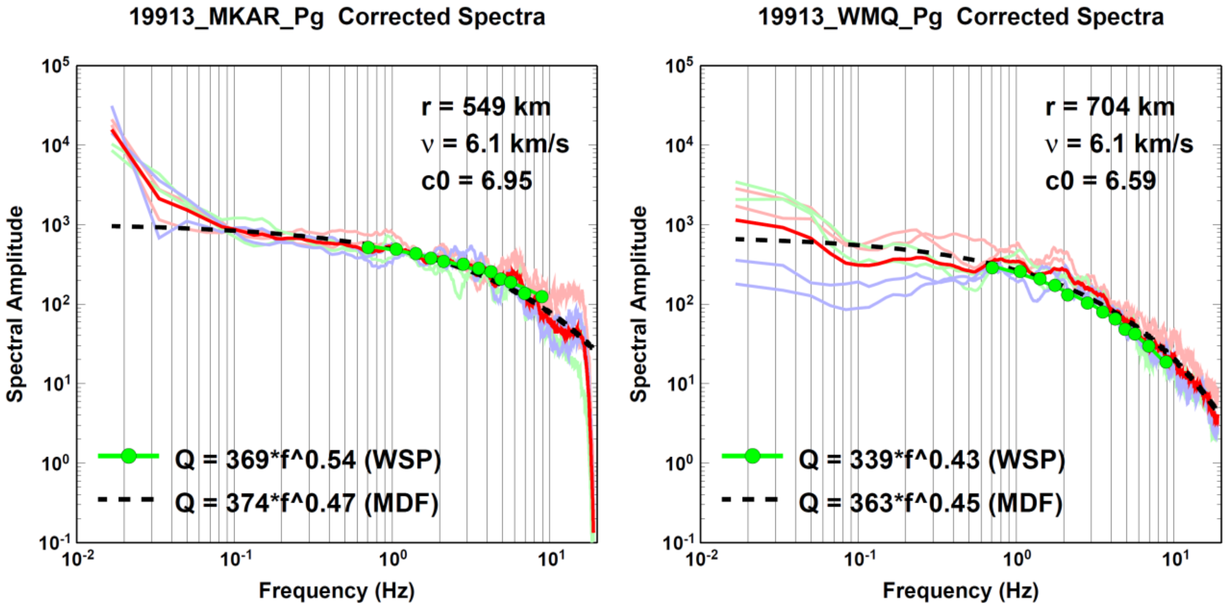

Figure 60. Source-corrected Pg spectra and *Q* results at MKAR and WMQ for the same cluster.

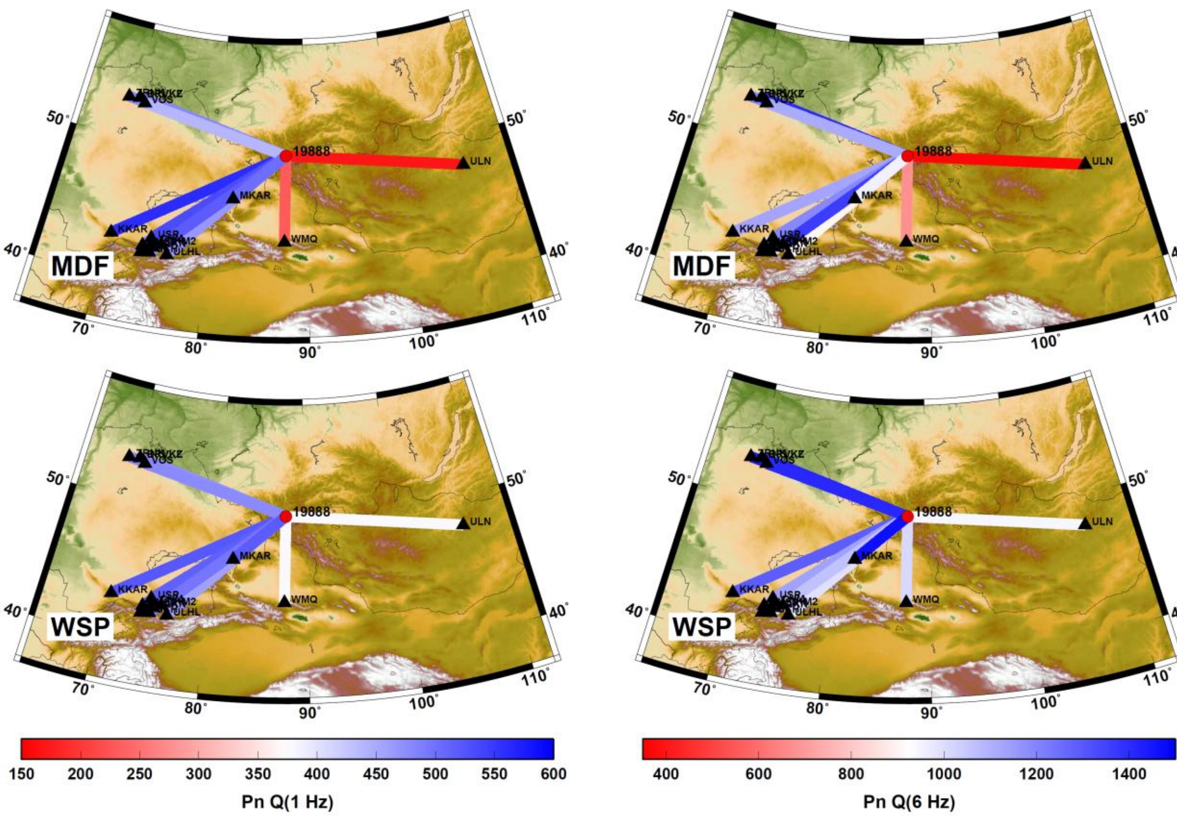

Figure 61. Comparison of Pn *Q* estimates from spectral fitting (top) and tomography (bottom) at 1 Hz (left) and 6 Hz (right) for paths from an earthquake cluster in southwestern Siberia.

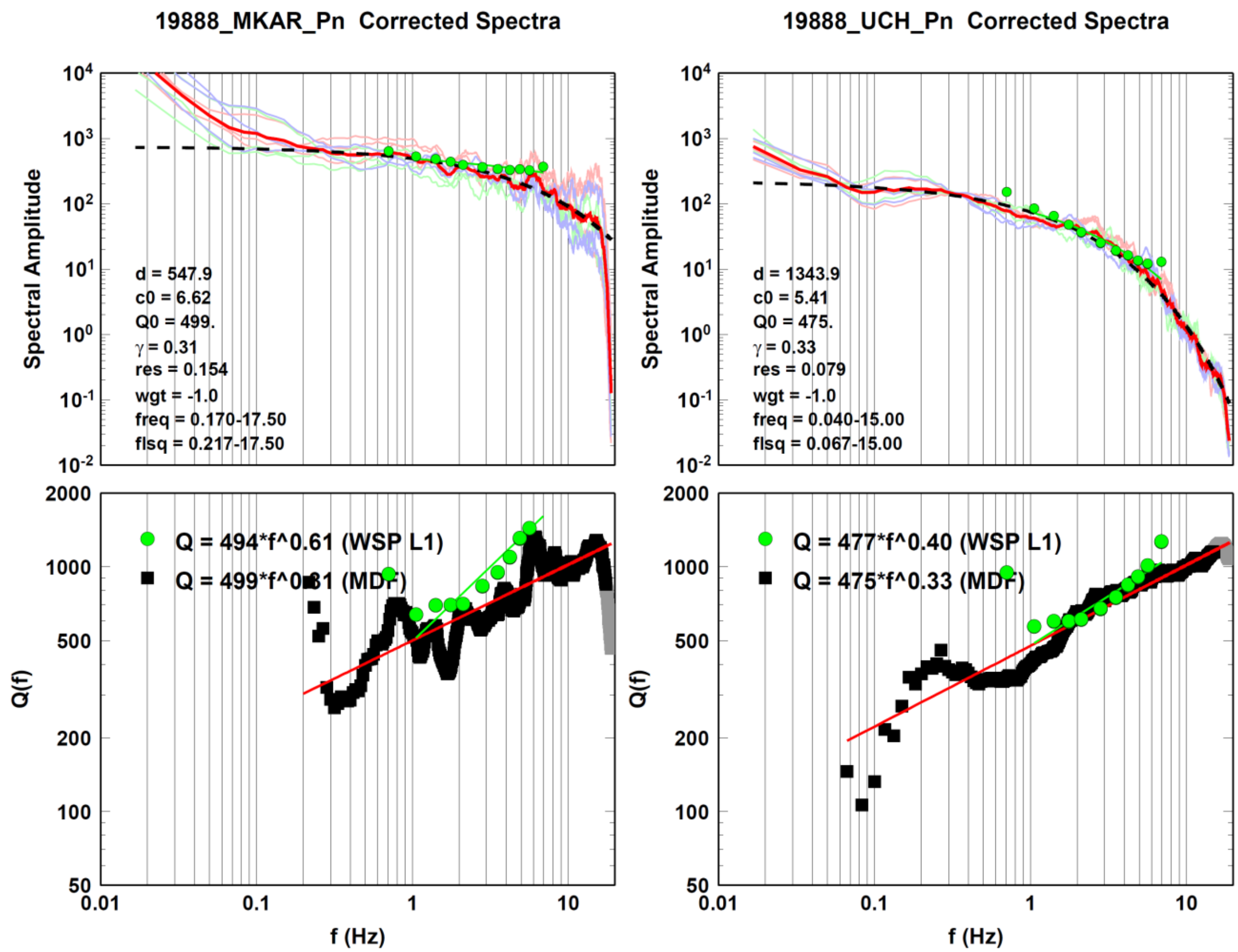

Figure 62. Source-corrected Pn spectra and *Q* model fits at two stations for the same cluster.

As a final result for this cluster, to indicate how we also use the fits of source-corrected spectra to quantify geometric spreading, Figure 63 shows the spectral fit constants (the *c0* values listed in many of the preceding plots) for each station versus distance, separated by phase. Also shown are regression fits that are related to geometric spreading, as we will describe in Section 9. Note the disparity in the number of Pg versus Pn observations (i.e., 2 versus 19). Although data for a single cluster are insufficient to estimate reliable spreading rates, collectively these results show how we use source-corrected spectra to estimate frequency-dependent attenuation and frequency-independent geometric spreading effects.

In our progress reports, we presented many other case studies, showing good agreement of our Q estimates with those from amplitude tomography for many paths and various regional phases, but also indicating how comparing our results to tomography can uncover physical effects that cause errors and biases in the Q estimates. We will touch on some in subsequent sections and discuss very important implications.

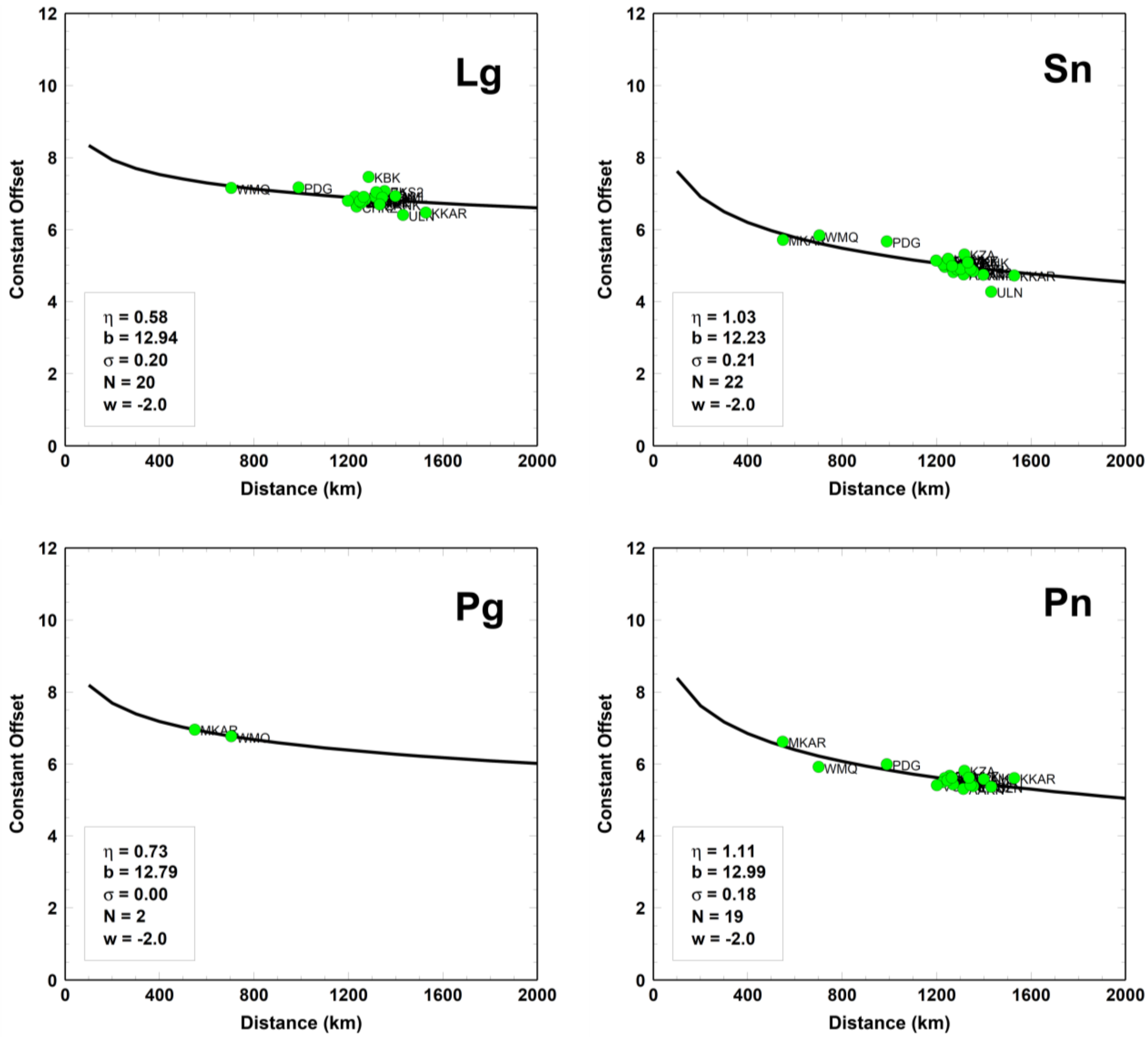

Figure 63. Constants of source-corrected spectral fits versus distance for each phase and station. The regression curves for each phase are related to geometric spreading.

6 TREATING SITE EFFECTS

For many stations, the source-corrected spectra do not exhibit strong site frequency effects that significantly impact our Q estimates, as evidenced by (1) comparisons to amplitude tomography, (2) log-linear *Q(f)* behavior, and (3) comparisons of spectral residuals (i.e., corrected for source and Q effects) to independent coda site terms. However, some stations do have significant site effects, whose treatment will improve Q estimates. We proposed and investigated two main strategies to address them, as described in this section.

6.1 Double-Difference Spectra

Analogous to our approach of canceling all but source effects using relative spectra for similar event pairs, an approach to eliminate all but attenuation effects is to compute the ratio of source-corrected spectra for clusters or pairs of events along similar azimuths to a given station, but at different distances. Starting with Eq. (5) in the Section 5, this ratio is simply modeled by

$$\ln\frac{\tilde{A}_1(f)}{\tilde{A}_2(f)} = \frac{\pi f^{1-\gamma}}{Q_0 v}\Delta r + c, \qquad (6)$$

where Δr is the separation of the clusters and c is a constant with respect to frequency, related to spreading and radiation pattern differences. We refer to this as a *double difference* because we subtract log source terms and then the resulting log spectra, also canceling site effects. This gives an average of Q^{-1} along the path between the clusters that has no trade-off with other effects. We illustrate this approach for two clusters along a northern path to MKAR (Figure 64). Figure 65 shows the ratio of source-corrected Lg spectra for the two clusters, which cancels the site term, and the spreading terms are just different constants, independent of frequency, assuming the standard model of Eq. (1). The fit of Eq. (6) (dashed curve in Figure 65) gives the Q_0 and γ estimates listed in the legend. For comparison, the legend also lists estimates of the Q parameters from tomography for this inter-cluster path, depicted by the green curve and circles. Figure 66 shows contours of the residuals from the grid search over the Q parameter space. This quantifies uncertainties of the Q_0 and γ estimates, although more work is needed to formalize this into rigorous statistical confidence regions. Note that there is a range of Q_0 and γ, inversely related, that provide similar residuals to the ratio of source-corrected spectra in Figure 65. The star shows that the Q parameters from tomography correspond to small residuals, near the minimum.

Based on this encouraging result, we examined additional paths to MAK, MAKZ, and/or MKAR (Figure 67). This is an excellent set of clusters to examine because we have good/verified source terms, and some have similar azimuths, but different distances to Makanchi stations. Figure 68 shows the ratio of source-corrected Lg spectra for a more southern path, compared to Figure 64. It includes the Q model fit (black curve) and comparison of Q estimates. These results illustrate how Q along intermediate paths between pairs or clusters of events can be estimated from the ratio of source-corrected spectra, giving Q parameter estimates that are free of source, spreading, and site, provided the corner frequencies are valid from our earlier EGF analysis. They can be used in tomographic inversions to constrain the average Q^{-1} along such paths. Note also that if Q is fairly constant along the path, we can further apply the Q correction to the source-corrected spectra, and recover the frequency dependence of the site term. This site term can then be applied to all spectra for that station, to improve estimates of Q for all paths to that station.

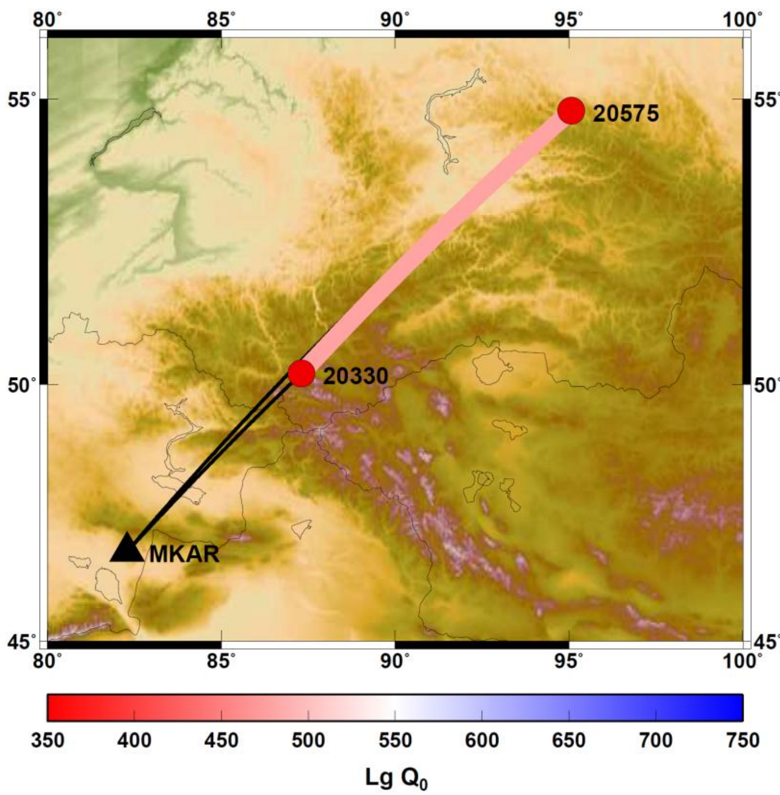

Figure 64. Paths for two clusters with similar azimuths, but different distances, to MKAR.

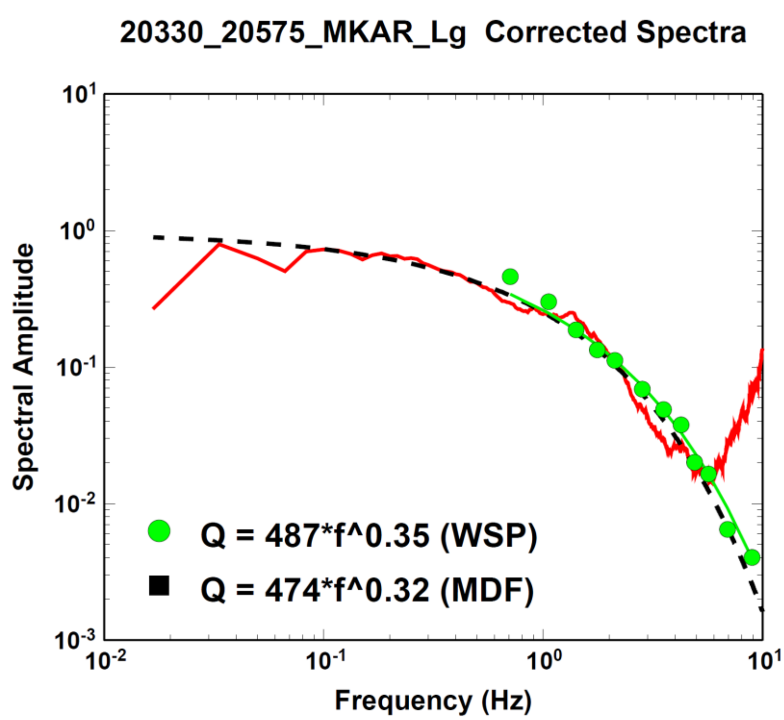

Figure 65. Ratio of source-corrected median Lg spectra for two clusters along a northern path to MKAR, canceling the site effects to give a *true* estimate of Q for this path.

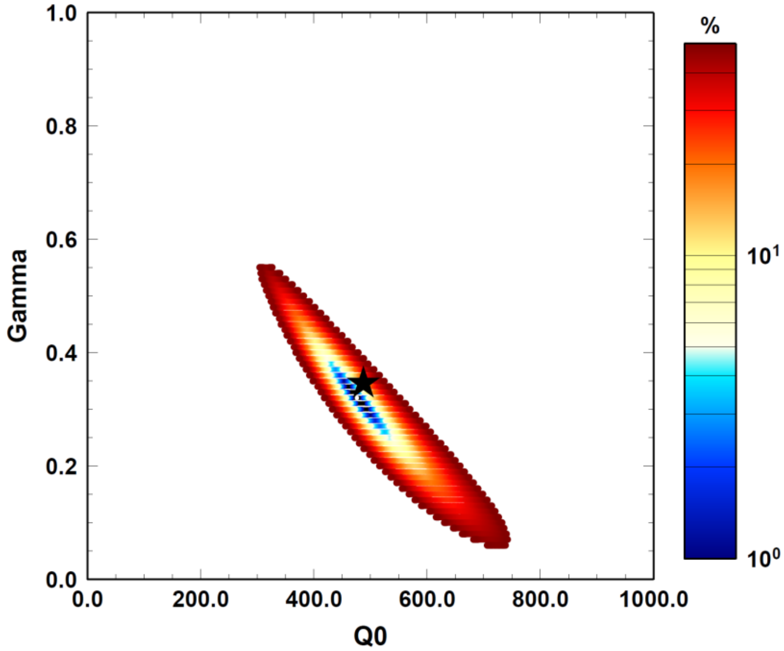

Figure 66. Contours of residuals over the Q parameter space, in percent relative to the minimum residual. The star shows the Q parameters estimated from Lg amplitude tomography.

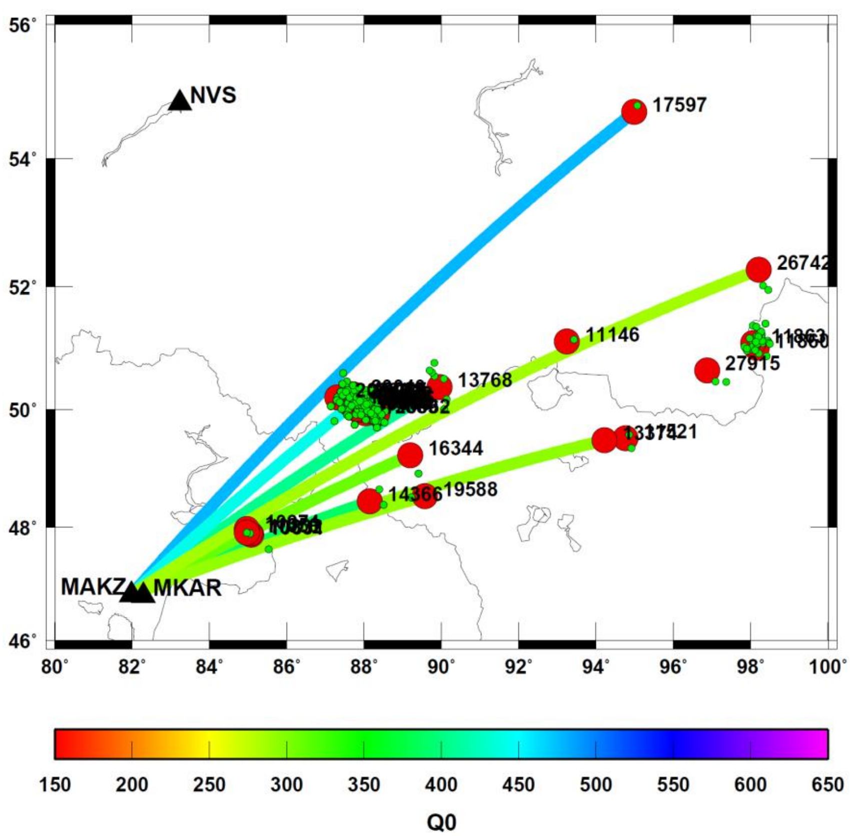

Figure 67. Effective Lg *Q0* for paths to MAK, MAKZ, and MKAR, using source corrections estimated from various pairs/clusters.

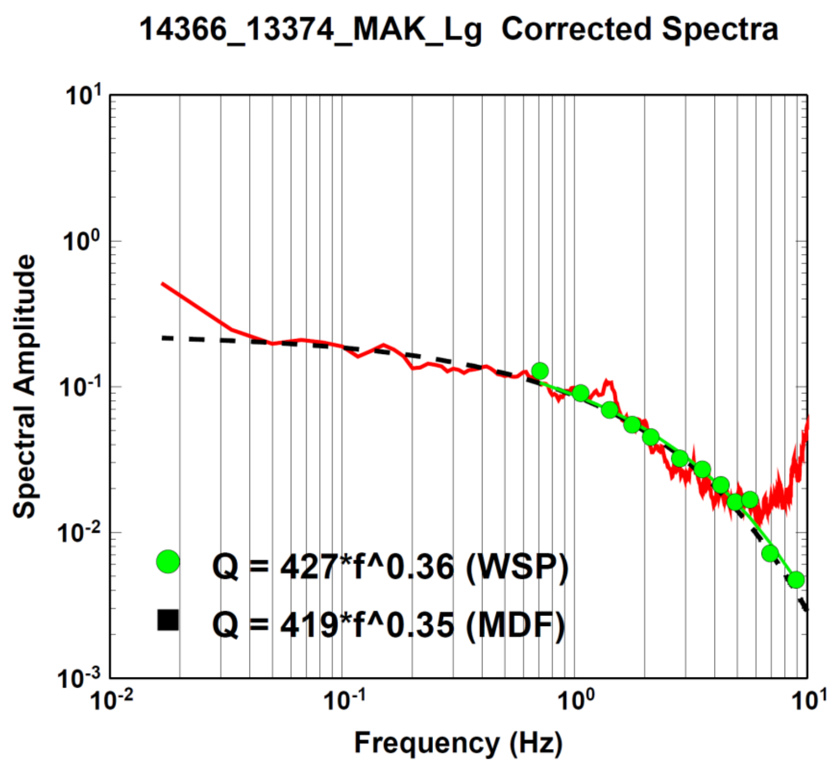

Figure 68. Ratio of source-corrected median Lg spectra for two clusters along a southern path to MAK, and comparison of Q estimates.

To explore the site effects and variations of Q along the path, we also fit source-corrected Lg spectra for the full paths from the individual clusters (i.e., not using ratios of source-corrected spectra). For example, Figure 69 shows source-corrected Lg spectra and Q model fits for the individual clusters. Except for the lowest tomography band, the Q estimates for the inter-cluster path, as well as those from the individual clusters to station MAK, are well corroborated by independent analyses (i.e., tomography in discrete bands versus fitting source-corrected spectra over broad frequencies for fixed paths). The results for MAK, and many other stations, indicate that, although there are site resonances and fluctuations (cf. Figure 71, below), there is no significant site trend that biases the Q estimates substantially. Figure 70 shows residual contours for Lg Q parameters along the corresponding paths. There is a region of Q_0 and γ values, whose shape depends on spectral variations, that gives very similar residuals. This indicates that the individual parameter estimates have uncertainties and a trade-off, but note that the combinations of Q_0 and γ estimates are often well constrained, and there is negligible difference in the Q corrections for this range.

We have found a few cases like the ones shown here, where the double-difference approach works very well. However, at present, there do not appear to be enough such cases to make this approach broadly applicable. Among the complications, it is necessary to have clusters or pairs of events with good source terms along sufficiently similar azimuths, and both not too close to (or far from) the station or each other. This is especially problematic for low Q paths, where the cluster at the farther distance often does not have sufficient bandwidth with adequate S/N to obtain a reliable fit.

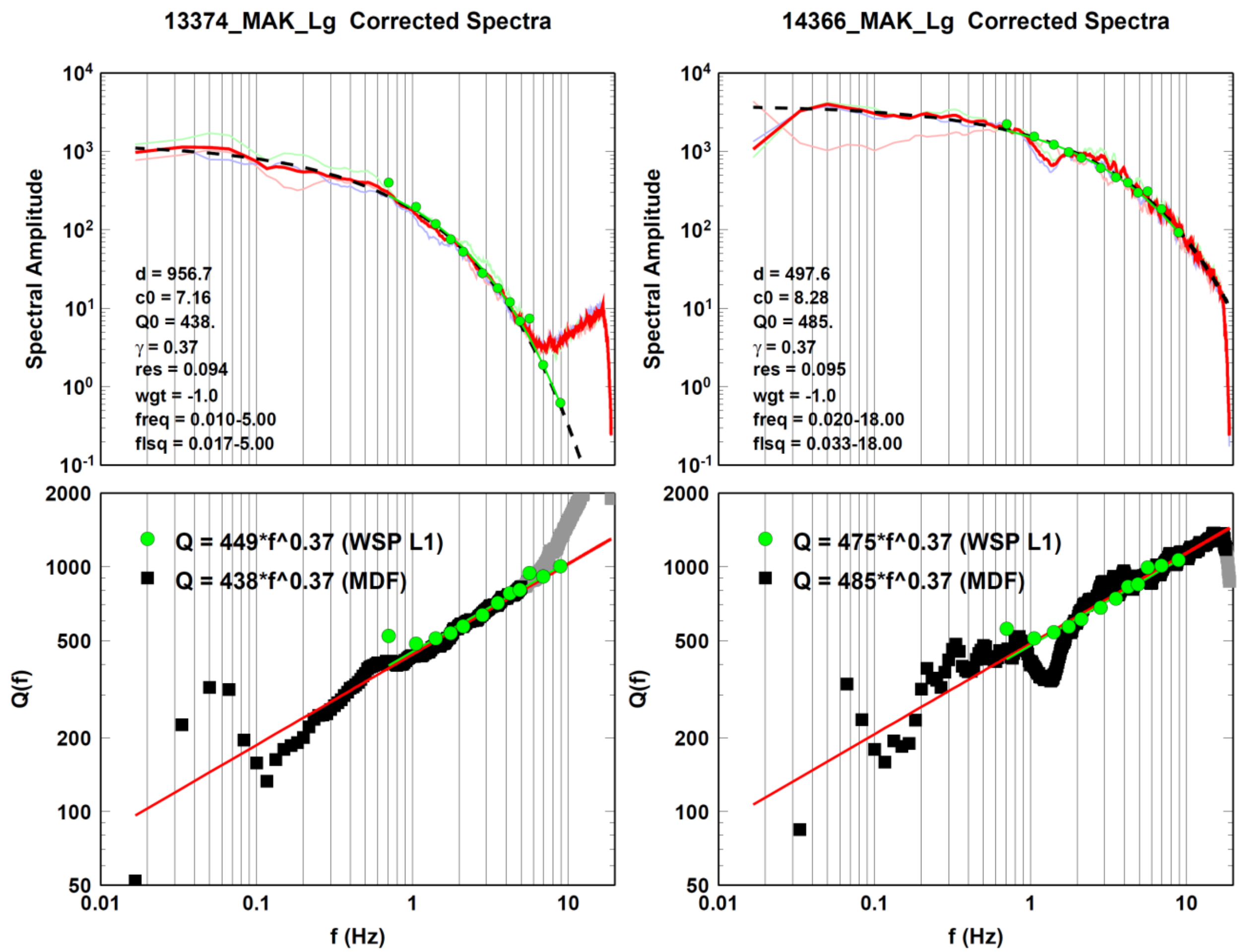

Figure 69. Source-corrected Lg spectra and Q model fits for two clusters (one at 957 km and the other at 498 km) along the more southern path to station MAK.

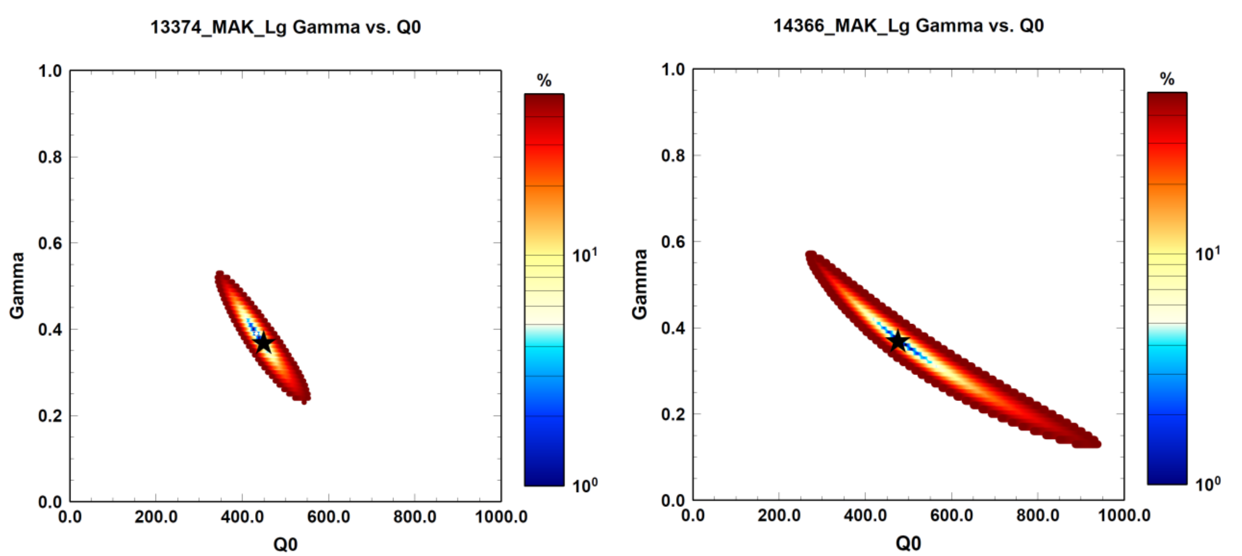

Figure 70. Residual contours corresponding to Figure 69. Stars are the tomography Q estimates.

6.2 Independent Coda Site Corrections

Another approach we discussed in our proposal is to use independent site terms estimated from coda methods. To illustrate the potential applicability, Figure 71 shows relative site terms for MK31 and MAKZ, based on different sets of events and measurements of either direct Lg or Lg coda. Except for some minor differences, all of the curves are in good agreement, including a spectral bump at about 1-2 Hz and similar relative decay at higher frequencies. This suggests that site terms already estimated at LANL by Dr. Phillips from coda tomography, independent of his amplitude tomography work for direct regional phases, or my fitting of source-corrected spectra, can be applied to the direct Lg spectra without circularity.

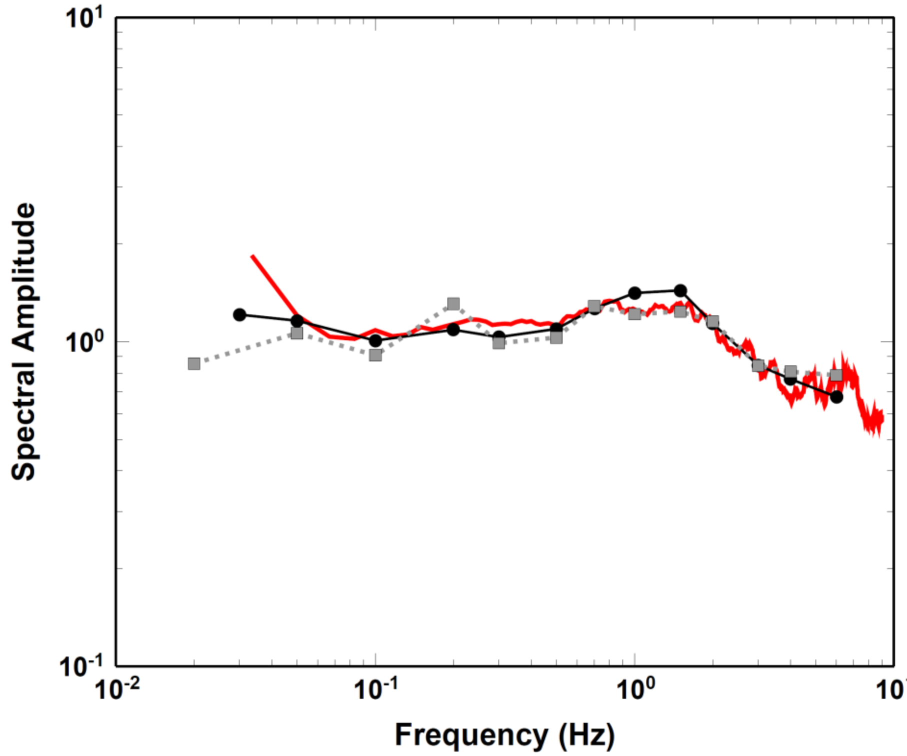

Figure 71. Relative Lg site effects for MK31/MAKZ(IU). The red curve is the mean relative spectra of direct Lg for three events recorded by both stations. The gray squares are coda results in discrete bands for one of the events. The black circles are the ratio of coda site terms for the two stations, estimated at LANL using many events.

As a direct example, Figure 72 shows the source-corrected Lg spectra at TLY for an earthquake in Mongolia, exhibiting a strong spectral bump at about 2 Hz. This causes significant departures of the spectra from the standard log-linear Q representation of $\log Q(f) = \log Q_0 + \gamma \log f$, as seen in the lower plot of Figure 72. This resonance biases the Q_0 estimate from spectral fitting higher than that from amplitude tomography. To demonstrate that this is a site effect, Figure 73 compares the residual spectrum, after correcting for the estimated source and Q terms, to site effects for vertical (BHZ) and horizontal (BHH) channels of TLY that were independently estimated from a coda tomography analysis at LANL. A shift between the spectral residual and the coda site terms at low frequency depends on how the centroids of the coda bands are defined and simply spectral variability. Like Figure 71, this supports the premise that coda site terms are applicable to direct Lg spectra.

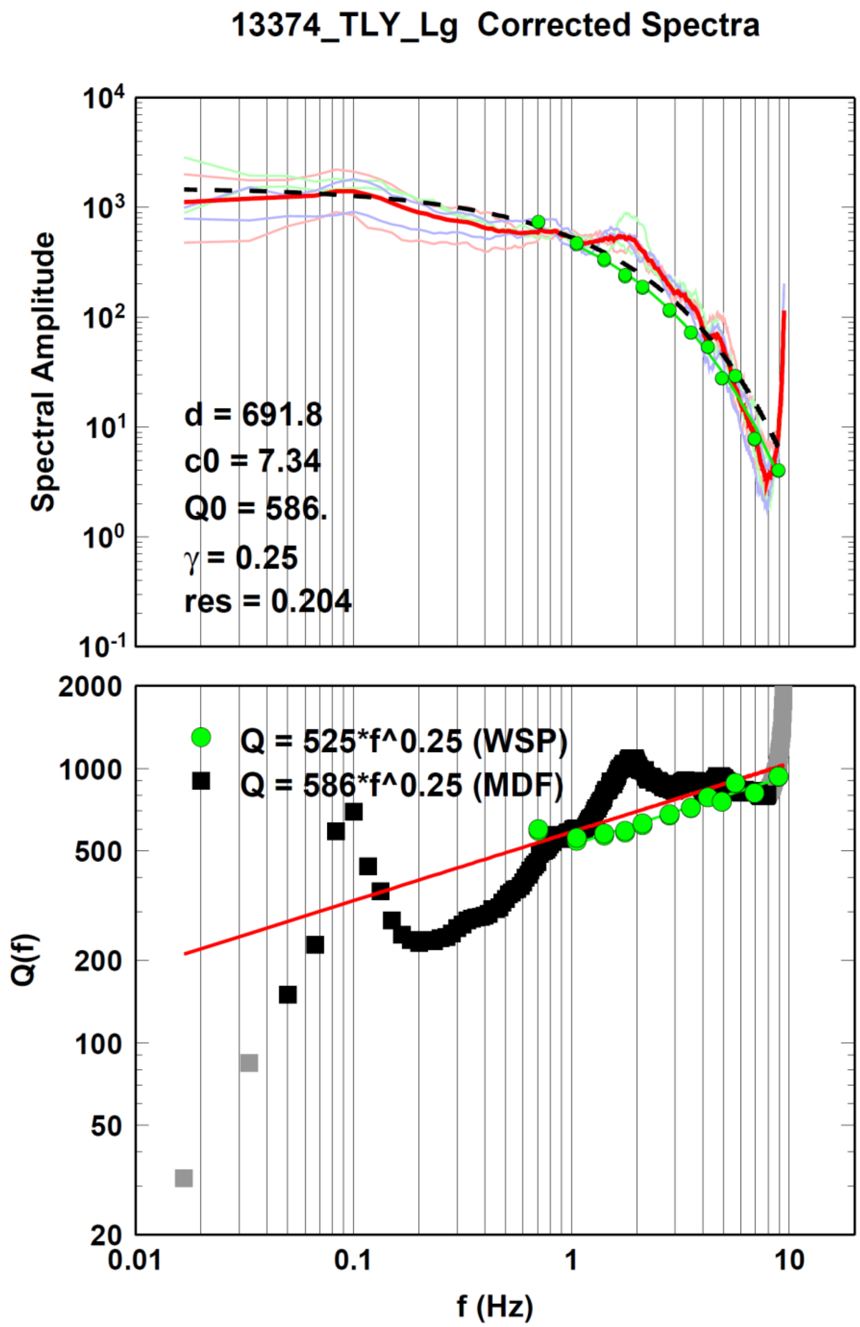

Figure 72. Source-corrected Lg spectra at TLY and *Q* model fits for an earthquake in Mongolia. Strong site effects at TLY cause a prominent spectral resonance at about 2 Hz.

Figure 74 shows similar results as in Figure 72, but now also correcting the source-corrected Lg spectra for the coda site terms. This corrected spectrum now exhibits more consistent log-linear *Q(f)* behavior (lower plot of Figure 74) , the fit gives a Q_0 estimate that is more consistent with that from tomography, and the RMS residual is reduced from 0.204 to 0.075, almost a factor of three. The new γ estimate is now slightly higher (0.28 versus 0.25), but this seems more accurate, considering that (1) the original spectral residual and the coda site terms decay sharply for frequencies greater than 3 Hz (i.e., the original estimate of γ is biased low by this site effect) and (2) excluding the two highest bands when regressing the tomographic direct-Lg Q(f) values gives an estimate of $\gamma = 0.27$.

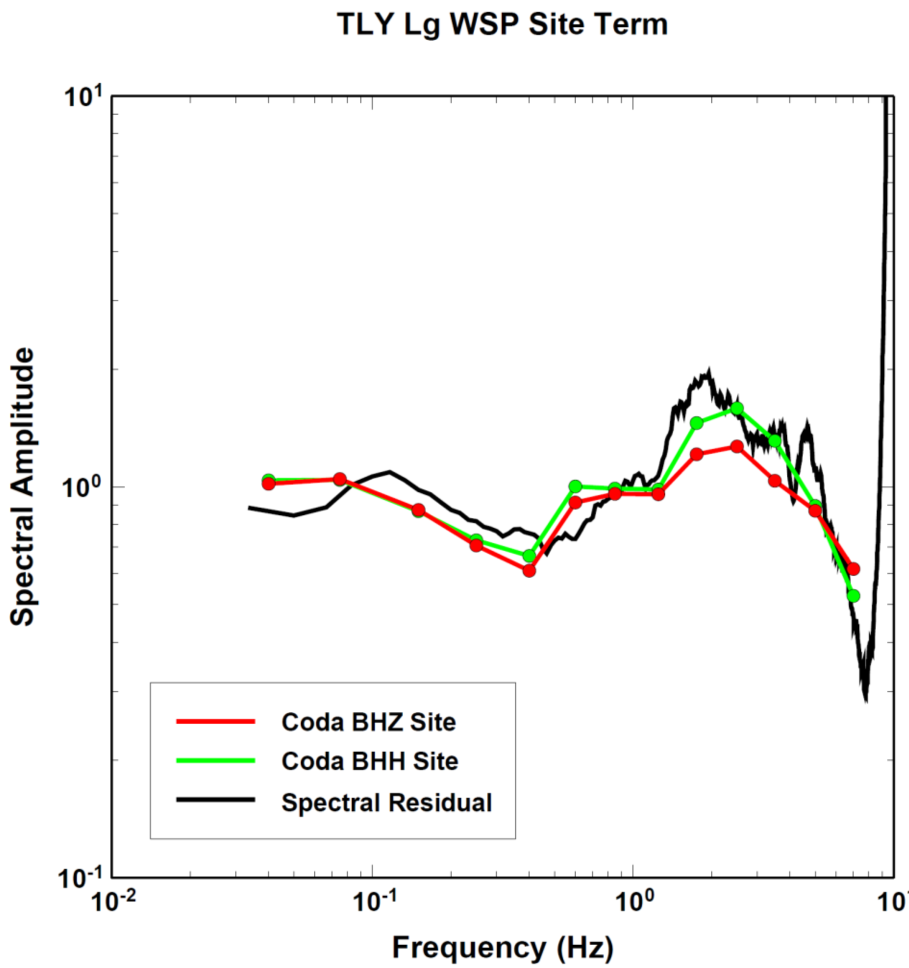

Figure 73. Comparison of the Lg residual spectrum at TLY (removing estimated source and Q terms) to site terms estimated from coda for vertical and horizontal channels.

Note, however, that even for this relatively strong site resonance and high-frequency attenuation, the Q_0 and γ estimates both differ by only about 10%. A significant drawback for broad practical application is that the coda site terms were estimated in more limited range of frequency bands, which is why the corrected Lg spectrum in Figure 74 is restricted to 0.05–7 Hz. Despite loss of spectral content, the source- and site-corrected spectrum is more stable for this case. For other cases, the limited spectral range and errors in the coda site terms, due to data quality issues, degrade the quality of the Q-model fits. We need to further explore application of coda site terms (improving data quality and extending their frequency range) to the source-corrected spectra, to improve Q estimates. For now, we assume that frequency-dependent site effects have marginal impact for most stations. In Section 10, we present additional comparisons of our median spectral residuals for given stations to coda site terms, showing remarkable similarities, analogous to Figure 73, for many stations and various regional phases.

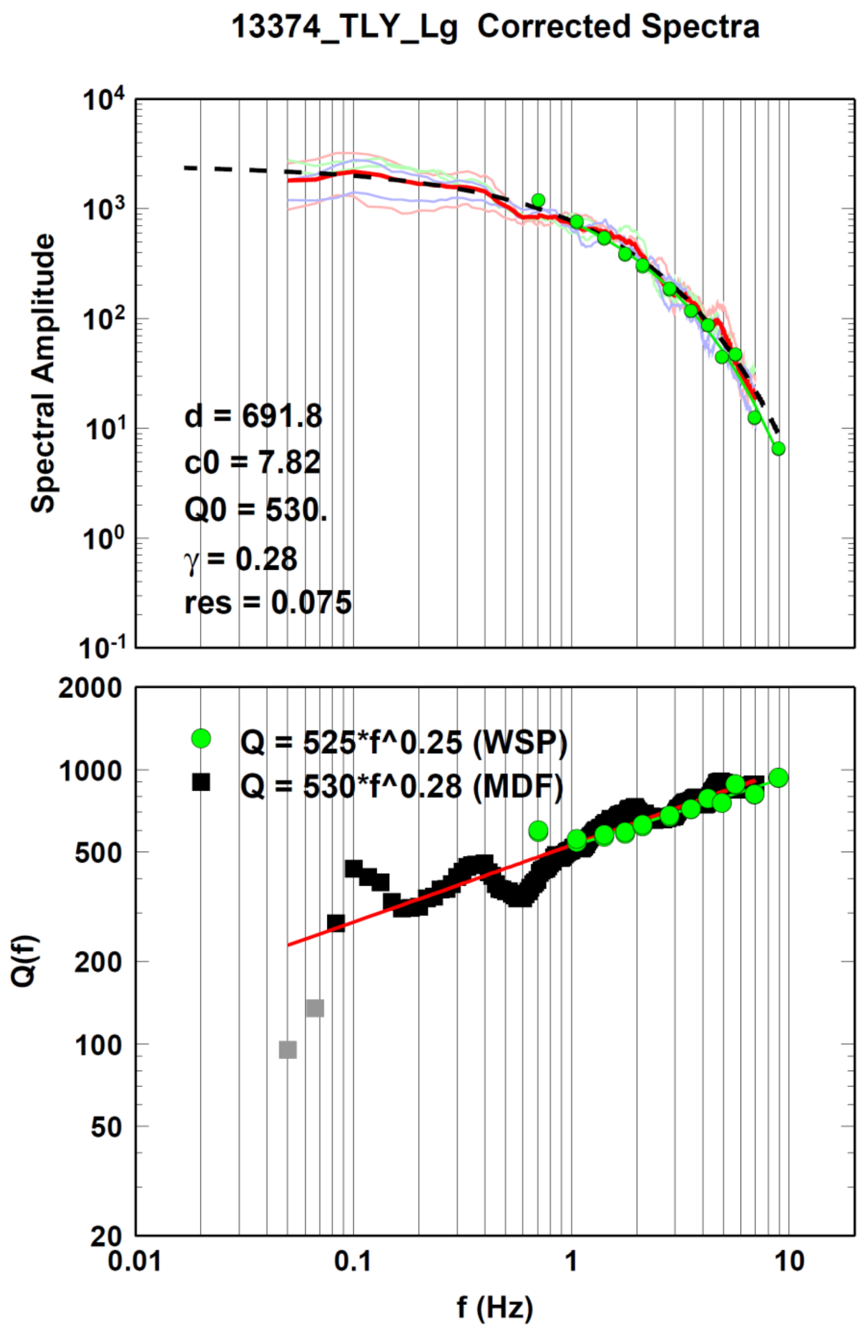

Figure 74. Similar to Figure 72, but also correcting the spectra by the coda site terms in Figure 73. The strong site effects are removed, leading to a more stable fit.

7 COMPARISONS OF Q GRIDS

Given the investigations in Sections 5 and 6, bolstering our approach and assumptions, we processed and fit source-corrected spectra of Lg, Sn, Pg (as available), and Pn for the paths shown in Figure 9. We have shown many cases with excellent agreement between our Q estimates and those from tomography. Here we present the overall results and Q grids for each phase, highlighting spatial comparisons. In Section 8, we examine significant discrepancies, the various causes, and how they can be reconciled by improving both methods.

7.1 Lg Q Grids

Figure 75 depicts the effective (i.e., inverse path averaged) Lg Q_0 estimates from the two methods for a preliminary set (roughly half of the clusters). There is generally fairly good agreement for a majority of the paths. Some significant discrepancies can be seen, e.g., for paths to station ABKT. The western edge of the tomography grid is at 50 degrees longitude.

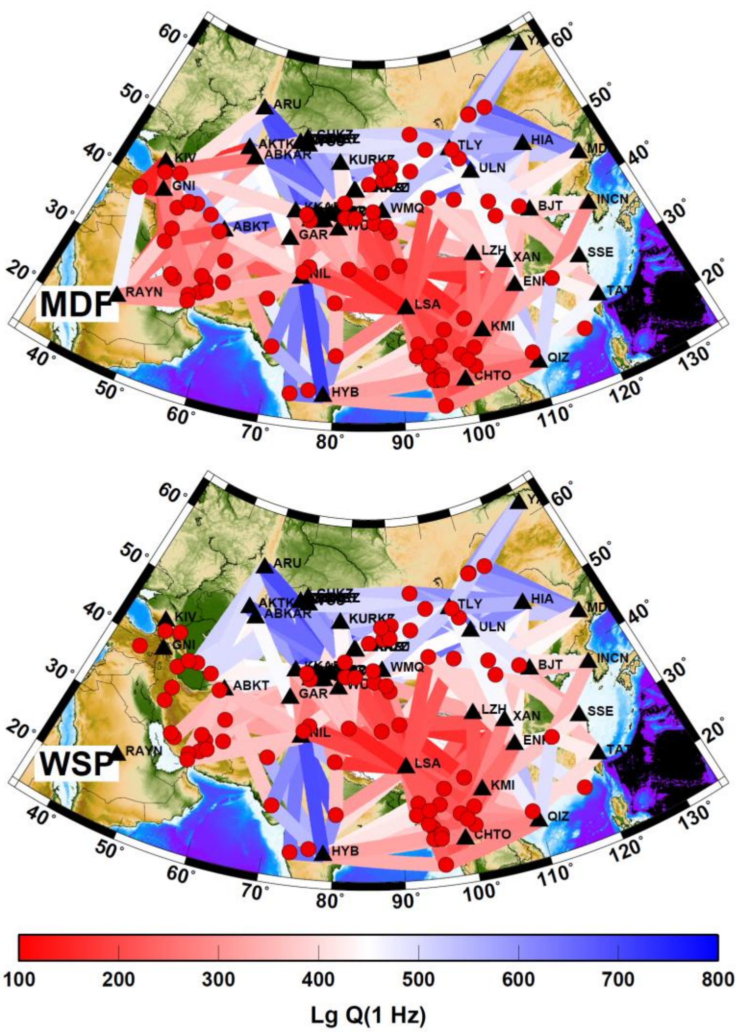

Figure 75. Comparison of effective Lg Q_0 estimates from source-corrected spectra (top map) and amplitude tomography (bottom map) for a preliminary set of ray paths.

At this stage, we have processed Lg for about 2200 paths. For display purposes, we interpolate the effective *Q* estimates (color-coded rays in Figure 75) using a tomography code that inverts Q_0 and γ estimates for a suite of paths into a grid. (This is different from amplitude tomography, which inverts amplitude data into *Q* grids.) Figure 76 compares the Lg *Q* grids at 1 Hz. They are similar, both showing higher Lg Q_0 for the Kazakh Platform and India, low values for Tibet, and intermediate values for eastern China. The fits of source-corrected spectra yield lower *Q* than from tomography in Iran and nearby areas, at the edge of the grid.

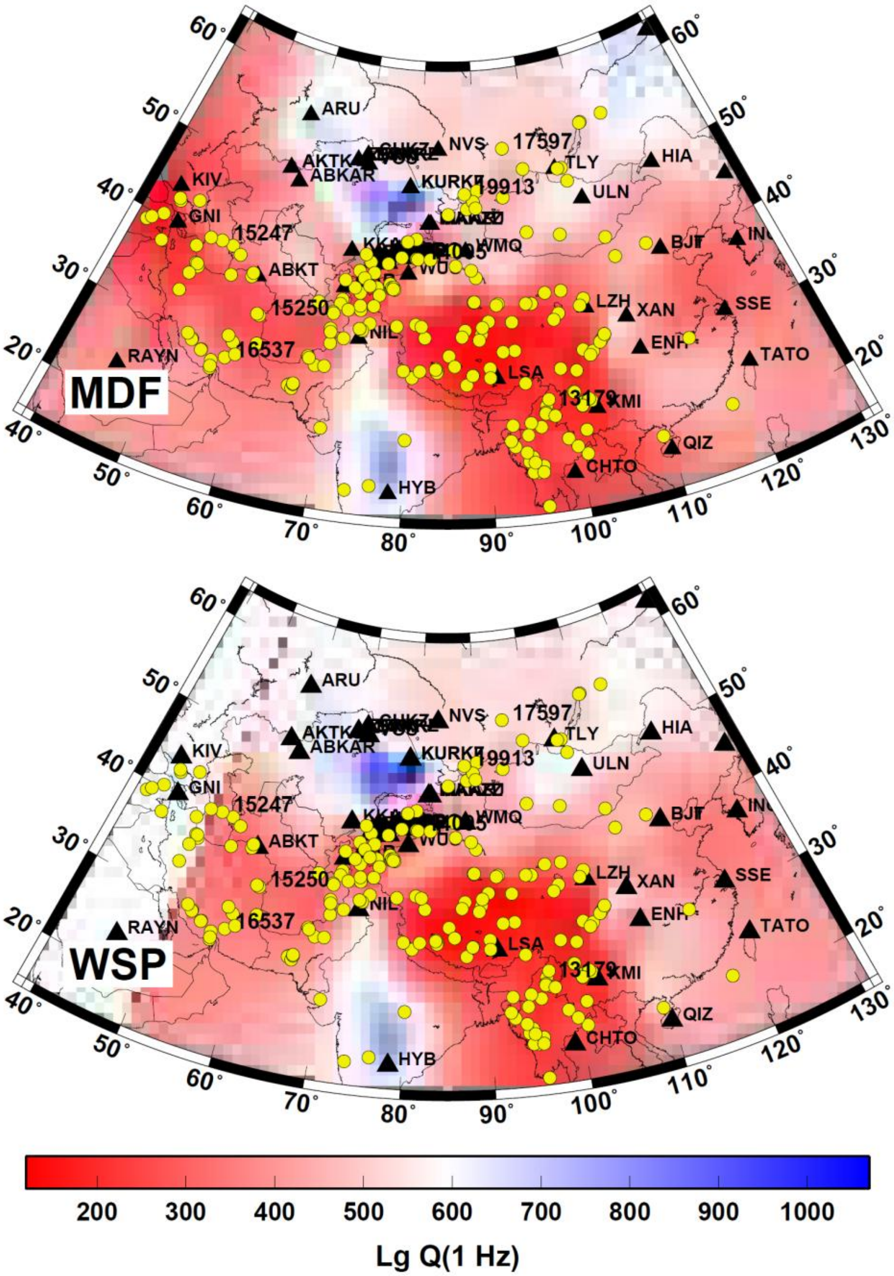

Figure 76. Comparisons of Lg Q_0 (1 Hz) grids from spectral fitting (top) and amplitude tomography (bottom). Circles show events used in the analysis.

Figure 77 compares Lg Q grids at 5 Hz, showing even lower Q estimates from spectral fitting than from amplitude tomography for the Middle East. (Once the path-wise Q_0 and γ estimates are interpolated, these grids may be easily computed for any desired frequency, without re-running the code.) Note that the lower maps of these figures are not the full (more detailed) amplitude tomography grids for discrete bands that were generated by Dr. Phillips at LANL. They are samplings of those grids, which we regressed into Q_0 and γ estimates for each path, and then interpolated, so that they may be compared directly (i.e., apples to apples). To gain the full benefit of both methods, we plan to merge our results as constraints on amplitude tomography.

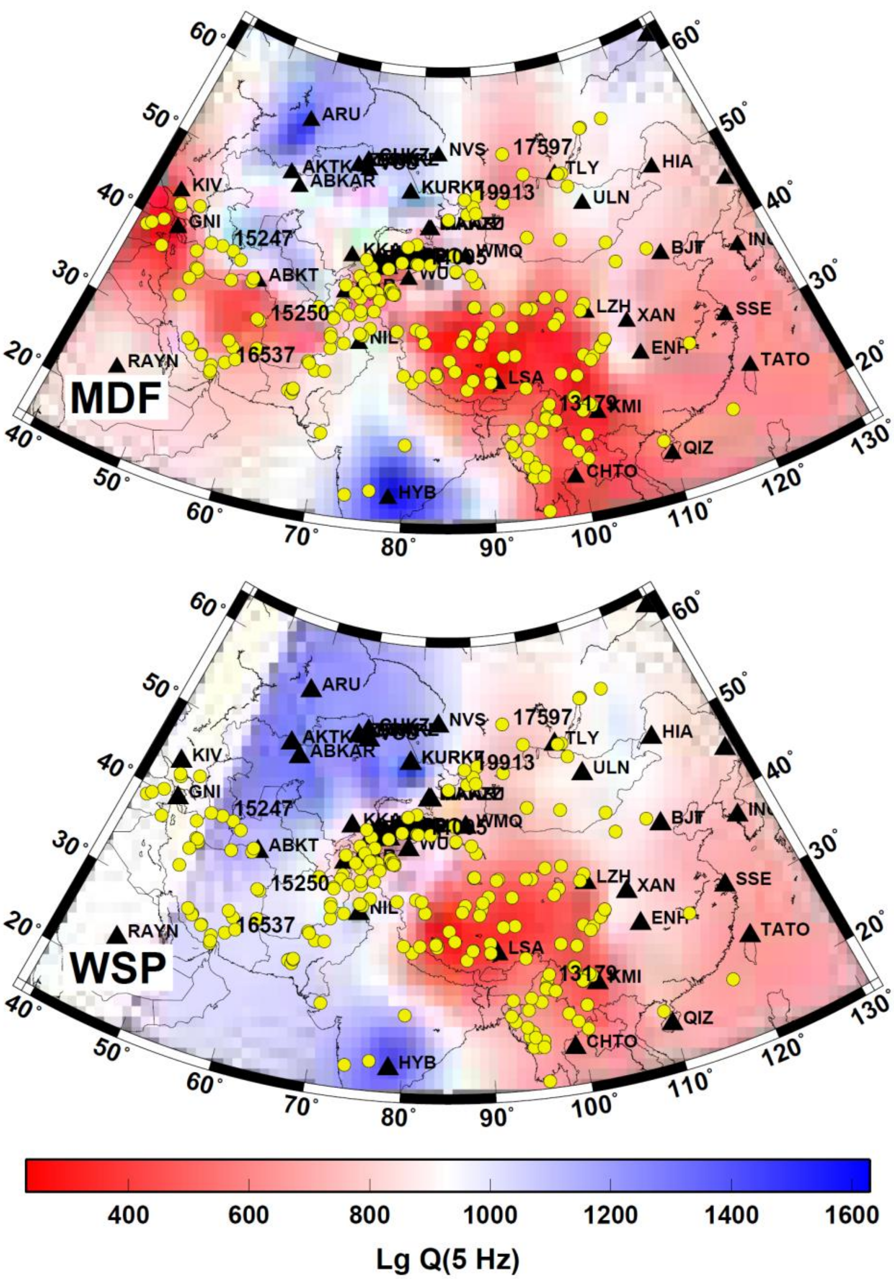

Figure 77. Similar to Figure 76, but for Lg Q at 5 Hz.

7.2 Sn Q Grids

We also processed and fit source-corrected Sn spectra for the same high-quality set of earthquake pairs/clusters, corresponding to 2347 regional paths in Eurasia. Using the same Q tomography code to interpolate Sn Q_0 and γ estimates for these paths into a grid, Figure 78 compares our latest Sn Q_0 (1 Hz) grid (top) to that from amplitude tomography (bottom). As for Lg, the Sn Q_0 results from the two methods have a high degree of similarity, but some clear differences.

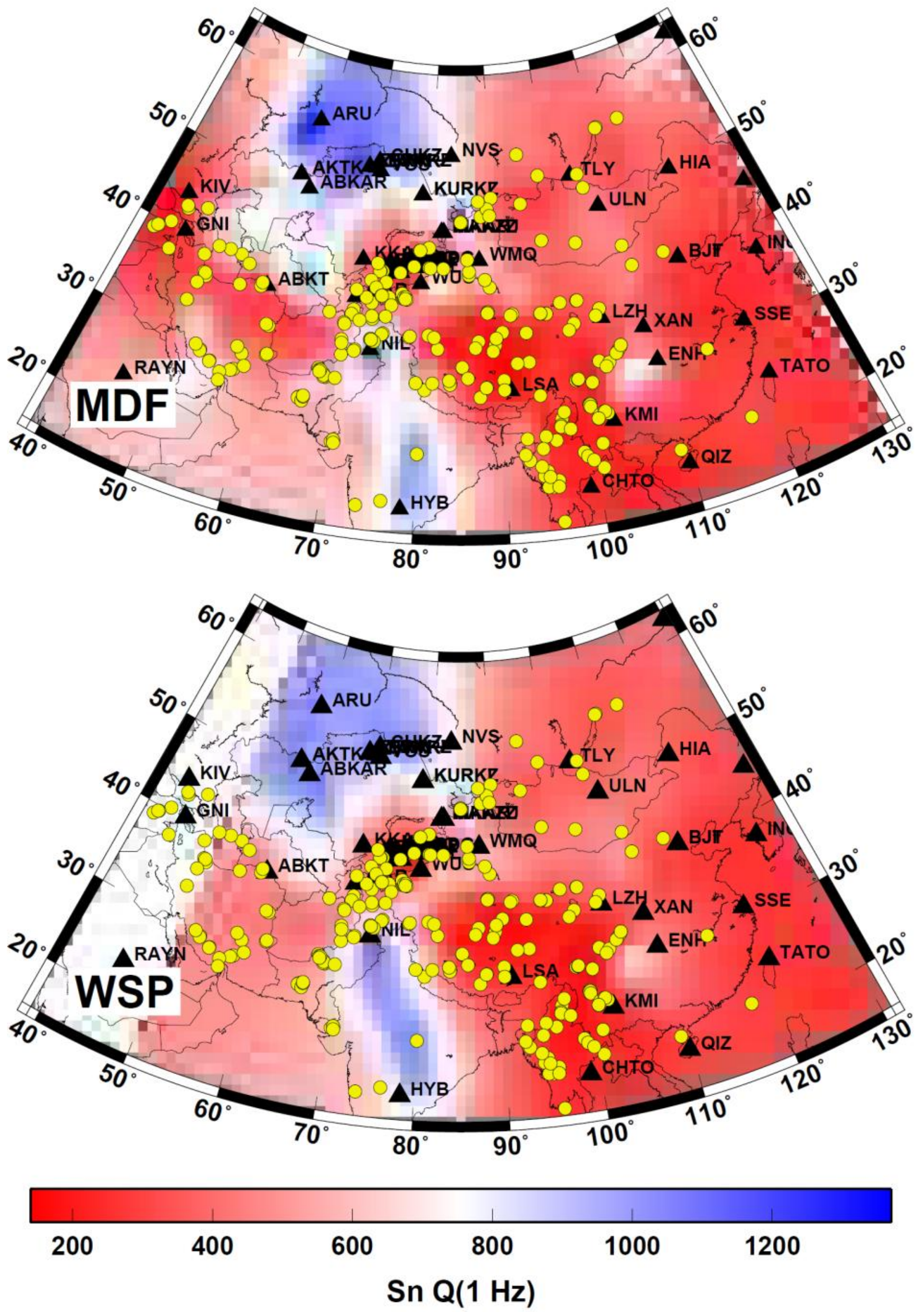

Figure 78. Similar to Figure 76, but comparing Sn Q_0 (1 Hz) grids.

Figure 79 compares the Sn Q grids at 5 Hz. The most prominent differences in the Q maps for both Sn and Lg are at the western boundary of the grid, including the Middle East, where there are few or no crossing ray paths (needed for amplitude tomography, but not this approach). The differences are even larger for higher frequencies (e.g., 5 Hz). Accurate calibration of regional phases, particularly for application of high-frequency P/S discriminants, has never been more important for this area.

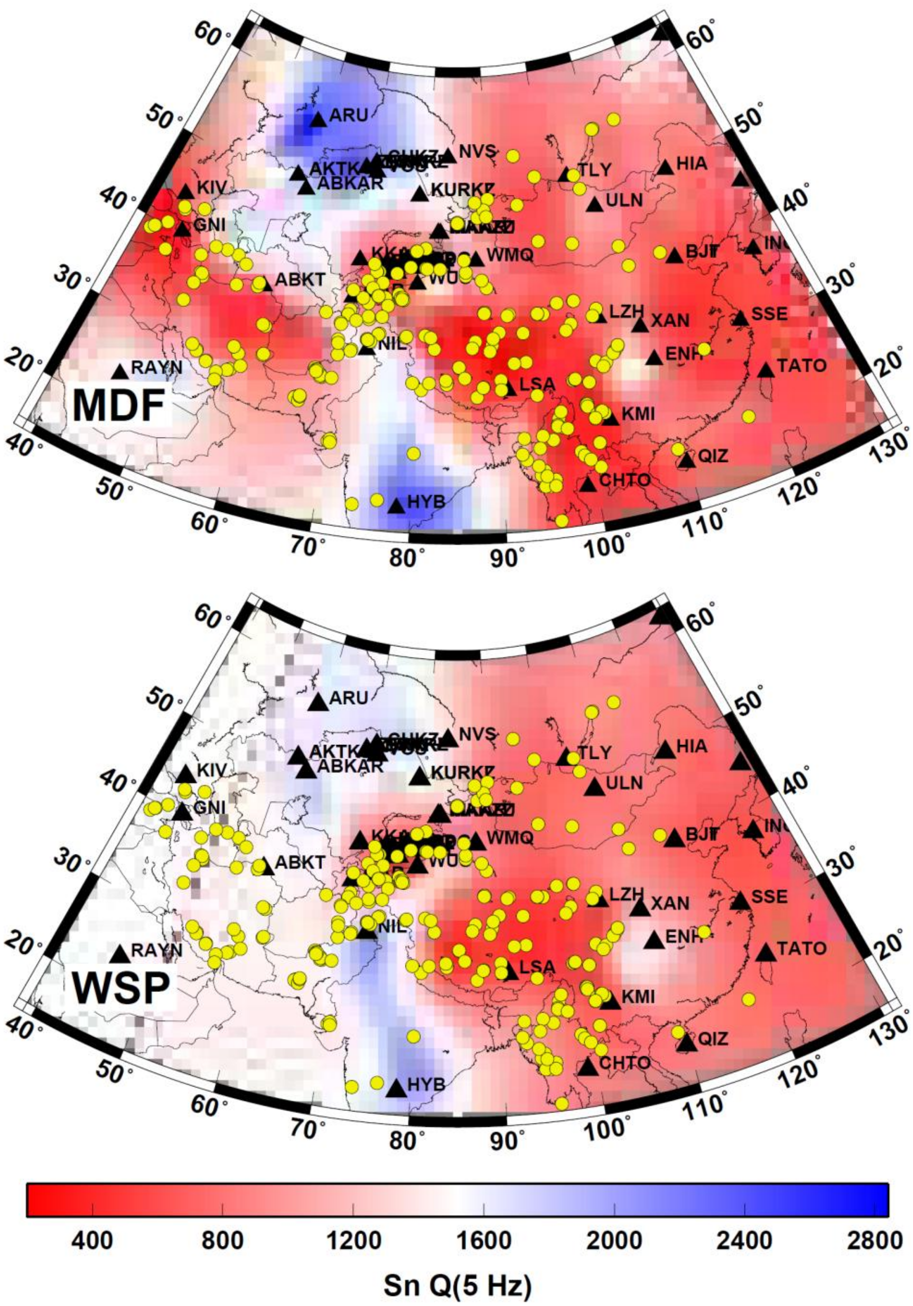

Figure 79. Similar to Figure 76, but comparing Sn Q grids at 5 Hz.

To better visualize the spatial dependence of differences in Q estimates from spectral-fitting vs. amplitude tomography, we computed difference Q grids, given in percentage, for various phases and frequencies. For example, Figure 80 shows the percent difference of Sn Q at 1 Hz and 5 Hz. The upper plot for 1 Hz shows some modest differences. The lower plot for 5 Hz indicates differences as large as 200% in some areas, generally to the west and south of most IRIS stations, systematically biased higher for tomography, mostly due to edge effects and data quality issues. In Section 8, we present the physical explanations and discuss the implications.

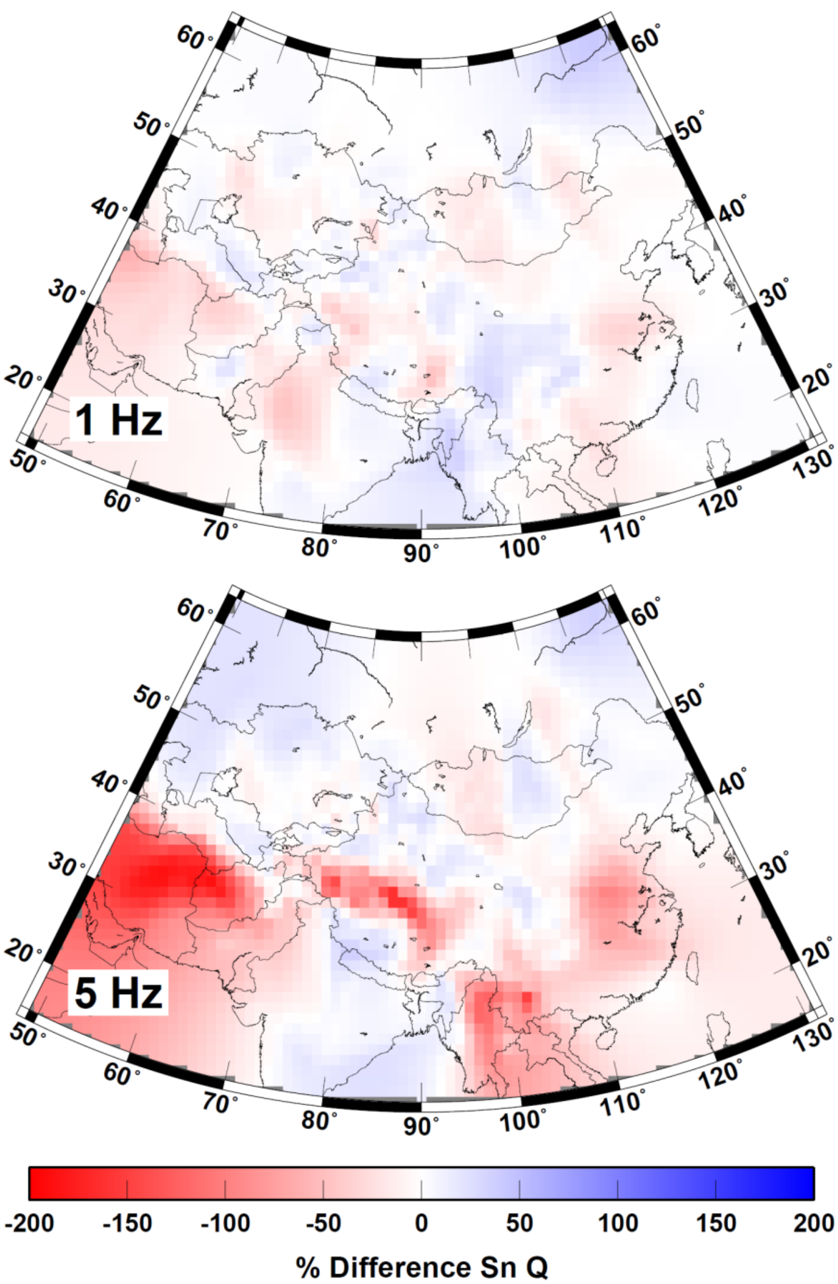

Figure 80. Percent difference of Sn Q estimates from tomography and fitting source-corrected spectra at 1 Hz (top) and 5 Hz (bottom).

7.3 Pg Q Grids

Of a total of about 2600 paths sampled in Figure 9, corresponding to events with corroborated source terms, Pg picks are available for a much smaller subset because the IASP91 Pg travel-time table has limited range. We reviewed the automatic processing and fits of source-corrected Pg spectra. Figure 81 shows effective Pg Q_0 estimates for available paths, corresponding to the same set of events used to estimate Q for Lg and Sn. Because Pg does not propagate as far as other regional phases, there are much fewer paths and worse spatial coverage.

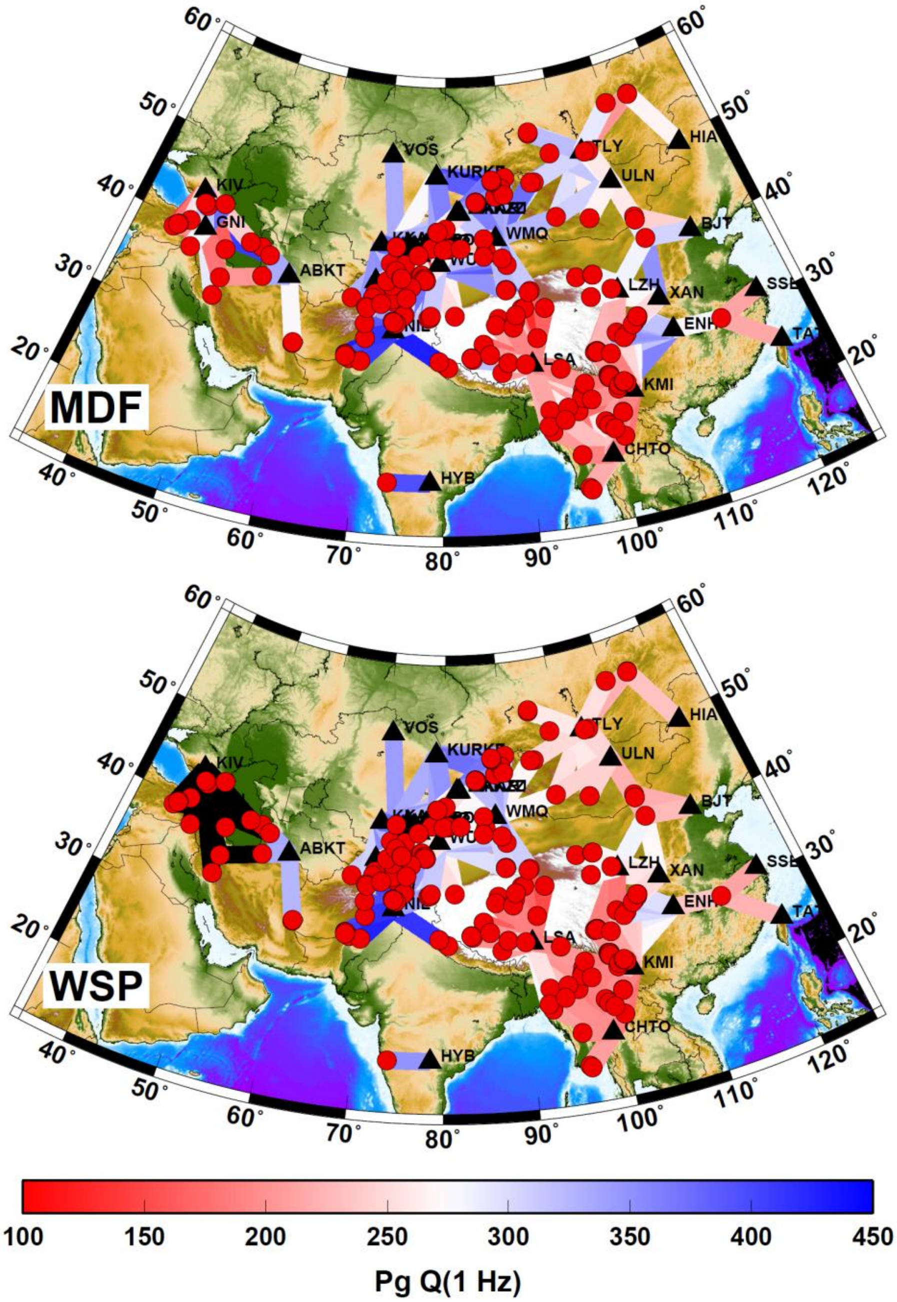

Figure 81. Similar to Figure 75, but comparing effective Pg Q_0 estimates for 714 paths.

Figure 82 shows the interpolated Pg Q results at 1 Hz, using the Q tomography code to invert Q_0 and γ estimates for the set of paths into a grid. The poor sampling of paths (viz. Figure 81) limits the reliability of the absolute grids; they are merely intended to visualize the spatial comparison. As for Sn and Lg, the Pg Q_0 grids of the two methods are similar, but differ noticeably. Figure 83 compares the Pg Q grids at 5 Hz. The most prominent differences in the Q maps for Pg are at the western boundary of the grid, including the Middle East, where there are few or no crossing ray paths (needed for amplitude tomography, but not this approach).

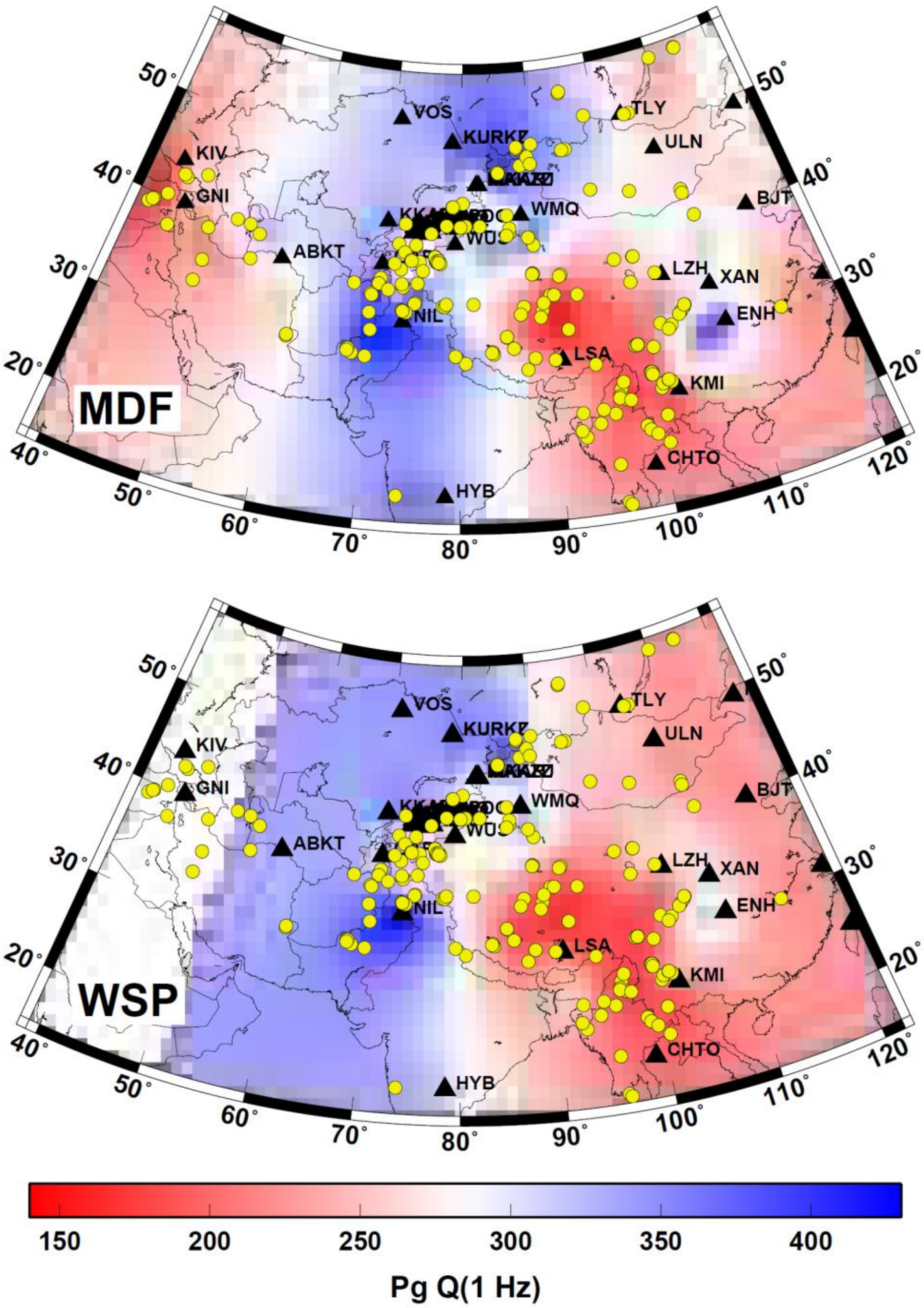

Figure 82. Similar to Figure 76, but for Pg Q at 1 Hz.

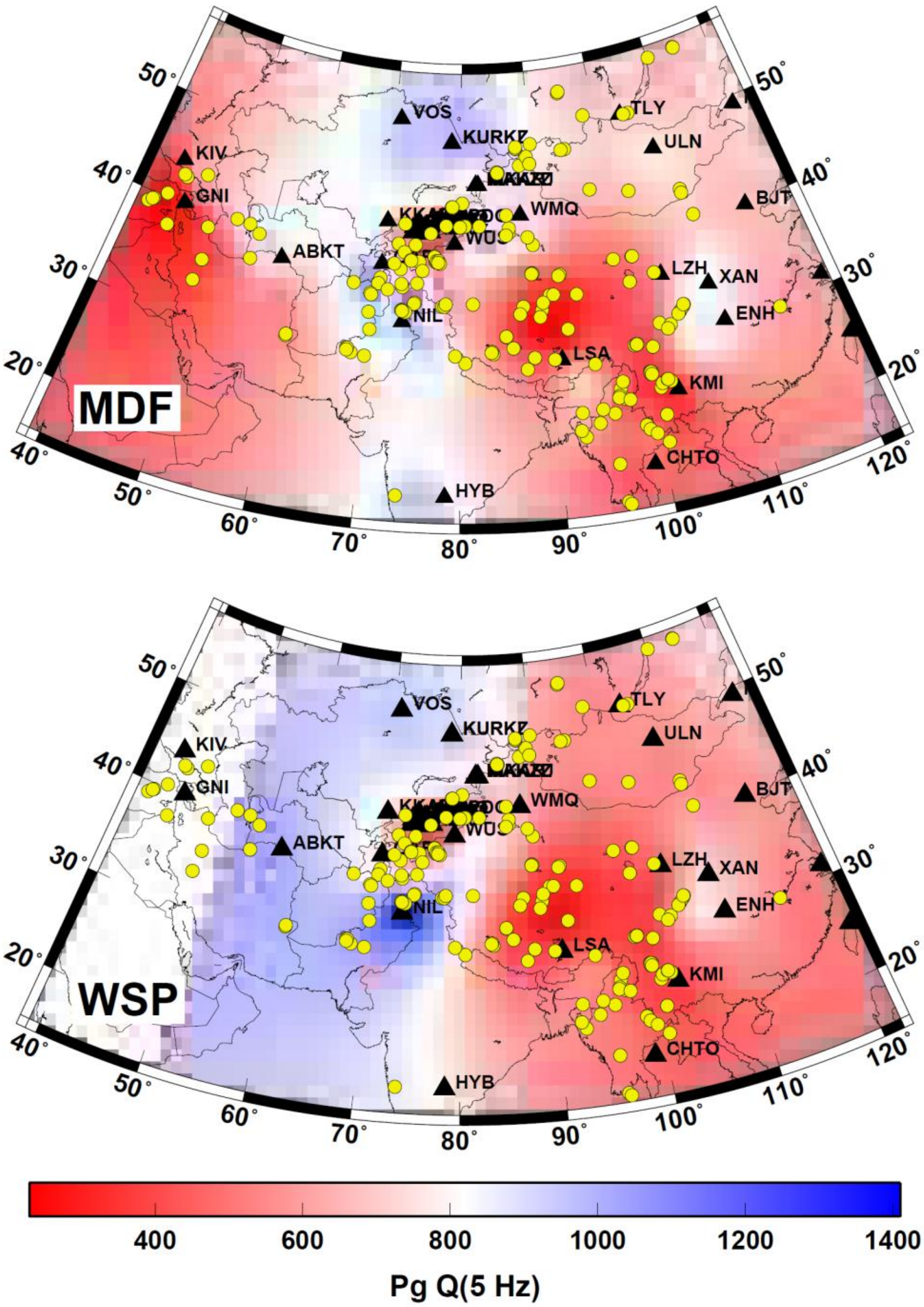

Figure 83. Similar to Figure 76, but for Pg Q at 5 Hz.

7.4 Pn Q Grids

We also processed, fit, and reviewed source-corrected Pn spectra for 2672 paths, of which 2237 have reasonable results. Figure 84 compares the interpolated Pn Q results at 1 Hz. Figure 85 shows the results at 5 Hz. Of the various regional phases, the results for Pn exhibit the greatest variability and differences with amplitude tomography. Much more work is needed to assess the reliability of these results. At this stage, we do not know whether the structure seen in the upper maps of both figures indicate real physical effects or artifacts of Pn spectral variability.

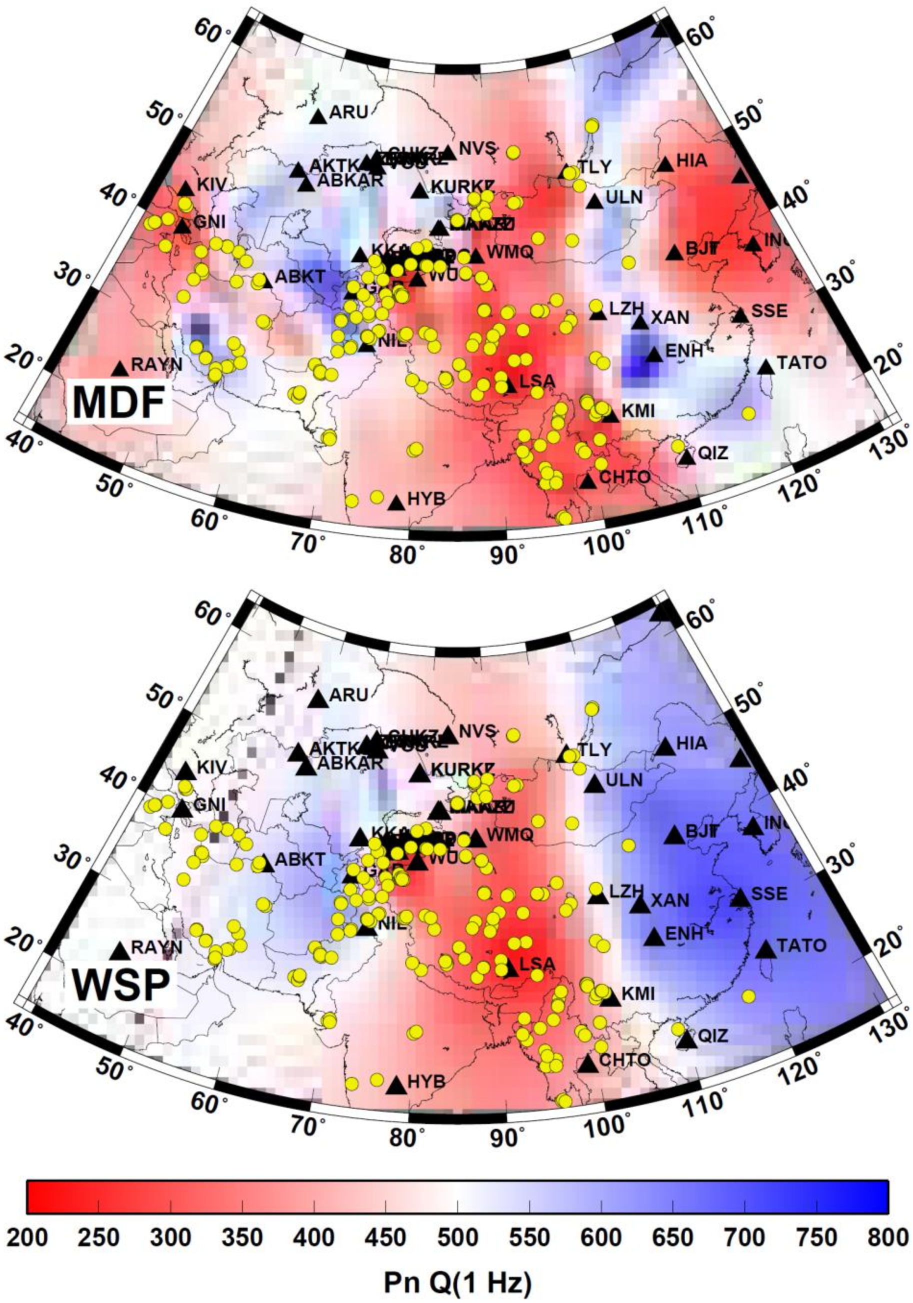

Figure 84. Similar to Figure 76, but for Pn Q at 1 Hz.

Both amplitude tomography and our fitting of source-corrected Pn spectra are the least stable. For example, tomography runs at LANL obtained some very high, or even negative, Pn *Q* estimates (i.e., predicting increasing Pn amplitudes with increasing distance). We also find some spectral fits that give very high Q_0 estimates (five greater than 1000); our approach does not give negative Q estimates. Examples of Pn discrepancies and how to improve the results are presented in Section 8.4. In Section 9, we also discuss Pn geometric spreading, and how those results may rectify the very high and negative Q estimates from tomography.

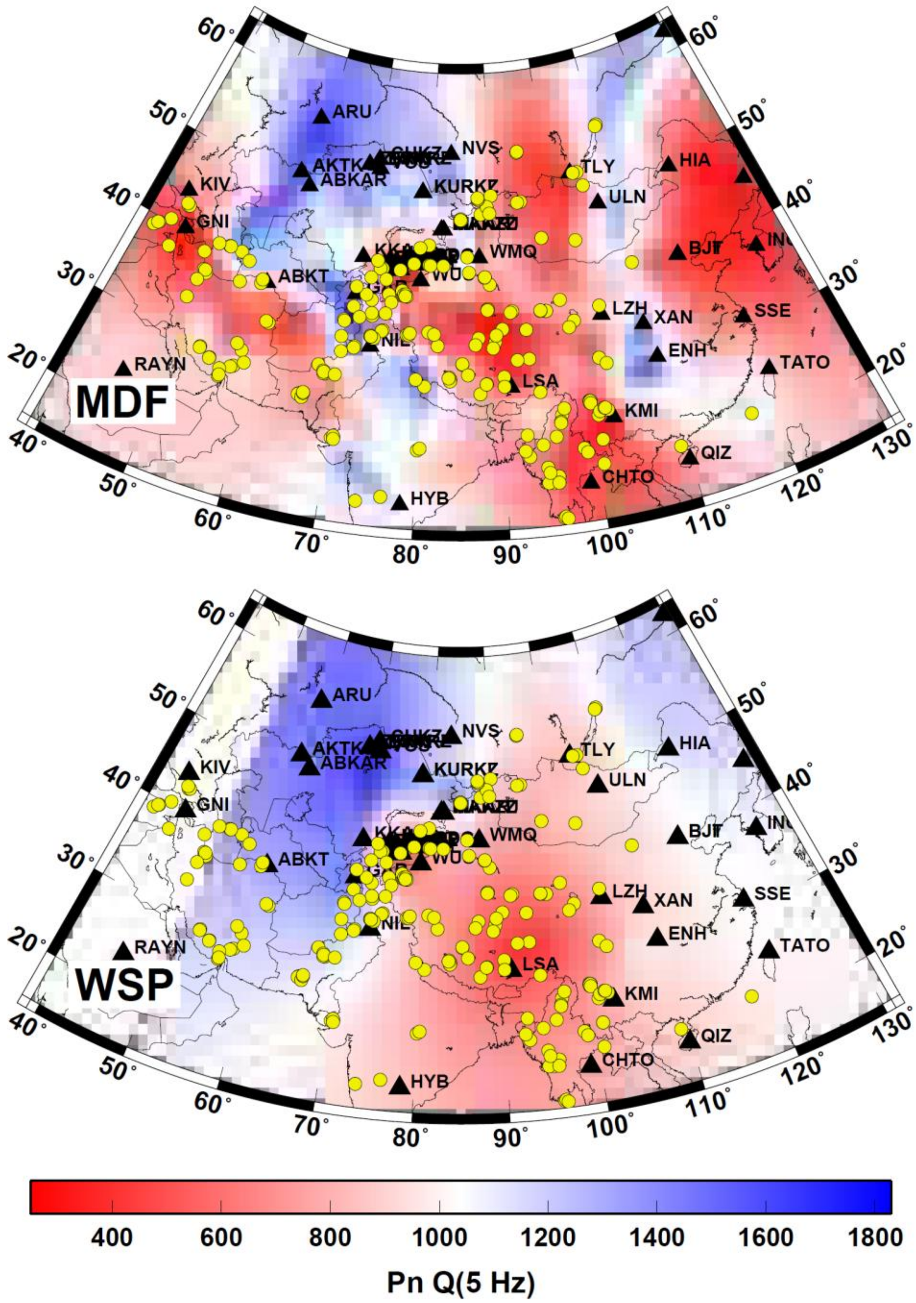

Figure 85. Similar to Figure 76, but for Pn Q at 5 Hz.

8 INVESTIGATIONS OF Q DISCREPANCIES

Fisk and Phillips (2011) verified *Q* estimates for many paths and investigated various prominent discrepancies, most of which can be attributed to data quality issues in higher frequency bands and grid edge effects, both of which impact tomography results, and strong site effects for some stations (e.g., KMI), that impact *Q* parameter estimates from fitting source-corrected spectra. Here we highlight these key discrepancies and discuss important implications. While all are important and relevant to accurate calibration of regional phases and, hence, monitoring capability, we find that the impact of tomography edge effects on P/S discrimination errors for Iran (Section 8.3) are the most alarming.

8.1 Data Quality Issues

Figure 86 (left) illustrates a prevalent problem in which tomography *Q(f)* results agree with the source-corrected spectrum for lower bands, but deviate significantly higher in bands above 3 Hz, for this case, due to noise effects. (As shown below, over-estimating *Q* for regional S phases biases P/S ratios high, i.e., making earthquakes seem more explosion-like.) The signal-to-noise criteria used for tomography (pre-Pn S/N>2 and pre-phase S/N>1.1) are intentionally lax, to utilize more data. If S/N tests are too stringent, data sampling issues arise. Excluding the tomography *Q(f)* values in higher bands, Figure 86 (right) shows that the Q_0 and γ estimates now agree. Many amplitudes, especially at higher frequencies for low *Q* paths, are corrupted by noise. Results of our distinct methods can be reconciled to corroborate *Q* estimates. Note that our spectral fit (black curve) in Figure 86 is automatic, including determining the frequency range of the fit. The inflection at about 2 Hz, where noise starts biasing the spectrum high from expected decay, is usually straightforward to find. Although not all cases are easy, examination and fitting of thousands of spectra suggests that such valid frequency ranges can be found for most, which could be used to improve data quality before performing amplitude tomography.

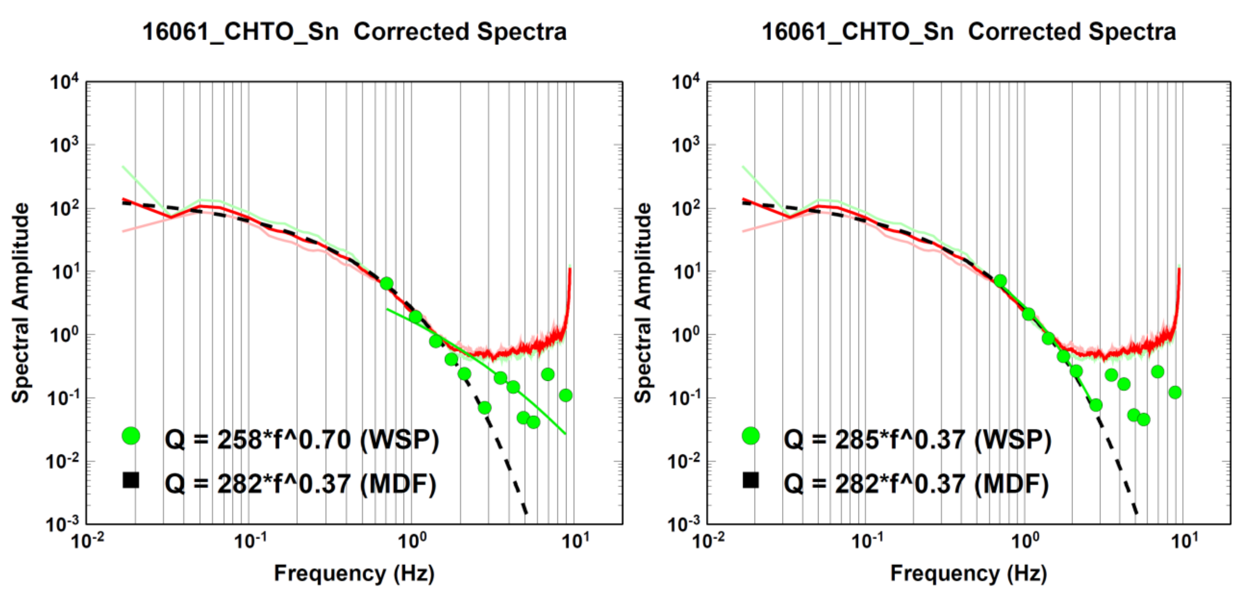

Figure 86. Comparisons of Sn Q results for an earthquake in Tibet to station CHTO, including all (left) and excluding amplitude tomography Q results in bands > 3 Hz.

Figure 87 compares Lg Q_0 and γ estimates for regional paths to XAN that were processed at the time. Although there are a few outliers for γ, there is not a complete, systematic bias, indicating that this is not a site effect. In fact, the coda site terms for XAN do not exhibit strong frequency dependence, as those for KMI do (see next example). Figure 88 shows the source-corrected Lg spectrum and Q comparison for a path from an earthquake in Mongolia to XAN, corresponding to the largest γ discrepancy. This is a low Q path for which the Lg spectrum is above the noise only up to ~2 Hz. The tomography *Q(f)* estimates are consistent with the source-corrected Lg spectrum up to 2 Hz, but then deviate higher for higher frequencies. Figure 88 (right) shows the result of refitting the tomography *Q(f)* values only up to 2 Hz, which reconciles the Q_0 and γ estimates. Thus, the tomography *Q(f)* values are reliable up to 2 Hz, but noise effects are biasing the results in higher bands. This issue appears to be particularly prevalent for low Q paths. We often find that the tomography Q estimates are unreliable in bands higher than used to fit the corresponding source-corrected spectra for that path.

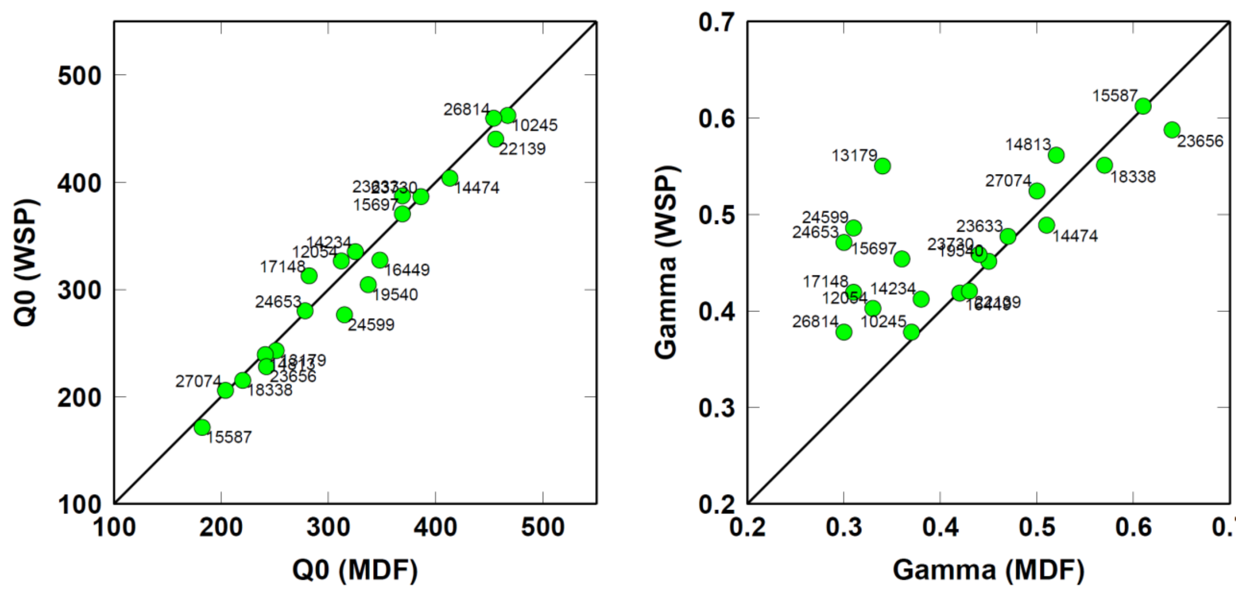

Figure 87. Comparison of Lg Q_0 (left) and γ (right) estimates for regional paths to XAN.

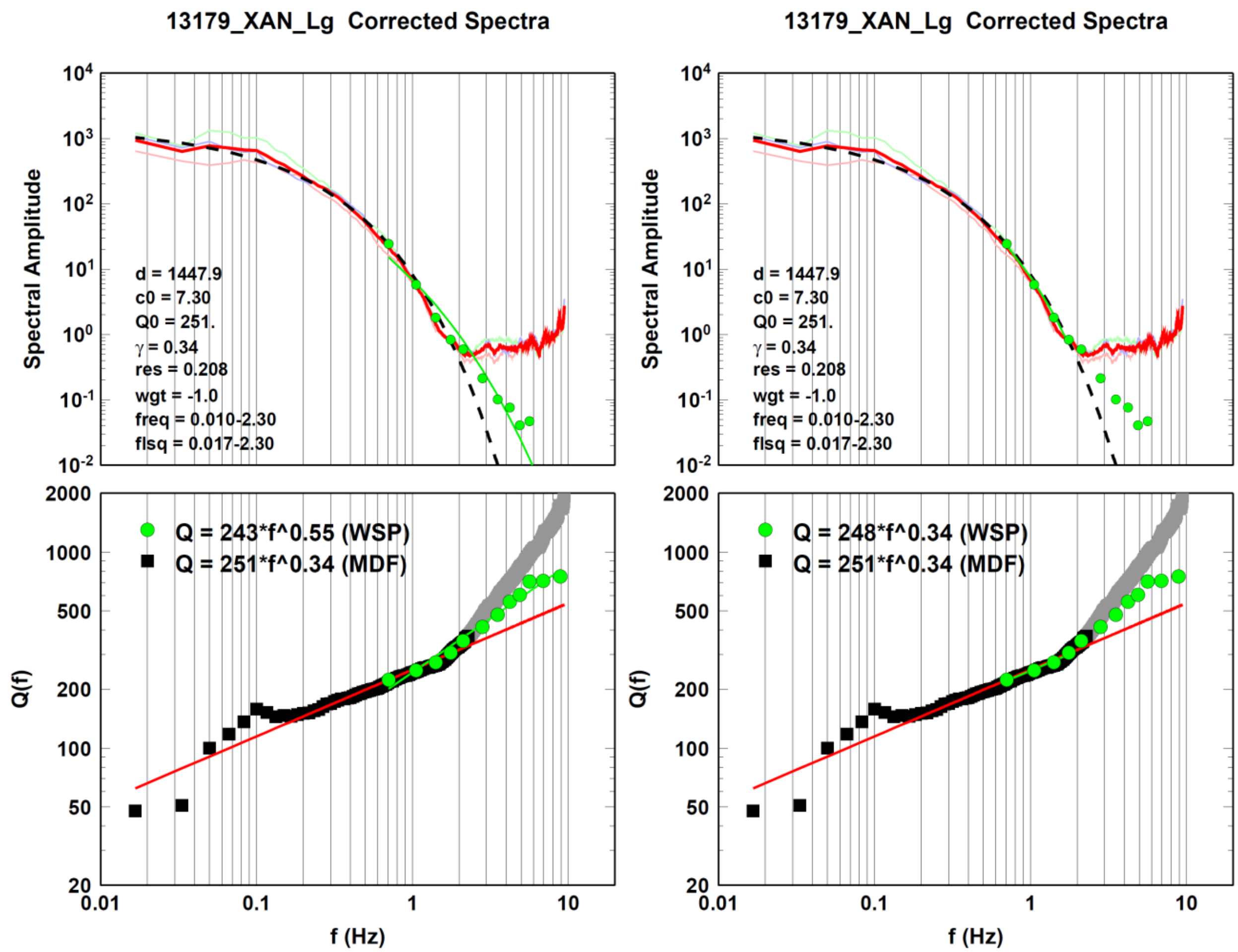

Figure 88. Source-corrected Lg spectra and *Q* comparison for a path from Mongolia to XAN, (left) fitting tomography *Q(f)* estimates for all 12 bands and (right) just fitting those up to 2 Hz.

8.2 Site Effects and Data Quality

It is also worth examining site effects with regard to resolving significant discrepancies in Q estimates from spectral fitting and tomography. KMI is one of the stations with the largest, systematic differences in γ estimates for Lg, as shown in the lower left plot of Figure 89 for a preliminary subset of paths. The Lg Q_0 estimates agree reasonably well (upper left plot). The Lg Q predictions at 5 Hz are compared geographically on the maps, showing that the largest discrepancies are for paths from Myanmar to KMI. The systematic bias in γ estimates prompted us to examine site effects for KMI. Note that the bias, while systematically higher for tomography, is not uniform for all paths because there are also varying signal-to-noise effects, which depend on Q and propagation distance. Figure 90 shows the site terms estimated from coda tomography for KMI, showing strong site attenuation at frequencies greater than about 1-2 Hz. Note also the difference in coda site terms for horizontal versus vertical channels. This behavior is also observed in the direct Lg spectra. The left plot in Figure 91 compares the Lg Q results for one such path. The results agree below about 3 Hz, giving similar Q_0 estimates, but deviate at higher frequencies, leading to the discrepancy in γ. Applying the coda site corrections to the source-corrected Lg spectra, and also excluding the two highest bands when regressing tomography *Q(f)* estimates to estimate Q_0 and γ, yields the results shown in the right plot of Figure 91, which agree very well. Thus, strong site attenuation is partially responsible for the different γ estimates by the two methods, but poor data quality in higher bands used for tomography is also a cause.

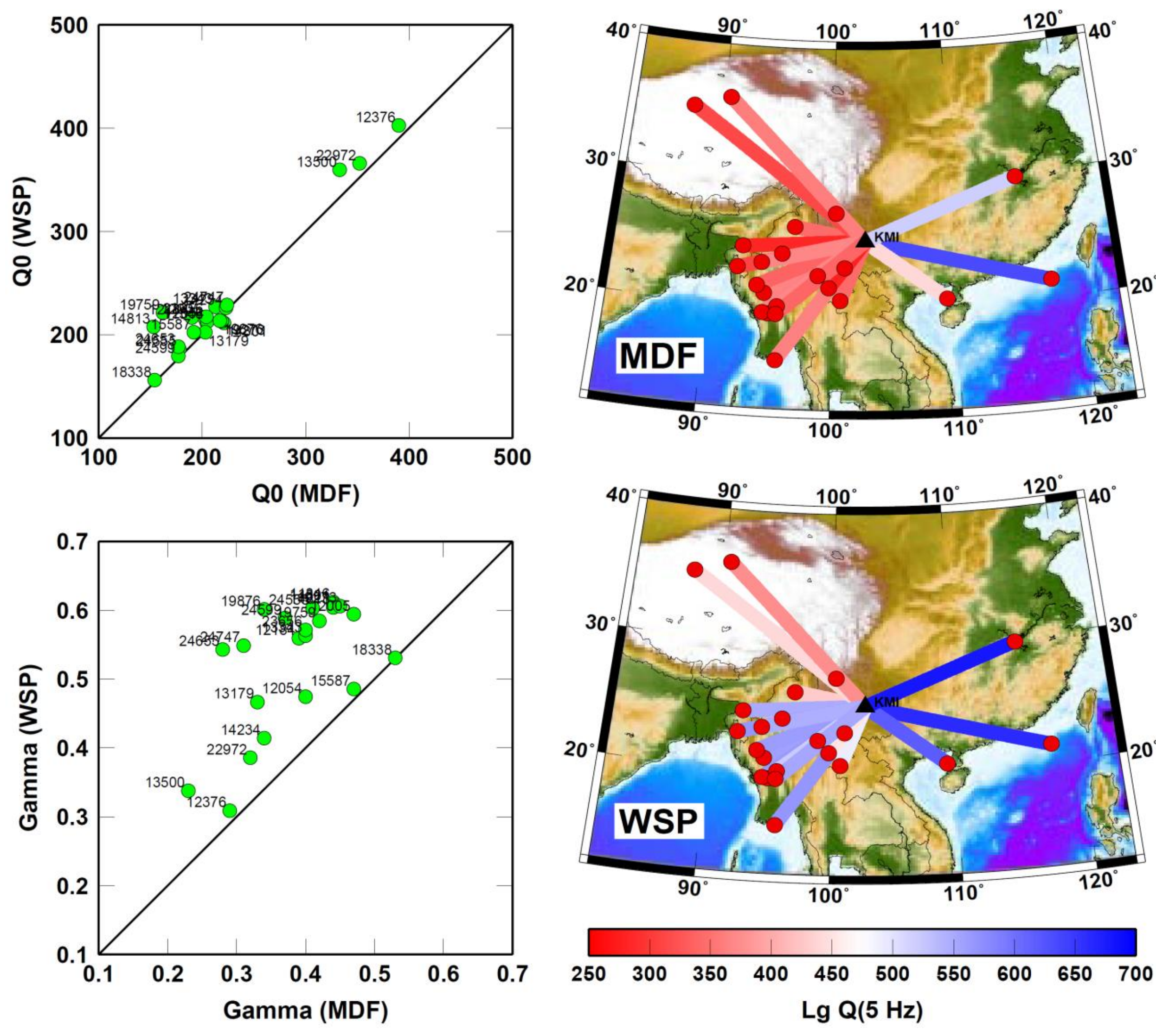

Figure 89. (left) Comparison of Lg Q_0(top) and γ (bottom) estimates for regional paths processed to KMI. Spectral-fitting estimates of γ are lower than those from tomography. (right) Spatial comparisons of Q estimates at 5 Hz, which differ most notably for Myanmar and nearby paths.

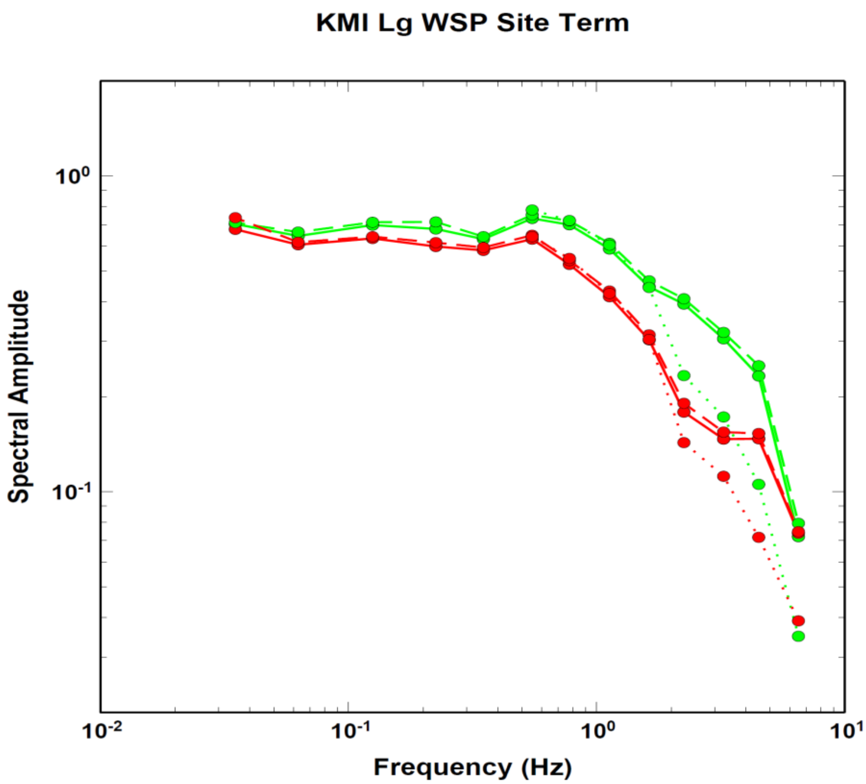

Figure 90. KMI site terms estimated from coda for various vertical and horizontal channels.

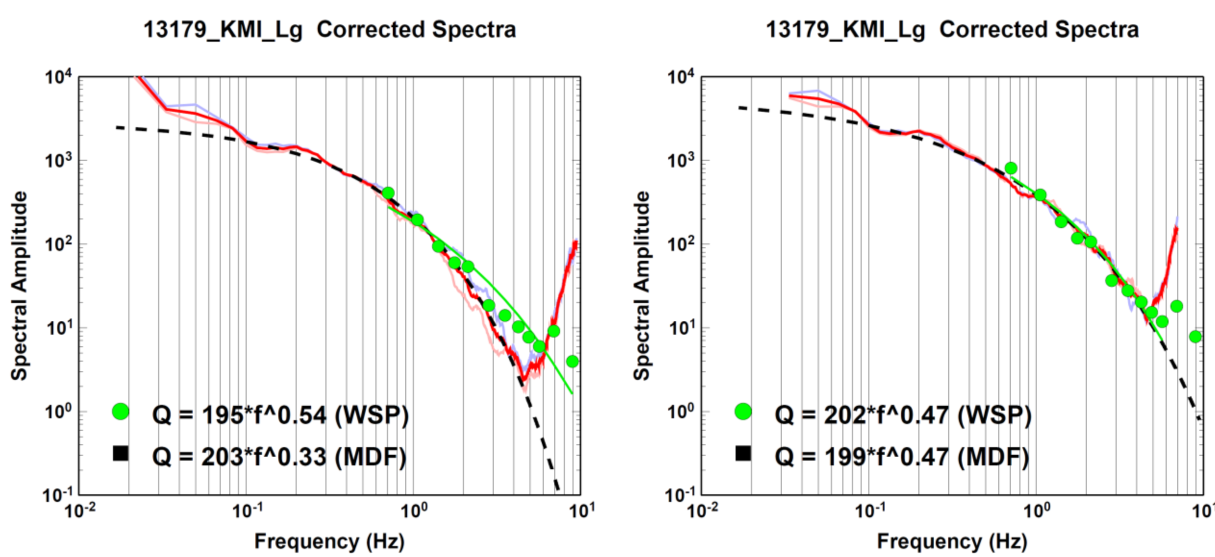

Figure 91. Source-corrected Lg spectra and *Q* results at KMI for an earthquake in Myanmar. The plot on the left shows the original results. The plot on the right is similar, but now correcting the Lg spectra by the coda site terms and excluding the two highest tomography bands

Performing this analysis (i.e., applying the coda site corrections to source-corrected Lg spectra and excluding anomalous *Q(f)* estimates from tomography in higher bands) for all of the paths to KMI that were processed at the time, Figure 92 shows updated results. Except for a couple of marginal outliers, the results of the two methods now compare very favorably. It is encouraging that proper treatment of these site and data quality effects leads to results that converge to the same answer.

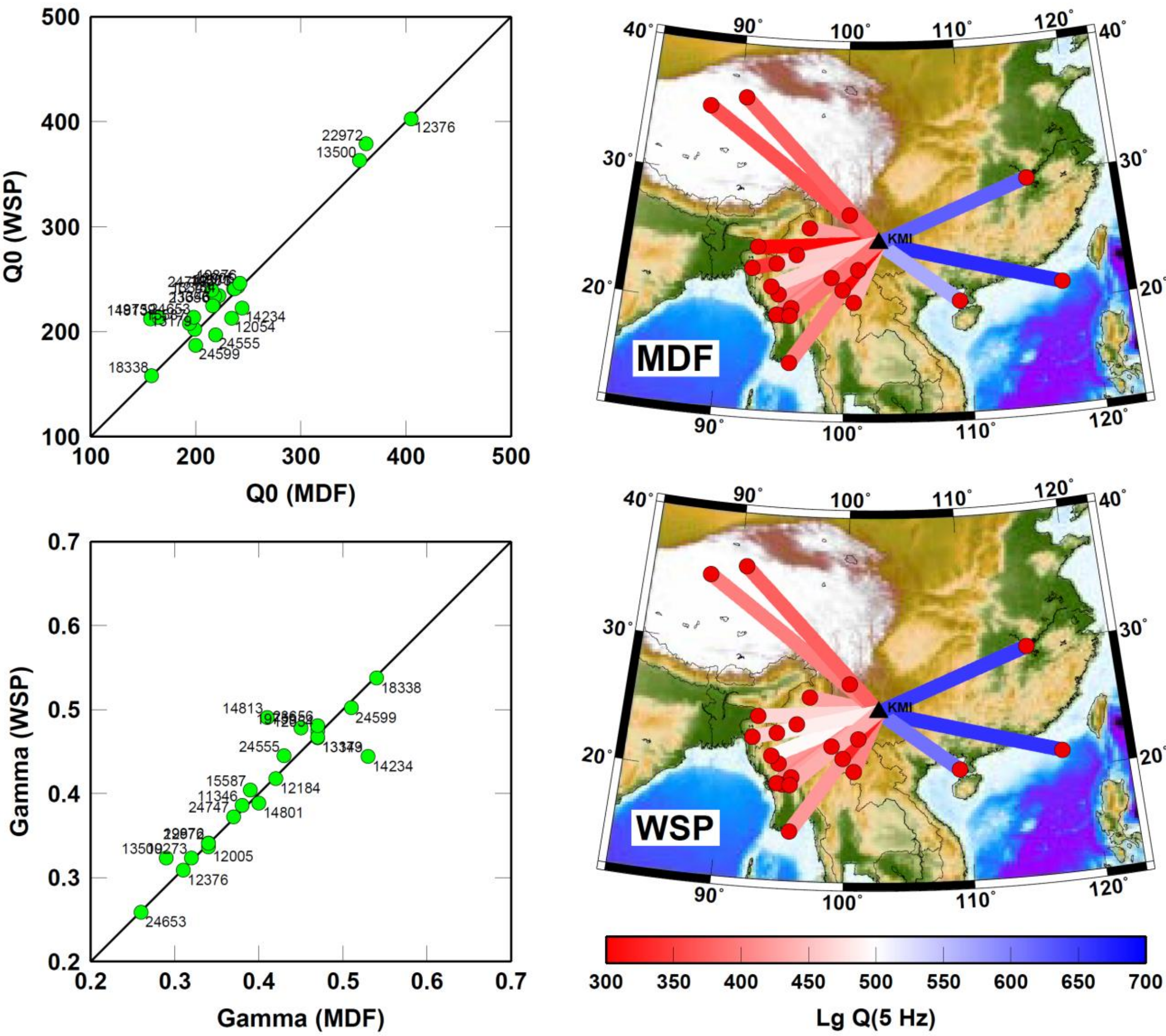

Figure 92. Updated comparison for paths to KMI treating site effects in my spectral analysis and excluding anomalous high-frequency bands for the tomography results.

8.3 Tomography Edge Effects and Implications for P/S Discrimination

An important issue we have noted throughout this project (e.g., Fisk and Phillips, 2011) is that amplitude tomography results have large errors near the boundaries, where there are insufficient crossing ray paths to resolve various physical effects. In fact, many of the clearest discrepancies between the Q grids from fitting source-corrected spectra and amplitude tomography (cf. Section 7) are near the tomography grid boundary. Now that we have estimated *Q* for regional S and P phases, and given that some key areas are near grid edges, it is interesting to assess how those errors impact P/S discrimination. Figure 93 depicts earthquake clusters in or near Iran. We have processed some, including those labeled by the master orid, considered in subsequent figures. Figure 94 shows that there are some very good Q comparisons, typically for higher Q paths with better station coverage, in this case for the path from orid 15247 to station AKT in Kazakhstan.

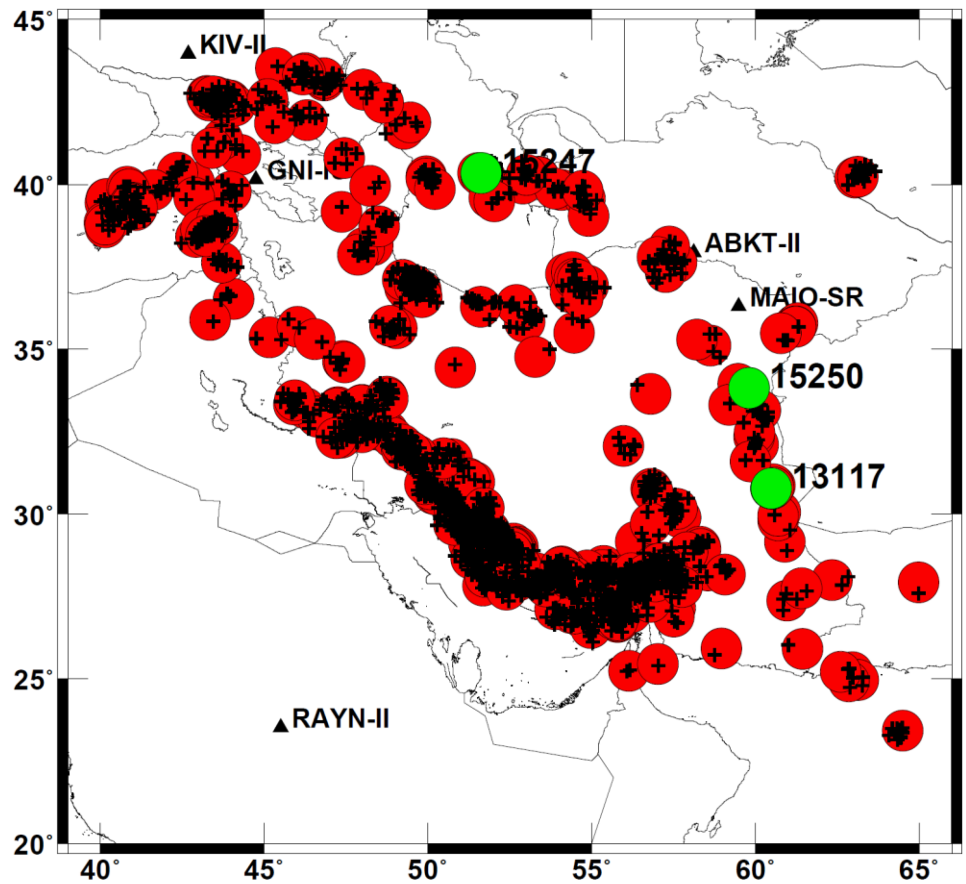

Figure 93. Map of earthquake clusters in or near Iran. Events considered below are labeled.

Figure 95 compares Lg (left) and Pn or Pg (right) *Q* results for two more southern paths at the western edge of LANL's grid. Discrepancies are progressively worse for lower *Q* and poor ray-path sampling. In fact, the bottom left plot of Figure 95 is one of the largest γ discrepancies we found for Lg. Note that the lower bands of the tomography results (green circles) in these plots agree with the source-corrected spectra, but deviate higher for higher bands (important for P/S discrimination), due to worse sampling (fewer crossing paths), particularly at higher frequencies.

The blue curves in the lower plots are corrected LANL amplitude data, which confirm that our independent measurements of amplitudes and spectra are consistent. Our estimates of source and Q effects from spectral fitting do not depend on sampling issues (e.g., crossing ray paths); hence, they can be used to improve amplitude tomography results at grid edges. A key question is how these errors affect P/S discrimination.

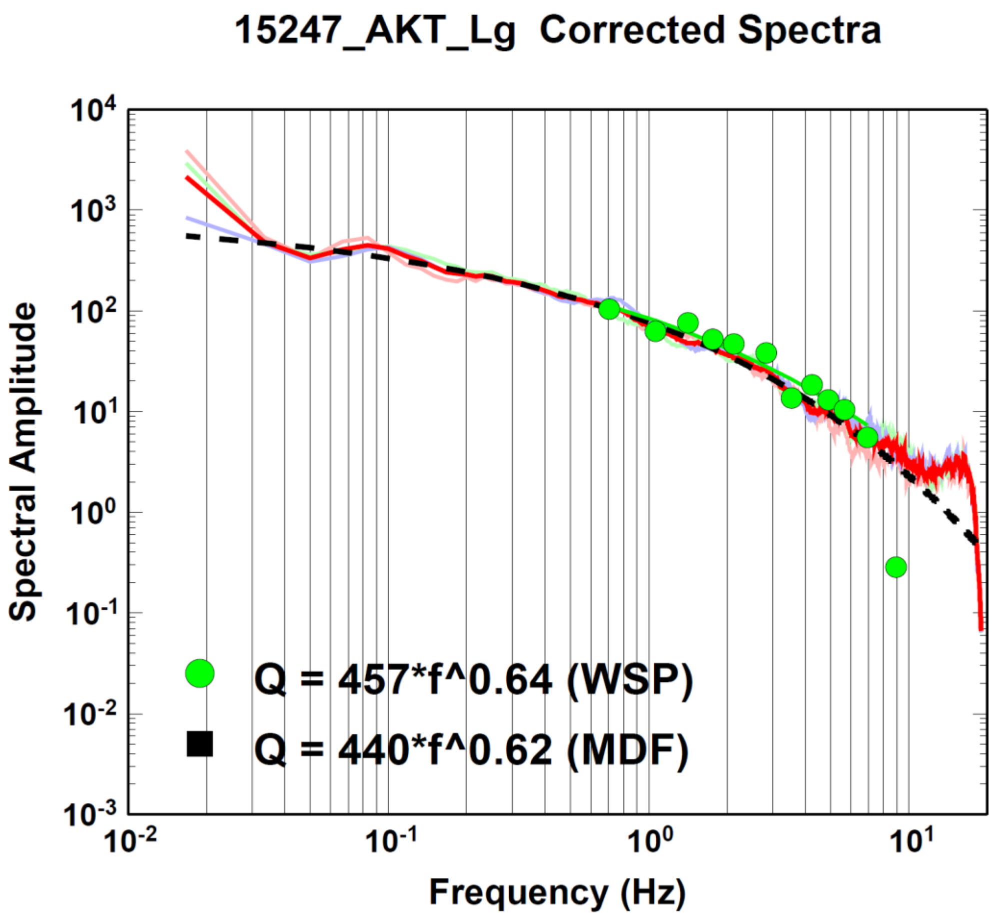

Figure 94. Source-corrected Lg spectra and Q comparison for a northern, relatively high Q path.

The top plot of Figure 96 shows Pn/Lg and Pn/Sn ratios at AKT for orid 15250. The green and red curves correspond to using our Q corrections, and those from tomography, respectively. The Note that the corresponding tomography *Q* predictions (cf. upper plots of Figure 95) are both higher than the source-corrected Lg and Pn spectra at high frequencies, but the errors are comparable and largely cancel, giving corrected P/S ratios near one, appropriate for earthquakes. The bottom plot of Figure 96 shows that the errors do not cancel for any of the P/S ratios using tomography *Q* corrections from either LANL (red curves) or LLNL (magenta curves), leading to P/S ratios as high as 10-20 at higher frequencies, i.e., very explosion-like. For comparison, the corrected Pn/Lg mean for Nevada Test Site explosions is 5.5 for the 4-6 Hz band, and 5.8 for the 6-8 Hz band (Fisk et al., 2010), as depicted by the horizontal black lines in the lower plot.

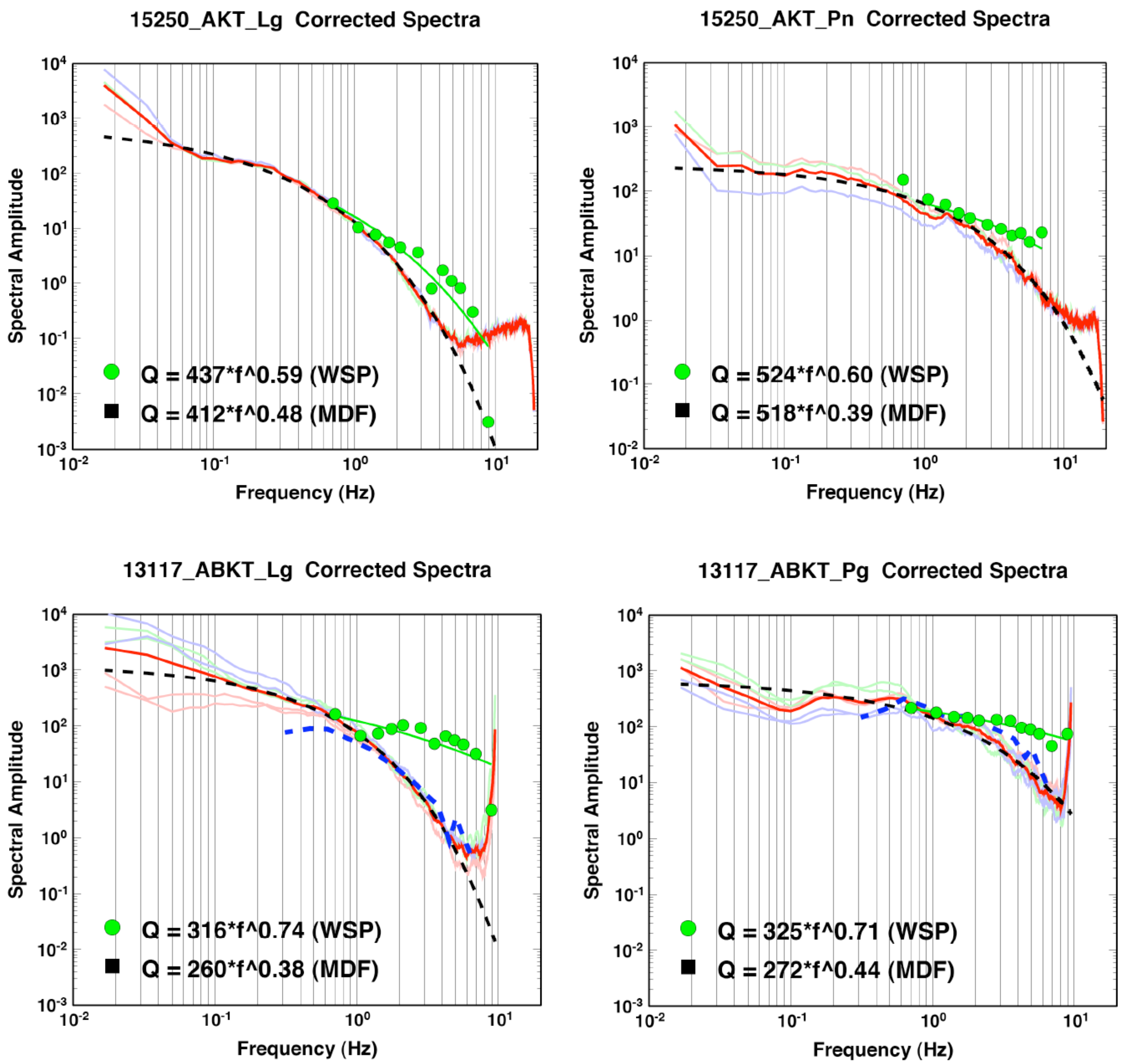

Figure 95. Comparisons of Lg (left) and Pn or Pg (right) spectral fits and tomography results for two clusters in Iran. The dashed blue curves are source-corrected amplitudes from LANL.

We have thoroughly investigated possible explanations for the high P/S ratios, when using the tomography *Q* corrections. Without going into the details, we have excluded (1) measurement differences (as shown by the blue curves in the lower plots of Figure 95), (2) corner frequency effects, (3) very different site effects at ABKT for Pn and Pg, than for Sn and Lg, and (4) frequency-dependent spreading. The problem is the well-known fact that tomography is unstable in areas with limited or no crossing ray paths, and depends of the number of observations, crossing ray paths, and SNR for various phases. To avoid false alarms, large uncertainties can be assigned to tomography *Q* estimates. However, given these errors and reasonable uncertainties, no event in this area would be discriminated. Given the importance of this region, this problem must be fixed, providing *Q* estimates that are verified by multiple methods and datasets (viz. the cases shown in Section 5).

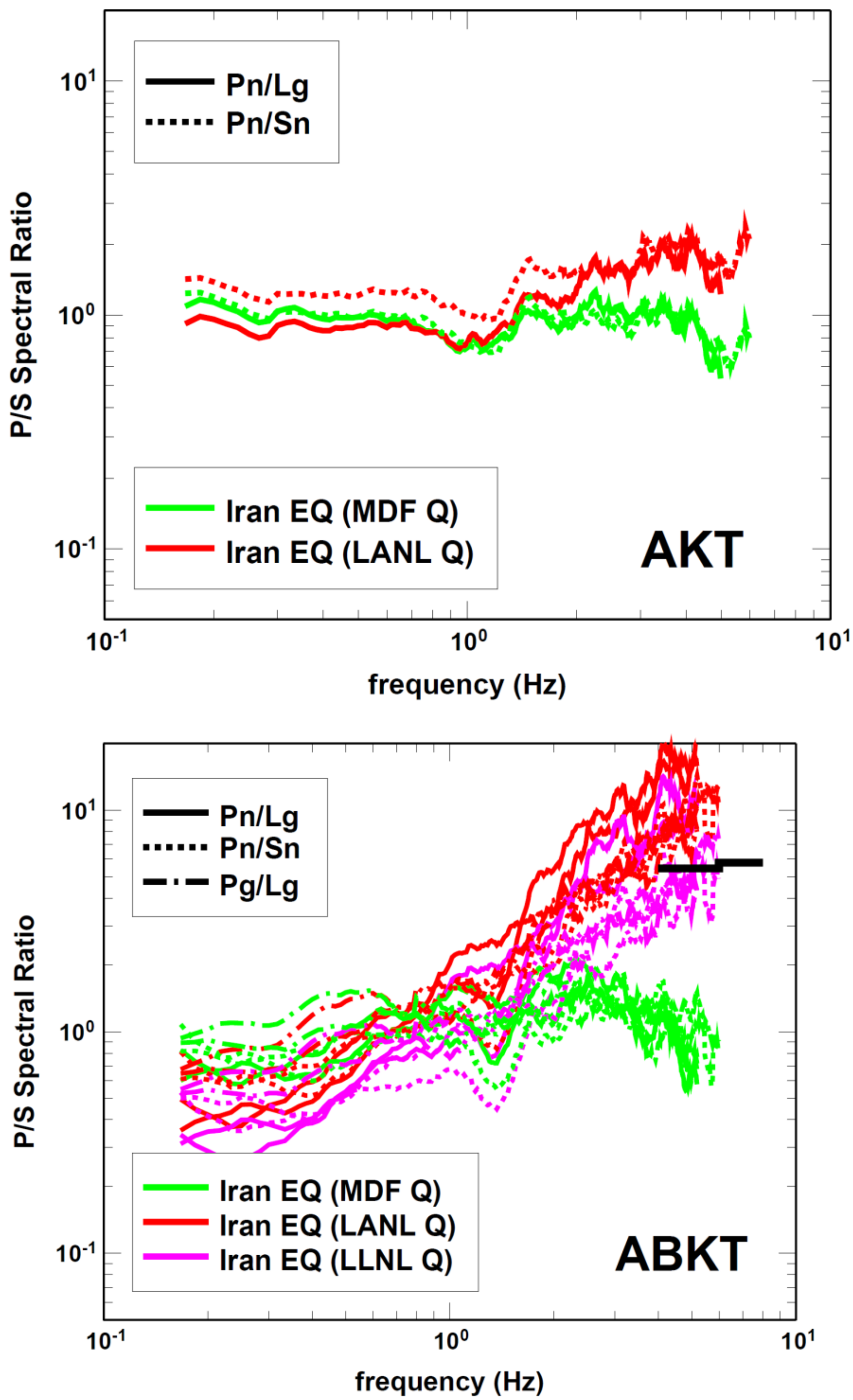

Figure 96. P/S spectral ratios at AKT for orid 15250 (top) and ABKT for orid 13117 (bottom), using my Q corrections from fitting source-corrected spectra, and from tomography by LANL and LLNL (see legends).

8.4 Pn Spectral Variability and Tomography Edge Effects

As noted in Section 7.4, of all the regional phases, Pn Q results from amplitude tomography and fitting source-corrected spectra are both the most unstable. This comes as no surprise to anyone who has worked on Pn modeling and calibration problems. One case we examined near the western boundary of the tomography grid emphasizes fundamental problems for both of the methods, but suggests that there are solutions, as we will show. Figure 97 shows our original processing of source-corrected Pn spectra for two representative paths (of 23 total). Like many of the stations, the low-frequency Pn spectra are variable, our Q_0 estimates are considerably higher than from tomography (904 is among the highest we obtained), and the *Q(f)* representations in the lower plots deviate from expected log-linear behavior. For comparison Figure 98 shows the corresponding results for Sn, agreeing much better with tomography and having much lower residual variances. These results for both Pn and Sn use the average of 3C spectra. For Pn, one of the channels for each station, BHN for AAKN (KNET station AAK) and BHE for AKTK, are considerably lower than the other channels. A key question is whether this variability can be reduced to improve our Pn Q results.

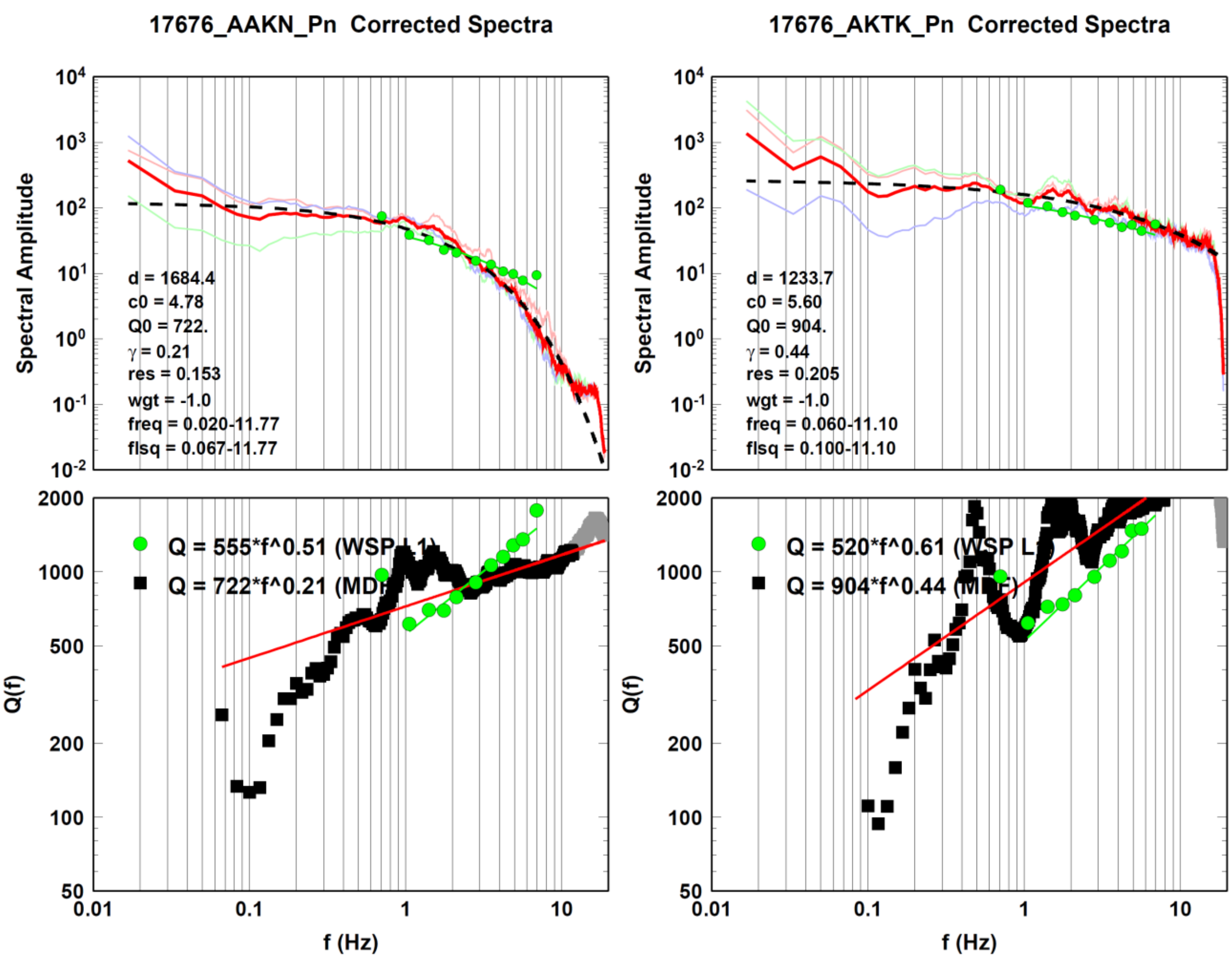

Figure 97. Examples of source-corrected Pn spectra and Q discrepancies for two paths at the western edge of the tomography grid.

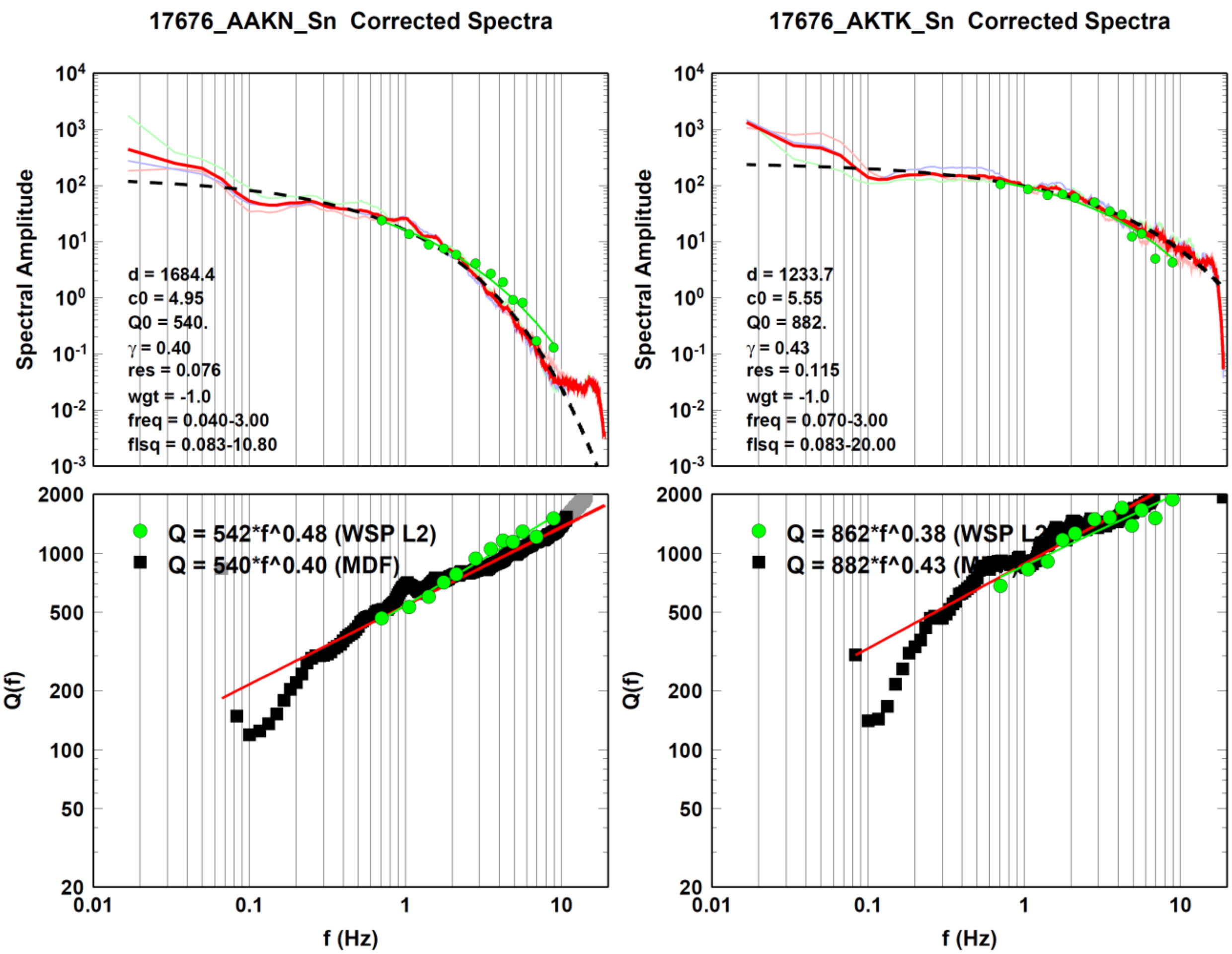

Figure 98. Similar to Figure 97, but showing Sn results for the same event and stations.

Based on the robustness of network median relative spectra to estimate source parameters, we also tested using the median, rather than the average, of source-corrected 3C spectra to estimate Q, mostly for Lg and Sn in our early efforts. The median is much more robust to outliers, but it is also known to be less reliable for small samples. The median worked well for network relative spectra because it excluded outliers (e.g., due to data quality problems), and there were typically at least 3 (as many as 25) regional stations with 3C data, giving 9 to 75 samples. However, when fitting source-corrected spectra for each path/station, this limits the number of samples. To mitigate this, we also considered averaging spectra over all events in a given cluster. We found that, even with fairly stringent S/N criteria, using smaller events in each cluster often biased both Q_0 and γ estimates higher than just using the largest event(s) and led to other instabilities. Thus, the average of 3C Lg and Sn spectra, often for a single (master) event, led to more reliable results than using the median, as expected statistically. Given the greater variability of Pn spectra, we re-examined using the median. For example, Figure 99 shows similar results to Figure 97, but now for the median. This excludes the low outlying channels, giving Q estimates that are more consistent with tomography, significantly reducing the residual variances (cf. “res” values in the legends), now on par with the Sn spectra, and recovering the expected log-linear *Q(f)* behavior (cf. the lower plots in Figure 99 to those in Figure 97).

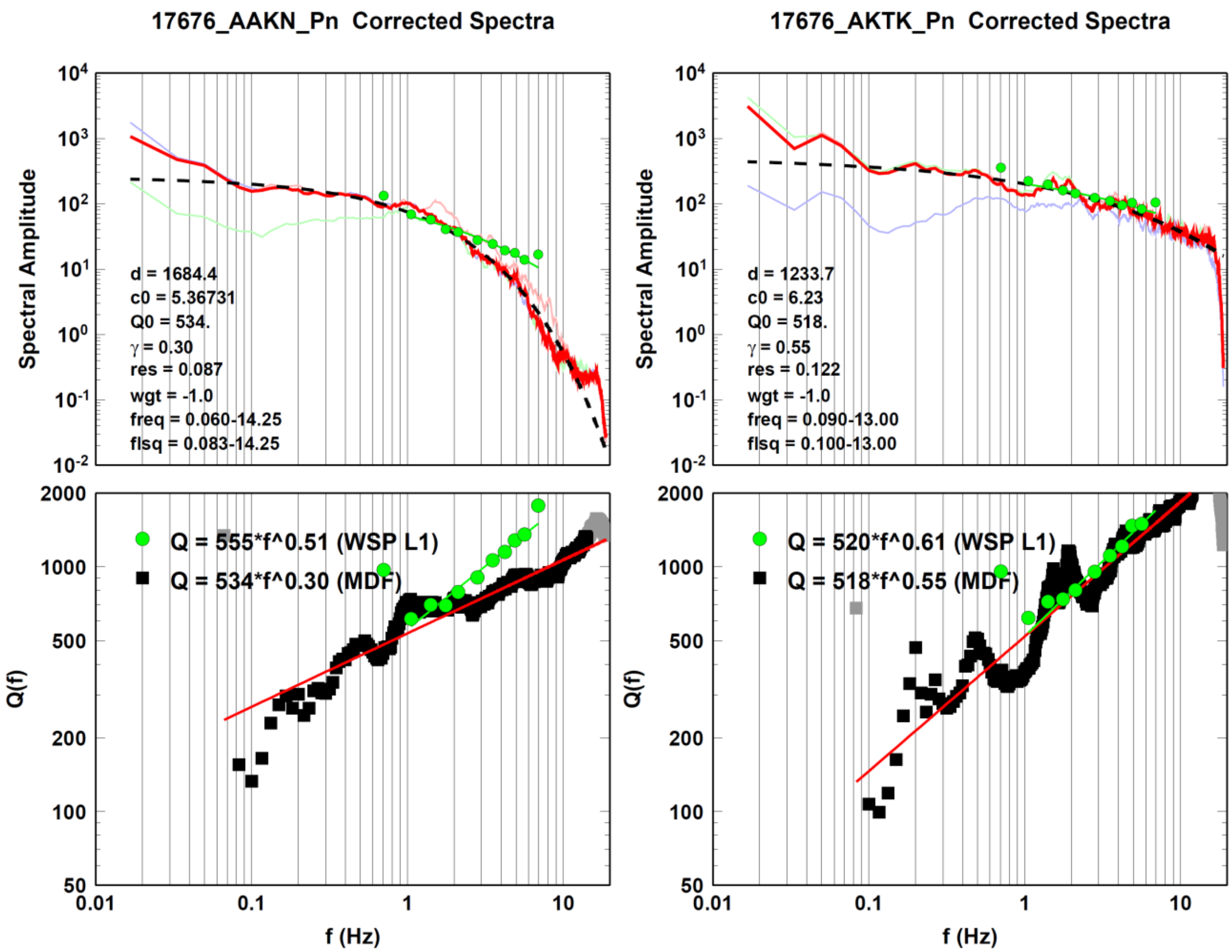

Figure 99. Similar to Figure 97, but using the median of source-corrected Pn spectra.

Note, however, that the Pn γ estimates from spectral fitting are still lower than from tomography, especially for AAKN. In fact, of 23 stations, only ARU has a Pn γ estimate from our analysis as high as from tomography. Figure 100 shows that while the Q_0 (1 Hz) are very comparable (left plot), the Q estimates at 6 Hz are uniformly higher (except for ARU) from tomography than our method, typical of tomography edge effects. (The black rays in the lower maps indicate a lack of tomography results for the paths to KIV, GNI, and RAYN.) Note, in this case, that because the tomography Pn γ estimate is relatively higher than that for Sn at AAKN, this causes the Pn/Sn ratio to be too low at higher frequencies. This does not pose a problem of misidentifying this earthquake as an explosion, as seen in the previous subsection, but it does inflate the variance of the earthquake population, making it even harder to discriminate actual explosions.

As for previous examples of discrepancies, the Pn results here can be rectified to give reliable calibration and discrimination results. Although the median of 3C spectra anecdotally improves Pn Q results for many paths/stations, it is not a panacea. For example, Figure 101 shows that even the median Pn spectra at ARU and KIV are highly variable. We need to further enhance Pn processing to stabilize general results. All of the cases in this section demonstrate key areas that should be addressed for future enhancements to calibration methods.

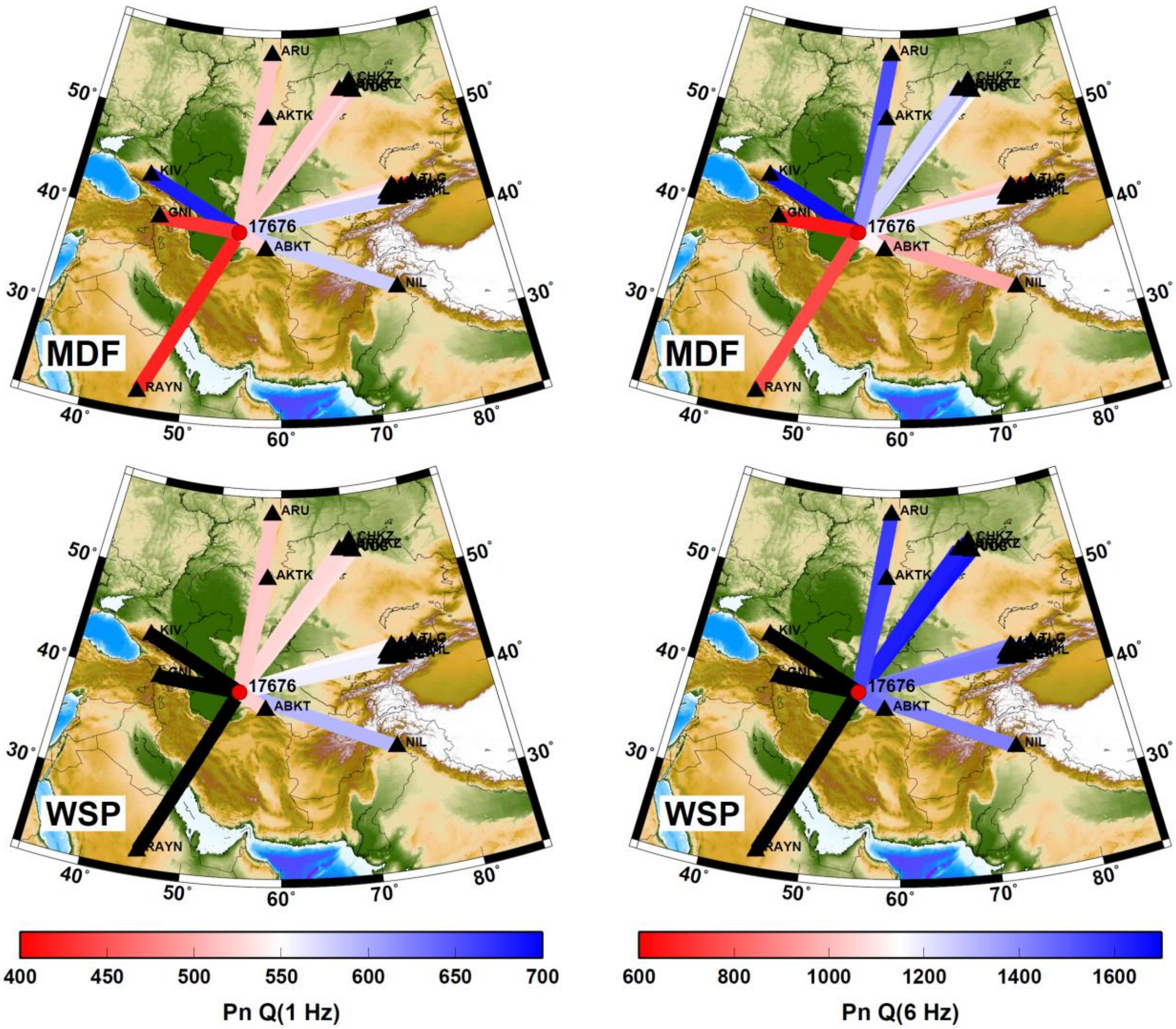

Figure 100. Comparisons of Pn Q estimates for 1 Hz (left) and 6 Hz (right).

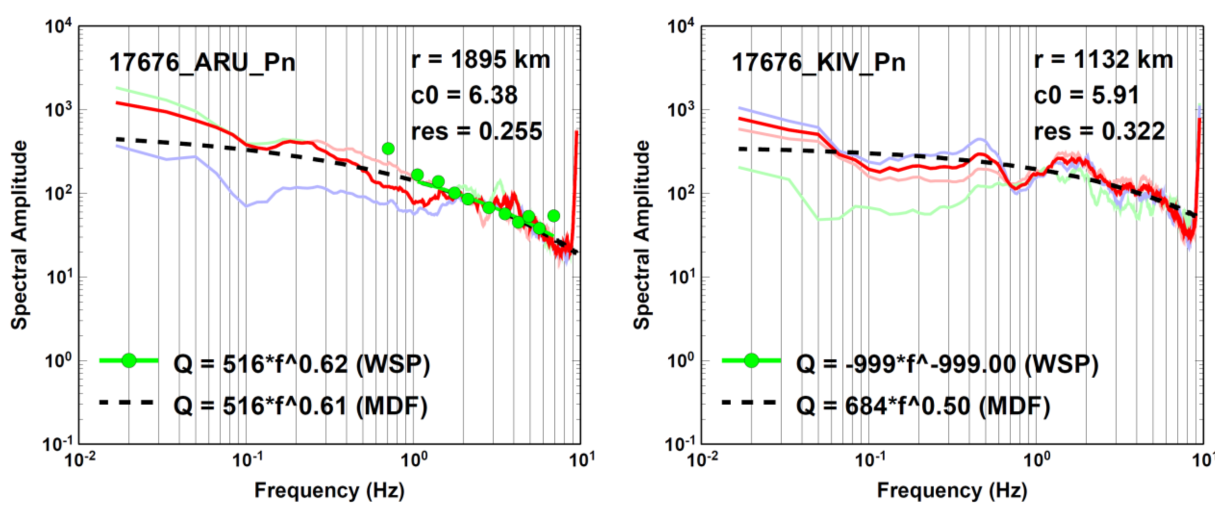

Figure 101. Highly variable source-corrrected Pn spectra and Q results for ARU and KIV.

9 GEOMETRIC SPREADING

In addition to estimating Q, the fits of source-corrected spectra, using Eq. (5) in Section 5, also give constants (viz. *c0* in Figure 45), related to spreading and site factor, the first two terms on the right-hand side of Eq. (5). We will see that the spectral constants also depend on Mw errors, which were tied to values in the PDE for larger (master) earthquakes. In this section, we show how geometric spreading rates are estimated for each regional phase, and how this information is also used to update the absolute moments (Mw values), to provide a very consistent set. Using Street et al. (1975), frequency-independent geometrical spreading, beyond a transition distance r_0, from spherical spreading to a spreading rate η, is represented by

$$G(r) = r_0^{-1}(r_0/r)^{\eta} \quad \text{for} \quad r \geq r_0. \tag{7}$$

For Lg, r_0 is typically taken to be 100 km. For purposes of fitting data recorded at distances beyond r_0, we can linearly regress

$$c_0 = -\eta \ln r + (\eta - 1)\ln r_0 + b, \tag{8}$$

where the last two terms are independent of distance, *r*. The site factors, *b*, may be defined to average to zero over the network of stations.

9.1 Lg Geometric Spreading Results

Figure 102 shows initial results of fit constants to source-corrected Lg spectra versus distance, tagged with the station names to see any station-dependent deviations. For example, the lowest outliers correspond to KUR of the Kazakhstan network. Excluding the outliers depicted by gray circles in the regression analysis, the estimate of η is 0.69, corresponding to the solid line, with a standard deviation of 0.65. This estimate of η is fairly consistent with the value of 0.6 used by Taylor et al. (2002), which is represented by the dashed line. In fact, given the scatter in the data, these two values of cannot be distinguished with statistical significance. The level of scatter and the number of outliers of these initial results were surprising, prompting us to investigate the causes. First, comparing spectra for common events recorded by both KUR (KZ network) to KURK (IU network), indicates that there is a response gain error for KUR. We also examined night-time noise plots for various stations, indicating calibration problems for KUR and ZRN of the KZ network. All but one of the highest outliers correspond to IC network stations in China.

At distances less than 400 km, a low outlier for station WMQ stands out. Figure 103 shows the fit constants versus distance for that earthquake in northwest China, not far from the Lop Nor test site (LNTS). This case is a microcosm of the three key problems causing the scatter observed in Figure 102. First, the Lg spectral fit constants, and their regression, are all shifted low relative to the Eurasian average (gray curves). This shift corresponds to about 0.5 moment-magnitude (Mw) units. That is, the PDE Mw estimate of 5.8 for this event seems to be too high by approximately 0.5. To corroborate that this is the right interpretation of this shift, we compared Mw estimates for many events to a set of high-quality regional moment estimates compiled by LANL, for which this event has a value of 5.4, 0.4 units lower than the PDE Mw of 5.8, and much more consistent with our updated estimate of 5.3. The second obvious problem in Figure 103 is that the fit constants for KUR and ZRN are shifted even lower due to gain errors. Such problems, while very significant, are rare compared to the entire data set, and are simply excluded for now.

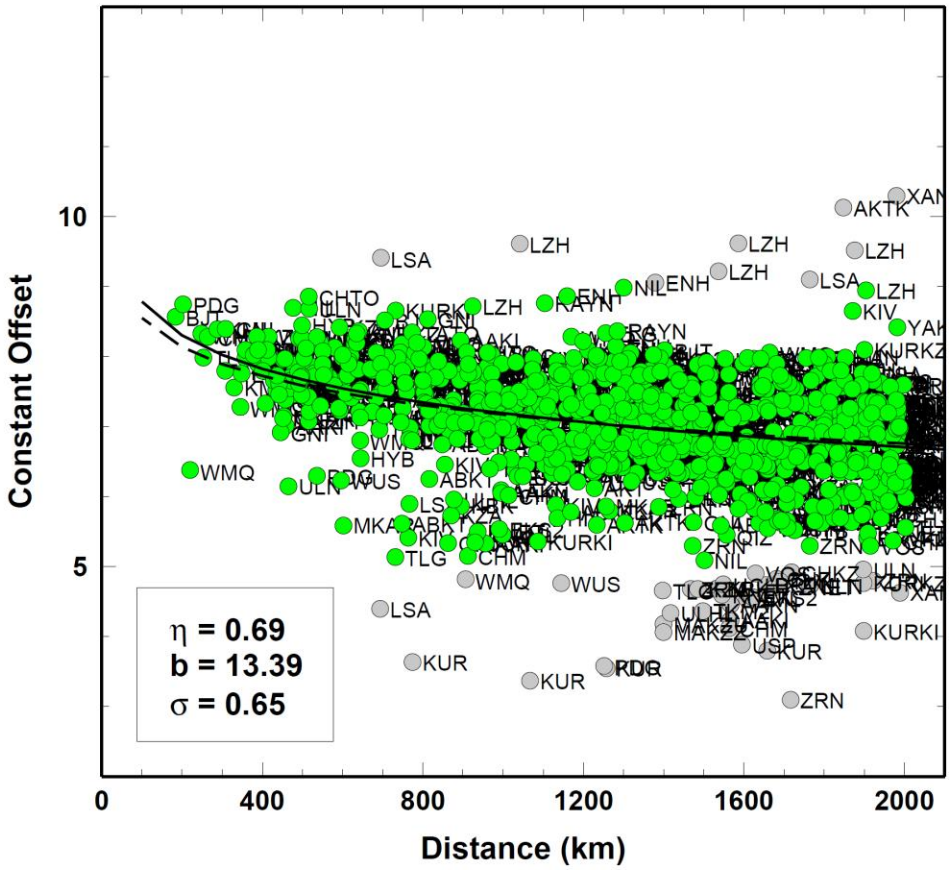

Figure 102. Initial set of Lg spectral fit constants (circles) versus distance. The solid curve is the fit with η as a free parameter, giving an estimate of 0.69. The dashed curve is the fit with η = 0.6.

The third major cause is due to less obvious data quality problems and spectral variability for some events/stations, particularly at low frequencies, which affect the fits of the source-corrected spectra. Figure 104 shows updated results, after shifting Mw lower to 5.3 and refitting some of the spectra. The Mw error and the gain issue for the BHN channel have miminal effect on the Q estimate. Response errors at KUR and ZRN have not been treated. Note that the spreading results for 23 of the 25 stations are now consistent with the Eurasian average and the standard deviation is much lower. For BRVKZ, the inconsistency of the spectral fit constant with the other stations (Figure 103) was also due to an instrument gain error, but only for the BHN channel, as shown in Figure 105. It does not significantly affect the Q parameters. Figure 106 shows the updated results, which (as indicated in Figure 104) is now consistent with the other stations.

Based on such investigations, we reviewed all of the Lg source-corrected spectra and their fits, fixing various problems. Figure 107 shows Lg spectral constants versus distance for 2186 paths throughout Eurasia. The gray squares depict the initial results. As described, the red “+” markers for the earthquake near LNTS are all shifted low relative to the Eurasian average, indicating a PDE Mw error of 0.5 m.u. (one of the largest). The red circles show the spectral constants after correcting Mw. The green circles show the Lg results after addressing most problems, giving an estimated spreading rate (beyond 100 km) of 0.59, consistent with previously published results of 0.5 to 0.6 (e.g., Sereno et al., 1988; Taylor et al., 2002; Walter and Taylor, 2002).

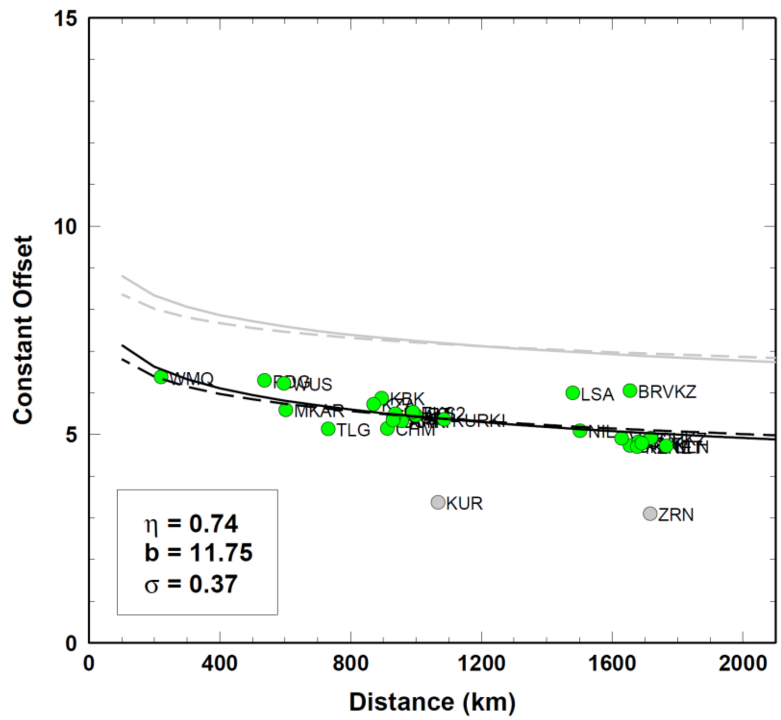

Figure 103. Lg spectral fit constants versus distance at 25 stations for an earthquake in China. The black curves show regressions to these data with η free (solid) and fixed at 0.6 (dashed). The gray curves show regressions to the full Eurasian data set.

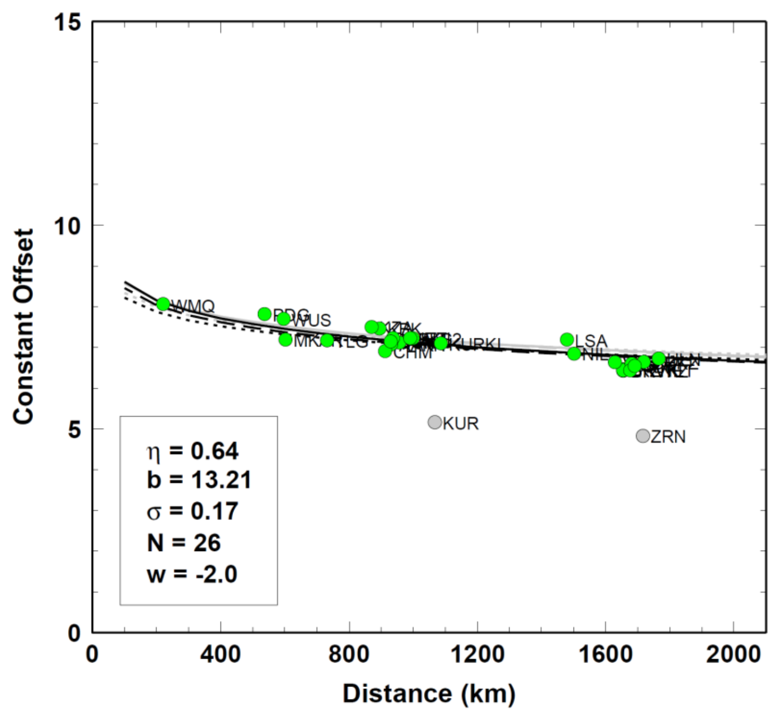

Figure 104. Similar to Figure 103, but reducing Mw for this event from 5.8 to 5.3 and refitting source-corrected Lg spectra at a few anomalous stations (e.g., LSA and BRVKZ).

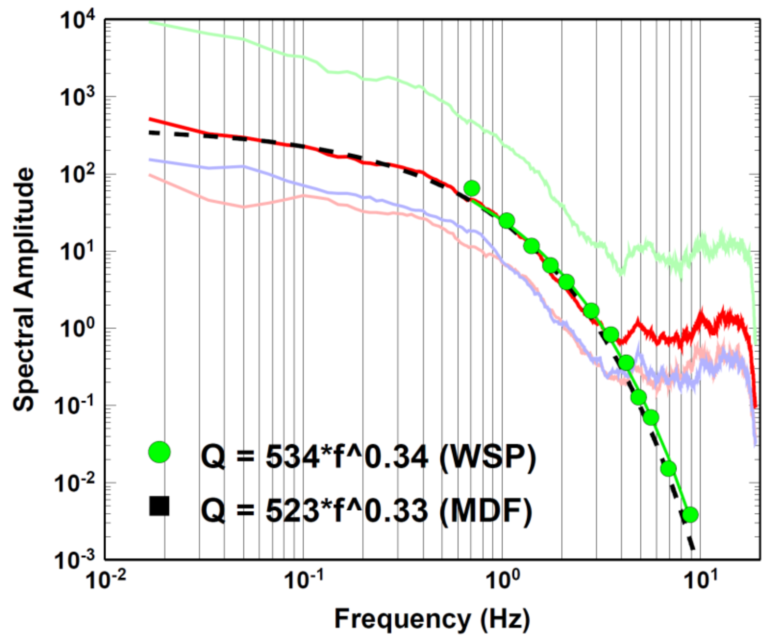

Figure 105. Source-corrected Lg spectra (using Mw 5.8) at BRVKZ and Q model fit. Channel BHN is an outlier of the others, causing the fit constant to be higher than for the other stations.

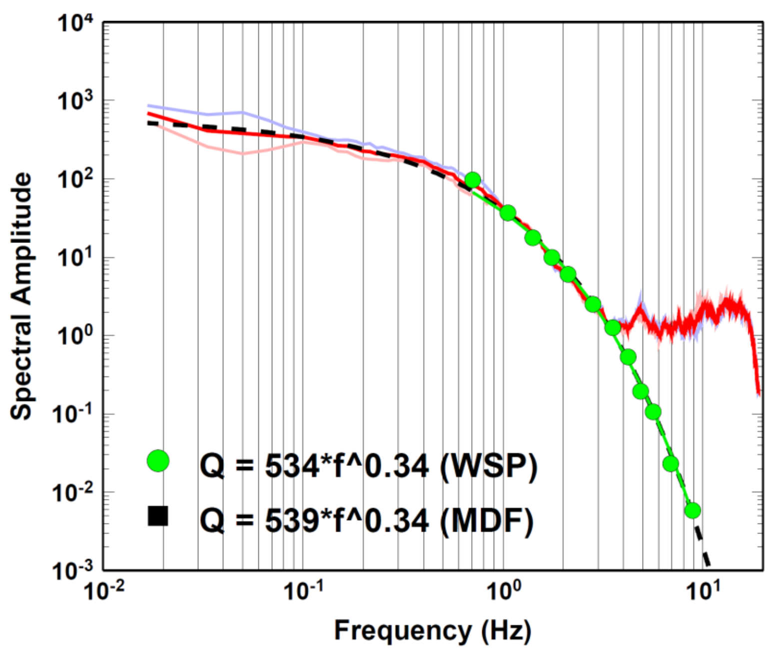

Figure 106. Updated spectral fit results for BRVKZ, excluding channel BHN and using Mw 5.3.

Note that at the very outset of our analysis, we fit relative spectra for event pairs to estimate corner frequencies and relative moments. We tied the absolute moments to PDE Mw's for the larger events, assumed to be better recorded and more accurate. This does not affect our f_c estimates, which, in turn, does not affect our *Q(f)* estimates. A high/low Mw simply shifts all source-corrected spectra for the event low/high. Our ultimate goal is to improve tomography results, which can be affected by Mw errors. We started with minimal assumptions, but have now updated the results to give a consistent set of absolute moments, corner frequencies, *Q* estimates, and spreading rates. We delivered these to LANL for future use as constraints.

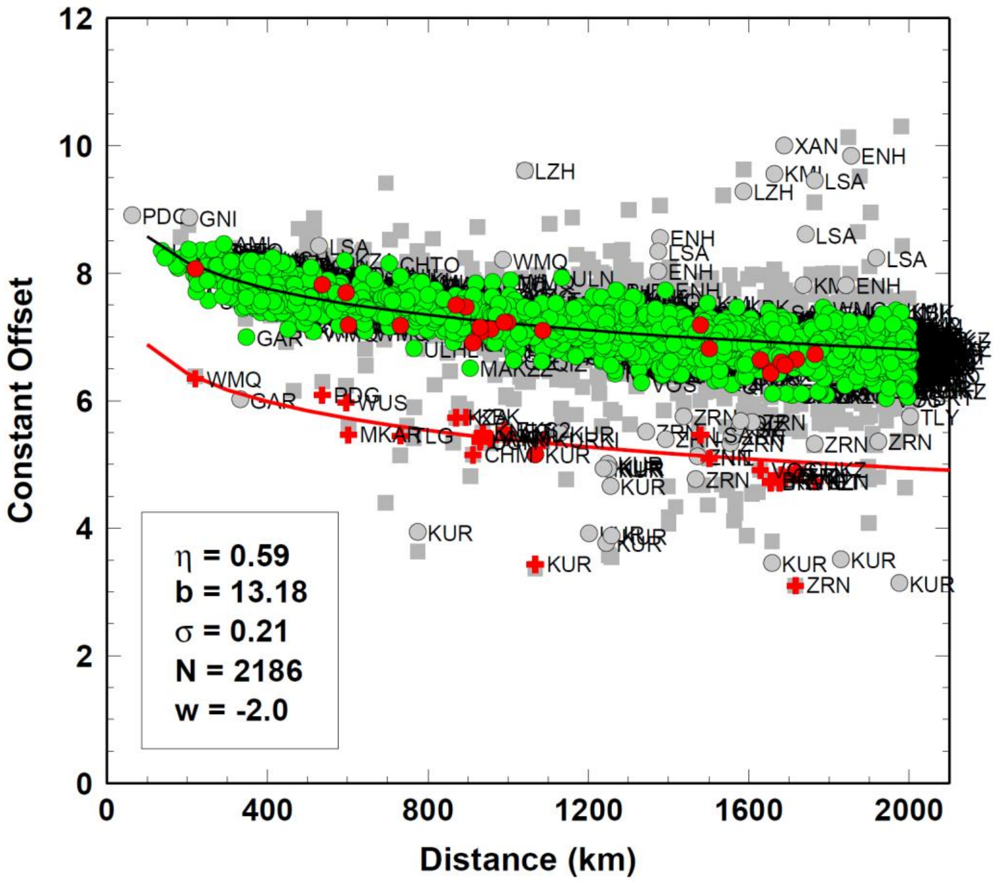

Figure 107. Lg geometric spreading results based on 2183 paths. Gray (green) markers show initial (reviewed) results. The black curve is the regression fit giving η = 0.59.

9.2 Sn and Pg Geometric Spreading Results

Figure 108 shows regression of Sn spectral fit constants versus distance, giving an estimated spreading rate of 1.06. This plot exhibits much less scatter than the initial results for Lg, largely because Mw errors are now redressed from the Lg analysis, and the lessons learned helped streamline and improve our analysis of Sn. Note that the red circles in Figure 108 are the Sn spectral constants for the same event as in Figure 107. The gray circles correspond to remaining data quality problems (e.g., gain errors). We also reviewed fits of source-corrected Pg spectra. Because Pg does not propagate as far as other regional phases, there are many fewer paths and worse spatial coverage for the same set of events with verified source terms. Figure 109 shows Pg spectral fit constants versus distance for 714 paths. Regression gives an estimated spreading rate of 0.68. The red circles in Figure 109 are the updated spectra fit constants for the earthquake near LNTS, using Mw 5.3, giving consistent results, with the respective Eurasian averages, for all regional phases. Also, our estimated spreading rates for Lg, Sn, and Pg are all consistent, within the statistical uncertainties, with previous studies cited, and with values used at LANL.

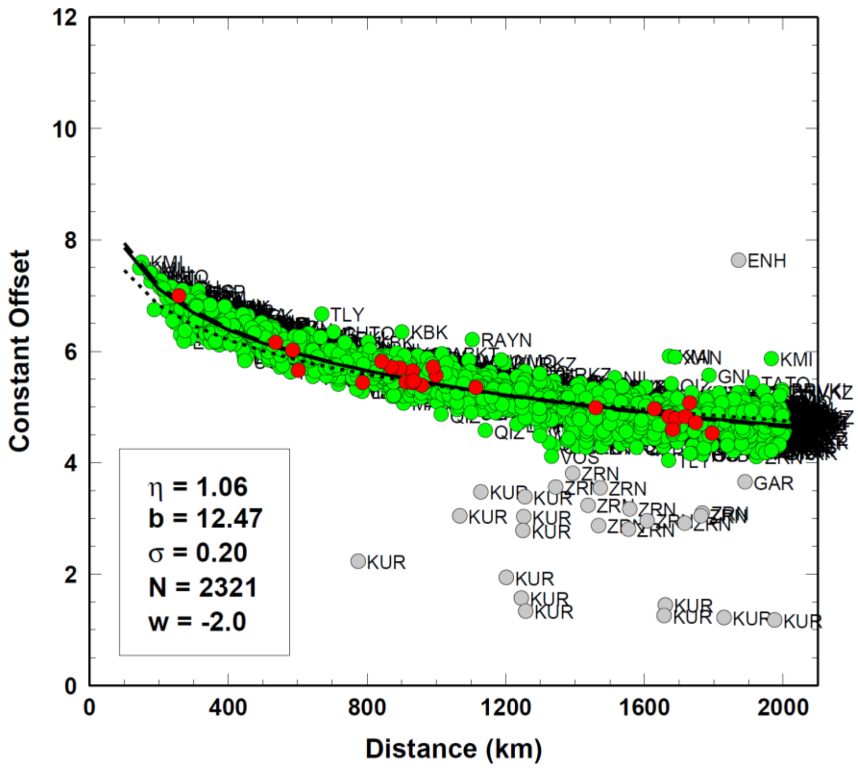

Figure 108. Sn spreading results for 2321 paths. The estimated spreading exponent is η = 1.06.

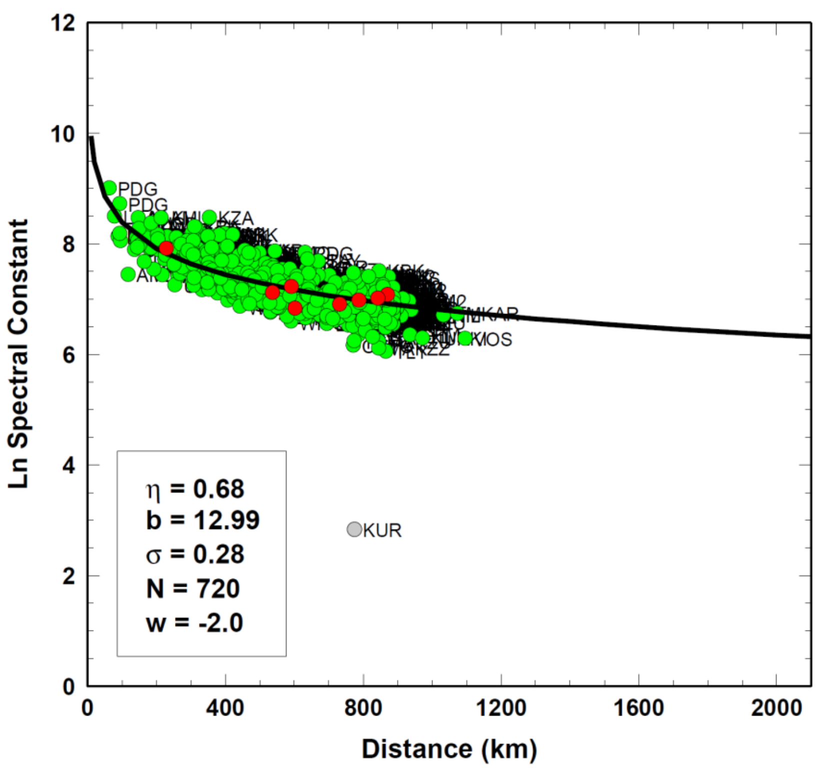

Figure 109. Pg spreading results for 714 paths. The estimated spreading exponent is η = 0.68.

We have also been reviewing Pn (checking picks, data quality, and spectral fits) for 2672 paths. Pn spectra for distances less than ~300 km are complicated by short time windows and ones that measure noise or Pg, depending on actual versus predicted arrival times. Pn spectra are the most variable and most time consuming to review. Although Pg/Lg typically has the lowest variance of various P/S discriminants, Pn/Lg and Pn/Sn discriminate better for calibrated areas (e.g., Walter et al., 1995; Fisk et al., 1996, 2001). In addition, for broad area monitoring, the ratio of Pg to Pn observations is roughly 1:4 (e.g., 714 versus 2672) for the same set of events. This is why it is so important to obtain good calibration for Pn. The green circles in Figure 110 are Pn spectral fit constants versus distance for 2237 reviewed paths, so far. Fitting Eq. (8) to all points out to 2000 km gives a standard deviation of $\sigma = 0.37$. Fitting data out to 1500 km, gives $\eta = 1.06$ and $\sigma = 0.28$ (black curve). The spectral constants are much higher at greater distances, on average, than the black curve. We have investigated this carefully, using a subset of large earthquakes, and find that this is not a noise effect. It is a physical departure from constant power-law spreading for Pn, presumably due to upper mantle triplication, sphericity, and other complicated Pn propagation effects (noted by, e.g., Yang et al., 2007; Yang, 2011; Avants et al., 2011). We have also tested quadratic (blue curve in Figure 110) and piecewise regression fits.

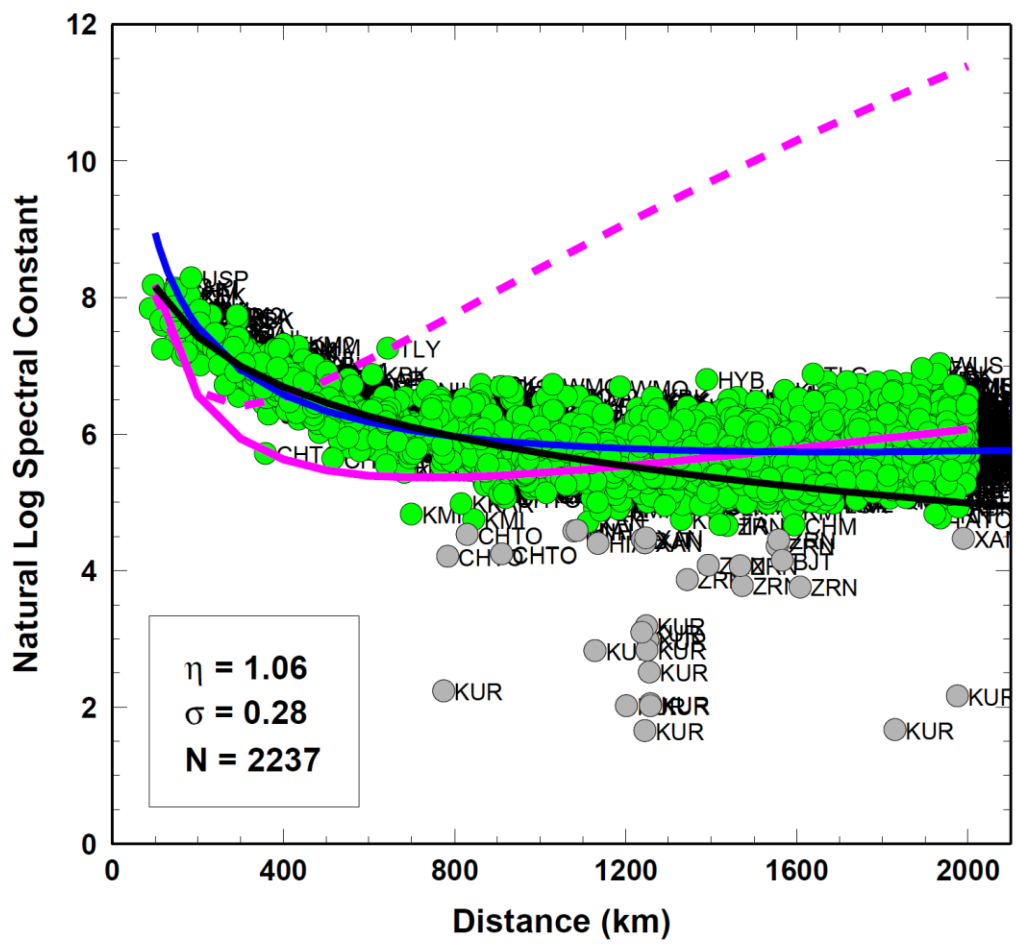

Figure 110. Pn spreading results for 2237 paths. The black curve is the regression fit out to 1500 km. The blue curve is a quadratic fit out to 2000 km. Magenta curves are the spreading model of Yang (2011) for frequencies of 1 Hz (solid) and 10 Hz (dashed).

The magenta curves in Figure 110 show the Pn spreading predictions of Yang (2011) [Y2011] for 1 Hz and 10 Hz. In deriving the model, he (1) applied generic Brune source corrections, using MDAC scaling relations of moment and corner frequency to mb, (2) corrected the amplitudes by the simulations of Yang et al. (2007) [Y2007], using a homogeneous, two-layer, spherical model, (3) estimated an average Q for Eurasia from those corrected data, (4) applied that Q correction, excluding the Y2007 spreading correction, and (5) then fit 6 or 12 parameters to represent the resulting frequency and distance behavior. Comparing spreading models with or without frequency dependence is complicated, but note that the magenta curves predict elastic 10-Hz Pn amplitudes at 1500 km a factor of 36 larger than at 300 km, and 73 times larger than 1-Hz Pn at 1500 km. Y2007 explain this as whispering gallery effects and argue that their spreading model leads to reasonable Pn Q. This assumes that the source corrections he used are valid. However, as we have shown (cf. Figure 1), the XP99 (used by Y2007) and MDAC (used by Y2011) source scaling relations both have significant errors. Using our large set of verified source terms, we can directly test whether Y2011, or any other, spreading corrections really yield reasonable Pn Q.

9.3 Pn Q and Spreading Comparisons for the Lop Nor Test Site.

For example, Figure 111 shows Pn Q results at 1 Hz (left) and 6 Hz (right) for paths to 25 regional stations from an earthquake on January 30, 1999 at LNTS. Figure 112 compares the estimates of Q_0 and γ. Except for TLY, LSA, and WMQ, they agree reasonably well. As we find for many Pn cases, the Pn comparisons have more scatter than for other regional phases. Figure 113 shows that the spectral fit constants versus distance are consistent with the Eurasian average, and the behavior of increasing values at far regional distances. Figure 114 illustrates good agreement of Q estimates for stations CHK and KUR, the log-linear behavior of our Q results, and ubiquitous biases in the lowest and highest bands for tomography. Although the spectrum for KUR is low, due to a gain error, the corresponding Q estimates are unaffected. Figure 115 compares results for AAK and TLY, indicating the range of agreement, as well as the need for improvements. These plots also show the Pn spreading predictions of Y2011 versus frequency. For AAK (at a distance of 1158 km), if we apply that correction prior to fitting for Q, it gives $Q(f) = 68\, f^{\,0.67}$, very inconsistent with the source-corrected spectral behavior and the Q estimates in Figure 115. We have discussed these results with Dr. David Yang and Prof. Thorne Lay.

To understand the physical issues, the standard model of Eq. (1), used by countless researchers, assigns all frequency-dependent distance effects to $Q(f)$ because data alone cannot separately estimate a frequency-dependent spreading term. Y2007 splits the distance terms into sphericity effects, simulated for a homogeneous model, and a definition of $Q(f)$ that includes anelastic and all unmodeled elastic scattering effects. (The simulations are also embedded in the semi-empirical Y2011 spreading model.) Avants et al. (2011) note that fully inclusive spreading would consider elastic scattering in a heterogeneous earth. They find that mantle lid velocity gradients systematically alter frequency-dependent spreading from that found for constant velocity, and random lateral heterogeneities in the uppermost mantle give Pn spreading approaching power-law behavior as the RMS strength of heterogeneity increases. (The "spreading" simulations of Y2007 do not treat these important elastic scattering effects.) So the distance effects are split differently, but neither has a purely anelastic definition of $Q(f)$, nor gives better corrections or physical interpretation, until realistic velocity gradients and heterogeneities can be modeled on large 3D scales. Lay and Yang have proposed research that should improve scientific understanding on this very important problem. The hardest part will be to validate the model simulations, given empirical limitations to resolve these effects.

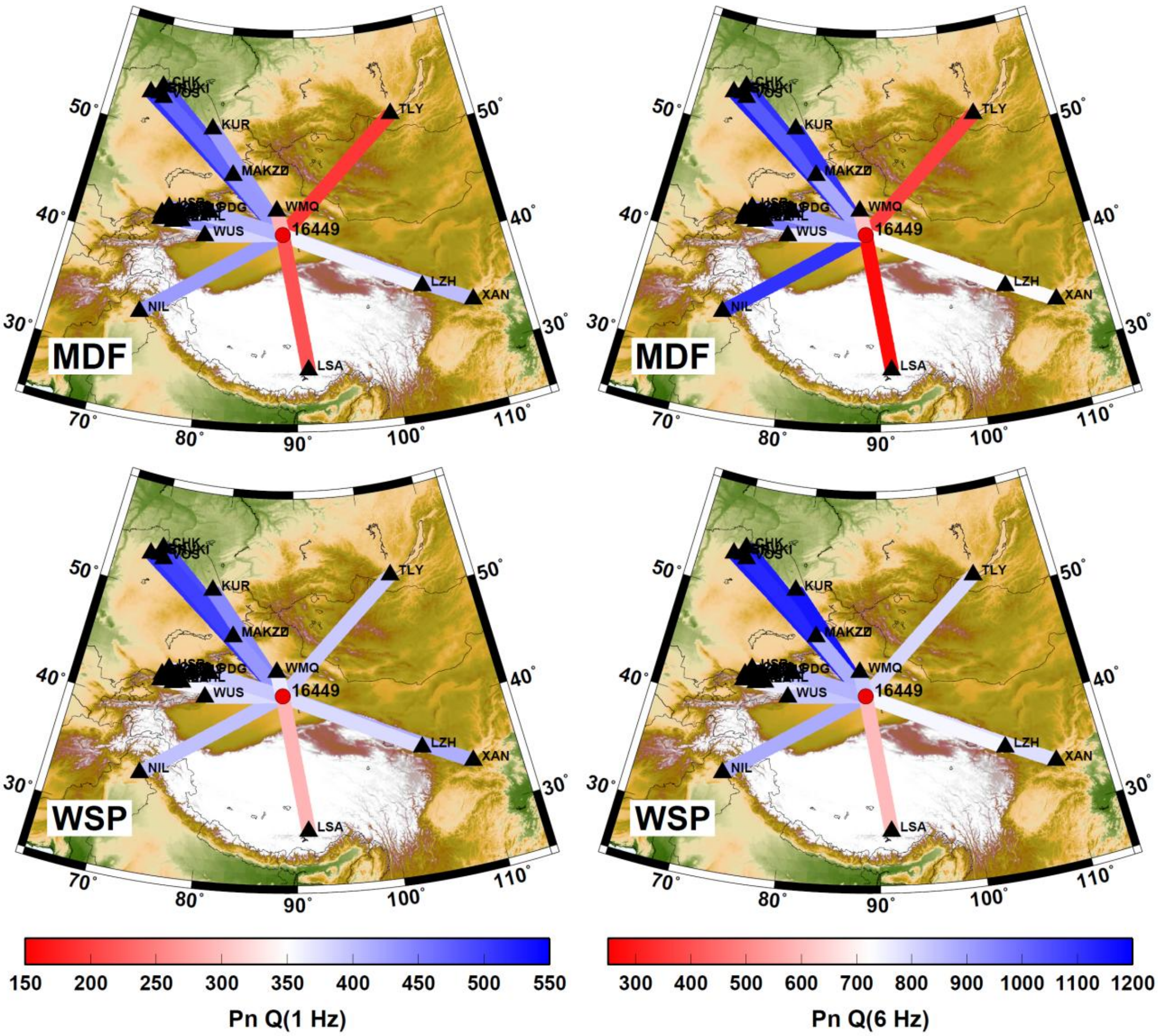

Figure 111. Comparison of Pn Q estimates at 1 Hz (left) and 6 Hz (right) from spectral fitting (top) and tomography (bottom) for regional paths from an earthquake at LNTS.

These results show the importance of Pn for P/S discrimination, based on the relative numbers of Pn and Pg observations, as well as the need to improve Pn geometric spreading and *Q* models. Using reviewed data with well constrained source terms, the Pn spectral fit constants (green circles in Figure 110) clearly depart from constant power-law spreading, showing the need for a better model. As illustrated for Lop Nor, Pn *Q* estimates are verified for many paths, but there are also many large discrepancies (e.g., for TLY), much more so for areas lacking good ray-path sampling. Previous Pn tomography runs at LANL obtained some very high, or even negative, *Q* estimates (i.e., predicting increasing amplitudes with increasing distance). A Pn spreading model that accounts for the rise at far regional distances (cf. Figure 110) due to, e.g., triplication effects, may remedy unphysical Pn *Q* values from amplitude tomography. Calibration of Pn is a very difficult problem because of its variability from a host of complicated effects. However, more accurate, robust, and compact Pn Q and spreading models are attainable than currently exist.

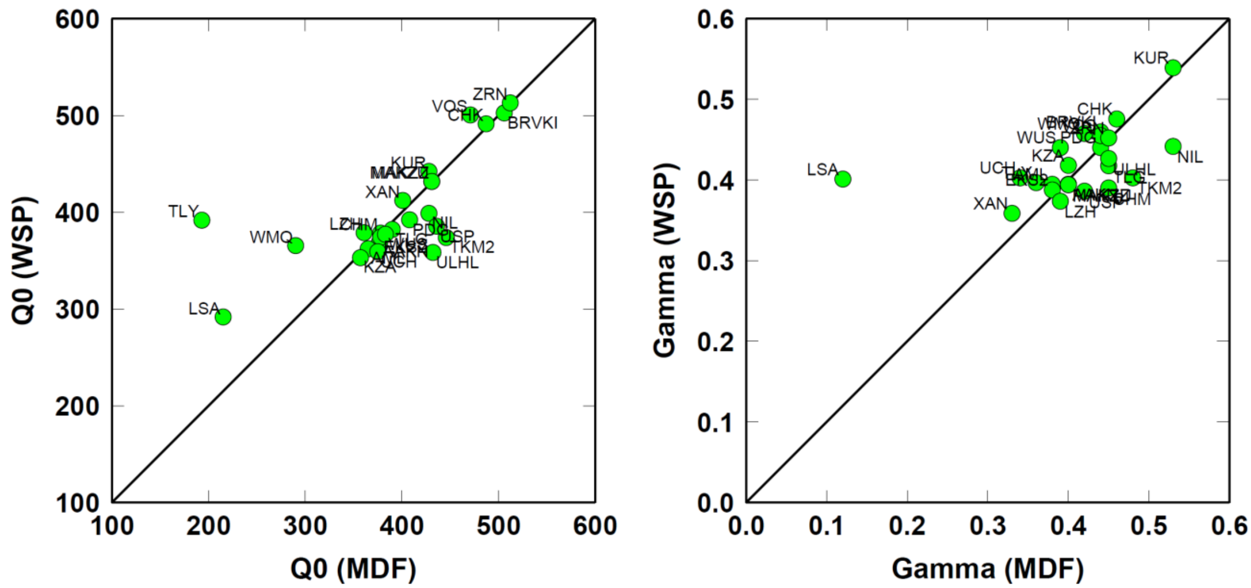

Figure 112. Comparisons of Pn Q_0(left) and γ (right) estimates for paths shown in Figure 90.

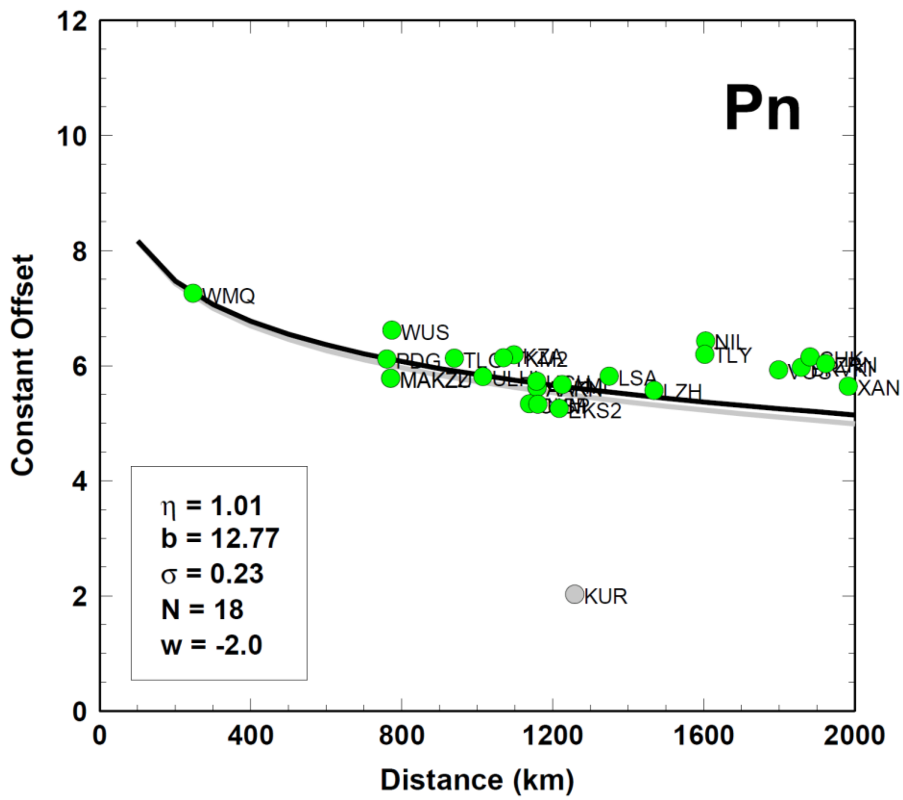

Figure 113. Constants of source-corrected Pn spectral fits versus distance. The black and gray curves are regression fits to these data and the full Eurasian dataset, respectively.

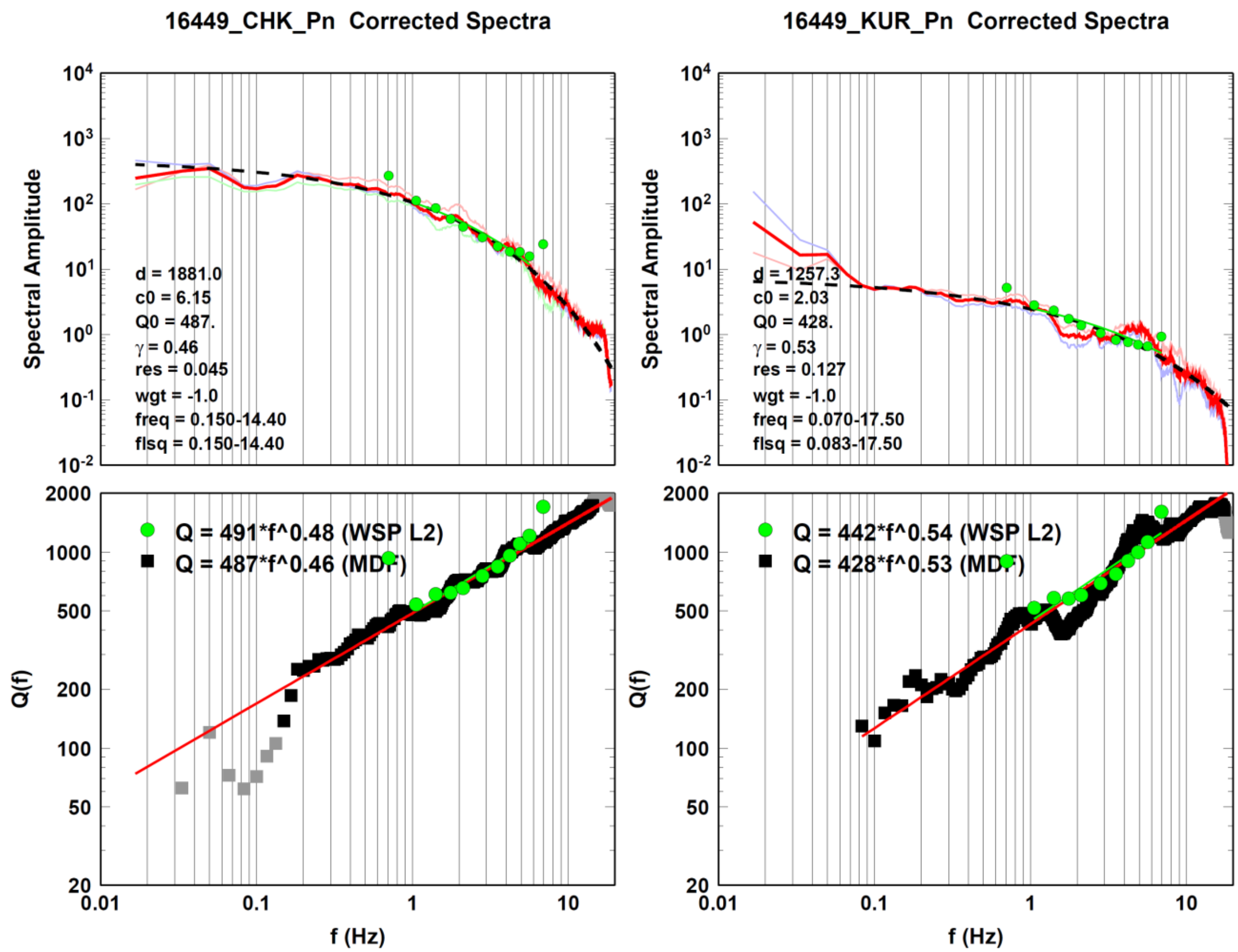

Figure 114. Source-corrected Pn spectra and Q comparison at CHK and KUR for LNTS.

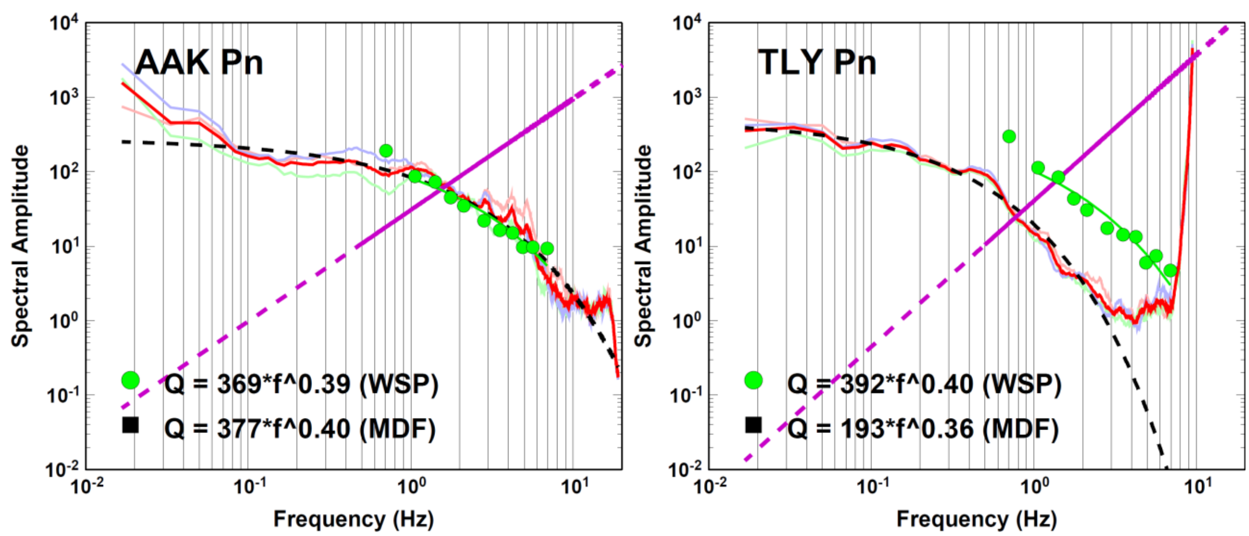

Figure 115. Source-corrected Pn spectra, Q model fits, and tomography results at AAK and TLY for an earthquake at LNTS. The magenta lines are Y2011 Pn spreading predictions.

10 FREQUENCY-DEPENDENT SITE EFFECTS

At this stage in the analysis, we further corrected the spectra for source, Q, and spreading terms. We then computed the median residual, to estimate the site frequency dependence, $\varepsilon(f)$ in Eq. (5), for Lg, Sn, Pg, and Pn at each station. Figure 73 compared direct Lg spectral residuals for a couple of events to Lg coda site terms for TLY. Figure 116 shows the median Sn spectral residuals (i.e., site effects) over all events we processed for various channels of TLY. The magenta and cyan circles are vertical and horizontal site terms in discrete frequency bands from Lg coda tomography, showing similar behavior from independent measurements and analysis. Not all compare this well. For example, Figure 117 is a similar plot for HYB, exhibiting reasonable consistency for frequency bands lower than about 1.5 Hz. For higher frequencies, the coda results are biased progressively higher by noise effects. This effect is more apparent in Figure 118, showing that the medial Lg spectral residuals at HYB are also biased high by noise for frequencies greater than about 3 Hz. They would be biased high at lower frequencies, if we included smaller events, like the coda site analysis. Figure 119 shows the median Sn spectral residuals at four more stations, illustrating reasonable agreement with the coda site terms. Figure 120 compares the results for KZNET stations, BRVK, CHKZ, VOS, and ZRNK. The coda site terms are all very similar for the four stations, including a bump at about 0.5-1.0 Hz and increasing values for higher bands. All are higher than the median spectral residuals at higher frequencies. As we noted in Section 5.3, Lg and Lg coda are biased high by Sn coda for the Kazakh Platform, where Sn propagates very efficiently.

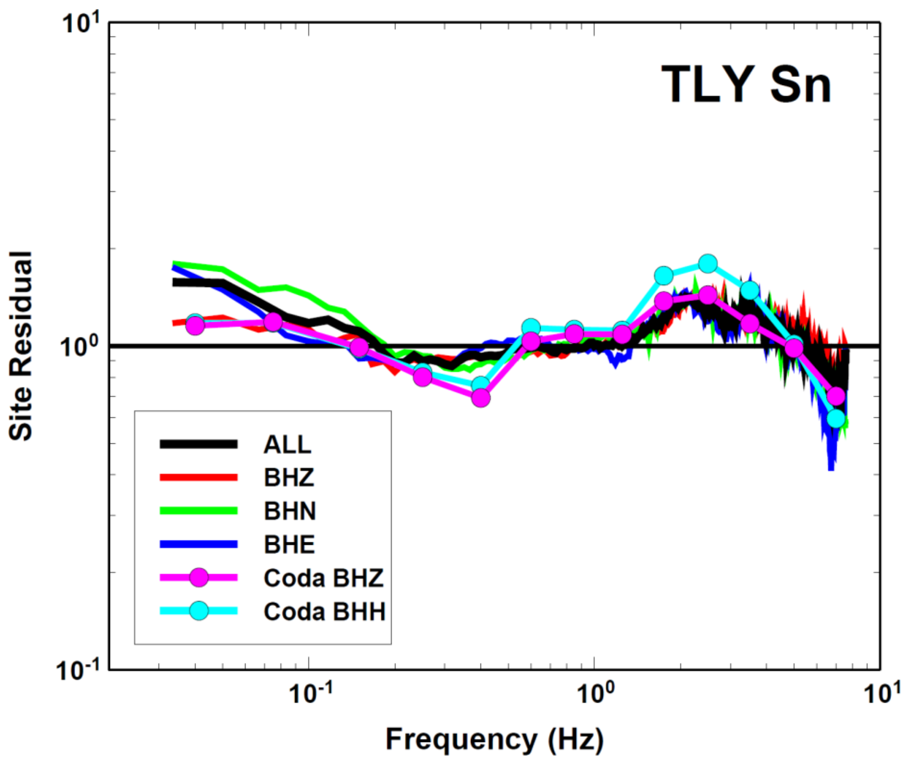

Figure 116. Sn site frequency dependence for various channels of TLY, and estimates from Lg coda tomography (cyan and magenta).

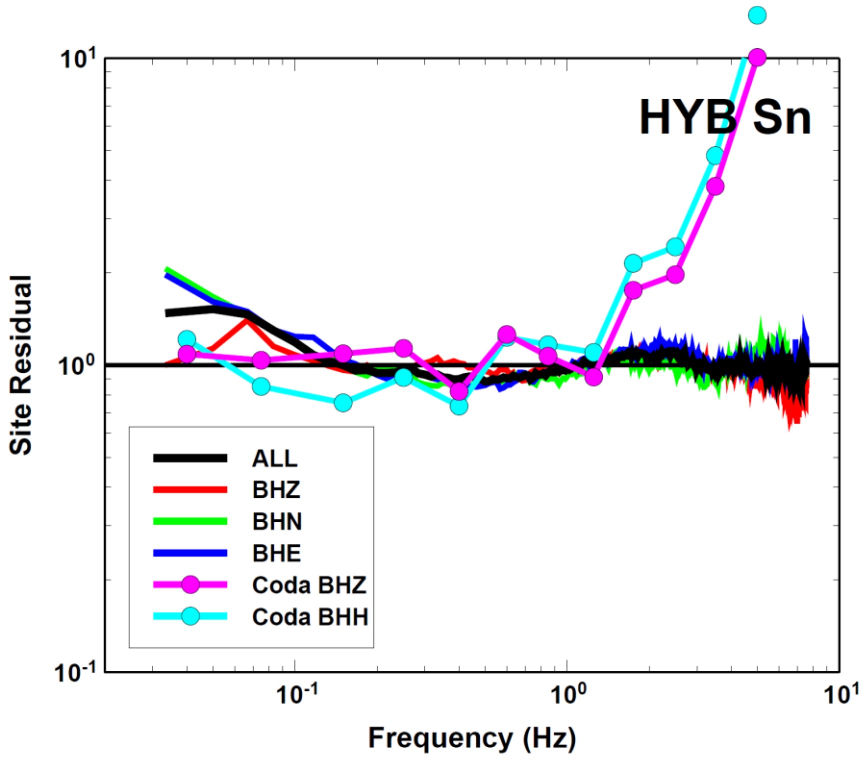

Figure 117. Similar to Figure 116, but for Sn residuals at HYB, showing a stark inconsistency.

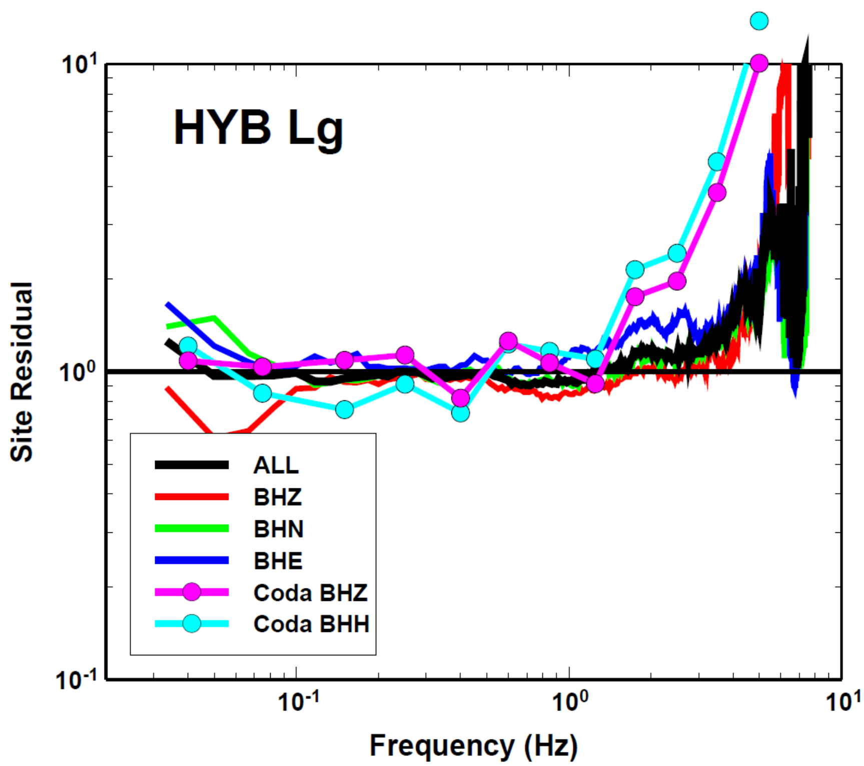

Figure 118. Similar to Figure 117, but for Lg spectral residuals at HYB.

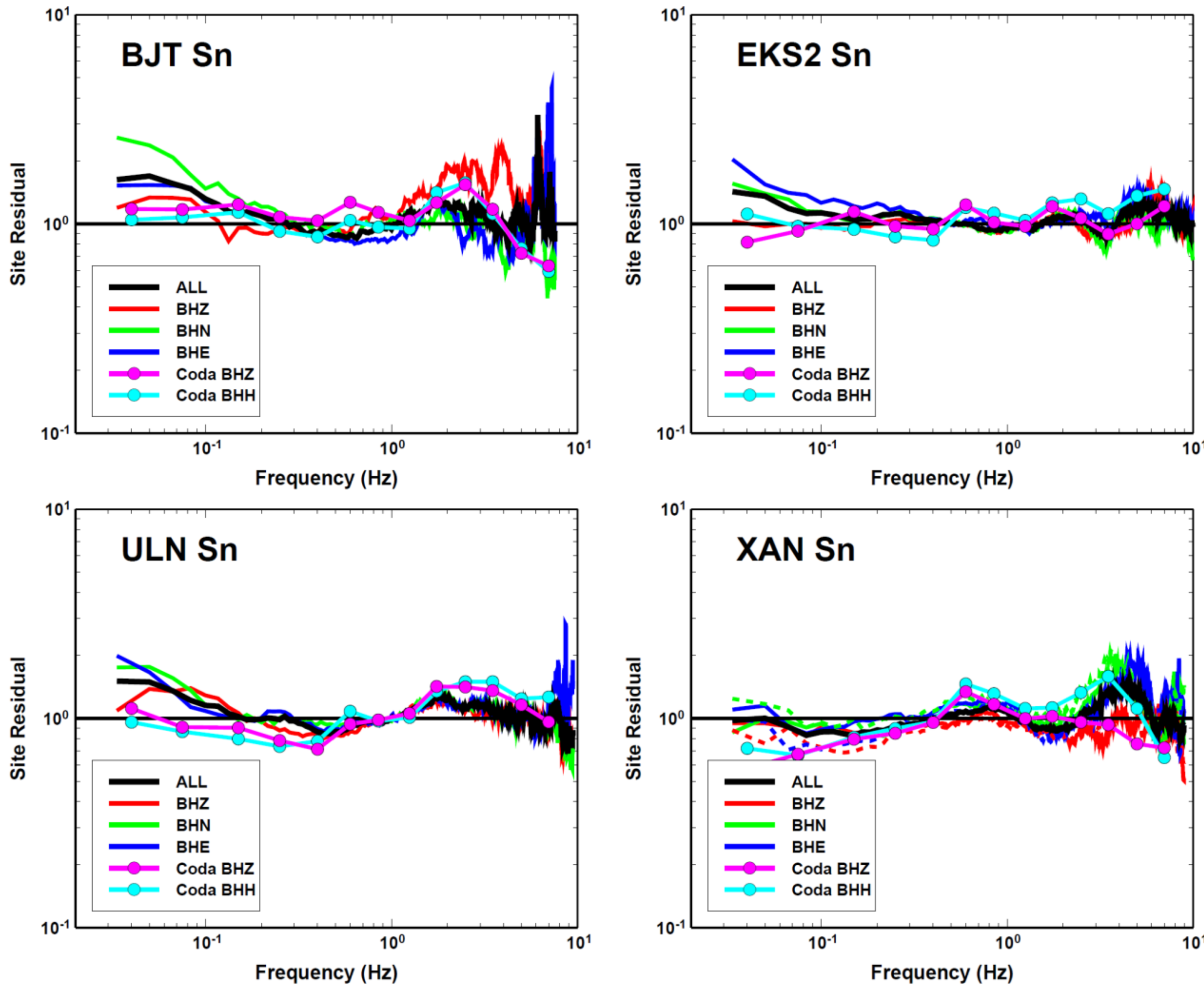

Figure 119. Comparisons of Sn spectral residuals to Lg coda site terms at four more stations.

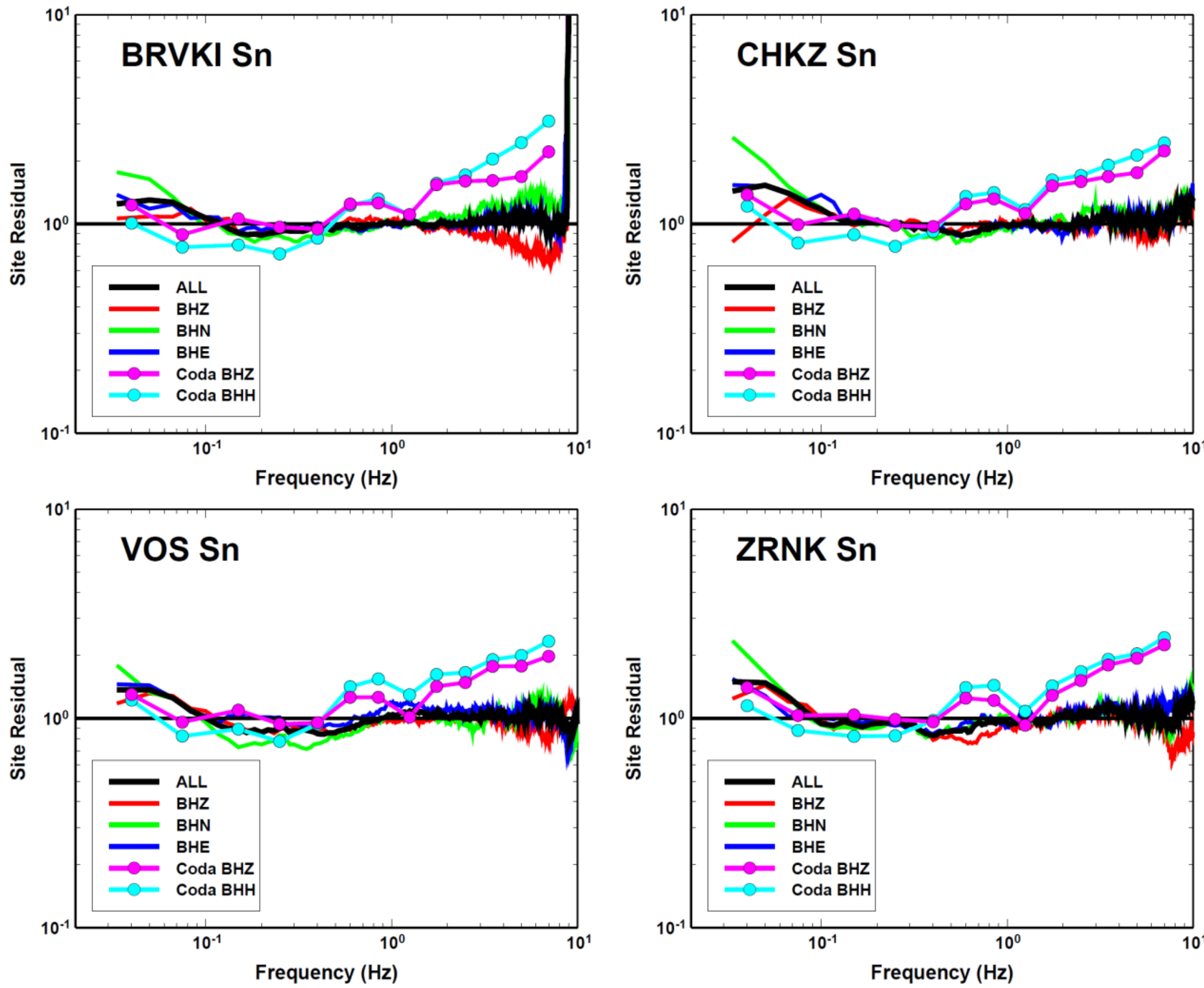

Figure 120. Comparisons of Sn spectral residuals to Lg coda site terms at four KZNET stations.

Figure 121 shows additional examples for Lg, indicating reasonable agreement for HIA and ULHL, and discrepancies for CHKZ and KMI. As noted, the coda site terms for CHKZ deviates higher in the higher bands. The median Lg spectral residuals are also biased high, but at higher frequencies because we use larger events with higher S/N. The discrepancy for KMI is the effect we discussed in Section 8.2. As we showed, applying the coda site corrections to our source-corrected Lg spectra leads to Q_0 and, especially, γ estimates that are much more consistent with direct Lg amplitude tomography. (The Lg spectral residuals shown here do not include the coda site correction.) Thus, comparing the independent estimates of site frequency dependence indicates good agreement for some stations, but also various discrepancies for which either our site terms or those estimated from coda have significant errors.

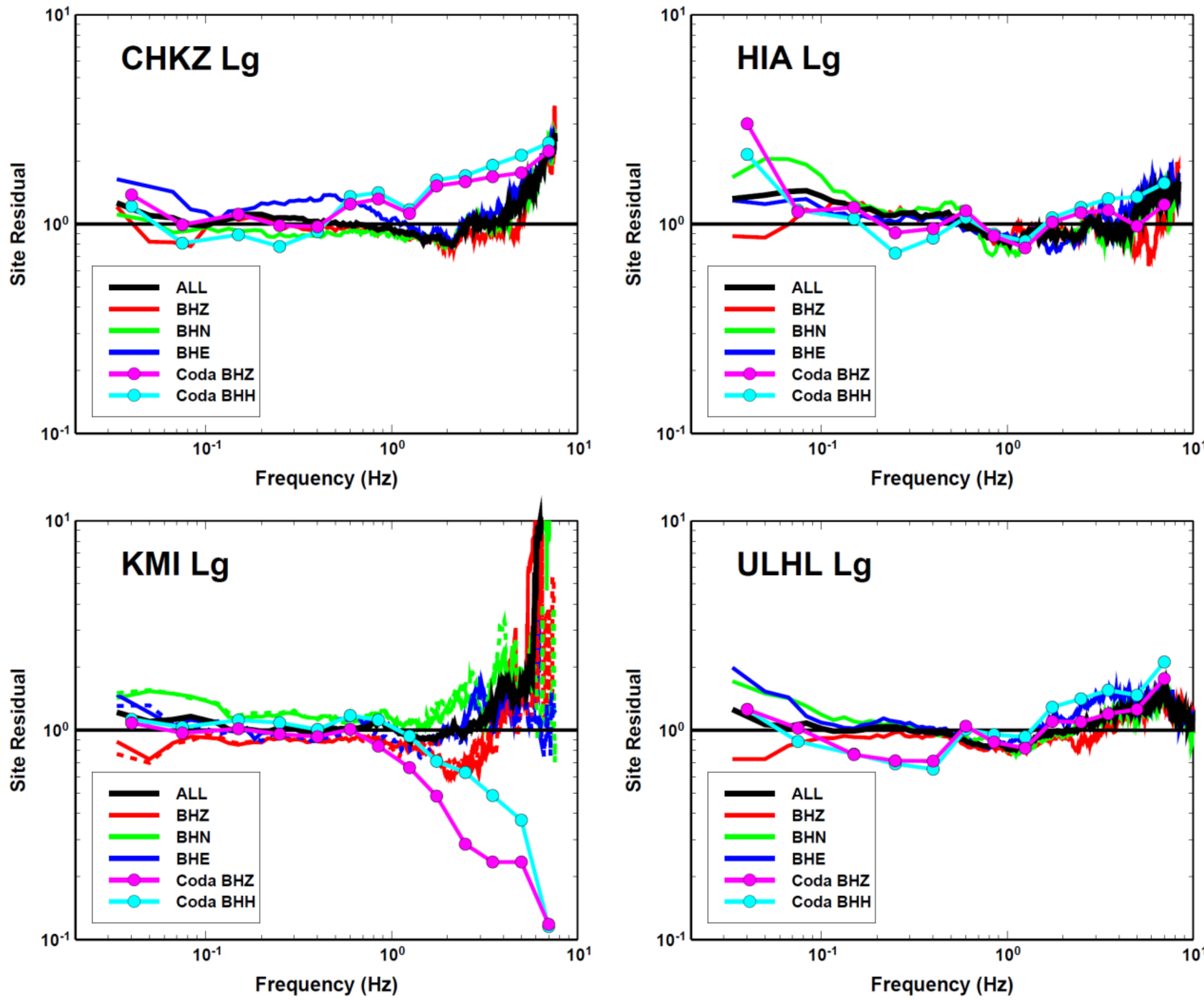

Figure 121. Examples of Lg spectral residuals and comparisons to Lg coda site terms.

Figure 122 shows examples of Pg site terms at six stations, along with the Lg coda site terms for those stations. Site terms for direct Pg and Lg coda do not always compare this well, nor do we know of a physical basis that they generally should. Nevertheless, it is interesting that they do agree remarkably well for many stations.

Similarly, Figure 123 shows Pn examples, again comparing favorably with Lg coda site terms, except for the highest coda bands for stations ABKAR and CHTO, likely due to data quality issues. In comparing all of the plots in this section, the Pn spectral residuals exhibit the greatest variability from one channel to another. The Pn residuals for BVAR are particularly interesting, showing a notch in the horizontal channels at about 3-6 Hz, but no such notch in the vertical channel. The corresponding coda site terms exhibit similar behavior (i.e., no notch in the vertical and a corresponding notch in the horizontal), although the notch in the coda result is not as deep.

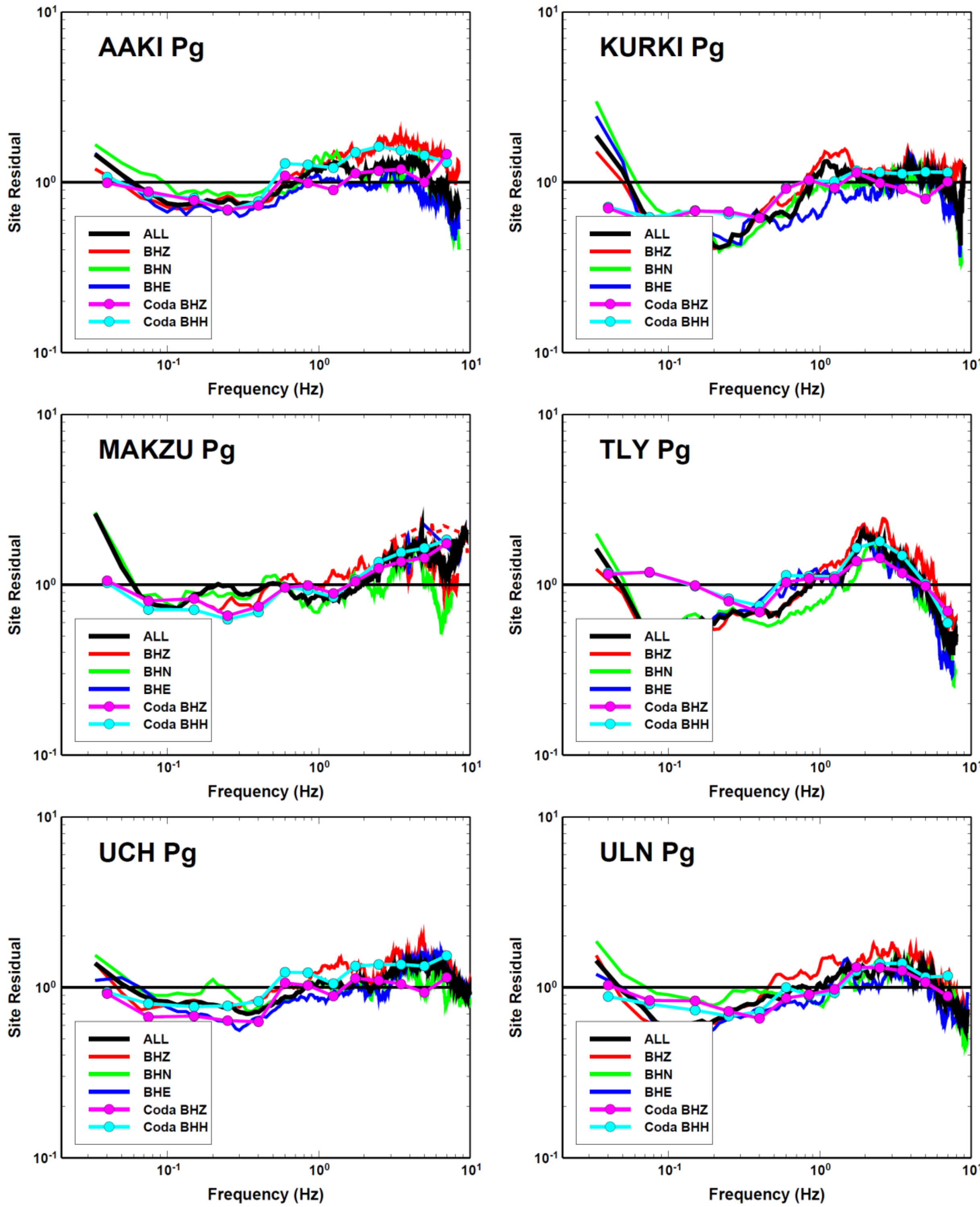

Figure 122. Median Pg spectral residuals at six stations, compared to Lg coda site terms.

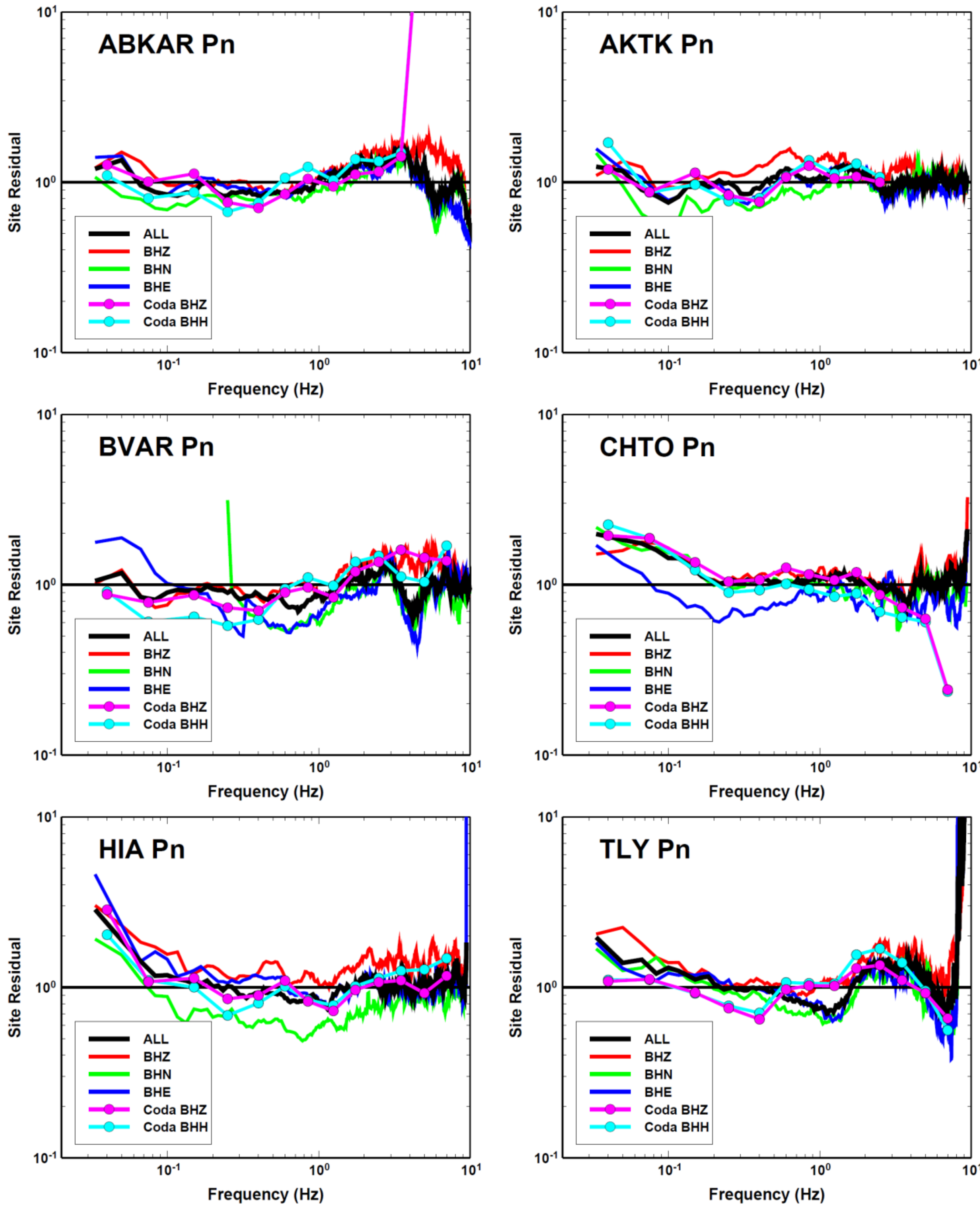

Figure 123. Examples of median Pn spectral residuals, compared to Lg coda site terms.

Figure 124 is also quite interesting, showing a very pronounced notch centered at about 3 Hz for the horizontal channels of all direct phases and Lg coda. There are also some significant differences. While Pg and Pn have similar behavior for the vertical channel, i.e., higher than the horizontal channels, the presence of similar spectral modulations, and no notch, the vertical direct Sn and Lg residual, and the coda site term are very different, indicating a different effect for P waves than S waves recorded on the vertical component of NIL.

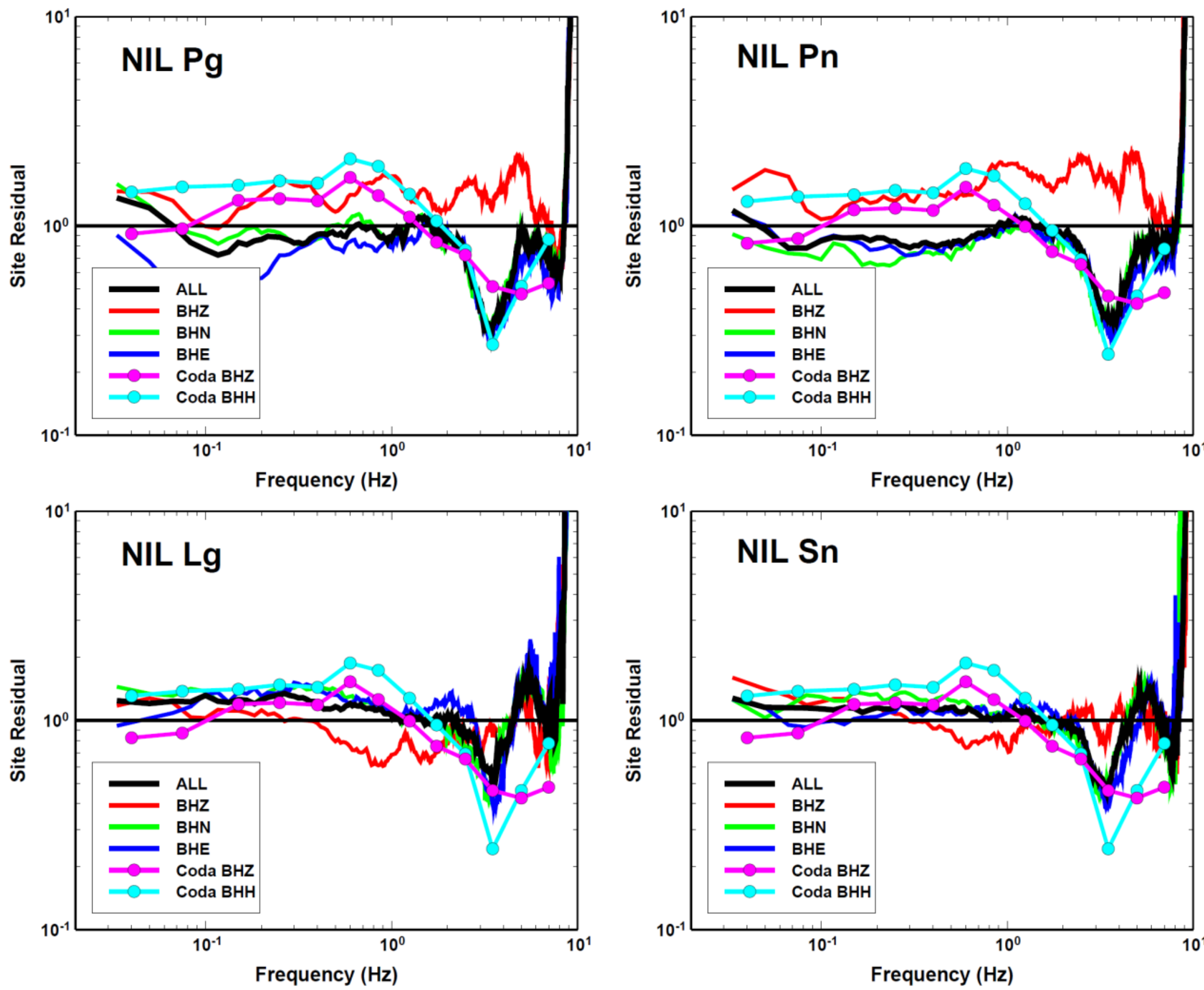

Figure 124. Median Pg, Pn, Lg, and Sn spectral residuals at NIL, compared to coda site terms.

These examples show that direct P and S spectral residuals agree very well with coda site terms for many stations, corroborating our analysis, like our Q comparisons to direct Lg tomography. KMI is one of the few stations examined for which the coda site terms have a strong monotonic trend that significantly impacts Q parameter estimates. Even for TLY, which has among the strongest site resonance, the Q estimates are only affected by about 10%, as shown in Section 6.2. As also shown, there are data quality issues and interesting physical site effects that need to be resolved and treated. Further work is needed to examine all of the various site terms in detail, to understand the physical effects, and to establish a final set of reliable site terms for the set of stations and various phases.

11 CONCLUSIONS AND RECOMMENDATION

We have shown that traditional inversion methods of Eq. (1) have many trade-offs, leading to large errors in distance and source corrections. This motivated our development of innovative techniques to separate the terms, canceling path and site effects to estimate reliable source terms, and then correcting for source effects to estimate more reliable attenuation, geometric spreading, and site terms. A key aspect of our approach was also to compare our results to those of independent methods at every stage of the analysis, to understand the reliability of the results and assess ways to improve the analyses and calibration terms. We assembled and processed a large volume of IRIS data for earthquakes listed in the PDE for Eurasia over a 20 year period. This included processing of waveform cross-correlations, spectra of direct regional P and S phases, and coda envelopes. Our unique and large-scale application of relative spectra for multiple direct phases and coda has generated a large set of corroborated source terms, with good spatial distribution throughout Eurasia. We used discrepancies in source parameter estimates to (1) cull unreliable results, (2) understand various problems, and (3) improve the analysis.

Because reliable source terms are an important foundation for this effort, we made significant efforts to compare coda and direct results, and improve the processing of both. We highlighted dependencies of moment and corner frequency estimates on station coverage, source size, epicentral distance, and the similarity of focal mechanisms for earthquake pairs used in the EGF analysis. Detailed investigations of the single-station results show that source terms estimated from relative coda envelopes generally have lower variance than those from spectra of direct phases, as expected, based on the well-documented stability of coda (e.g., Mayeda et al., 2007). However, direct-phase results often compare very well, even for single stations, for similar event pairs with good data. Our results also agree with published studies based on dense local networks, for the Bhuj, India cluster with very limited regional data, and for Wells, Nevada earthquakes that have strong source directivity effects. Examples shown highlight that direct phases are more sensitive to clipping, and can be variable for event pairs with non-similar focal mechanisms. Coda results are generally more susceptible to data quality issues because coda has lower S/N than direct Lg, and measurement windows are much longer, particularly for the lower frequency bands, increasing the probability of including spurious signals. Note that processing a data set of this size requires a high degree of automation; it is impractical to examine all of the data. Agreement of the coda and direct-phase results helps to validate the source terms. The inter-station EGF analysis can be used to quantify the uncertainties in the network estimates of relative moments and corner frequencies.

We have also examined spatial variations of the estimated stress drop parameters (e.g., Fisk et al., 2008). We found that it is highly variable, with relatively short correlation length (i.e., stress drop does not correlate well for clusters at different locations). This has important implications regarding the limited utility of historical data to predict the corner-frequency scaling relations at other locations. In turn, this limits the ability to properly correct discriminants formed as combinations of regional amplitudes in different frequency bands for source corner-frequency effects. Thus, the main benefit of accurately estimating the source terms is that it then allows distance and site terms to be estimated accurately, which are very important for reliable P/S discrimination.

The set of earthquakes with consistent source estimates yields a large set of representative paths throughout Eurasia for which we estimated distance and site effects. Comparisons of our independent *Q* estimates from source-corrected spectra verify amplitude tomography results for many paths and various regional phases. The two sets of results use independent measurements and orthogonal inversion/fitting methods. There are also some large discrepancies, which are mainly attributed to data quality issues in higher frequency bands and grid edge effects, both of which impact amplitude tomography results, and strong site effects for some stations (e.g., KMI), that impact *Q* parameter estimates from fitting source-corrected spectra. We showed how many of these discrepancies could be rectified by treating these effects, leading to Q parameter estimates from both methods that converge to the same answer.

We also used the constants of the fits of source-corrected spectra to estimate geometric spreading. These constants represent the low-frequency asymptotes of the source-corrected spectra, which depend on spreading, frequency-independent site factors, and Mw errors. We used their regression versus distance to estimate spreading rates for various regional phases. Our estimated spreading rates for Lg, Sn, and Pg are consistent with previous studies (e.g., Sereno et al., 1988; Walter and Taylor, 2002), within the uncertainties. The spreading behavior of Pn is more complicated, with large deviations from constant power-law spreading at far regional distances (discussed further below). We also showed how the fit constants can be used to identify Mw errors when compared for the recording stations to the Eurasian average over all stations and events. From this analysis, we obtained a consistent set of absolute moments for the earthquakes in our dataset. Note that at the outset of our analysis, we fit relative spectra for event pairs to estimate corner frequencies and relative moments. We tied the absolute moments to PDE Mw's for the larger events, assumed to be better recorded and more accurate. This does not affect our f_c estimates, which, in turn, does not affect our *Q(f)* estimates. A high/low Mw simply shifts all source-corrected spectra for the event low/high. Our ultimate goal is to improve tomography results, which can be affected by Mw errors. Thus, we started with minimal assumptions, but have now updated the results to give a consistent set of absolute moments, corner frequencies, *Q* estimates, and spreading rates. We delivered these to LANL for future use as constraints on tomography.

Likewise, our estimates of frequency-dependent site residuals compare well with those estimated from independent coda methods for many stations and various S and P phases. We showed how KMI, with very strong, monotonic site attenuation at higher frequencies, systematically biased our Q γ estimates high, discovered by comparison to direct Lg tomography. We further showed that coda site terms could be applied to our source-corrected spectra to rectify this problem, giving consistent Q parameter estimates from our analysis with tomography. Some stations also have strong site resonance effects (e.g., TLY), which impact Q_0 and/or γ estimates, depending on the frequencies at which these resonances occur. However, in most cases, such resonances and other site variability had only a modest effect (e.g., 10%) on our Q estimates. As also shown, there are data quality issues and interesting physical site effects that need to be resolved. Further work is needed to examine all of the various site terms in detail, to understand the physical effects, and to establish a final set of reliable site terms for the set of stations and various phases. A remaining step in our analysis is to also apply the site corrections, to quantify residual variances versus frequency, and partition them by physical contributions

By comparing results of independent measurements and methods, we have also found critical ways that *Q* and spreading models must be improved and evaluated. In fact, prior to our analyses, numerous serious calibration errors in source, Q, and spreading parameterizations have gone unnoticed. Our methods and analyses have provided the capability to uncover and rectify these problems. First, given that some key areas are near grid edges, where tomography results are known to have especially large errors, leading to egregious discrimination errors for Iran (e.g., P/S ratios as high as 20 for earthquakes, using tomography corrections from LANL and LLNL), we need to incorporate our source and Q constraints in tomography runs at LANL and LLNL. Not only would the calibration results be more accurate for the explicit paths corresponding to our results, but also for nearby and crossing ray paths, promulgating our relatively sparser, yet well-distributed results throughout the grid. This would combine the strength of our method to accurately distinguish various physical effects, with the strength of tomography to interpolate the results, using a vast abundance of data.

With regard to edge effects and calibration for the Middle East (Iran, in particular), our approach can be very beneficial. Specifically, LLNL has assembled considerable data from stations in Iran. However, many of these stations lack reliable response information to be used in amplitude tomography (Pasyanos, 2012, pers. comm.). Our relative spectra would cancel the response terms, allowing accurate source terms to be estimated. We would need to ensure that the response did not change over the time period of the events in a given pair. We could do this by comparing to coda at even a single reliable station, given its stability. We could also focus on event pairs fairly close in time. The resulting source terms could then be used as constraints in tomography runs, using only stations with valid responses. This would eliminate the trade-off and the events with good source terms would act as effective stations. As a second approach, we can also perform tomography on P/S ratios directly, using a much denser set of stations and paths, and completely canceling the response effects for Iranian stations.

Second, data quality directly impacts calibration. Quality control (QC) is a very important and non-trivial aspect of any seismic data processing. S/N thresholds are typically used. However, there are many ways that bad data can pass an S/N test and good data can fail. For example, clipped data have spurious high-frequency signals that can easily pass the test. Alternately, aberrant signals in the noise window can cause good signals to be rejected. This is especially complicated for secondary phases because pre-phase noise measurements include preceding phases. For example, a valid Lg signal may be rejected, depending on the threshold, because the noise window includes Sn. Alternately, using pre-Pn noise can accept Sn or Lg signals that are actually coda of P phases. There is no simple way to automate noise windows and S/N thresholds that avoids all such complications. Correcting amplitudes for “noise” is fraught with the same problems. In this project we used a straightforward (automated) approach to find low and high frequencies of a spectrum where it departs from *normal* physical behavior, i.e., inflections at frequencies where noise starts biasing the spectrum high from expected decay (cf. Figure 86). Although not all cases are easy, examination and fitting of thousands of spectra suggests that such frequency ranges can be found for most. Further work is needed to implement and test fully automatic criteria to supplement the SNR tests, and assess improvements to tomography results, particularly for low Q paths.

Third, while Pg is typically more stable than Pn, there are only a fraction of Pg observations, compared to Pn. The results we presented indicate the importance of Pn for discrimination, and the need to improve calibration of Pn geometric spreading and *Q* models. Using reviewed data with well-constrained source terms, Pn clearly departs from constant power-law spreading (cf. Figure 110), due to upper mantle triplication, sphericity, and other complicated Pn propagation effects (e.g., Yang et al., 2007; Yang, 2011; Avants et al., 2011). We compared our results to the frequency-dependent, semi-empirical spreading model of Yang (2011). The Y2011 Pn spreading predictions are very inconsistent with source-corrected Pn spectra, leading to unrealistically low Q estimates, illustrated for LNTS (e.g., Pn Q_0 = 68 for the path to AAK, compared to about 370 from our analysis and amplitude tomography). Based on research by Avants et al. (2011), we discussed deficiencies in the Y2007 model simulations, which cause their model to predict considerably higher Pn amplitudes at farther distances and higher frequencies than exhibited by real data. In addition, the Y2011 model uses either 6 or 12 parameters to characterize the distance and frequency dependence of Pn spreading, a single physical effect. Note that past Pn tomography runs, using constant power-law Pn spreading corrections, obtained some extremely high, or even negative, Pn *Q* estimates. Accurate source terms and a Pn spreading model that accounts for this rise at far regional distances may remedy unphysical Pn *Q* results from amplitude tomography.

Comparing our results to tomography, we also showed that Pn *Q* estimates are verified for many paths, but there are also many large differences, much more so for areas lacking good ray-path sampling. Tomography Pn Q estimates in the lowest and higher bands are consistently higher than our estimates. Pn spectral variability also causes some of our fits of source-corrected spectra, and Q estimates, to be unreliable. We showed that the median of 3C spectra, rather than the average, is more robust for cases where one channel is more affected than the other two. For other paths/stations (e.g., ARU and KIV), spectral variability was so pronounced that our Q estimates have large uncertainties (i.e., residuals to the Q model fits), even using the median. In such cases, averaging over more events may be necessary to reduce the variability. Pn spectral variability is exacerbated for paths shorter than about 500 km, for which the measurement windows must necessarily be shorter to not include Pg signals. Pseudo-spectral amplitude measurements in the time domain may improve the stability and resulting Q estimates. Further work is needed to test enhancements to Pn processing. It should be stressed that calibration of Pn is a very hard problem because of its variability from a host of complicated effects. However, more accurate, robust, and compact Pn *Q* and spreading models are attainable than currently exist. These three problems are not minor; we showed order-of-magnitude errors that directly impact P/S discrimination results. Rectifying them and incorporating the enhancements in calibrations are essential.

12 ACKNOWLEDGEMENTS

We thank David Yang and Thorne Lay for useful discussions regarding Pn geometric spreading. Seismic data from the IRIS Data Management Center were used for this study. This work was sponsored by the Air Force Research Laboratory and the Department of Energy National Nuclear Security Administration under contracts FA8718-09-C-0005 and LA09-BAA09-01-NDD03.

REFERENCES

Abercrombie, R. E., K. M. Mayeda, W. R. Walter, G. M. Viegas, and Rengin Gok (2009). Seismic source scaling and discrimination in diverse tectonic environments, *in Proceedings of the 2009 Monitoring Research Review: Ground-Based Nuclear Explosion Monitoring Technologies*, LA-UR-09-05276, Vol. 1, pp. 419-429.

Antolik, M., and D. S. Dreger (2003). Rupture process of the 26 January 2001 M_w 7.6 Bhuj, India, earthquake from teleseismic broadband data, *Bull. Seism. Soc. Am.* **93,** pp. 235–1248.

Avants, M., T. Lay, X.-B. Xie, and X. Yang (2011). Effects of 2D random velocity heterogeneities in the mantle lid and Moho topography on Pn geometric spreading, *Bull. Seism. Soc. Am., 101*, pp. 126-140.

Bodin, P., and S. Horton (2004). Source parameters and tectonic implications of aftershocks of the Mw 7.6 Bhuj earthquake of 26 January 2001, *Bull. Seismol. Soc. Am.*, **94**, pp. 818–827.

Bodin, P., L. Malagnini, and A. Akinci (2004). Ground-motion scaling in the Kachchh Basin, India, deduced from aftershocks of the 2001 Mw 7.6 Bhuj earthquake, *Bull. Seismol. Soc. Am.*, **94**, pp. 1658–1669.

Bottone, S., M. D. Fisk and G. D. McCartor (2002). Regional seismic event characterization using a Bayesian formulation of simple kriging, *Bull. Seism. Soc. Am.,* **92**, pp. 2277-2296.

Brune, J. N. (1970). Tectonic stress and the spectra of seismic shear waves from earthquakes, *J. Geophys. Res.,* **75**, pp. 4997-5009.

Choy and Boatwright (1995). Global patterns of radiated seismic energy and apparent stress, *J. Geophys. Res.,* **100**, pp. 18,205-18,228.

Fisk, M. D. (2007). Corner frequency scaling of regional seismic phases for underground nuclear explosions at the Nevada Test Site, *Bull. Seism. Soc. Am*., **97**, pp. 977-988.

Fisk, M. D. (2006). Source spectral modeling of regional P/S discriminants at nuclear test sites in China and the Former Soviet Union, *Bull. Seism. Soc. Am*., **96**, pp. 2348–2367.

Fisk, M. D., S. Bottone, and G. D. McCartor (2001). Regional Seismic Event Characterization Using Bayesian Calibration, MRC-R-1621, Mission Research Corp., Santa Barbara, CA.

Fisk, M. D., H. L. Gray and G. D. McCartor (1996). Regional discrimination without transporting thresholds, *Bull. Seism. Soc. Am.,* **86**, pp. 1545-1558.

Fisk, M. D., H. L. Gray, and G. D. McCartor (1993). Applications of Generalized Likelihood Ratio Tests to Seismic Event Identification, PL-TR-93-2221, Mission Research Corp., Santa Barbara, CA.

Fisk, M. D., G. D. McCartor, and S. R. Taylor (2008). Robust Magnitude, Distance, and Path-Specific Corrections for Regional Seismic Phases by Constrained Inversion and Enhanced Kriging Methods, ATK/NCR-0608-501, Alliant Techsystems, Newington, VA.

Fisk, M. D. and W. S. Phillips (2011). Constraining source terms, regional attenuation models, and site effects, *in Proceedings of the 2011 Monitoring Research Review: Ground-Based Nuclear Explosion Monitoring Technologies*, Vol. 1, pp. 59-68.

Fisk, M. D. and W. S. Phillips (2010). A stepwise, iterative procedure to constrain stress drop, regional attenuation models, and site effects, *in Proceedings of the 2010 Monitoring Research Review: Ground-Based Nuclear Explosion Monitoring Technologies*, Vol. 1, pp. 57-66.

Fisk, M. D. and W. S. Phillips (2009). A stepwise, iterative procedure to constrain stress drop, regional attenuation models, and site effects, *in Proceedings of the 2009 Monitoring Research Review: Ground-Based Nuclear Explosion Monitoring Technologies*, Vol. 1, pp. 52-61.

Fisk, M. D. and S. R. Taylor (2008). Applications of a constrained inversion and an extended kriging method to improve source, path, and site corrections for regional seismic phases, *in Proceedings of the 30th Monitoring Research Review, Ground-Based Nuclear Explosion Monitoring Technologies*, Vol. 1, pp. 40-49.

Fisk, M. D. and S. R. Taylor (2006). Robust magnitude and path corrections for regional seismic phases in Eurasia by constrained inversion and enhanced kriging techniques, *in Proceedings of the 28th Monitoring Research Review, Ground-Based Nuclear Explosion Monitoring Technologies*, Vol. 1, pp. 15-24.

Fisk, M. D., S. R. Taylor, W. R. Walter, and G. E. Randall (2010). Seismic Event Discrimination and Modeling Using Two-Dimensional Grids of Regional P/S Spectral Ratios, ATK-R-1744, Final Technical Report, NNSA Contract DE-AC52-07NA28116.

Madariaga, R. (1976). Dynamics of an expanding circular fault, *Bull. Seism. Soc. Am.,* **66**, pp. 639-667.

Malagnini, L., P. Bodin, K. Mayeda, and A. Akinci (2006). Unbiased moment-rate spectra and absolute site effects in the Kachchh Basin, India, from the analysis of the aftershocks of the 2001 M_W 7.6 Bhuj Earthquake, *Bull. Seism. Soc. Am.,* **96**, pp. 456-466.

Mayeda, K. M., L. Malagnini, and W. R. Walter (2007). A new spectral ratio method using narrow band coda envelopes: evidence for non-self-similarity in the Hector Mine sequence, *Geophys. Res. Lett.,* **34**, L11303.

Mayeda, K., A. Hofstetter, J. L. O'Boyle, and W. R. Walter (2003). Stable and transportable regional magnitudes based on coda-derived moment-rate spectra, *Bull. Seism. Soc. Am.,* **93**, pp. 224-239.

Mendoza, C., and S. Hartzell (2009). Source analysis using regional empirical Green's functions: The 2008 Wells, Nevada, earthquake, *Geophys. Res. Lett.,* **36**, L11302, doi:10.1029 2009GL038073.

Phillips, W. S. (1999). Empirical path corrections for regional seismic phases, *Bull. Seism. Soc. Am.,* **89**, pp. 384-393.

Phillips, W. S., G. E. Randall and S. R. Taylor (1998). Path correction using interpolated amplitude residuals: An example from central China, *Geophys. Res. Lett.,* **25**, pp. 2729-2732.

Phillips, W. S., R. J. Stead, G. E. Randall, H. E. Hartse and K. Mayeda (2008). Source effects from broad area network calibration of regional distance coda waves, *in Scattering of Short Period Waves in the Heterogeneous Earth*, H. Sato and M.C. Fehler, Editors, pp. 319-351.

Schaff, D. P. and P. G. Richards (2004). Repeating seismic events in China, *Science*, **303**, 1176-1178.

Sereno T. J., S. R. Bratt and T. C. Bache (1988). Simultaneous inversion of regional wave spectra for attenuation and seismic moment in Scandinavia, *J. Geophys. Res.,* **93**, 2019-2035.

Singh, S. K., J. F. Pacheco, B. K. Bansall, X. Pe´rez-Campos, R. S. Dattatrayam, and G. Suresh (2003). A source study of Bhuj, India, earthquake of 26 January, 2001 (M_w7.6), in *Proc. of the Indo–US Workshop on Seismicity and Geodynamics*, National Geophysical Research Institutue, Hyderabad, India, 6–10 October 2003.

Street, R., R. Herrmann, and O. Nuttli (1975). Spectral characteristics of Lg wave generated by central United States earthquakes, Geophys. *J. R. Astron. Soc.,* **41**, pp. 51-63.

Taylor, S. R., and H. E. Hartse (1998). A procedure for estimation of source and propagation amplitude corrections for regional seismic discriminants, *J. Geophys. Res.,* **103**, pp. 2781-2789.

Taylor, S. R., A. A. Velasco, H. E. Hartse, W. S. Phillips, W. R. Walter, and A. J. Rodgers (2002). Amplitude corrections for regional seismic discriminants, *Pure and Appl. Geophys., Special Edition on Monitoring the Comprehensive Nuclear-Test-Ban Treaty: Seismic Event Discrimination and Identification,* **159**, pp. 623-650.

Walter, W. R., K. M. Mayeda, and H. J. Patton (1995). Phase and spectral ratio discrimination between NTS earthquakes and explosions. Part I: Empirical observations, *Bull. Seism. Soc. Am.*, **85**, pp. 1050-1067.

Walter, W. R. and S. R. Taylor (2002). A Revised Magnitude and Distance Amplitude Correction (MDAC2) Procedure for Regional Seismic Discriminants: Theory and Testing at NTS, UCRL-ID-146882, Lawrence Livermore Naitonal Laboratory, Livermore, CA.

Xie, J. and H. J. Patton (1999). Regional phase excitation and propagation in the Lop Nor region of central Asia and implications for P/Lg discriminants, *J. Geophys. Res.,* **104**, pp. 941-954.

Yang, X. (2011). A Pn spreading model constrained with observed amplitudes in Asia, *Bull. Seism. Soc. Am.,* **101**, pp. 2201-2211.

Yang, X., T. Lay, X.-B. Xie, and M.S. Thorne (2007). Geometric spreading of Pn and Sn in a spherical Earth model, *Bull. Seism. Soc. Am.,* **97**, pp. 2053-2065.

DISTRIBUTION LIST

DTIC/OCP 8725 John J. Kingman Rd, Suite 0944 Ft Belvoir, VA 22060-6218	1 cy
AFRL/RVIL Kirtland AFB, NM 87117-5776	2 cys
Official Record Copy AFRL/RVBYE/Robert Raistrick	1 cy